Enhancing additively manufactured polymers through functional diamond-like carbon coatings

Frank Dangnan

Submitted in accordance with the requirement for the degree of

Doctor of Philosophy

The University of Leeds

School of Mechanical Engineering

November, 2021

The candidate confirms that the work submitted is his own, except where work which has formed part of jointly authored publications has been included. The contribution of the candidate and the other authors to this work has been explicitly indicated below. The candidate confirms that appropriate credit has been given within the thesis where reference has been made to the work of others.

In these papers listed below, the primary author completed all experimental studies, evaluation of data and preparation of publications. All authors contributed to the proofreading of the articles before publication and discussion of the results presented.

Papers contribution to this thesis:

‘F. Dangnan, C. Espejo, T. Liskiewicz, M. Gester and A. Neville, "Friction and wear of additive manufactured polymers in dry contact," Journal of Manufacturing Processes, vol. 59, pp. 238-247, 2020’.

‘F. Dangnan, C. Espejo, T. Liskiewicz, M. Gester and A. Neville, “Water barrier performance of additive manufactured polymers coated with diamond-like carbon films,” Diamond and Related Materials, 2021,119’.

Acknowledgements

First and foremost, I would like to extend my sincere gratitude to my supervisor, Prof. Anne Neville, who has the attitude and substance of a genius and continually conveyed the spirit of adventure and positivity throughout this work. Your insight and numerous anecdotes made the entire research work very enjoyable, thank you.

I would also like to express my sincere gratitude to my secondary supervisors, Prof. Tomasz Liskiewicz and Dr Cayetano Espejo Conesa for providing invaluable guidance throughout this research. Thanks to my industrial supervisor, Dr Gester Matthias for his countless support on project discussions and delivery. I appreciate you all for the excellent guidance and challenging questions posed during our brainstorming sessions on this project.

Special thanks go to the staff and technicians of both IFS and LEMAS for their helpful suggestions, most specifically to Tony and Stuart for their contributions in both material characterisation Labs and SEM imaging respectively.

To all my friends and colleagues, I shared a common office and aspiration with at the School of Mechanical Engineering Room 3.34a, especially Sam, Blake and Taufiq, I say thanks to you all for the good laugh.

Finally, a big thank you to my family most especially my lovely parents Mr. & Mrs Damtarl, my wife Mrs Afia Dangnan, my son Zayne, siblings, and Nana. Without your continued support over the past couple of years, this noble achievement wouldn't have been possible. God richly bless you all for your kindness.

Abstract

By providing the required structural modification to polymeric materials through functional coatings, polymer-based materials (PBMs) can provide significant material functionality and improve performance in both material design and product finishing. This added advantage may provide extended durability, aesthetic appeal, barrier functions and improve tribological performance to the polymer. PBMs especially additively manufactured polymers (3D printed polymers) come with enormous physical, structural, mechanical and chemical challenges in both design and product application phases and can only be mitigated using an integrated surface engineering approach.

In this study, the use of a novel microwave-plasma-enhanced chemical vapour deposition (MW-PECVD) technique has been assessed for its viability in depositing single layer diamond-like carbon (DLC) coatings directly unto 3D printed polymers.

Before the deposition, a comprehensive assessment to understand the performance limitations of the mechanical, thermal, pore structure and water absorption properties of all selected 3D printed parts were made.

The Hauzer Flexicoat 850 system which houses within two microwave sources was utilized in the DLC deposition process to offer a uniquely designed and tailored coating structure. Three DLC coatings were developed and deposited onto two photocurable additively manufactured polymers namely acrylonitrile butadiene styrene-like (3D ABS) and Verogray. The parameters of particular interest for the deposition process including N_2, C_2H_2 gas flow rates and micro-wave power input were studied to determine the effect these process variations have on the coating architecture, structure and performance from the nano to the macro scale. Initial adhesion testing of the coating using scratch testing showed complete coating failure at loads < 5N.

A preliminary design of experiment (DOE) approach was established as a base framework to understand the relationship between the process parameters and coating adhesion. Further coatings based on this design were produced to explore the variable applications and limitations for characterising the hard-on-soft polymer-coating matrix. Coating characterisation techniques such as scratch testing, nano-indentation, Raman spectroscopy, X-ray photoelectron spectroscopy (XPS) were employed to assess both the mechanical and structural properties of the coating.

The coating produced in this work has shown measurable mechanical and structural properties, in particular high hardness and improved adhesion in comparison with similar DLCs reported in the literature. The ability of the coating to provide additional functionality such as tribological and water vapour barrier functions is assessed in this work. This study has shown that it is viable to use DLC for both barrier and tribological applications.

Table of Content

Acknowledgements ..... **iii**

Abstract ..... **iv**

Table of Content ..... **vi**

List of Figures ..... **xi**

List of tables ..... **xx**

Chapter 1 ..... **1**

Introduction 1

1.1 Tribology application for additively manufactured polymers 4

1.1 Aims and objectives 5

1.2.1 Aim 5

1.2.2 Objectives 6

1.3 Thesis outline 7

Chapter 2 ..... **9**

Literature Review 9

2.1 Introduction 9

2.2 Theory of polymer science 9

2.3 Additive manufacturing 11

2.3.1 Photopolymerization in additive manufactured polymers 12

2.3.2 Additive manufacturing technique 19

2.3.3 Challenges and prospects of additive manufacturing 24

2.4 Coating synthesis 25

2.4.1 Introduction 25

2.4.2 Plasma synthesis and characterisation 25

2.4.3 Thin film deposition techniques 26

2.5 Diamond-like carbon coating 28

2.5.1 DLC structure and bonding mechanism 28

2.6 DLC as a functional coating for polymer-based materials 33

2.7 Thin film adhesion on polymer 38

2.8 Tribology 41

2.8.1 Fundamentals of tribology 41

2.8.2 Friction of polymers 41

2.8.3 Wear of polymers 42
2.8.4 Tribology of coated polymers 45
2.8.5 Tribology of additively manufactured polymers 46
2.9 Polymer permeability 47
2.9.1 Introduction 47
2.9.2 Mechanism of gas permeation 48
2.10 Water sorption 50
2.11 Overview of current coatings for improving barrier properties 51
2.12 Surface texturing 53
2.12 Summary 54
Chapter 3 ..... **56**
Experimental methodology 56
3.1 Introduction 56
3.2 Sample preparation and characterisation 57
3.2.1 Polymer selection and preparation 57
3.2.2 Thermal analysis 59
3.2.4 Mechanical property analysis 61
3.2.5 Water absorption 63
3.2.6 Mercury porosimetry 63
3.2.7 Surface texturing 64
3.2.8 Surface roughness measurement 65
3.2.9 Mechanical surface polishing 65
3.3 DLC coating and deposition 66
3.3.1 Introduction 66
3.3.2 Coating system 66
3.3.3 Substrate preparation 68
3.3.4 Coating deposition using MW-PECVD 68
3.3.5 Substrate temperature control 70
3.4 Coating assessment and performance analysis 71
3.4.1 Surface morphology 71
3.4.2 Chemical composition and bonding characterization 72
3.4.3 Mechanical Properties 73
3.4.4 Contact angle measurement 75
3.4.5 X-ray photoelectron spectroscopy (XPS) 75
3.4.6 Water sorption 77
3.4.7 Barrier properties 77

3.4.8 Tribology 79
Chapter 4 ..... **83**
Results & Discussion: 3D Polymer characterisation 83
4.1 Thermal characterisation 83
4.1.1 Thermal stability of additively manufactured polymers using TGA 83
4.1.2 Activation energies and degradation of additively manufactured polymers 86
4.1.3 Glass transition analysis using DSC 88
4.2 Mechanical testing 89
4.3 ASTM D570 water absorption test 93
4.4 Surface chemistry analysis 94
4.5 Roughness measurement 95
4.6 Pore size distribution 97
4.7 Material selection 99
4.8 Summary 99
Chapter 5 ..... **101**
Results & Discussion: DLC film deposition and characterisation 101
5.1 Introduction 101
5.2 Process recipe characterisation 101
5.3 Substrate heating 102
5.4 Surface roughness 105
5.5 Coating adhesion 106
5.6 Modification of DLC coating 107
5.6.1 Substrate heating 109
5.6.2 Deposition rate 110
5.7 Modified DLC coating adhesion 112
5.7.1 Surface energy and wetting 112
5.7.2 Scratch test 113
5.8 Coating fracture toughness 116
5.8.2 Coating failure 117
5.8 Summary 120
Chapter 6 ..... **121**
Results & Discussion: Coating structure and composition 121
6.1 Introduction 121
6.2 Coating structure 121
6.3 Atomic force microscopy (AFM) 122
6.4 Nano-Indentation 125

6.4.1 Polymer hardness properties 126
6.4.2 DLC composite hardness 127
6.5 Raman spectroscopy 128
6.5.1 Correlation between coating hardness and ID/IG 131
6.6 X-ray photoelectron spectrum (XPS) 131
6.7 Summary 133
Chapter 7 ..... **134**
Results & Discussion: Friction and wear 134
7.1 Introduction 134
7.2 Friction 134
7.2.1 Time frictional response for uncoated additively manufactured polymers 134
7.2.2 Time frictional response for DLC coated additively manufactured polymers 137
7.2.3 Steady-state friction response 140
7.2.4 Wear analysis and mechanism 142
7.2 Summary 148
Chapter 8 ..... **150**
Results & Discussion: Barrier and water absorption function 150
8.1 Introduction 150
8.2 WVTR of barrier films 150
8.2.1 Effect of nitrogen gas flow rate on the WVTR function 150
8.2.2 Surface texturing effect on the WVTR 152
8.3 Dynamic water vapour sorption (DVS) 157
8.3.1 Water sorption at constant temperature and relative humidity 157
8.3.2 Temperature dependence water vapour sorption properties 158
8.4 Summary 161
Chapter 9 ..... **163**
General Discussion 163
9.1 Introduction 163
9.2 Effect of the 3D substrate 163
9.3 Coating deposition & characterisation 166
9.4 Tribology 168
9.5 Barrier function 171
9.6 Uniqueness of this coating system 174
Chapter 10 ..... **178**
Conclusions 178

10.1 Sample preparation and characterisation 178
10.2 DLC coating and deposition 179
10.3 Coating assessment and performance analysis 179
10.4 Further work 180
References **182**
Appendix I **1**
Appendix II **2**
Appendix III **4**
Appendix IV **6**
Appendix V **7**
Appendix VI **9**

List of Figures

Figure 1-1- Current application and projected future potential of 3D printing by industry [7]... 2
Figure 1-2- Part manufacturing using AM systems in the production industry [8]. 2
Figure 2-1- Mayo and Flory Mechanism [33]. 10
Figure 2-2- Schematics of the chain structure of (a) an amorphous (b) Semi-crystalline polymer [36]. 11
Figure 2-3- Basic structure of an epoxide group [39]. 12
Figure 2-4- Photopolymerization reaction [48]. 15
Figure 2-5- Anionic polymerisation (a) initiation (b) propagation(c) termination steps [56]. 16
Figure 2-6- Cationic polymerisation (a) initiation (b) propagation (c) termination steps [56]. ... 17
Figure 2-7- Commercially available monomers used in cationic 3D photopolymerization [60].. 17
Figure 2-8- Schematic representation of an SLA technique [67]. 20
Figure 2-9- Object Polyjet 3D printing [66]. 21
Figure 2-10- Basic selective laser sintering technique [70]. 22
Figure 2-11- Fused filament fabrication process principle and schematics 23
Figure 2-12- The hybridization bonding state of carbon showing sp^3, sp^2, sp^1 [101]. 29
Figure 2-13- Electronic configuration of carbon [102]. 29
Figure 2-14- Carbon structure showing (a) sp^3 tetrahedral bonds in diamond (b) sp^2 planar bond in graphite [101]. 29
Figure 2-15- A ternary phase diagram showing the classification of DLC structures [101] 31
Figure 2-16- Schematic diagram showing the mechanism of DLC formation using MW-PECVD technique [105]. 32
Figure 2-17- Deposition rate of a-C:H by PECVD vs. ionization potential of some useful precursor gases [101]. 33
Figure 2-18- Temperature development measured for different engineering materials [129]. ... 36
Figure 2-19- Substrate temperature dependence curve [130]. 37
Figure 2-20- Abrasive wear mechanism showing (a) two-body (b) three-body abrasion mechanism [158]. 43
Figure 2-21- Fatigue wear damage on epoxy resin [146]. 44
Figure 2-22- Diagram showing a typical adhesive wear process [158]. 44
Figure 2-23- Polymer fragmentation transfer film against steel showing the deformation on (a) and (b) HDPE, (c), (d) and (e) PA and (f) PTFE [158]. 45
Figure 2-24- Tribological behaviour of pure acrylonitrile butadiene styrene manufactured using fused deposition modelling (FDM) (a)friction coefficient and (b) specific wear rate. * - P is the negative gap width +P is the positive gap width [83]. 47
Figure 2-25- Diffusion through polymer membrane showing the different resistance [181]. 49

Figure 2-26- Sorption models for polymer sorbate interaction at equilibrium [181]. 51
Figure 3-1- Summary outline of the experimental methodology utilised in this study. 56
Figure 3-2- Sample diagram of (a) Stratasys® Objet 1000TM 3d printer (b) P3 mini multi lens envisionTech™ P4K series 3d printer [201]. 58
Figure 3-3- Process flow diagram for the development and manufacture of the 3D printed parts for both Polyjet and envisionTech™. 58
Figure 3-4- Schematic presentation of TGA [203]. 61
Figure 3-5- Sample plot showing force-displacement cycle curve from a uniaxial tension test [204]. 62
Figure 3-6- Schematic representation of the ASTM D638 Type IV tensile specimen with geometric specification in mm. 62
Figure 3-7- Image of the proposed textured surface for (a) texture A and (b) textured B. 64
Figure 3-8- Optical image of the Polyjet printed substrate detailing both textured substrates A and B. 64
Figure 3-9- Schematic view of the central part of the bending device and definition of direction used for the three-point test. 65
Figure 3-10- Top view deposition chamber of the Hauzer Flexicoater 850. 66
Figure 3-11- Schematic diagram showing the microwave power source antenna (a) frontal view (b) side view. 67
Figure 3-12- (a) Schematic representation of a typical AFM scanner probing a macroscopically flat surface by a sharp contact probe. (b) at very small separation distance, the atomic structure of both surfaces become very important defined by the separation distance (Z). (c) Varying atomic force interactions are determined from different heights in the Z direction [211]. 72
Figure 3-13- Schematic representation of the X-ray photoemission process [215]. 76
Figure 3-14- Shows the three-stage fabrication procedure for masking the individual test samples for WVTR testing with (a) lapping of the individual test samples using Aluminium mask (b) complete masking procedure (c) test sample showing exposed test area of 1cm^2. 78
Figure 3-15- Schematic representation showing (a) dimensions of the masked additively manufactured samples (b) cross-sectional view with the corresponding dimension. 78
Figure 3-16- Schematic representation of the WVTR test showing both (a) Untextured (b) textured surfaces. 79
Figure 3-17- Graphic representation of the Polyjet printer bed orientations (flat) and raster angle [0/90] investigated in this experiment. 80
Figure 3-18- Contact schematics used for the friction test. 80
Figure 4-1-TGA Curves showing the percentage mass change (%) of 3D printed (a) ABS (b)Verogray (c) Veroblue (d)LS600 (e) RCPO30 in both air and nitrogen as a function of varying temperature. 85

Figure 4-2- Arrhenius plot of degradation for additively manufactured (a) 3D ABS (b) Verogray (c) Veroblue (d) LS600 (e) RCP30 using Murray and White methods. 87
Figure 4-3- DSC plot showing both experimental and literature glass transition temperature for all additively manufactured samples using DSC Q20. 89
Figure 4-4- Schematic plot showing the relevant tensile stress-strain properties calculated in this study. 90
Figure 4-5- Plot showing the stress-strain properties of all 3D printed polymers (ABS, Verogray, Veroblue, LS600 and RCP30) using an INSTRON close-loop axial loading system. 91
Figure 4-6- A photograph of the gage section of all tested 3D printed polymers showing the common failure modes. 92
Figure 4-7- ASTMD570 water absorption plot showing the percentage of water absorbed after 24hrs of testing for the individual 3D printed polymers. 93
Figure 4-8- FTIR spectra showing the transmittance(%) for the individual 3D polymers studied. 94
Figure 4-9- Surface roughness profile of 3D printed substrates. 96
Figure 4-10- Average surface roughness of all printed substrates 97
Figure 4-11- MICP plot for both 3D ABS and Verogray showing the capillary pressure variation against saturation fraction for mercury 98
Figure 4-12- MICP plot showing the pore size distribution function against pore size radius for both 3D ABS and Verogray samples. 98
Figure 5-1- Temperature evolution during deposition leg for DOE-1,2 and 3 with plots showing each deposition step made to deposit the DLC coating. 103
Figure 5-2- Plot of the average heating rate of DLC deposition step for each deposition Leg determined from individual rotating thermocouples located at the same working distance as the substrate during. 103
Figure 5-3- Variation of (a) coating thickness and (b) deposition rate for all DOE Legs studied on both 3D ABS and Verogray samples. 104
Figure 5-4- The relationship between the roughness of the DLC coated surfaces and that of the pristine substrate surface for (a) 3D ABS and Verogray(b). 105
Figure 5-5- SEM Image showing the surface morphology for both uncoated and coated 3D ABS (shown as (a) and (b) for coated and uncoated 3D ABS respectively) and Verogray (shown as (c) and (d) for uncoated and coated Verogray respectively) for DOE 1. 106
Figure 5-6- Coating adhesion response to progressive load scratch test from 0-5N on 3D ABS and Verogray for DOE1 (a), DOE2 (b) and DOE3 (c). 107
Figure 5-7- Plot showing the (a) temperature evolution during deposition leg for DLC/1 with plots showing each deposition step made to deposit the DLC coating (b) combine average minimum and maximum temperature attained for each DLC coating during coating. 109

Figure 5-8- Plot showing the average heating rates for DLCs 1-5 110
Figure 5-9- Deposition rate for modified DLC coatings. 111
Figure 5-10- Coating thickness for modified DLC coatings. 111
Figure 5-11- Water contact angle measurement for both pristine and plasma surface etched after 3mins for 3d printed ABS and Verogray. 112
Figure 5-12- Typical failure mode of DLC/1 coatings on pristine additively manufactured (a) ABS (b) Verogray. Black arrow shows scratch direction. 114
Figure 5-13- Typical failure of DLC/2 coating on pristine additively manufactured (c) ABS and(d) Verogray. 114
Figure 5-14- Shows the Individual critical loads defining the coating deformation regimes for DLC/1-5 for unpolished 3D ABS (a) and Verogray (b). 114
Figure 5-15- Typical failure mode of DLC/1 coatings on polished 3D printed (a) ABS (b) Verogray. The black arrow shows scratch direction. 115
Figure 5-16- Typical failure mode of DLC/2 coatings on polished 3D printed (c) ABS (d) Verogray. The black arrow shows scratch direction. 115
Figure 5-17- Shows the Individual critical loads defining the coating deformation regimes for DLC/1-5 for polished 3D ABS (a) and Verogray (b). 116
Figure 5-18- A typical flexure curve of 3D- polymer showing the kinking and bending failure of the crack during its propagation. 117
Figure 5-19- Cracking behaviour of DLC/1 coating on 3D ABS after bending showing coating deformation pattern on all three surfaces defined as (a) untextured coated surface (b) textured type A (c) textured type B. 119
Figure 5-20- Morphology of DLC/1 coating on 3D Verogray showing no surface deformation after bending on all three surfaces defined as (a) untextured coated surface (b) textured type A (c) textured type B. 119
Figure 5-21- Coating deformation behaviour exhibited by DLC/2 coating on 3D ABS after bending showing coating deformation pattern on all three surfaces defined as (a) untextured coated surface (b) textured type A (c) textured type B. 119
Figure 5-22- Morphology of DLC/2 coating on 3D Verogray showing no surface deformation after bending on all three surfaces defined as (a) untextured coated surface (b) textured type A (c) textured type B. 119
Figure 6-1- Cross sectional SEM image showing coating thickness properties on both 3D ABS and Verogray substrates. Cross section shown as (a),(c),(d),(e),(g),(i) represents 3D ABS samples coated under DLC/1-5 respectively. Samples (b),(d),(f),(h),(j) represents Verogray coated samples for DLC/1-5 respectively. 121
Figure 6-2- AFM Image of uncoated samples showing 3D printed ABS (a) and Verogray (b). Red arrows indicate surface defects in the form of micro and macro-pits on polymer surfaces. 123

Figure 6-3- AFM image of DLC/1 films deposited on (c) 3D ABS and (d) Verogray. 123
Figure 6-4- AFM image of DLC/2 film deposited on 3D ABS (e) and Verogray (f)..... 123
Figure 6-5- AFM image of DLC/3 film deposited on 3D ABS (g) and Verogray (h)..... 124
Figure 6-6- AFM surface scan showing quantitative depth-sensing of substrate nanoscale cavities for 3D printed ABS (a) and Verogray(b) for all coated and uncoated samples. 124
Figure 6-7- Surface roughness quantification using AFM scan of the individual surfaces. P/O is the pristine uncoated 3D printed samples. DLC/1, DLC/2, and DLC/3 are the coated samples deposited with 0, 10 and 20sccm of nitrogen flow. 124
Figure 6-8- Hardness of pristine (P/0) 3D ABS and Verogray at different indentation depths. 126
Figure 6-9- Young's modulus for pristine (P/0) 3D ABS and Verogray polymers measured at different depths. 127
Figure 6-10- Hardness values of DLC coating structures on both 3D ABS and Verogray substrate. 128
Figure 6-11- Young's modulus of MW-DLC coated samples..... 128
Figure 6-12- Raman spectra of DLC films grown at different nitrogen and acetylene gas flow rates. 130
Figure 6-13- Correlation between I_D/I_G and hardness. 131
Figure 6-14- C1s and N1s atomic concentration as a function of depth for (a) Carbon and (b) Nitrogen. 133
Figure 7-1- A comparative plot showing the variation of friction coefficient behaviour under varying contact load and print orientation: (a) parallel to print for 3D ABS (b) perpendicular to print orientation for 3D ABS (c) parallel to print orientation for 3D Verogray (d) perpendicular to print orientation for 3D Verogray..... 136
Figure 7-2- A comparative plot showing the variation of friction coefficient behaviour under varying contact load and print orientation for DLC/1 coated polymers: (a) parallel and (b) perpendicular to print orientation for 3D printed ABS, (c) parallel and (d) perpendicular to print orientation for 3D printed Verogray. 138
Figure 7-3- A comparative plot showing the variation of friction coefficient behaviour under varying contact load and print orientation for DLC/2 coated polymers: (a) parallel and (b) perpendicular to print orientation for 3D printed ABS, (c) parallel and (d) perpendicular to print orientation for 3D printed Verogray. 139
Figure 7-4- A comparative plot showing the variation of friction coefficient behaviour under varying contact load and print orientation for DLC/3 coated polymers: (a) parallel and (b) perpendicular to print orientation for 3D printed ABS, (c) parallel and (d) perpendicular to print orientation for 3D printed Verogray. 140
Figure 7-5- Steady-state summary result showing the coefficient of friction result for the uncoated 3D printed (a) ABS and (b) Verogray. 141

Figure 7-6- Steady-state summary result showing the coefficient of friction results for the coated 3D printed (a) ABS and (b) Verogray. 142
Figure 7-7- Specific wear rate at 1, 5 and 10N for (a) 3D ABS (b) Verogray. 143
Figure 7-8- Specific wear rate of DLC coated 3D printed (a) ABS (b) Verogray at 5N load. ... 144
Figure 7-9- SEM images of 3D-printed ABS showing the influence of polymer print orientation on wear under dry reciprocating sliding condition oriented parallel to the sliding direction at varying applied load for (a) 1N (b) 5N (c) 10N. 145
Figure 7-10- SEM images of 3D-printed ABS showing the influence of polymer print orientation on wear under dry reciprocating sliding condition oriented perpendicular to the sliding direction at varying applied load for (a) 1N (b) 5N (c) 10N..... 145
Figure 7-11- SEM images of 3D-printed Verogray showing fatigue damage under dry reciprocating sliding condition oriented parallel to the sliding direction at varying applied load for (a) 1N (b) 5N (c) 10N. 145
Figure 7-12- SEM images of 3D-printed Verogray showing the influence of polymer print orientation on wear under dry reciprocating sliding condition oriented perpendicular to the sliding direction at varying applied load for (a) 1N (b) 5N (c) 10N. 145
Figure7-13- DLC/1 coated ABS substrate showing the deformation on (a) parallel (b) perpendicular orientation to the applied load of 1N. 146
Figure7-14- DLC/1 coated Verogray substrate showing the deformation on (c) parallel (d) perpendicular orientation to the applied load of 1N. 146
Figure 7-15- Wear track showing coating damage on 3D ABS for (a) DLC/1 (b) DLC/2 (c) DLC/3 for dry reciprocating sliding at 5N load for parallel orientation. Red arrow shows the sliding direction 147
Figure 7-16- Wear track showing coating damage on 3D ABS for (a) DLC/1 (b) DLC/2 (c) DLC/3 for dry reciprocating sliding at 5N load for perpendicular orientation. Red arrow shows the sliding direction. 147
Figure 7-17- Wear track showing coating performance on Verogray for (a) DLC/1 (b) DLC/2 (c) DLC/3 for dry reciprocating sliding at 5N load for parallel orientation. The red arrow shows the sliding direction. 148
Figure 7-18- Wear track showing coating performance on Verogray for (a) DLC/1 (b) DLC/2 (c) DLC/3 for dry reciprocating sliding at 5N load for parallel orientation. The red arrow shows the sliding direction. 148
Figure 8-1- MOCON WVTR rate curve showing the WVTR function with time for both 3D printed ABS and Verogray. 151
Figure 8-2- A comparative plot showing the average WVTR rate function for both 3D ABS and Verogray. 152

Figure 8-3- MOCON WVTR rate curve showing the WVTR function with time for both 3D printed ABS and Verogray for textured surface A and B. 153
Figure 8-4- A comparative plot showing the average WVTR rate function for both ABS and Verogray. 153
Figure 8-5- A comparative plot showing the effect of surface texturing on the WVTR function of 3D printed ABS polymer for (a) DLC/2 and (b) DLC/5. 154
Figure 8-6- A comparative plot showing the effect of surface texturing on the WVTR function of 3D printed Verogray polymer for (a) DLC/2 and (b) DLC/5 155
Figure 8-7- A comparative plot showing the change in WVTR for textured surface A and B deposited with DLC/2 and DLC/5 on 3D ABS (a) and Verogray (b). 156
Figure 8-8- A comparative plot showing the WVTR function with time for both 3D ABS (a) and Verogray (b) coated with DLC/3 and DLC/5. 157
Figure 8-9- (a) Sorption isotherm plot for uncoated 3d printed ABS, Verogray and moulded ABS showing the percentage mass change with time. (b) Total average moisture absorbed (mg) per mg sample mass (mg). 158
Figure 8-10- Summary plot showing the individual total gravimetric water sorbed for both coated and uncoated polymers analysed using the Dynamic Vapour Sorption at 25 ℃ and 80 % RH. 158
Figure 8-11- Typical isotherm plot for uncoated 3D ABS, Verogray and moulded ABS showing both sorption and desorption curves at 25 ℃ and 40 ℃ 160
Figure 8-12- Typical isotherm plot for DLC/1 coated 3D ABS, Verogray and moulded ABS showing both sorption and desorption curves at 25 ℃ and 40 ℃ 160
Figure 8-13- Hysteresis of the isotherm plot for 3D ABS at (a) 25 ℃ and (b) 40 ℃ 160
Figure 8-14- Hysteresis of the isotherm plot for Verogray at (c) 25 ℃ and (d) 40 ℃ 161
Figure 8-15- Hysteresis of the isotherm plot for moulded ABS (e) 25 ℃ and (f) 40 ℃. 161
Figure 9-1- Heat flow versus temperature plot for the determination of Tg for Verogray sample. 164
Figure 9-2- Coefficient of friction with coating thickness for 3D ABS for 1N (a) and 5N (b) loads showing the friction performance for each DLC coating. 170
Figure 9-3- Coefficient of friction with coating thickness for Verogray for 1N (a) and 5N (b) loads showing the friction performance for each DLC coating. 171
Figure 9-4- Coating thickness plot using one and two microwave sources at different heights from the bottom along with the substrate holder [310]. 175
Figure 0-1- Typical failure mode of DLC/3 coatings on pristine 3D printed ABS (a) Unpolished (b) polished. 2
Figure 0-2- Typical failure mode of DLC/3 coatings on pristine 3D printed Verogray (c) Unpolished (d) polished. 2

Figure 0-3- Typical failure mode of DLC/4 coatings on pristine 3D printed ABS (e) Unpolished (f) polished. 2
Figure 0-4- Typical failure mode of DLC/4 coatings on pristine Verogray (g) Unpolished (h) polished. 3
Figure 0-5- Typical failure mode of DLC/5 coatings on pristine 3D ABS (i) Unpolished (j) polished. 3
Figure 0-6- Typical failure mode of DLC/5 coatings on pristine Verogray (k) Unpolished (l) polished. 3
Figure 0-1- Cracking behaviour of DLC/3 coating on 3D ABS after bending showing coating deformation pattern on all three surfaces defined as (a) untextured coated surface (b) textured type A (c) textured type B. 4
Figure 0-2- DLC/3 coating on Verogray after bending showing coating deformation pattern on all three surfaces defined as (a) untextured coated surface (b) textured type A (c) textured type B. 4
Figure 0-3- Cracking behaviour of DLC/4 coating on 3D ABS after bending showing coating deformation pattern on all three surfaces defined as (a) untextured coated surface (b) textured type A (c) textured type B. 4
Figure 0-4- DLC/4 coating on Verogray after bending showing coating deformation pattern on all three surfaces defined as (a) untextured coated surface (b) textured type A (c) textured type B. 5
Figure 0-5- Cracking behaviour of DLC/5 coating on 3D ABS after bending showing coating deformation pattern on all three surfaces defined as (a) untextured coated surface (b) textured type A (c) textured type B. 5
Figure 0-6- DLC/5 coating on Verogray after bending showing coating deformation pattern on all three surfaces defined as (a) untextured coated surface (b) textured type A (c) textured type B. 5
Figure 0-1- DLC/2 coated ABS substrate showing the deformation on (a) parallel (b) perpendicular orientation to the applied load of 1N. 6
Figure 0-2- DLC/2 coated Verogray substrate showing the deformation on (a) parallel (b) perpendicular orientation to the applied load of 1N. 6
Figure 0-3- DLC/3 coated ABS substrate showing the deformation on (a) parallel (b) perpendicular orientation to the applied load of 1N. 6
Figure 0-4- DLC/3 coated Verogray substrate showing the deformation on (a) parallel (b) perpendicular orientation to the applied load of 1N. 6
Figure 0-1- Typical isotherm plot for DLC/2 coated 3D ABS, Verogray and moulded ABS showing both sorption and desorption curves at 25 °C and 40 °C 7

Figure 0-2- Typical isotherm plot for DLC/3 coated 3D ABS, Verogray and moulded ABS showing both sorption and desorption curves at 25 ℃ and 40 ℃..... 7
Figure 0-3- Typical isotherm plot for DLC/4 coated 3D ABS, Verogray and moulded ABS showing both sorption and desorption curves at 25 ℃ and 40 ℃..... 7
Figure 0-4- Typical isotherm plot for DLC/5 coated 3D ABS, Verogray and moulded ABS showing both sorption and desorption curves at 25 ℃ and 40 ℃..... 8
Figure 0-1- CoF plot showing experimental repeat for 1N load on 3D ABS (a) parallel orientation (b) perpendicular orientation..... 9
Figure 0-2- CoF plot showing experimental repeat for 1N load on Verogray (a) parallel orientation (b)perpendicular orientation..... 9
Figure 0-3- CoF plot showing experimental repeat for 5N load on 3D ABS (a) parallel orientation (b) perpendicular orientation..... 10
Figure 0-4- CoF plot showing experimental repeat for 5N load on Verogray (a) parallel orientation (b) perpendicular orientation..... 10
Figure 0-5- CoF plot showing experimental repeat for 10N load on 3D ABS (a) parallel orientation (b) perpendicular orientation..... 10
Figure 0-6- CoF plot showing experimental repeat for 10N load on Verogray (a) parallel orientation (b) perpendicular orientation..... 10

List of tables

Table 2-1- Multifunctional and non-functional monomers [39]. 13
Table 2-2- Typical photopolymer binders used in 3D additive manufacturing. 13
Table 2-3- Commercially available photoinitiators [50]. 15
Table 2-4 Common Polyjet digital materials utilised in most Polyjet printers. 21
Table 2-5- Typical parameters for various types of plasmas [87]. 26
Table 2-6- A comparative physical property table of amorphous carbon with diamond, graphite, C_{60}, and polyethene [101]. 30
Table 2-7- Different sorption interaction modes. 50
Table 2-8- WVTR for a single layer thin coating deposited by sputtering. 52
Table 2-9- PECVD deposited film for WVTR application 52
Table 3-1- General properties of selected additively manufactured polymers [69]. 58
Table 3-2- Polyjet 1000 printer parameters for fabricating 3D polymers. 59
Table 3-3- EnvisionTEC™ P4K printer series parameters for fabricating 3D polymers. 59
Table 3-4- Substrate design types with dimension and characterisation methods. 59
Table 3-4- Initially proposed DOE parameters used as the basis for formulating the coating recipe for this thesis. 69
Table 3-5 Actual deposition parameters for 3 Leg DOE design deposition. 70
Table 3-6 Proposed parameters used to deposit the DLC coatings. 70
Table 3-7- Calculated maximum contact pressure at each applied load tested. 82
Table 4-1- Initial degradation temperature, final decomposition temperature, total mass loss after decomposition and total inert residue left after decomposition. 86
Table 4-2- Activation energy for the degradation of 3D polymer material. 87
Table 4-3- Results of statistical analysis 88
Table 4-3- Mechanical properties of additively manufactured materials. 91
Table 4-4- FTIR plot summary showing the corresponding individual wave numbers and functional groups present in each of the 3D samples analysed. 95
Table 4-5- Show a summarised material ranking proforma for the individual 3D-printed materials. The numerical grading assigned to each polymer indicates the performance of each polymer to the other. The final grading provides the overall performance of the individual samples studied under thermal, water and tensile testing properties. 99
Table 5-1- Proposed parameters used to deposit the initial DLC coating. 101
Table 5-2- Actual parameters used to deposit the initial DLC coating. 101
Table 5-3- Proposed parameters used to deposit the modified DLC coating. 108
Table 5-4- Actual parameters used to deposit the modified DLC Coating. 109

Table 6-1- Raman data showing 'D' and 'G' peak intensities for DLC films 1 to 5 produced using MW-PECVD technique on 3D ABS. 129
Table 6-2 - Raman data showing 'D' and 'G' peak intensities for DLC films 1 to 5 produced using MW-PECVD technique on Verogray. 130
Table 9-3- Mechanical properties of 3D printed materials. 166
Table 9-4- Hardness of DLC coating measure at 10% coating thickness on 3D ABS and Verogray. 167
Table 9-5- Interaction effect of both surface texturing and DLC single layer coating on the water vapour barrier performance for both coated 3D ABS and Verogray samples. 173
Table 9-6 - Hardness properties of diamond-like coatings deposited on polymer substrates from the literature 176
Table 9-7- WVTR performance properties of carbon coating deposited on polymer from the literature 177

List of Acronyms

0D	**Zero-dimensional "0D"**
3D	**Three-dimension**
a-C	**Amorphous carbon (a-C)**
ABS	**Acrylonitrile butadiene styrene**
AFM	**Atomic force microscopy (AFM)**
AM	**Additive manufacturing**
CAD	**Computer-aided design**
CNTs	**Carbon nanotubes (CNTs)**
CVD	**Chemical vapour deposition**
DLC	**Diamond-like carbon**
DSC	**Differential scanning calorimetry (DSC)**
DLP	**Digital light processing (DLP)**
DVS	**Dynamic vapour sorption (DVS)**
FDM	**Fused deposition modelling**
FTIR	**Fourier transform infrared spectroscopy**
HiPIMS	**High power impulse magnetron sputtering**
MW-PECVD	**Microwave -plasma-enhanced chemical vapour deposition**
PEI	**Polyetherimide**
P/Po	**Water saturation pressure/partial pressure**
POM	**Polyoxymethylene**
PolyDADMAC	**Polydiallyl dimethylammonium chloride**
PMMA	**Polymethylmethacrylate (PMMA)**
PI	**Photoinitiator (PI)**
PSs	**Photosensitizers (PSs)**
PC	**Polycarbonate**
PVC	**Polyvinylchloride (PVC)**
PTFE	**Polytetrafluroethylen (PTFE)**
IR	**Infra-red**
rf	**Radiofrequency**
SIMS	**Secondary Ion mass spectrometry**

SL	**Stereolithography (SL)**
SLS	**Selective laser sintering (SLS)**
SZM	**Structural zoning model (SZM)**
ta-C:H	**Hydrogenated tetrahedral amorphous carbon(ta:C-H)**
ta-C	**Tetrahedral amorphous carbon (ta-C)**
TGA	**Thermogravimetric analysis (TGA)**
T_g	**Glass transition temperature (T_g)**
XPS	**X-ray photoelectron spectroscopy**

Chapter 1

Introduction

In recent times, the introduction of well-engineered materials with varied applicability and exploitability; for example, high-temperature superconductors, graphene, diamond-like coatings (DLC) and electrically conducting polymers are generating new and interesting challenges as well as creating new engineering opportunities in the study of material science. The object of choice for most consumer goods has seen a paradigm shift from the more traditional oriented applications to well advanced and bespoke product designs. Today, almost all the products we interact with at home and in our various offices, all fall underneath the "umbrella" of functional coated materials [1]. These coatings play an essential role in resolving key performance issues in critical operational environments where corrosion, wear, scratch and chemical resistant surfaces are required for optimum performance.

In the year 2011, the total output of manufactured engineering parts worldwide was valued at $11.3 trillion [2]. A major chunk of these parts relied solely on subtractive processes, forming and casting manufacturing techniques, where large volumes of material wastage are encountered. This led to the concept of additive manufacturing (AM) which is a much more intrinsic process where the manufacturer has control over composition, deposition and product geometry without the need for any expensive tooling as utilized in injection moulding.

The principle behind AM technique is to produce well-engineered parts from three-dimensional (3D) computer-aided design (CAD) models into working parts. This technique dates to the early 1980s where the process of stereolithography (polymerization processes that solidify liquid resin layers into 3D objects using laser beam) was first pioneered and developed for producing 3D cured polymer samples. In fairness, the technique was originally restricted to producing model parts of materials with deficient mechanical and resolution properties. Nonetheless, with further advancement in engineering material process, the application of this technology has extended into a wide scope of engineering product design in the aerospace [3], automotive [4], medical [5, 6] and other specialized areas where product quality and speed, material availability, workforce knowledge and business interest is required for driving growth (Figure 1-1) [7].

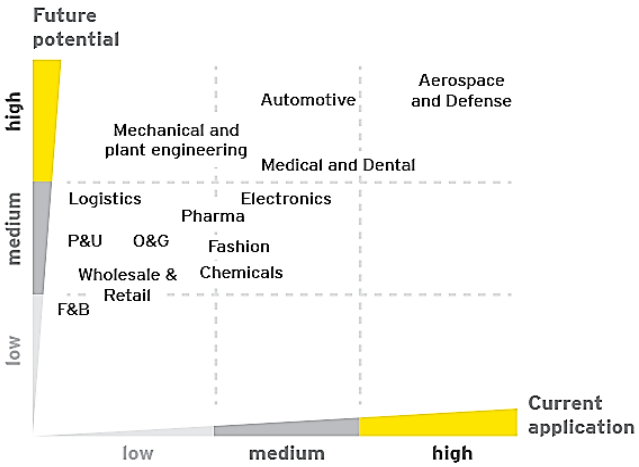

Figure 1-1- Current application and projected future potential of 3D printing by industry [7].

Even though the growth of the AM industry for the past decade has been very sluggish with an average growth rate of less than 0.02 % of the total global manufacturing output per annum, its forecast for the next decade is refreshing and the industry is expected to grow by some 40 % within the next decade [8] with polymer and polymer-based materials (PBMs) accounting for over 50 % of the total production output [Figure 1-2] [7].

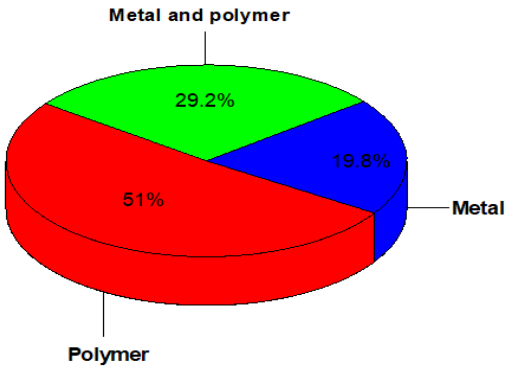

Figure 1-2- Part manufacturing using AM systems in the production industry [8].

3D printing has been demonstrated over the last few years as a game-changer in producing both low-volume and complex high-volume parts with high-performance efficiency during operations. From a processing time lasting a few hours [9], AM has revolutionized and made simple the printing of complex geometries, internal structures, and voids with contorted features possible without the need for expensive tooling or machining methods. With the ability to produce multilayered parts to enhance material performance, AM has provided a great deal of material adaptability and uniqueness in revolutionizing product design and architecture. Notwithstanding their numerous advantages and great attributes of comparison between the rate, quality, cost, and flexibility to the traditional moulded or

machining technique, AM performance currently is low with aspect trade-off against the advantages in terms of product quality and material performance.

The dynamics of polymer chain structure at the near-surface may end up functionally very different from the repeating units making up the entire bulk material of the polymer matrix if their polymerization process was as a result of the incorporation of both initiating and termination species [10]. In principle, the homopolymer near-surface structure after AM may vary significantly from the bulk material in molecular weight distribution, end-group concentration and where appropriate, crystalline to amorphous ratio [10]. This notwithstanding provides the manufacturers with varied surface properties and critical performance issues when utilized in product design. These include properties associated with surface adhesion, wear, optical, compatibility, crazing, permeability etc. [10]. By visualizing a 3D manufactured part, one gets the true sense of the fine degree of texturing as well as the granularity that is both the strength and weakness of a 3D printing product overall. Hence, the ability to control these surface properties for enhanced material performance in real-time application is key to increasing the longevity of polymers.

Like all other engineering materials, polymers have their advantages and limitations due to their physical, mechanical, chemical, and thermal properties. They are very lightweight, malleable, corrosion and chemically resistant and easy to synthesize at a very low cost compared to metals. These inherent properties make polymer materials the choice for most engineering applications. However, that is not to say they do not have their limitations. The inability to withstand high temperature and high load applications due to their relatively low glass transition temperatures and low modulus make them less attractive for major engineering work requiring high strength materials. In most polymer applications, the surface of the substrate always undergoes tremendous physical, mechanical and chemical modification with time. Consequently, the adjustment of these surfaces to mitigate the effect posed by these alterations are key to providing appropriate functionality to the material.

Modification of material surfaces through surface engineering techniques is all about getting the right functionality balance for advantage. Surface engineering methods have been primarily aimed at techniques designed to modify material surfaces either through the use of physical or chemical modification processes or coatings without altering the bulk of the material or substrate. PBMs are generally known for their low surface energy in the range of 25 to 50 $\mathrm{mJ/m^2}$ [11] and are particularly unsuitable for all forms of protective coating processes being, electroplating, painting or physical vapour deposition (PVD), due to the surface energy miss-match between the high energy particle and the low surface energy polymer material, thus, forming droplets instead of fully wetting the surface [12]. Enhancing polymer surface adhesion and wetting requires having to boost its polar interactive component and surface free energy using high level thermal or electrical energy sources for example, through the use of plasma, corona, discharge flame or reactive gases [12].

Throughout the various stages and technique optimization for adding functionality to materials through surface coating, the use of high-energy plasma treatment methods such as PVD and plasma-enhanced chemical vapour deposition (PECVD) as well as other techniques including electroplating and painting has proved vital in today surface treatment techniques [11]. These surface coating techniques provide improved functionality by enhancing material properties such as surface hardness, wear resistance, reduced friction and in some metallic applications may provide improved oxidation resistance as well as barrier function against water and gases ingress into the bulk material.

The use of both physical and chemical vapour deposition with assisted plasma sources has shown enormous potential in the polymer industry by creating some of the best interactive polymer surfaces in the automotive and electronic industries. In each of these deposition methods, there are sound debates and literature backing as to why either PVD or CVD is the best deposition option. One of the reasons is the temperature requirement needed for both systems to operate. A typical CVD process on average operates at much higher deposition temperatures of between 500 to 1050 ℃ [13] compared with a process temperatures of 250 to 450 ℃ for most PVD processes even though temperatures of below 70 ℃ could be achieved [14] in cold plasm applications [15].

The advancement in the application of PVD and plasma-enhanced deposition of thin films in coating polymers have led to more specific applications where weight, size and cost is big challenge to overcome. Plastic material can now be made to look and perform similar functions as its metallic counterpart, thus reducing weight and opening an unlimited opportunity for all sorts of industrial applications.

1.1 Tribology application for additively manufactured polymers

Currently, the science of wear and friction is evolving in the direction of deep exploration into the mechanics of contact interaction. In the last decade alone, a lot of work has been accomplished in both academia and industry exploring the functionality and material performance of PBMs in tribological applications. As well as the old-fashioned PBMs such as polyoxymethylene (POM) and polytetrafluoroethylene (PTFE), high-performance polymer materials and composites are progressively used in sliding components such as artificial joints, rollers, ball bearings and bushings due to their inherent self-lubricating properties [16]. The variance in the application of PBM in tribological contacts juxtaposition with metals and ceramic-based materials relates primarily to both the surface and bulk properties definition as well as their physical and chemical structure [17]. The ability to control and modify certain physiochemical properties in a sliding and frictional body system makes PBMs materials uniquely interesting in a tribological system and most especially under dry sliding contact compared with their metals and ceramics counterparts. To meet this goal, numerous books and authors of polymer friction have already exhausted most of the topical issues relating to polymer tribology [18, 19],

however, more work is needed in highlighting their tribological performance, especially in friction and wear characterisation. This is particularly true for AM polymers and all emerging polymer composites.

The introduction of surface definition through texturing as a deliberate concept or otherwise on a polymer surface has essentially focused on improving both frictions and wear performance behaviour at the contact surface [20]. By this concept of surface defining, the resulting micro cavities depression created as a consequence of AM processes or through deliberate surface texturing methods have shown to facilitate micro-wedge effect by creating micro channels for improved tribological performance [20]. Depending on the type of AM technique employed in the manufacturing process, material properties such as surface roughness, hardness, elastic modulus, etc., which serves to provide the bulk and surface properties of the product are altered in the process.

By observing the advantageous opportunities linked with additively manufactured polymers, there is the need to understand their tribological behaviour and limitations when used in practical applications. Hence, as part of this study, one of the aims is to explore the possibility of using Polyjet printed AM polymers, enhancement through novel surface engineering methods, as new candidates for tribological application. To bridge this knowledge gap, two Polyjet materials (3d ABS and Verogray) have been studied and presented in this work.

In most polymer applications, the surface of the substrate always undergoes tremendous physical, mechanical and chemical modification with time. Consequently, the adjustment of these surfaces to mitigate the effect posed by these alterations are key to providing appropriate functionality to the material. The fundamental principle for material science is that structure leads to material property, thus if we can control effectively the structure of the material at the atomic scale then we should be able to engineer whatever property of the material we so desire.

1.1 Aims and objectives

1.2.1 Aim

In this study, the advantageous combination in assessing the framework for developing potential functional coatings on additively manufactured polymer substrates (3D printed polymers) with the aim of increasing material robustness is made. Diamond-like carbon (DLC) coatings are produced using microwave enhanced plasma-enhanced chemical vapour deposition (MW-PECVD) at temperatures below 40 °C. There is currently no work reported on the synthesis and deposition of DLC films using MW-PECVD on 3D printed polymers and as such, a thorough study of the micro and nano-scale interaction between coating and polymer bulk shall be discussed. Further studies on their tribological properties under dry reciprocation sliding conditions with varying load and The main objectives of this thesis are detailed below:

1.2.2 Objectives

1.2.2.1 **Phase 1: Sample preparation and characterisation**

Photo-curable acrylate, urethane and epoxy-based resins manufactured using 3D printing techniques available at the University of Leeds prototyping laboratory were investigated to:

- Understand the thermal, mechanical and physical properties as well as any structural limitations of the cured resin.
- Compare the properties of the selected photo-curable 3D printed polymers and to determine the suitability of the polymers for plasma treatment and deposition.
- Develop pre-treatment processes that make these substrates suitable to MW-PECVD coating.
- Structuring polymer surfaces using a variety of microfabrication and surface engineering techniques.
- Determine the tribological performance and limitations of photo-curable 3D manufactured polymers under real load applications.

1.2.2.2 **Phase 2: DLC coating and deposition**

The coating deposition process was designed around the use of MW-PECVD process accessible in the University of Leeds advanced coating laboratory, using the Hauzer Flexicoat 850 deposition coating system. The potential for coating complex features on polymer surfaces with micron-size features was assessed and investigated to:

- Gain adequate familiarity with the process operations of the Hauzer Flexicoat 850 coating system and develop suitable benchmark coatings as functional coatings on 3D printed polymers.
- Provide a coating on a polymer substrate only a few μm thin without destroying the substrate.

1.2.2.3 **Phase 3: Coating assessment and performance analysis**

Coatings were optimised for maximum adhesion and bending strength. The study was to develop a realistic function simulator to guide the design process in the following areas with the objectives

- To evaluate the coating techniques from nano to micro-scale level by studying the relationship between thin film properties (such as; hardness, modulus, structure, etc.), polymer properties (such as; mechanical, chemical structure, etc.) and deposition process conditions (such as; gas flow rates, deposition and micro-wave power input).
- To understand the functional limitations of the MW-PECVD coated substrate for both barrier and tribological functions.

- To optimize coating structure.

1.3 Thesis outline

- **Chapter 1** provides an introductory outline to establishing the scope of this research by summarising the background theory pertaining to this study and also providing the main aims and objectives as defined in the project specifications and deliverables.
- **Chapter 2** provides a comprehensive literature review covering basics in polymer science, additive manufacturing, tribology, diamond-like coating, plasma theories and thin-film synthesis and deposition. It also covers coating methods for depositing DLC coating onto PBMs using either PVD or CVD techniques.
- **Chapter 3** provides an overview of all experimental methods used in this study, including methods for 3D printing of photo-curable resins, pre-coating characterisation of the 3D printed parts, pre-coating treatment, deposition methods for coating, post-coating analysis techniques for coating characterisation and tribological analysis.
- **Chapter 4** which is the first results section presents the characterisation of the 3D printed PBMs chosen for this study pre-coating. The characterisation methods employed in this study centre around the quantitative and qualitative analysis of the physical, structural mechanical, thermal and water absorption properties of the uncoated 3D polymers.
- **Chapters 5 and 6** present the results for the study of the DLC coating structure deposited using MW-PECVD and evaluate the varying deposition parameters on coating growth, and temperature evolution within the coating chamber. They also present a mechanical characterisation of the different coating structures, coating roughness and adhesion. Discussion on the bending strength of the structured coated surfaces in response to forces that act in real applications is presented also in this section. The coating structure and chemical composition results are presented in **Chapter 6**.
- **Chapter 7 and Chapter 8** provide a detailed analysis of the functional properties of the DLC coated 3D substrate. In **Chapter 7**, the tribological properties of both coated and uncoated substrates are discussed. **Chapter 8** discusses the water vapour transmission and sorption function for both coated and uncoated substrates.
- **Chapter 9** provides a comprehensive discussion of the result section in this work, alongside the uniqueness of the varying coating structure deposited unto the different polymer substrates.
- **Chapter 10** provides a summary of the main findings, conclusions and suggestions for future work.

Chapter 2

Literature Review

2.1 Introduction

This chapter presents a comprehensive review of the literature on polymer-based materials with greater emphasis on additively manufactured polymers. DLC synthesis and coatings using plasma-assisted deposition methods have been discussed. Further discussions on coating characterization methods, tribology and barrier functional properties of DLC films on polymer materials are made.

2.2 Theory of polymer science

Polymer-based materials (PBMs) form a unique group of engineering materials composed of complex repetitive units of single or multiple chain-like structures commonly referred to as monomers. Their primary attributes, which stem from material property uniqueness and their ability to be partly consolidated into a complex geometrically stable structure, provide them with excellent variable strength and applicability. The term polymer originated from the ancient Greek words: *poly* meaning "many" and *meros* meaning "parts" [21] of which entails a large number of single repetitive unit structures (*monomers*) linked together regularly, usually by means of a covalent bond [22].

Chemically, polymer molecules are composed of a "skeleton" [23] of a very high molecular weight structure that may be branched, linear or a network of both [21, 22]. Depending on the type of polymer synthesis utilized and monomer species, the size of a polymer could range from a few hundred to a thousand or possibly a million in molecular size or molar mass [21]. This could either be a low weight or high weight polymer depending on the length and structure of the molecular structure. Low weight polymers have a characteristic molecular range of between 1,000 - 20,000, whilst those classified as high weight polymers are those with molecular structures >20,000 [24].

The fundamental process of forming a repetitive backbone structure for any molecular polymer structure is controlled by the mechanism governing the stepwise addition of monomers to a growing polymer chain [25]. Flory [26] underlined the very importance of appreciating the different polymerization mechanisms in molecular structure build-up in defining the process, however, the very definition characterising the mechanism is consistently varied in most cases. Later, he defined the process of polymerization using the "condensation" and "addition" polymerization terms as supposed

to be both step and chain-growth polymerization terms [27, 28]. Davis [25] defined the polymerization process by focusing primarily on the chain growth process of radicalized monomers.

Condensation polymerization occurs when monomers bond together chemically to form polymers with the release of a lower weight molecular structure as the by-product [29]. Addition polymerization requires an initiation step followed by a multiplicity of continuous addition of monomer units to an increasing free radical chain [30]. Commonly used initiators are the peroxides and persulfate [31]. Davis [25] noted that polymerization in itself could be self-initiated in the absence of any added initiator through a self-induced adventitious free-radical. Mayo [32, 33] in the formation of polystyrene noted that radical initiation proceeds Diels-Alder dimerization of styrene, where molecular assisted homolysis amongst the dimer (AH) and a third styrene produces the monodical initiators A* and HM*. However, Flory [33, 34] suggested that styrene dimerizes to form a singlets 1,4 diradical (M_2*) where a third styrene molecule extracts a hydrogen atom from the diradical to produce a single radical initiator capable of initiating the polymerization process as shown in Figure 2-1.

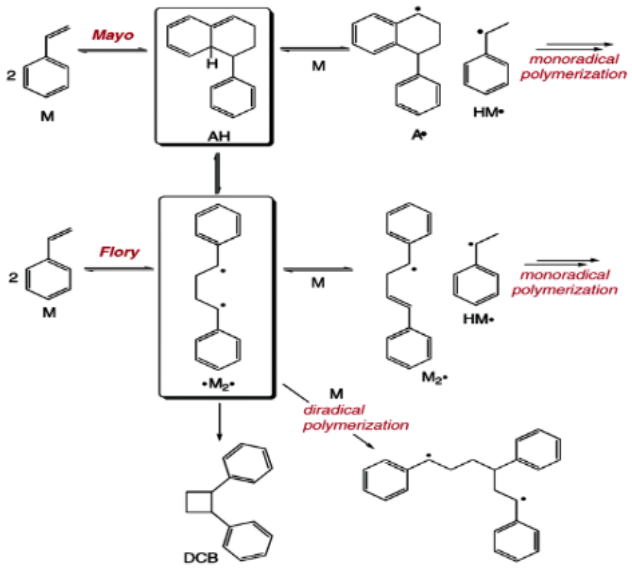

Figure 2-1- Mayo and Flory Mechanism [33].

The propagation step which follows on from the initiation step is, of course, the core of the polymerization process and primarily dependent on the monomer unit availability, a determining factor of the molecular weight of the final PBM [27]. The termination step, in the case of a free radical polymerization process, is the final stage, where the free terminal radicals combine to stop further the growth of the polymer chain unit.

Depending on the polymeric chain arrangement as shown in Figure 2-2, polymer molecules can be partially crystalline (semi-crystal), amorphous or in a state where crystalline regions are distributed within the amorphous material [35]. In an amorphous state, individual polymer chain units making up

the entire molecule are arbitrarily distributed as opposed to a more structured and well-defined molecule in a crystalline state. This means the onset of the glass transition temperature in amorphous materials is much lowered than the melting temperature (T_m) for crystallites as a result of the early onset of molecular chain movement [36]. The wide variation and uniformity in these polymer structures produce uniquely varied polymer molecules with unique physical features. The extent of variation in their physical state could result in materials with good dimensional stability, high rigidity, and strong physical properties. However, in the same breath, materials could exhibit completely different physical properties under the same conditions, most especially under tension.

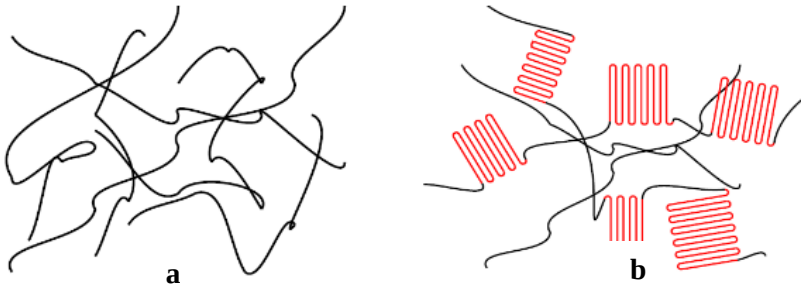

Figure 2-2- Schematics of the chain structure of (a) an amorphous (b) Semi-crystalline polymer [36].

The term plastic originated from the Greek word, *plastikos*, meaning able to shape or mould with the help of heat. Therefore, temperature input is a basic requirement in the manufacturing process. Like in most metals which can be divided into ferrous and nonferrous metals. Plastics, on the other hand, can be divided into types. The most common ones are synthetic plastics which are derived from hydrocarbon-based materials, usually crude oil or gas. However, depending on the way these key ingredients react when heated, they could either form *thermosetting plastics* or *thermoplastics.*

2.3 Additive manufacturing

Thermoplastics (such as Nylon, ABS, and PEEK), as well as thermosetting polymers (like epoxy base resin), have over the years become the main active catalyst in pioneering the process of manufacturing functional engineering prototype parts using AM techniques. In most traditional polymer extrusion-mould based systems, the thermoplastic polymer is simply melted and squeezed directly onto a temperature-controlled plate or predesigned structure to create a replica of the object. Even though the design set-up for any AM process is complex, its delivery in terms of the material build is less sophisticated as the process combines both structural layering and precision of a base polymer to achieve object unity. For example, in the manufacturing of epoxy resin, the use of UV or thermally

assisted curing process are simply very useful in the completion of the polymerization process. Consequently, epoxy resins are most appropriate for UV or heat-assisted 3D-printing processes because of their highly reactive nature when exposed to these conditions [37]. Additionally, they are extensively utilized in most 3D-part manufacturing processes and applications because of their varied physical and mechanical properties, easiness to acquire or manufacture and are flexible to many low energy fabrication systems. In all cases, thermosetting polymers may be personalised based on the need to satisfy a particular process requirement, but the preparation, formulation and processing information are usually retained as trade secrets [38].

Epoxy resin defines a broad group of thermoset polymeric materials in which the principal crosslinking between the molecules is a result of the presence of an epoxide group. The structure usually consists of a three-membered ring, comprising two carbon atoms and one oxygen (Figure 2-3). Though the existence of this functional group defines an epoxide to some extent, the molecular extension of this structure may vary, producing different classes of epoxy resins in the polymerization process. The most important base material in epoxy resin manufacture is epichlorohydrin, which is primarily used as a precursor in almost all commercially available epoxy resins.

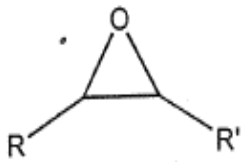

Figure 2-3- Basic structure of an epoxide group [39].

2.3.1 Photopolymerization in additive manufactured polymers

The approach behind 3D Photopolymerization is centred on building a well-structured polymer unit using monomer/oligomer in a liquid base form that could be polymerized using an external light source of a specific wavelength to form a thermoset polymer [40].

The polymerization of acrylic and prepolymers or epoxy-based materials through light-activated radical or cationic reactive species is a universal model that provides high photosensitivity and good selectivity with well-defined cured properties [40]. Chemically, photopolymers may constitute several fractions of binders, photoinitiators, additives, colourants, chemicals and plasticizers at varying percentages [41], however, the primary component that provides the build for the process of delivering a photocurable PBM are primary monomers, binders and photoinitiators [42].

During the photopolymerization sequencing process, the controlling index of modulation which is optically induced is provided for by the base monomer. Irrespective of their chemical structure and

composition, monomers are required to have at least one reactive polymerizable group [43]. Monomers of acrylate or methacrylate functionality have become standard photoinitiators, generally because of their high reactivity nature, making up 10-40 % of the monomer composition [39]. Other than these highly suggestive photoinitiators, whose reactive sites are located at the terminal end of the monomer backbone structure, monomers can vary tremendously based on their functionality and could act singularly or multifaceted as either a diluent, cross-linker or both. Examples of such monomers are shown in Table 2-1.

Table 2-1- Multifunctional and non-functional monomers [39].

Multifunctional monomers	Monofunctional monomers
Trimethylolpropane triacrylate (TMPTA)	Acrylic acid
Ethoxylated TMPTA	Methacrylic acid
Trimethylolpropane trimethacrylate	Isodecyl acrylate
Hexanediol diacrylate	N-vinyl pyrrolidone

2.3.1.1 **Binders**

Binders are molecules of highly reactive monomer units, generally of dimers, trimers, and tetramers. They are mostly liquid at room temperature due to their low to intermediate molecular weight, functionality, and structure [44]. In principle, the host polymer binder provides the supporting matrix contained within the additive mix [45]. However, Allen [46] noted that the functional performance of a binder resin should not just provide physical advantage through molecular weight refinement but the ability to resist dissolution during the polymerization steps within the aqueous base. Typically, binders consist of 50-80 % of most photopolymers [46] and provide varying functionality during the activation process. Typical binders used photopolymers are shown in Table 2-2.

Table 2-2- Typical photopolymer binders used in 3D additive manufacturing.

Photopolymer binders
Styrene family: Oligomer of Styrene-Tetramer-Alpha Cumyl End Group, A-Methyl Styrene-Dimer **(**1), A-Methyl Styrene-Tetramer, etc.
Methacrylate family: Methyl Methacrylate Oligomers, Acrylic Acid Oligomers, Methyl Methacrylate Tetramer, etc.
Olefine family: Poly Isobutylene
Vinyl alcohol family: Vinylacetate trimer, Vinyl alcohol trimer, Vinylacetate oligomer.
Polypropylene Glycol Family: Polypropylene glycol (Dihydroxy Terminated) etc.

2.3.1.2 **Photoinitiators**

Photoinitiators (PIs) are chemical compounds that undergo a chemical transformation on exposure to UV light, producing reactive species (e.g., radicals) [47] that promote chemical reaction process and ultimately are consumed during the reaction process [48]. Figure 2-4 shows the conversion process of transforming soluble liquid formulation into a highly dense crossed linked and insoluble polymer network [48] using near UV light of 300-400 nm [47]. In the process, Mondschein *et al.* [49] noted PIs with characteristic high molar extinction coefficient at relatively short wavelengths (typically < 400nm) are always good candidates for initiating the photopolymerization process [49]. Decker *et al.* [50] demonstrate the reliance of the polymerisation process on the degree of UV intensity and exposure time. They further noted that the rate of polymerisation is related to the square root law and up to the upper threshold for UV particle fluence rate greater than 100 mW/cm^2. The majority of the commercially available PIs experience Norrish type I α-cleavage reaction (this is a photochemical reaction that results in the formation of two free-radical intermediates from the cleavage of ketones and aldehydes) during photopolymerization which causes radical particles fragmentation under light irradiation [51, 52]. Based on the chemical structure, the level of cleavage induced formation and method of 3D printing technique employed in the polymerisation process is always determined by the UV wavelength and intensity of the exposed light. 2-hydroxy-2-methyl-1-phenyl-propane-1-one (Irgacure1173) and, 2-dimethoxy-2-phenylacetophenone (DMPA) are two well-known PIs suitable for stereolithography (SLA) based processes due to their relatively low UV energy level absorption band [53]. Phosphine oxides containing PIs, however, present an activation energy state shift from the lower peak levels to the higher π^* state, which is most preferred for the digital light processing (DLP) 3D print system.

Even though the science behind 3D photopolymerization has been well established in the literature, exposure of the base formulation liquid to high-level UV- wavelength may cause a few shortcomings in the polymerisation process such as slow 3D printing rates due to the low UV photon penetration depth, cellular damage in most bio 3D printable parts resulting in chromosomal and genetic alterations in some bio cells [54, 55] and the promotion of side step reactions with diminishing consequences on product formation. As a result, the conscious effort in developing a suitable 3D photopolymerization technique for a longer irradiation wavelength activation process to address the above-mentioned challenges has been one of the key active research areas in recent times.

The most widespread application developed so far are the cationic and radical photoinitiators which produce either a Bronsted or Lewis acid to initiate a cationic polymerization process or through radical polymerization of acrylate or styrene-based formation respectively [47]. Commercially, there is a huge range of photoinitiators currently in circulation that do not only polymerizes in the UV region but

extends into the visible or infra-red (IR) range. Table 2-3 shows an example of the most widely used PIs in the 3D manufacturing process.

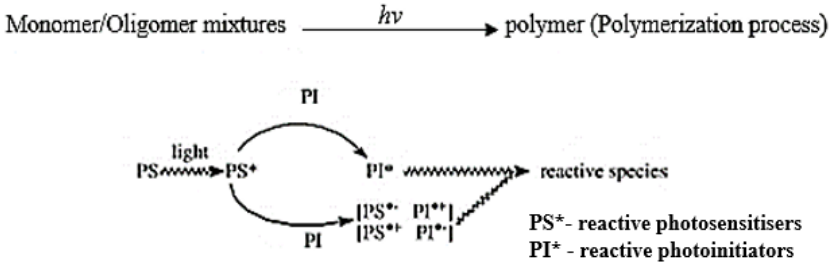

Figure 2-4- Photopolymerization reaction [48].

Table 2-3- Commercially available photoinitiators [50].

UV-Light–sensitive photoinitiators	Visible-light-sensitive photoinitiators	Water-soluble photoinitiators
Trimethylbenzoyl diphenylphosphine oxide (TPO)	NDP2	2-Hydroxy-1-[4-(2hydroxyethoxy) phenyl] -2-methyl-1-propanone (I2959) [50].
phenylbis(2,4,6-trimethylbenzoyl)-phosphine oxide (BAPO)	ATNA 1	Hybrid nanoparticles (HNPs) [50].
Irgacure 184 and 369	Ivocerin	Semiconductor-metal HNPs [50].

2.3.1.3 **Photopolymerization of additively manufactured polymers**

In all photochemical reactions, the formulation materials which serves as the feedstock for 3D manufacturing of PBMs is primarily composed of photoinitiators, oligomers or binders and monomer systems [54]. Amongst the varying issues that play into material efficiency and performance during processing, the photoinitiator (PI) has been acknowledged to an extent as the key backbone to every polymerization reaction process. Direct light polymerisation activated reaction focuses on the reaction of a base formulation additive mixture through a set chain reaction initiated by light. Since the process of activation and the formation of reactive species is highly dependent on the presence of PI, the absorption of light alone by monomer species provide a less efficient route to creating reactive species to initiate the polymerisation process reaction. The excitation extension of the spectra sensitivity which relates to the emission of a light source and the absorption spectrum of the base formulation is further enhanced when photosensitizers (PSs) are used. By extension, this reaction could be defined as sensitized light-induced polymerization as shown in Figure 2-4.

Further to the polymerisation mechanism, which is described favourably by a chain reaction regime, the process of generating reactive species is applied and defined by many selective sequential processes such as anionic, cationic, free radical and step-growth polycondensation [47].

In the anionic polymerisation process, an active anionic site is activated by the reaction of a monomer and a negative ion is created. The negative carbanion end of the monomer resulting from the monomer-PI interaction subsequently forms an ion pair with the photoinitiation ionic species. The overall dipole effect created by the uneven sharing of charge species allows the partial interaction between the anion in the catalyst and the partially positive end of the monomer. Similarly, a further addition to the polymer chain is enhanced through the reaction of both activated anionic monomer residue and the monomer to create a polymerization sequence activated by the resulting carbanion monomer. Chain termination occurs when termination active sites encounter species that consists of exchangeable protons e.g. water and alcohol. Examples of such polymers are acrylonitrile, styrene and methyl methacrylate.

Cationic polymerisation, on the other hand, has functional groups that can react with free proton species to generate a positively charged active site. Examples include vinyl methyl ether, styrene and vinyl group [56]. The free proton synthesis begins with the introduction of either a Lewis acid co-catalysed with an exchangeable proton species or a strong acid. A carbon-hydrogen bond is subsequently formed from the ionic reaction between the weak nucleophilic double bond electrons from the vinyl group and the strong electrophilic proton from the acid (Figure 2-5)**.**

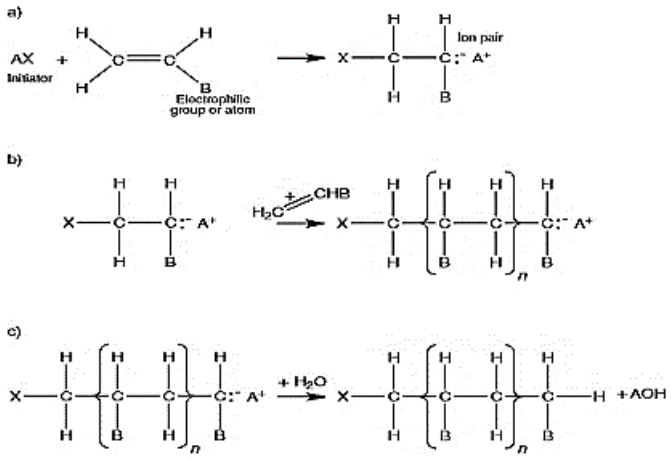

Figure 2-5- Anionic polymerisation (a) initiation (b) propagation(c) termination steps [56].

The resulting terminal carbon atom becomes positively charged as a result (carbocation), thus providing reactive species for chain propagation in the process whereas the counter negatively charged ion maintain charge neutrality.

The termination process (Figure 2-6) occurs when there is a transfer of cationic protons back to the PI catalyst, thus disengaging the polymer chain growth process.

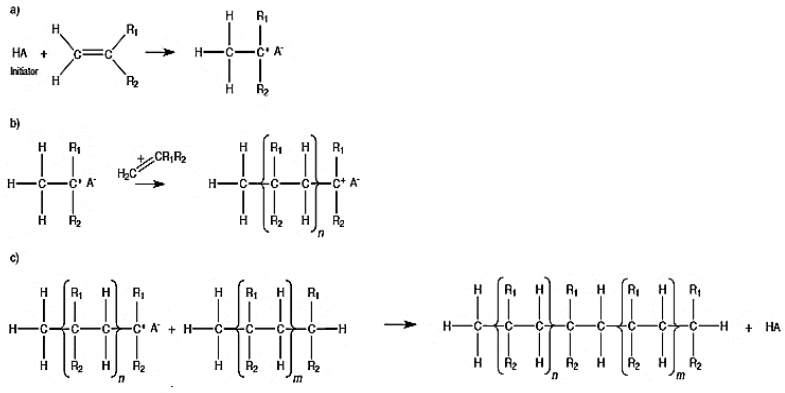

Figure 2-6- Cationic polymerisation (a) initiation (b) propagation (c) termination steps [56].

Commercially, epoxy monomers including 3, 4 epoxy cyclohexane methyl 3, 4 epoxycyclohexylcarboxylate (EPOX) [57, 58, 59] and bisphenol a diglycidyl ether (DGEBA) [60] have been actively involved in formulating PI monomers for 3D polymer synthesis (Figure 2-7). Structurally, cationic photopolymerizes differ and provide varying responses during polymerisation, for example, cycloaliphatic epoxides experience faster polymerisation due to their high double bond strain.

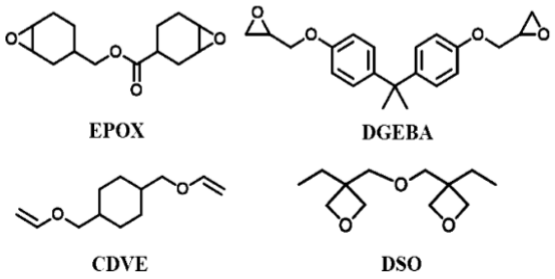

Figure 2-7- Commercially available monomers used in cationic 3D photopolymerization [60].

Epoxides have shown greater applicability in most SLA 3D printing systems due to their low volumetric shrinkage (~ 3 %) during ring-opening polymerisation [57] and improved water resistance properties [61, 62]. To prevent the shrinkage effect observed under free-radical polymerisation of the additively manufactured parts, Al Mousawi *et al.* [57] demonstrated the use of bis (4-tert-butylphenyl)-iodonium hexafluorophosphate (Iod) and azahelicenes to initiate a cationic reaction process of EPOX to construct an AM part. The molecular structure of every monomer, in theory, provides the platform for each chain polymerisation reaction and cationic curing process and this is not an exception. The chain reaction provides several cross-linking points along with the polymer structure, leading to elevated brittleness. To mitigate this problem, chain transfer agents for example polyether diols and polyester at lower weight concentrations (5-20 wt %) are used [53]. Thus, the application of photocurable systems composed of two or more polymerisation mechanisms aimed at providing specific functionality within the 3D printed part serves to control the chain reaction process and prevent incompatibility in the

process. Hybrid monomer 3,4-epoxy-cyclohexylmethyl methacrylate (containing both epoxide and methacrylate groups) can undergo both free-radical and cationic polymerisation mechanism with the sole aim of preventing incompatibility during the reaction process [63].

Free radical polymerisation produces a highly reactive monomer species that provides the propagating sequence for monomer addition. The process of radicalising a monomer begins with a highly receptive monomer capable of accepting and transferring a radical species onto another monomer in the polymerisation process. During the first stage of initiation, a free radical species transfer a highly energetic radical electron to the terminal end of the monomer by attacking the double bond. The unpaired activated electron from the monomer then reacts with another monomer in a step chain polymerisation reaction creating an activated dimer, having *n* (polymerisation number) number of polymers. When two activated terminal sites of a growing polymer chain meet, termination occurs in the process and chain propagation seizes. Most commonly, (meth) acrylate, thiol-ene and additional-fragmentation chain transfer (AFCT) agents or monomers are commonly utilised in radical polymerisation systems. However, (meth) acrylate-base resin has gained great success in AM applications due to its wide applicability and varied functionality such as, in the printing of 3D memory shape polymers, highly functional bio adaptable and stretchy photopolymers [64]. The most common commercially available meth (acrylate) monomers/oligomers available on the market are triethylene glycoldimethacrylate (TEGDMA), bisphenol A-glycidyl methacrylate (Bis-GMA) and trimethylolpropane triacrylate (TTA). Reactions of the unsaturated double bond of carbon and thiols have been well established in the 3D manufacturing process, where these polymerisation reaction steps are governed by radical step-growth addition or Michael addition. Thiols act to facilitate the formation of reactive thiyl radical by donating highly reactive hydrogen ions, hence mitigating oxygen inhibition in the process. Thiols-ene- based resins have added advantage over (meth) acrylate-based resins due to their low shrinkage stress and higher bio-compatibility [53]. These added advantages coupled with other functionality make thiols-ene resin fitting for most 3D constructs in biodegradable hydrogel products, woodpile photonic crystal and the optical waveguide. However, issues such as poor shelf life (which relates to the oxidative disulphide bond formation), bad odour and the formation of low modulus and soft materials (as a result of the formation of homogeneous flexible thioether linkage) make thiols highly disadvantageous when working with them [53]. Bearing in mind that photocurable (meth) acrylate resins polymers are very brittle (as they are highly cross-linked), AFCT resins have been developed among others to purposefully improve the toughness of the 3D photocurable material produced using (meth)-acrylate or thiol-ene resin.

The chemistry governing the free radical photo-polymerisation of 3D systems has been identified as non-living, meaning the terminating monomer chain activation site after the polymerization step becomes inactive and cannot be re-activated to introduce new functionalities. The strategy behind the production of these thermoset materials is not exclusive to a particular regime but varied in terms of the

technique of 3D printing. Several photopolymerization regimes such as stereolithography (SLA), digital light processing (DLP) and continuous liquid Interface production (CLIP) are some of the uniquely developed systems that are commonly used within the industry [53]. The principle behind SLA polymerization involves the use of movable source photons to activate the photocurable resin in the process of building a 3D structure [65]. However, in the digital light processing technique, total illumination of the exposed layer is made all at once using a light source projected from the base of the resin bath [53]. In the CLIP process, the use of an oxygen-permeable window to create an inhibiting barrier to stop the polymerisation reaction process is used. In the succeeding sub-heading (2.3.2) detailed descriptions of these photopolymerization 3D techniques as well as other forms of 3D printing methods are discussed.

2.3.2 Additive manufacturing technique

Increasingly, 3D printing or AM has been used for the manufacturing of end used parts where large-scale manufacturing is made possible. The working principles and functionality of these systems define their properties in real-time applications and substrate unit build up. The issue relating to how to method manufacture parts is always a primary concern, most importantly, when it comes to surface definition, accuracy and refinement. The most widely used methods as employed in manufacturing polymeric engineering part may include:

- Stereolithography (SLA)
- Polyjet photopolymer or Jetted photopolymer (J-P)
- Selective laser sintering (SLS)
- Fused Filament Fabrication (FFF)

2.3.2.1 **Stereolithography (SLA)**

Stereolithography (SLA) is a 3D printing technique that transforms photocurable resin into fully functioning PMB using a movable UV laser or photon source to activate the photopolymerization process. By using a CAD model, a 3D-modelled part is built layer-by-layer through a reactive catalytic curing process using UV-light (Figure 2-8). Traditionally, most SLA techniques employ lightweight polymeric materials, like polyacrylates, which have over the years shown decreased performance levels mechanically and thermally [66].

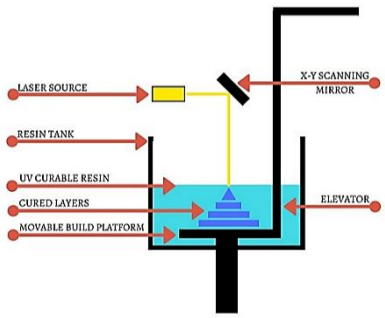

Figure 2-8- Schematic representation of an SLA technique [67].

Currently, polymeric materials with epoxy-based hybrid systems have shown greater acceptability and higher performance level because of their very low water absorption and shrinkage property as well as their high thermal tolerance properties (higher temperature resistance, high glass transition temperature) than previously available acrylate materials [66]. SLA method has provided a unique platform for refined manufacturing where materials print resolution as low as 10 µm can be achieved with the flexibility of fabricating organic-inorganic hybrid 3D structures.

2.3.2.2 **Polyjet photopolymer**

This technique, unlike the SLA method, uses liquid photocurable (UV sensitive polymers) material to create a solid object using layer deposition methods (Figure 2-9). Even though both methods share similar functionality in term of using UV energy to cure plastics, they differ extensively through their mode of operation and technique. The final part manufactured using SLA are not built fully cured and require further curing to drain off excess photopolymer resins. The Polyjet design printer comprises a liquid jetting head that moves in a well-defined x-y axis plane creating a single layer sketch of the photopolymer over the build platform. In this situation, the photopolymer liquid is cured instantaneously using the UV source, thus creating a precise model. The most widely used 3D advanced printers currently in circulation which uses Polyjet technology are the object Polyjet 3D printers. This technique can eject liquid polymer to build surfaces at incredible accuracy of 0.1 – 0.3 mm with very thin layers of 16µm steps [68]. In most Polyjet AM, polymeric compatible materials are made to printer specifications. The most widely utilised categories of polymeric materials are displayed in Table 2-4.

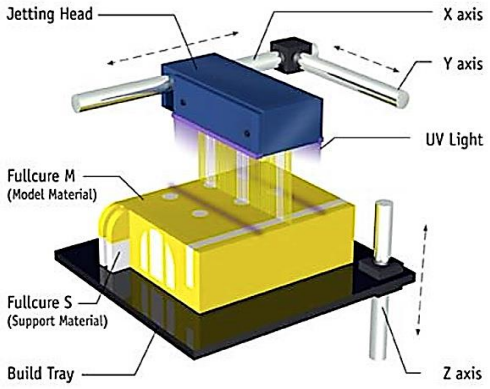

Figure 2-9- Object Polyjet 3D printing [66].

Table 2-4 Common Polyjet digital materials utilised in most Polyjet printers.

Name	Digital Materials
Rigid Opaque Material	VeroWhitePlus RGD835 VeroBlackPlus RGD875 VeroWhitePlus RGD835 TangoBlackPlus FLX980/TangoPlus FLX930 VeroBlue RGD840
Transparent Materials	RGD 720 VeroBlackPlus RGD875 TangoBlack FLX973 RGD810 TangoPlus FlX930/ TangoBlackPlus FLX980
Polypropylene-like-Materials	DurusWhite RGD430 VeroWhitePlus RGD835 VeroBlue RGD840, VeroBlackPlus RGD875 or RGD720
Rubber-like-Materials	TangoGray FLX950 TangoBlack FLX973 VeroBlackPlus RGD875

Digital ABS: The ABS digital or 3D ABS composite material fabricated from the combination of RGD515 and RGD535 has been designed to simulate ABS grade engineering materials by combining high-temperature resistance with high toughness [69]. These products are mostly designed to suit applications such as electrical parts, engine part covers, phones casing etc. Even though digital ABS has shown matching material properties to most traditionally manufactured polymers [69], their research remains unexplored in the existing literature. This work seeks to explore and contribute to future research into Polyjet materials technology for advanced material research and applications involving plasma deposition.

Rigid Opaque: This class of material gives perfect visualization effects to cured photopolymer materials and come in colours such as grey, blue, white and black with each having their application.

Rigid opaque materials are strong, durable and are mostly required in high precision and accurate 3D products. Moreover, its characteristics and shade could be significantly altered if combined with rubber-like materials or opaque white. This class include the family of Verogray (RGD850), Verowhite plus (RGD835), and Veroblue (RGD840) etc [69].

The basic principles underpinning all 3D printed polymers are quite similar in terms of their data input mechanism that rely on a 3D CAD drawing. This is later converted to a layered printer readable format file or the standard tessellation language (STL) file.

2.3.2.3 **Selective laser sintering (SLS)**

Selective laser sintering or melting is a uniquely different 3D fabrication technique that is similar to stereolithography fabrication method in that they both use support scanning laser source technique to create 3D model parts. In the SLS, a high-powered scanning laser beam (CO_2 laser) is used to melt plastic or metal powders to create a hemispherical cross-section material track [53]. Through continuous overlapping of sequential material tracks, layering of material to create a 3D object is achieved (Figure 2-10). Typically, an SLS 3D manufacturing technique provides a careful balance between laser power, scanning speed and scan space to effect particle adhesion and dimensional stability of the print.

SLS technique provides the flexibility of producing polymer, glassy or metallic 3D objects without the need for support material structure. Examples of some common plastics materials used in SLS processing are Polyamide (PA), Nylon 11, Duraform materials and Windfoam LX2.0 [53]. However, even though material coverage and usage have expanded over the past few years, the material build has been limited, largely because of the impairment in the advancement of SLS 3D technology.

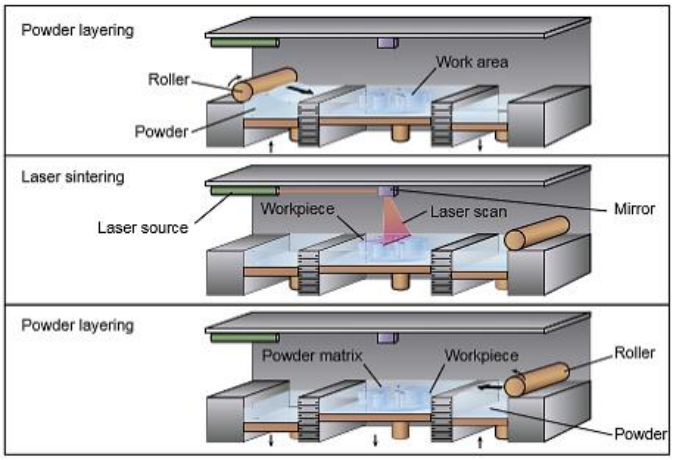

Figure 2-10- Basic selective laser sintering technique [70].

2.3.2.4 **Fused filament fabrication**

Fused Filament Fabricating (FFF) generally known as Fused Deposition Fabrication (FDM) is one of the most commonly used AM techniques today. As an extrusion-based process, printing is achieved by controlled deposition of molten thermoplastic feedstock material (Figure 2-11). During printing, the feedstock is heated up to 1 ℃ above its melting point [71] to follow up a predefined path on the print bed so sequential layers of the molten thermoplastic could be deposited layer by layer to form a working 3D part. Common materials used in this process are acrylonitrile butadiene styrene (ABS), polycarbonate (PC), polyphenylsulfone (PPSE), PC-ABS blend and PC-ISO which is a medically graded material [72].

The structural integrity of these printed parts is primarily derived from the bonding between adjacent and stack extruded roads [73]. Bonding between adjoining layers forms through a bonding coalescence mechanism which is always a function of the thermal history of the interface. Abbott *et al.* [73] further noted that the bond strength of the adjoining interface as the polymer cools off is limited by its glass transition temperature and the neck growth between the adjoining ratsers.

In comparison with other AM techniques such as Polyjet printing, FFF has no chemical post-processing requirement, less expensive tooling, no resin to cure and material processing and set-up are cost-effective. That being said, the FFF technique produces very low-resolution (0.2mm) for printed parts in the z-axis in comparison with other AM techniques and may require additional expensive surface treatment options if a smoother surface finishing is required. FFF is a slow process and may require several hours to print parts if complex features are involved.

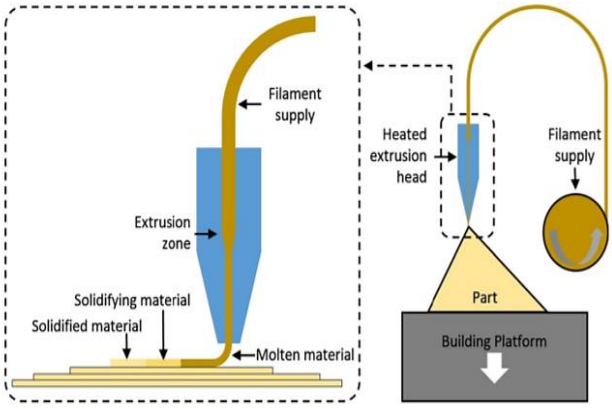

Figure 2-11- Fused filament fabrication process principle and schematics.

2.3.3 Challenges and prospects of additive manufacturing

The capability of using 3D printed parts in engineering applications have been explored for several years in many industrial applications. Some of the benefits of using this technique has already been explored in this chapter. Accuracy, thin layer resolution with the fine precision of 16µm resolution per layer with a 0.1mm accuracy for complex geometric structures [66] are offered by photopolymer. FDM technique has primarily been used for the fabrication of thermoplastic parts with low melting point [74], nevertheless, commercially available polymers such as ABS and PLA do not meet the required output property requirement due to certain material physical restrictions. ABS polymers generally have good mechanical properties but emit foul odours when processing while PLA is seen as environmentally friendly but with poor mechanical properties [75]. A study by Song *et al.* [76] showed that 3D printed PLA exhibited improved mechanical properties compared with an injection-moulded PLA polymer.

Higher substrate void between subsequent layers of 3D printed parts has been reported in the literature to promote higher porosity [77, 78], however, aside from its barrier properties being compromised, a higher material void can reduce the mechanical performance of the 3D printed material as a result of the decrease of interfacial bonding between the layered parts [77, 78]. The degree to which voids are formed can be related to the 3D printing method used and print material. Ngo *et al.* [78] noted that in techniques such FDM or contour crafting, the formation of voids are more common as a result of inferior and anisotropicity during printing. Later research by Gibbons *et al*. [79] showed that void formation in FDM parts can consequently result in the delamination of contact layers after printing. In another research conducted by Duigo *et al*. [80], they noted that increasing filament thickness, further decreases porosity by deteriorating cohesion between layered parts, thus subsequently reducing tensile strength while increasing water uptake.

Surface anisotropy is one of the main challenges of 3D manufacturing as a result of the method of layer sequencing. Ngo *et al.* [78] noted that material microstructure at the boundary layer exhibit different characteristics to the ones deposited within the inside parameter of the print body and as such, material mechanical properties are varied under both vertical and horizontal compressive loads. Caroll *et al.* [81] reported that changes that occur morphologically in the transverse direction produce a higher tensile strength and ductility compared with those produced longitudinally. However, surface anisotropy could be useful in certain applications where specific surface wettability is a requirement. For example, special surface wettability can be achieved by controlling parameters like speed and spacing of the 3D printing filament [78]. The frictional response to surface anisotropy for most 3D printer parts has been studied extensively in literature where in most cases, the majority of the work has been focused on improving dimensional accuracy [82] through surface roughness refinement. However, the presence of surface excesses post-printing has been shown to have a significant effect on the tribological performance of 3D parts especially in the case where the surface is rubbing perpendicular or parallel to

the raster print direction. A recent work conducted by Dawuod *et al.* [83] to understand the relationship between friction performance and the raster gap for FDM printed ABS showed an increase in the CoF when a positive raster gap was introduced.

Ongoing research and development in material science are pushing the limits of 3D manufacturing to circumvent the challenges faced with technique. This work sought to address key challenging issues relating to Polyjet manufacturing and key material properties that could be advantageously combined with surface coating for enhancing material performance in areas including tribology and barrier property applications.

2.4 Coating synthesis

2.4.1 Introduction

In this section of the thesis, a comprehensive literature review of plasma synthesis in thin film deposition coating is discussed. This will entail an introduction to plasma deposition using physical, chemical and plasma-enhanced vapour deposition processes.

2.4.2 Plasma synthesis and characterisation

The term plasma as initially proposed by Irving Langmuir in the early 1920s explained the properties and behaviour of ionised gas in a high vacuum state. In general terms, a plasma may be described as a pseudo neutral gas consisting of a collection of ions, electrons, molecular species, and neutral atoms that display a combined characteristic when exposed to an electromagnetic field [84]. The reason for this quasi-neutrality is to achieve an overall electrically neutral state within the plasma body. This means the number of electrons n_e should be equal to the number of ions n_i in a single ionized plasma state. Typically in the laboratory, gas-phase ionization of atomic species is achieved by some form of electric current, microwave or radio energy [85, 86]. This explanation is far-reaching enough to include the spectrum of man-made plasmas (including fusion reactors, high-pressure arc, etc.). These plasma types differ significantly in their charge species density *n* (number per cm^3) and may range from 10^7 - 10^{20} cm^{-3} in artificial applications. In most industrial plasma applications, plasma densities within the arc and glow discharge regions (10^8 - 10^{14} cm^{-3}) are highly exploited for thin film deposition. Table 2-5 shows the different plasma types and their properties found in the universe. However, for thin-film applications, plasma species within the glow discharge regime (process plasmas) are mostly exploited.

Table 2-5- Typical parameters for various types of plasmas [87].

	Length scale (m)	Particle density (m^{-3})	Electron temperature (eV)	Magnetic Field (T)
Interstellar gas	10^{16}	10^{6}	1	10^{-10}
Solar wind	10^{10}	10^{7}	10	10^{-8}
Van Allen belts	10^{6}	10^{9}	10^{2}	10^{-6}
Earth's ionosphere	10^{5}	10^{11}	10^{-1}	3×10^{-5}
Solar corona	10^{8}	10^{13}	10^{2}	10^{-9}
Gas discharges	10^{-2}	10^{18}	2	–
Process plasmas	10^{-1}	10^{18}	10^{2}	10^{-1}
Fusion experiment	1	10^{19}–10^{20}	10^{3}–10^{4}	5
Fusion reactor	2	10^{20}	10^{4}	5

Based on the variability and the role of the working gas or discharge gas, plasma may play very crucial roles in thin film deposition aside from deposition. This may include surface modification through surface etching or forming active functional surfaces for specific applications [85, 86].

2.4.3 Thin film deposition techniques

2.4.3.1 **Physical vapour deposition (PVD)**

Physical vapour deposition (PVD) is a generic term used to describe thin film deposition process in which physical discharge of atomic species onto specific targeted substrates occur within a vacuum environment. In all cases during deposition, plasma or ions are mostly the main constituents of the vapour phase [88]. Argon has become one of the most widely utilized gas for PVD processes due to their inertness (which prevent surface oxidation), low cost (cheapest of all the noble gases), higher atomic mass relative to other sputtering gases and relative abundance in the atmosphere ~1% of the atmosphere [89]. Sometimes, reactive deposition could be achieved by introducing reactive gases such as N_2 and O_2. A typical example is achieved in the formation of TiN or AlN coating [90]. Commonly, a PVD process may involve techniques such as sputtering, thermal evaporation, ion plating and arc plating.

Sputtering or sputter deposition is one of the most highly utilised PVD techniques in thin-film process deposition. It is a non-thermal process involving the ejection of atomic species from the surface of a target material by highly energised particles, mostly ions, onto the near-surface of the substrate material. In a typical sputtering process, the target source material from which the coating material is sputtered

is positioned in a high vacuum chamber (typically between $5 \times 10^{-7} - 5 \times 10^{-4}$ Torr) together with the substrate material to be coated.

2.4.3.2 **Chemical vapour deposition (CVD)**

The earliest patent literature for CVD technology was recorded by de Lodyguine in 1890 where he prepared tungsten deposits using hydrogen reduction of WCl_6 on carbon filament lamb [91]. By definition, a CVD is a thermally controlled process where vapour condensation of reactive compounds or molecular species from a gas phase react to form solid deposits or thin-film structures on a target surface [92]. In the process preceding the nucleation stage, the gaseous compound bearing the reactive compound if not already in the gaseous phase is formed by the volatilization from either the solid or liquid feed and carried to the substrate surface through the action of a carrier gas or pressure difference. The process of CVD compared to other deposition techniques such as PVD or electrodeposition finds its greatest application in the synthesis of complex coating structures that may not be available when using conventional methods such as sputtering, ion-plating and vacuum evaporation. With the limited application of PVD systems in the deposition of high melting temperature elements such as tungsten, tantalum and carbon, CVD systems can reach temperatures as high as 900 ℃ [93] as compared to most PVD systems that can deposit at temperatures below 70 ℃ or up to 600 ℃ [14]. CVD technique provides the additional advantage of being able to deposit many alloys, carbides, oxides and nitrites of most metals and alloys [92]. However, for applications involving very sensitive substrates requiring temperatures below 100 ℃, CVD applications may not be ideal as one risks damaging the substrate to be coated. Instead, there are low pressure, plasma-enhanced CVD alternatives that have been developed to deposit thin films at lower temperatures (< 100 ℃) for polymeric and other thermally sensitive composite materials.

2.4.3.3 **Plasma enhanced chemical vapour deposition (PECVD)**

The utilisation of PECVD technique in the deposition of thin films is derived from the very principle underpinning chemical vapour deposition, being that chemistry is involved in the process of film formation. In PECVD, working gases are decomposed by the introduction of a plasma energy source collision between the source gas and energetic electrons with the primary incentive of depositing thin films at much-reduced temperature compared with either CVD or PVD processes. Commonly, electron temperature range of between 2 – 5 eV is adequate to initiate reactive gas decomposition through the use of plasma sources such as microwave (MW) plasma (frequency = 0.5–10 GHz; commonly 2.45 GHz), DC plasma, radio frequency (RF) (frequency = 1–500 MHz; commonly 13.56 MHz) or a combination of both. This means active reactive species of ions and radicals are constantly formed throughout the deposition cycle. Thus, the process is more complex, as several factors including,

substrate temperature, gas flow, process power, substrate bias, reactor geometry, electrode spacing, etc., play key roles in controlling the deposition process [94]. This technique makes it an ideal choice for the deposition of DLC films onto polymer substrates at temperatures well below both PVD and CVD processes.

2.5 Diamond-like carbon coating

Carbon, being one of the most naturally occurring elements on earth aside from oxygen exists in several forms of diamond, graphite and amorphous carbon. In recent discoveries, many more allotropes of this element have been reported, beginning with the discovery of buckminsterfullerene (zero-dimensional "0D") in 1985 [95] to carbon nanotubes in 1991 [96] and finally, the isolation of single-layer graphene sheets [97]. These allotropes of carbon stretching from diamond through to the amorphous carbon to fullerenes encompass all conceivable dimensionalities of materials structure and property from 0D to 3D, a characteristic feature that has not been witnessed for any other element except carbon.

Diamond-like carbon (DLC) is a general term used to describe an array of amorphous diamond-like carbon derivatives. Consequently, it has been used rather universally to describe the many types of non-crystalline, hard carbonaceous thin films [98]. However, in reality, its properties can significantly vary to that of diamond [99] due to the inherent infinitely tunable array of properties resulting from the flexibility in their synthesis. Possessing superior film properties as a lubricative material in tribological applications, high hardness, and stable chemical properties, DLC thin films have intensified the drive away from a vapour-phase synthesis of crystalline diamond material [100].

This section will review the preparation, characterization, types, deposition mechanism, bonding, mechanical and electrical properties as well as some useful applications of DLC coatings.

2.5.1 DLC structure and bonding mechanism

Carbon can form a prodigious array of amorphous and crystalline structures because of its ability to assume different bonding types and arrangements and exists in three hybridization states: sp^3, sp^2 and sp^1 (Figure 2-12) [101]. Due to its 4 available valence electrons, two of which are in the P-orbital and the other 2 in the S-orbital, hence yielding a ground state electronic configuration of $1s^2 2s^2 2p_x^1 2p_y^1$.

Carbon can bond covalently with other elements. Hybridization in carbon can generally form two uniquely different covalent bond types; sigma(σ) bonds, which are the strongest carbon bonds formed by overlapping electron clouds around the nuclei and pi (π) bonds, which are weaker bonds formed between overlapping P-orbitals by localized electrons.

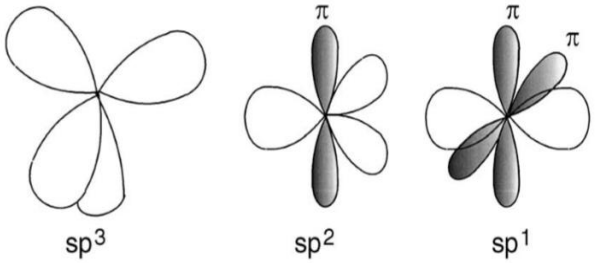

Figure 2-12- The hybridization bonding state of carbon showing sp^3, sp^2, sp^1 [101].

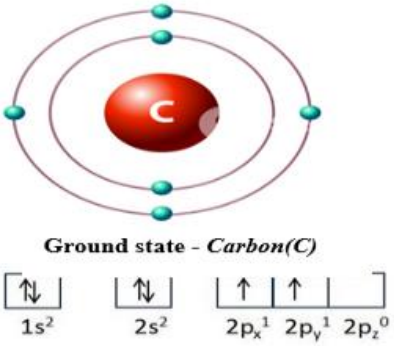

Figure 2-13- Electronic configuration of carbon [102].

The configuration involving sp^3 hybridization bonding, as seen in diamond, is such that, the four valence electrons of the carbon atom are each allocated to a tetrahedrally orientated sp^3 orbital, which makes a uniquely strong σ bond to a neighbouring available atom [102]. In the three-fold harmonized graphitic structure, characterized by sp^2 configuration (Figure 2-13), three out of the four valence electrons form σ bonds in a trigonally directed sp^2 orbital with the fourth unpaired electron of the sp^2 atom lying in the pπ orbital, oriented normal to the σ bonding plane. This delocalized pπ orbital has no affinity to bond with any neighbouring atom in the planar structure and so form a weaker π bond given graphite its characteristic layered structure (Figure 2-14). This property allows for a very low coefficient of friction to be achieved (as low as 0.001 [103]).

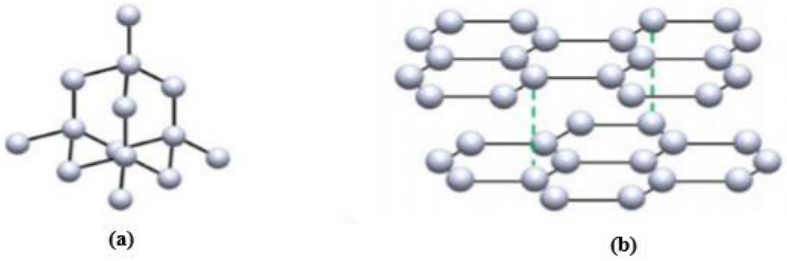

Figure 2-14- Carbon structure showing (a) sp^3 tetrahedral bonds in diamond (b) sp^2 planar bond in graphite [101].

In the sp^1 hybridization, two out of the four valence electrons enter the pπ orbital orientation in both the y and z directions whilst the remaining two electrons form σ bonds oriented along the ± x-axis. As a result of the wide physical and chemical properties exhibited by diamonds in real-life applications (high atomic density and bulk modulus, high thermal conductivity at room temperature) the search for artificial diamond-like materials to mimic these impressive properties has always been the focus for material scientists.

DLC films synthesized in the laboratory have over the years proven to be a great success with extremely similar physical and chemical properties to actual diamond, such as elastic modulus, hardness and chemical inertness [101]. However, these properties are attained in an isotropic disorderly fashion with no crystalline structure. Typical properties of DLC forms are compared with graphite and diamond in Table 2-6.

Table 2-6- A comparative physical property table of amorphous carbon with diamond, graphite, C_{60}, and polyethene [101].

	sp^3(%)	H(%)	Density(gcm^{-3})	Gap (eV)	Hardness(GPa)
Diamond	100	0	3.515	55	100
Graphite	0	0	2.267	0	0.2
C_{60}	0	0		1.6	
Glassy C	0	0	1.3-1.55	0.01	3
Evaporated C	0	0	1.9	0.4-0.7	3
Sputtered C	5	0	2.2	0.5	
ta-C	80-88	0	3.1	2.5	80
a-C:H hard	40	30-40	1.6-2.2	1.1-1.7	10-20
a-C:H soft	60	40-50	1.2-1.6	1.7-4	<10
ta-C:H	70	30	2.4	2.0-2.5	50
Polyethylene	100	67	0.92	6	0.01

The composition of DLC consists of not only amorphous carbon (a-C) but also hydrogenated allotropes, a-C:H with varying sp^2:sp^3 ratios. With a ternary phase diagram (Figure 2-15) showing the varying bonding types in amorphous carbon-hydrogen alloys, the true sense of the distinguishing C structures could be captured. The bottom left corner shows a disordered graphitized region predominantly composed of sp^2 hybridization where materials such as soot, char, glassy carbon and evaporated a-C. The limit of the triangle to the right is defined by two hydrocarbon polymers, polyethene, and polyacetylene beyond which the formation of C-C network bonds are restricted, and only molecules are formed [101]. Plasma enhanced deposition methods have been developed over the last few decades to push the limits from a more predominantly sp^2 regime to higher sp^3 fractions where diamond-like properties could be actualized for enhanced product functionality. In thin films where this becomes a reality, McKenzie [104] proposed a tetrahedral amorphous carbon (ta-C) instead of the sp^2 a-C form to distinguish the two materials. A range of deposition methods, for example, plasma-enhanced chemical

deposition (PECVD) technique, has shown to produce a-C:H films with diamond-like properties, hence being able to reach into the interior of the ternary phase diagram. Even though it is diamond-like, its hydrogen content is much larger than its sp^3 content producing a hydrogenated tetrahedral amorphous carbon(ta:C-H) in the process.

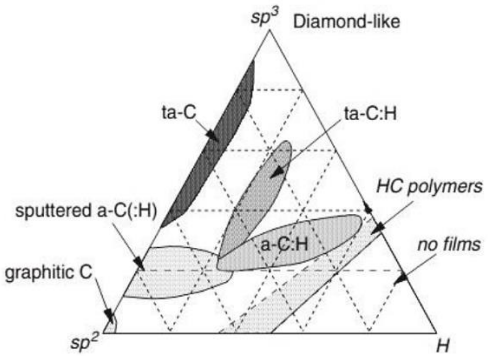

Figure 2-15- A ternary phase diagram showing the classification of DLC structures [101].

2.5.1.1 **Diamond-like carbon synthesis using PECVD systems**

Even though the mechanism of diamond synthesis is not fully understood, several authors like Setaka *et al.*, [105] have had greater success in understanding the synthesis of DLC coatings using MW-PECVD. Other research areas have also shown considerable potentials in the use of carbon targets in the synthesis of DLC coating using the PVD technique [106, 85]. However, the most important feature demonstrated by these findings is the use of hydrocarbon gases such as methane, acetylene and other forms of C-H containing compounds as working gases in the synthesis process.

For MW-PECVD deposition, Setaka *et al.* [105] proposed a conceptualised diagram describing the formation of DLC coating using methane gas (Figure 2-16). Here, the hydrocarbon species are decomposed in the plasma body with chemically active fragmentary hydrocarbon radicals and ions formed, which are later spontaneously diffused and adsorbed onto the substrate surface. During the early stages of carbon cluster formation, thermodynamically stable graphitic and amorphous structures are formed with an interspersed metastable diamond cluster. Setaka *et al*. [105] noted further that, since this chemical reaction rate between atomic hydrogen and graphite is 20 to 30 times faster than that of diamond, the exclusion of graphite as a result of the presence of higher atomic hydrogen is inevitable. This means by having differing target materials or precursor gases, pressure, temperature, electron or ion energies, thin films produced inevitably will display a varying array of physical characteristics from the soft and very lubricating a-C:H films, through to the formation of ta-C films with close performance to that of diamond [101].

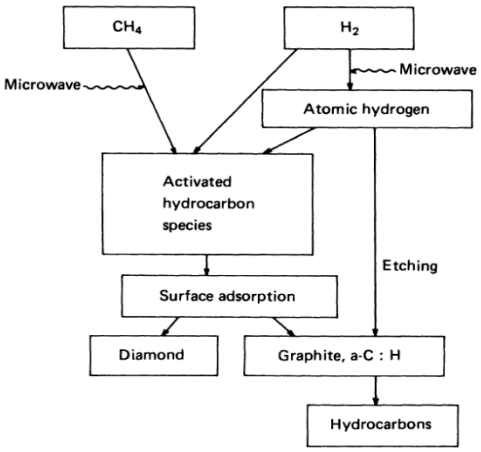

Figure 2-16- Schematic diagram showing the mechanism of DLC formation using MW-PECVD technique [105].

Plasma-assisted chemical vapour deposition (PECVD or PACVD) for DLC formation provide a hybrid deposition technique where chemical vapour deposition techniques are activated by energetic electrons (usually between 100-300 eV) within a plasma body. Whereas most PVD methods such as sputtering are initiated by inert precursor gases such as argon, PECVD allow the deposition of DLC using highly ionizable gases such as acetylene, benzene, etc. Precursors with low ionization potential such as benzene were primarily used as they promote higher deposition rates. However, research has shown that DLC properties rely on the ionic energy requirement per C atom and for benzene, this energy is equal to 100 eV per C atom [101]. Acetylene, on the other hand, has simple dissociating paths with a more acceptable ionization energy requirement of 200 eV, giving mainly $C_2H_n^+$ ions as seen in Figure 2-17. For mechanical applications, acetylene gas is always the preferred precursor choice, however, for electronic applications, the choice of selectivity is dependent on gas purity. Acetylene, on the other hand, is not available in high purity form and possesses a considerable high amount of nitrogen impurities which acts as a dopant in high-density plasma deposition systems [107].

It is well known that the temperature within the deposition chamber and on the substrate during plasma species bombardment is crucial to film growth. As a result, the stability and formation of highly preferred sp^3 or sp^2 sites are altered due to the preferential displacement by energetic ions and neutral species during thin film formation and growth. The growth and physical properties associated with a-C:H films are extremely dependent on the temperature variability during deposition and as such, the contribution to temperature build-up and film growth by the bombarding species are key during the deposition process. The contribution to film growth by neutral species was initially thought to have been heavily dependent on the mass deposition rate and as such higher deposition rates were expected. However, it was noted that the growth rate in itself is independent of temperature [101]. This was initially thought to be the case due to poorly adhered neutral species which will desorb at a higher temperature. Later on, it was concluded that this temperature reliance is as a result of the atomic

hydrogen etching effect on the thin film. Vacuum deposition involving either PVD or PECVD processes is pressure-dependent and tend to affect plasma stability and ionization of neutral atoms, film growth rate and sputter yield, and coating property. Typically, PECVD processes operating pressure is between 0.01 to 5Torr, allowing for the deposition of DLC films unto low thermal sensitive materials like polymeric materials.

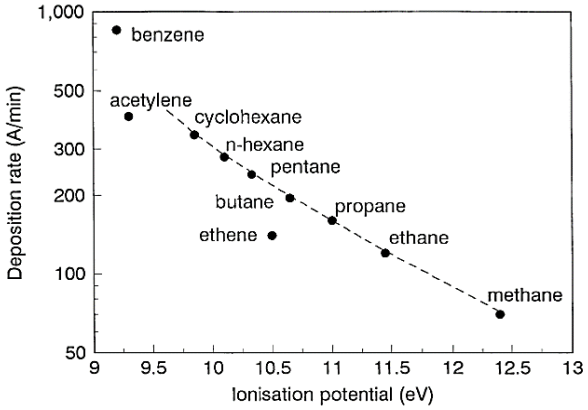

Figure 2-17- Deposition rate of a-C:H by PECVD vs. ionization potential of some useful precursor gases [101].

2.6 DLC as a functional coating for polymer-based materials

Modern assemblies of mechanical parts frequently operate within the boundary-lubricating regime where close contact asperity interaction can occur, as against thick lubricating film separating the sliding contact surfaces and consequently avoiding direct contact. Carbon-based coatings especially DLC films combine naturally the desired for low friction to high wear resistance.

Only until recently, has some efforts been made to deposit DLC coatings onto polymer substrates for tribological application. Pei *et al.* [108] noted that due to difficulty in measuring the coefficient of friction (CoF) for polymer materials, experimental data for DLC coated polymer materials were somehow contradictory, as Nakahigashi *et al.* [109] observed a CoF value close to 1 for DLC coated rubber compared with that of pristine rubber at 6. In contrast, other similar work reported a CoF in the range of 0.25 0.4 for DLC coated polymers as against a CoF value of 0.7-1.5 for uncoated polymers [110, 111] using He/C_2H_2 gas mixture at 0.15Torr. Carley [112] in an experiment to establish the CoF variability using MW-plasma from both Ar and O_2 treated ABS polymers and DLC coated ABS using MW-PECVD, observed that, at steady state, the lowest CoF of 0.45-0.52 can be achieved for both microwave Ar and O_2 plasma-treated ABS sliding against stainless steel. However, although these reported CoF values may seem rather high compared with other engineering materials like steel [113], the performance of coated DLC parts in reducing the overall CoF with time cannot be underestimated.

Many researchers have tried to clarify the role DLC coatings play in achieving such low frictional values by studying the structural transition between the bonding states of sp^2/sp^3 species giving rise to varying amorphization in diamond [109]. Early research studies showed that the graphitization of DLC coating may be solely responsible for such low frictional values [114], however, recent research has shown that, aside from the role DLC graphitization play in achieving low friction, the presence of high hydrogen levels within DLC films play a significant role in reducing the CoF value further by affecting film hardness, transfer layer generation and C–C bonding state [115]. Similar observations were made by Carley [112] when he deposited MW-PECVD on ABS substrate.

Carley [112] also compared the performance of different MW-PECVD DLC coatings on ABS and PEI polymer substrates to both indentation and Rockwell adhesion tests. His research showed improved quantitative results for coating hardness and scratch-resistance of the material surface. However, he observed that the substrate effect was still present at an indentation depth of < 5% of coating thickness. These substrate effects demonstrate to a larger extent the limitations an applied load has on coating strain failure during plastic deformation under repetitive stress. Damasceno *et al.* [116], further demonstrated a similar trend observed by Carley [112] but later noted rather opposite trends for both scratch and micro-hardness tests performed when DLC-Si coating was deposited on polyurethane polymer. This means, to increase the resistance to deformation of a polymer surface, the polymer must be elastic and same time hard.

Depending on the type of DLC coating one produces, hardness properties could vary significantly. These coatings characteristically come in two major forms: hydrogenated amorphous carbon (a-C:H) and amorphous (a-C). Subject to the sp^2/sp^3 ratios and hydrogen content, DLC films are classified as either soft or hard coatings [117]. Whereas hard DLC coatings may be suited for certain engineering materials with higher modulus such as steel, depositing similar coating types on a polymer may cause induced adhesion failure, leading to coating delamination as a result of the built-up of excessive compressive residual stress between the coating/substrate interlayer [117]. As the typical distance between two adjoining polymeric molecules is usually ~2.5, ~4.9 and ~7.4Å, whilst a 3-dimensional DLC structure has a typical distance of ~2.5Å, which is shorter than most polymers. The use of composite materials made of polymer and DLC may pose significant challenges due to their structural differences [118] as observed by Beak [119] and Baek *et al*. [120]. Bull [121] observed that the properties of both coating and substrate hardness have a positive correlation with the load-bearing capacity of the coating/substrate system. Carley [122] reported in an earlier study that a-C:H coating produced using MW-PECVD (2.7 - 4.9GPa) on ABS were prone to severe fracture and delamination when a nominal scratch load of 7N was applied. He attributed this to tensile failure as the coating H content reduces.

The load-bearing mechanics leading to DLC coating failure on coated polymers have not been extensively studied in the literature and for 3D printed polymers, are non-existent. Until now, few authors have dealt with polymer-DLC composites. Though authors like Ollivier *et al.* [123] and Carley [112] have assessed the adhesion performance of DLC films on Polyethylene Terephthalate (PET) and ABS using tensile testing, the composite of harder coating on a softer substrate always pose a complex mechanical response when deformed under load and in applications where friction and wear are involved. As a consequence, this work seeks to provide some understanding into how the resulting DLC coated 3D polymers studied in this work performs when under mechanical deformation at different loads and frictional regimes.

Apart from using DLC coatings for various tribological and mechanical applications, other modified variants could be synthesised and deposited onto polymers with the potential to resolve the problem of poor barrier performance for gases and water vapour. The use of DLC as an effective barrier can preserve material bulk properties by preventing material losses. Uncoated polymers usually have a WVTR in the 0.1-100 g/m^2-day range which is generally satisfactory for food packaging but not ideal for electronic applications [124]. Dennler et *al.* [125] noted that to achieve a sufficient lifetime usage for electronic application, a WVTR in the range of 10^{-6} g/m^2-day range is required. The application of thin layers of a few microns is shown to improve this property. Although there are no reported cases where these WVTR rates have been achieved using DLC films in literature, a few researchers have shown its viability in reducing the WVTR function. Ray *et al*. [126] after depositing 81nm of a-C:H on PET substrate observed a 49.87 g/m^2-day WVTR. This was approximately 10 times better than its pristine value. Zhang *et al.* [127] proposed that the degree of DLC film amorphization leading to varying sp^2 and sp^3 content produces unique WVTR responses. They observed a 12 times improvement in WVTR function compared to the pristine PET substrate as the DLC film produces a 40 % sp3 content. As a majority of the attention has been focused on the study of DLC film-forming technology with greater emphasis on film structure and morphology characterisation using techniques such as atomic force microscopy (AFM), X-ray and scanning electron microscopy (SEM), the connection between material bulk porosity, DLC thin-film synthesis using MW-PECVD and its synergy with 3D printed polymers in improving barrier performance, especially WVTR is explored in this study.

2.6 Challenges in coating polymers

The limited use of polymer-based materials especially AM polymers in plasma deposition methods has been mainly due to the potential influence of heat on the substrate. These polymers have considerably low melting temperatures and poor thermal instability when compared with other metallic materials. Their glass transition temperature (T_g), which is one of the most important thermal properties of any polymer defines the temperature range within which the polymer transitions from being a rigid solid

mass (glassy material) to a more pliable or rubbery material at elevated temperatures. T_g is not a distinct thermodynamic transition state, but a temperature range within which microscopic polymeric chain mobility increases with increasing temperature. The state and change in molecular structure mobility of polymer to temperature variation are considered very useful when choosing any materials for high-temperature application.

Thin-film deposition using PVD or CVD is a high-temperature deposition process and depending on the coating selection method employed, vacuum deposition temperatures could range from 100 ℃ to 500 ℃ [128]. These deposition temperatures on average are by far greater than most T_g and T_m of essentially many engineering polymers. Acrylonitrile-butadiene-styrene (ABS) for example has a T_g and T_m of 105 and 230 ℃ respectively, as against carbon steel which has a T_m of 1363 ℃. This means similar deposition conditions cannot be used for both substrates as this may result in severe structural defects or deformation (through melting, degradation) of the polymer.

Plasma and neutral gas-phase particles, tend to be much thermalized and disperse energetic particles, which greatly increase the temperature of the substrate, most especially the near-surface temperature. A typical heating curve for polymer, glass and metallic substrate during film deposition and growth using an ion-assist deposition technique is illustrated in Figure 2-18. With an initial deposition temperature of about 22.5 ℃, the rates of temperature change with time for each sample varied significantly at each deposition stage until T_{max} was attained. The plot further showed polymer samples heated up quickly and had the highest T_{max} when 100 nm of thin film was deposited unto the substrate.

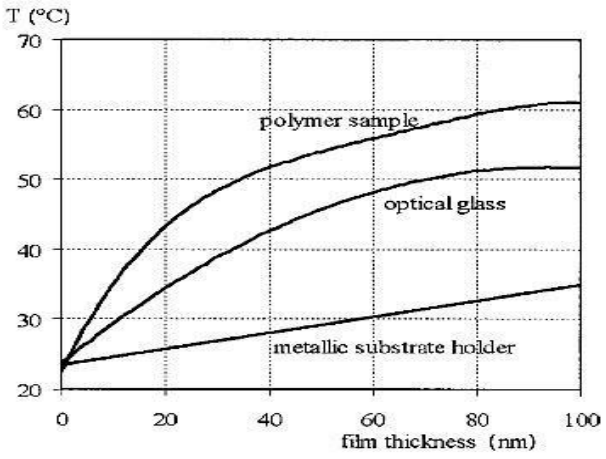

Figure 2-18- Temperature development measured for different engineering materials [129].

Schulz [129], in a review of modern techniques in characterising the antireflective behaviour of thermoplastic materials, indicated that the rate of substrate heating is a combined function of the average heat energy received from sputtered particles and the plasma source used in the sputtering process. However, Yamamoto *et al.* [130] further went on to demonstrate that the temperature of a polymer

substrate is a function of the radiation heat from the electrode and deposition chamber walls as well as the plasma source as shown in Figure 2-19.

The first task of any deposition process involving polymeric materials is to provide a coating method that minimizes the temperature upsurge during the process of thin-film deposition. However, depending on the type and mode of application, polymer materials can be coated with functionalized thin film by adjusting both the process and operational parameters during plasma generation and thin film deposition stages. The process of generating and sustaining a plasma body, most especially within the glow discharge region is highly dependent on the voltage applied, current and pressure of the system.

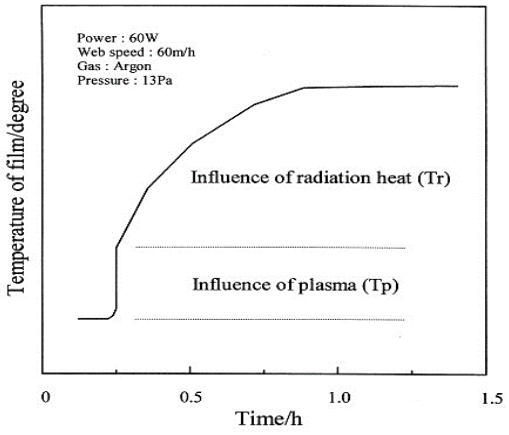

Figure 2-19- Substrate temperature dependence curve [130].

In other to sustain a plasma body, there is always the need to maintain high ionisation efficiency between the charged particles (electrons) on one hand and the neutral gas atoms on the other. Upon impacting the substrate surface, these energetic particles cause molecular vibration at the near-surface resulting in substrate heating in the process. To minimise this problem of substrate heating, the cathodic voltage and plasma energy must be adequately controlled during the deposition phase. This, however, has the added disadvantage of reducing sputter yield in the case of a PVD system, resulting in prolonged deposition time. Nonetheless, it is an effective way of introducing functionality to polymer substrates with low T_g and T_m values through time step deposition without causing any physical deformation to the substrate. *Sarto et al.* [131] in the study of the effect of low energy ion bombardment on polydiethylenei-glycol-bis allyl-carbonate (CR39) and polycarbonate (PC) polymer substrate, successfully deposited hard oxide thin film coating by keeping the substrate temperature below its T_g. He further demonstrated that PC polymers could be coated below 50 ℃ by using 3 runs of 12mins of intermittent cooling period lasting a total of 1hr. Carley [112] kept the temperature of both acrylonitrile butadiene styrene (ABS) and Polyetherimide (PEI) at 70 ℃ by depositing DLC coatings during a 16-26 minute run with an intermittent cooling period of 1hr.

2.7 Thin film adhesion on polymer

The adherence of thin-film and multi-layered structures, on surfaces especially polymer substrates often dictate reliability, most importantly in applications where devices undergo thermo-mechanical cycling. In recent times, the adhesion of thin films has mainly focused on understanding the mechanics of mechanical coupling and molecular bonding or surface chemistry interaction between deposited thin films and their substrate counterparts.

Mechanical coupling or surface interlocking mechanism is centred on the principles of physical interlocking of two surfaces such that one material or the other must fracture or distort for both materials to be separated. Currently, the debate surrounding the process of surface binding is very much divided with different sides to the argument. It is of the view by some researchers that adhesion is highly improved during mechanical interlocking whereas others believe the process of achieving higher molecular bonding between thin film and substrate is through surface roughening. Vasconcelos *et al.* [132] in an experiment to determine the adhesion mechanism existing between aluminium particles and an epoxy-based matrix concluded the process is controlled not only by the physical-mechanical interaction at the interface but also the weak chemical interaction between the two surfaces.

Molecular interaction through surface bonding is the most accepted mechanism for explaining the process of adhesion between two surfaces in contact. These intermolecular interactions could be electrostatic, chemical or Van der Waals type. Meaning both the deposited material and substrate have a major role to play in deciding the level of adhesion that could be achieved. Dos Santos Ferreira *et al.* [133], observed this phenomenon when depositing four different metallic thin films onto ABS substrates. The total fracture energy observed during the peel-off test showed a stronger adhesion in the following ranking sequence; Cu< (1.0) <Ti (1.4) <Cr (2.1) <Al (2.3), by qualitatively comparing all the adhesion responses with copper as the reference material. In another experiment to ascertain the effect of surface roughness contribution to adhesion through mechanical interlocking, the fracture energy for PP, PET, PC, PET-G and ABS were studied. Using ABS as a reference, the different fracture toughness value of the individual polymers were ranked as follows; PP (0.005) <PET (3.1) <PC (0.12) <PET-G (0.30) <ABS (1). However, the most striking findings observed were the huge fracture energy differences recorded for both PET and PET-G. polymers. With a highly rough PET-G polymer surface, it was expected the mechanism of surface interlocking will play a significant role in improving fracture toughness, however, the opposite was observed in this case with PET showing an increased fracture toughness value (almost a factor of 10). This goes to confirm that the chemistry of adhesion is very much reliant on the surface chemistry as well as the molecular bonding interaction between the contacting species, rather than exclusively relying on mechanical interlocking.

The key to achieving superior functionality in all coated polymer applications is to have a reproducible substrate surface. However, many of the properties, which define most polymeric materials, rely on the structure, chemical composition of the near-surface and most importantly the positioning of specific chemical functionality. In this regard, process parameters that lead to polymer surface modification are targeted at enhancing good bonding with any deposited layer.

In most cases, polymers surfaces have relatively very low surface energies per unit area as compared to other engineering materials such as metal. This in effect makes these materials unsuitable for direct coating or the deposition of either similar or dissimilar thin-film material. To resolve the issue of poor adhesion between polymer substrate and deposited thin-film material, surface energy modification is always considered key. However, this method alone does not guarantee good adhesion; but rather the flexibility of the process enhances the modification of the material chemistry for optimum adhesion [134].

This means surface preparation is critical in achieving the required physical and chemical surface modification. Most commonly, treatment methods such as plasma treatment, chemical treatment, ion beam, X-rays, and other heat treatment methods are mostly employed to influence adhesion, surface structure and morphology, texture and property [135]. Nevertheless, the consequences of these surface modification techniques are most often than not short-lived and degrade with time, hence must be utilised within the shortest time after activation [136].

Chemical surface modification is aimed at creating new functional groups at the boundary of the materials undergoing adhesion. Surface treatment of polymer using chemical treatment with specific chemical reagents such as acids and oxidisers have been extensively investigated to increase surface polarity by creating stronger adhesive molecular force between the substrate and deposited thin film [136]. The application of solvent-based surface primers especially toluene and xylene have been utilised in some cases to improve polymer adhesion despite the negative environmental effect associated with its usage. However, due to the risk associated with chemical surface treatment and the need to control cross-contamination during the MW-PECVD deposition phase, the use of chemical treatment for surface modification of the additively manufactured material was not be considered.

Polymer surface activation using plasma treatment has become one of the most vital techniques in achieving good adhesion between substrates and thin film. Its importance in surface modification processes provides the added advantage through the provision of a high-reliability bond structure at the near-surface rather than the modification of the entire bulk material. Functionalisation of the substrate species is key in this technique. Oxygen-containing plasma treatment of polymer substrate, for example, induces the formation of functional groups such as C-O, C-O-O, C=O, O-C=O and another hydroxyl group. These oxygen-containing functional groups especially C=O, has been linked with increased adhesion and improving surface wetting in PP polymer substrates [137, 138].

Research has shown, that short time plasma pre-treatment on most polymeric materials, for example, PP (<6s exposure time), can create a significantly higher adhesion bond than in primer pre-treatment applications and as a result, adhesion using surface oxidation techniques have become increasingly popular and effective in maintaining thermodynamically stable adhesion [137].

Plasma treatment methods and techniques come in various forms and the variability in the methods of treatment such as plasma condition and gas composition defines how ions, electrons, radicals, fast-moving neutrals and molecules affect the processes defined by the treatment method i.e. etching, crosslinking and plasma activation. The process of achieving surface modification through plasma treatment in a vacuum is an expensive process requiring expensive vacuum systems. However, new techniques involving atmospheric plasma treatment of polymer materials have been introduced recently to change the dynamics of surface modification. Messines *et al.* [139] using atmospheric plasma glow discharge successfully deposited saline group onto the surface of PP to enhance the surface adhesion property. Likewise, Guimond *et al.* [140] used a similar plasma treatment technique to alter the surface functionality of PP film using air corona and nitrogen. It was noted that the use of nitrogen improved significantly the surface energy of the polymer substrate by creating functional groups such as amine, amide and hydroxyl groups on the substrate surface.

Recent studies using a combination of different surface analysing techniques, for example, XPS, atomic force microscopy (AFM), secondary ion mass spectrometry (SIMS) have all shown a stronger correlation between atmospheric plasma treatment and stronger surface adhesion properties in polymers [141, 142]. Kwon *et al.* [141] in exploring the effect of plasma treatment time, power and gas flow rate on surface energy concluded that the changes in surface free energy as a result of plasma exposure was due to the simultaneous formation and breaking of polar bonds.

Köstler *et al.* [143] further reiterated this point when they investigated poly-diallyl dimethylammonium chloride (PDADMAC) polymer and found a direct link between surface energy and polymer chain arrangement at the near-surface. He concluded the experiment based on the contact angle measurement for this sample. Most importantly, the type of plasma utilized for the process of surface modification has a tremendous effect on surface adhesion and wettability as already pointed out. Research and academic papers have shown the importance of plasma surface modification play in modifying substrate surface energy through the addition of polar functional groups which is heavily linked to improving surface wettability [142]. An investigation into the properties exhibited by pre-treated PP by an O_2/Ar plasma concluded that although both treatment methods improved the surface energy of the polymer surface, Ar plasma outperformed O_2 plasma in improving substrate wettability [141]. This enhanced capability achieved through Ar treatment allows for enhanced adhesion at the polymer substrate interface as a result of the introduction of functionality to the otherwise neutral polymer substrate [142].

2.8 Tribology

2.8.1 Fundamentals of tribology

Friction is defined as the tangential resistance force (F) which opposes motion when two contacting surfaces are in relative motion [144].

$$F = \mu N \quad \ldots\ldots\ldots \qquad (2.1)$$

Where μ is the friction coefficient and N represent the normal force. As already articulated by Amonton in 1699, the friction resistance is directly proportional to the applied load. μ is independent of the apparent contact area between the two bodies in relative motion. The value and significance of μ are highly dependent on whether the motion between the two contacting solids has just started or is already in motion. In the former case before the two bodies are set in motion, static friction $\mu_s = \mathrm{F/N}$ is dominant. When in motion, the dynamic force or kinematic friction dominates this regime and is defined as the ratio of the force required to maintain motion at a set speed and applied load: $\mu_d = \mathrm{F/N}$. Friction contacts involving pure metals or alloys have been shown to promote high friction values due to their strong adhesion necessitated by their strong metallic bonding with μ_s equal to or greater than 2 [144]. Polymers, unlike metals and ceramics, exhibit low friction and high wear due to their low stiffness and strength.

2.8.2 Friction of polymers

The events characterising the tribology of polymers entails a host of complex surface mechanical and material interaction processes that differ from other engineering materials, for example, metals and ceramic. It is well established that the size and structure of the macromolecule composing the linear structure of a polymer molecule interlinked by weaker intermolecular forces provide a variety of tribological applications creating unique material performances under both dry and lubricated contact regimes. The basics of polymer tribology are such that, the key principal concepts defining tribological performance is attributed to two main mechanisms, deformation and adhesion [145]. In the case involving the deformation component, the resistance to deformation at the contact surface is primarily a material-dependent property, however, the adhesion component is attributed to the interfacial bonds formed or broken as a result of the weak polymer chains structure at the polymer surface or in the bulk material [145, 146]. This makes PBMs very promising tribologically with the functional ability to control both friction and wear behaviours under sliding contact on both non-polymer-on-polymer or polymer-on-polymer tribosystems.

It is a common phenomenon in polymer tribology to see a directly proportional relationship between frictional force and applied load as defined by Amontons's law of friction [147], however, at certain loads, this proportionality breaks down [148]. Several pieces of research have shown this phenomenon

experimentally, where at 10-100 N, the friction coefficient remained essentially constant when a steel ball slides over nylon, polymethylmethacrylate (PMMA), polyvinylchloride (PVC) and polytetrafluoroethylene (PTFE) [149]. Bowers *et al.* [150] also obtained a similar frictional response with similar materials at 2-15N.

To the right and left of this proportionality range, the relationship between the applied load and friction force breaks down [148]. Rees [151] showed that at moderate loads 0.02-1N the coefficient of friction decreases with increasing applied load. This typical behaviour is mostly associated with the elastic deformation of the surface asperities [148]. On the other side of the proportionality limit, the reverse occurs where there is an increase in friction force with increasing load due to the plastic deformation of the surface asperities. Hence, as proposed by Kragelskii [152], the friction coefficient value passes through an initial minimum elastic deformation contact region followed by a plastic deformation regime where the coefficient of friction increases with increasing load.

Velocity variation at the contact surface of polymers is shown to be independent of the sliding velocity, a good approximation that is only useful in the case where contact surface temperature variation, and interfacial behaviour, remain insignificant as a result. At low velocities, the shear viscous resistance of the surface asperities in the contact zone increases with increasing velocity. However, at high velocities, the contact asperities experience elastic behaviour and as a consequence, the friction force relies only marginally on the velocity. At a moderate range of velocities, all the above characteristics are in competition and highly dependent on the force-sliding velocity curve of which is primarily dependent on the polymer relaxation properties [153]. Due to the viscoelastic nature of polymers, they are very sensitive to frictional heat created during solid-solid contact movements, where typically mechanical energy is converted into heat energy in the process [154]. Hence, for smooth surfaces in a highly elastic state, the basic mechanism controlling polymer friction is adhesion. However, several processes relating to molecular chain incision due to the transformation of mechanical energy into heat at the contact surface results from several mechanisms relating to plastic deformation, hysteresis and viscous flow of the polymer material. For friction patterns as a function of temperature, a correlation is valid only when a change in temperature on the contact surface produces no effect on adhesion [155]. In the case where a polymer is transformed into a glassy state, mechanical loss contribution to the re-deformation of the polymer surface layer become greater and contributes more to the friction coefficient.

2.8.3 Wear of polymers

Wear on PBMs is controlled by a series of multi-faceted regimes often distinguished by four main modes; abrasive, adhesive, fatigue and tribo-chemical wear which results from the changes in the chemical structure at the boundary layer during solid-solid contact [156].

2.8.3.1 **Abrasive wear**

For most polymers, the fundamental mechanism which acts as the basis for wear relates to the cutting and ploughing of surface asperities or harder wear particles [144]. It may result from many causes including wear debris produced during limited lubrication conditions, wear particles suspended in lubricated contact regimes, corrosion products, dust particles and rough surfaces. Particulates generated under such regimes may move easily to abrade both surfaces in contact by a three-body abrasive mechanism. However, they may become partly embedded in either one of the two mating surfaces and act as an abrasive tool in a two-body abrasion [157]. Debris produced by abrasion commonly assume the shape of scratch, gouges and scoring marks [146] on a much finer scale as though produced from a material machining process.

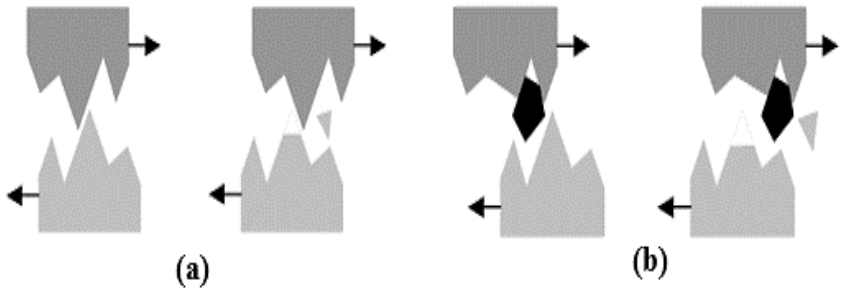

Figure 2-20- Abrasive wear mechanism showing (a) two-body (b) three-body abrasion mechanism [158].

The modes which form the foundation of deformation when abrasive particles act on plastic substrates takes the shape of plastic grooving or ploughing and cutting. Where in the latter, materials in the form of chips are displaced from the mating surface (Figure 2-20). Ploughing often results in the plastic displacement of material in a sideways continuous fashion to form ridges adjacent to the developing grove [146].

The loss in weight of solid material as a result of the continuous repetitive elastic and plastic deformation of surface asperities lead to material removal and defines the wear of a material. The quantification of wear defined by the specific wear rate μ_{sp} is the volumetric loss of the solid material V_{loss} with an applied force *F* and sliding length *D.*

$$\mu_{sp} = \frac{V_{loss}}{F.D} \quad \ldots\ldots\ldots \qquad (2.2)$$

2.8.3.2 **Fatigue wear**

The development of fatigue wear on polymers is a multi-faceted process where repetitive stressing on the material surface create progressive fracture deformation. Its distinctive feature is the accretion of irretrievable plastic deformation, giving rise to the generation and development of cracks (Figure 2-21). In a friction contact characterised by repetitive stressing at the mating contact of both surfaces, each asperity which forms part of the real contact area is capable of promoting pulse heating and plastic deformation at this junction. As a consequence, the nucleation of defects in the surface is favoured by two stress fields brought about by the local contact spots concentrated at the surface.

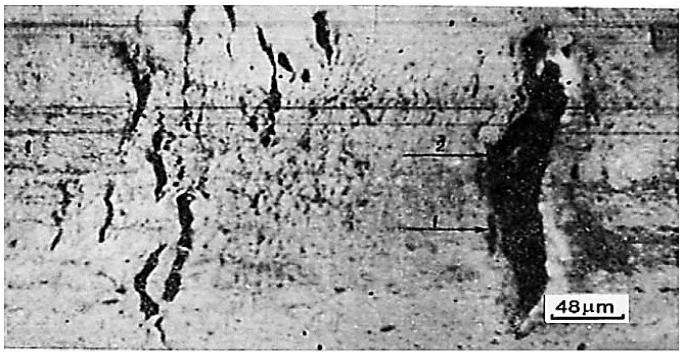

Figure 2-21- Fatigue wear damage on epoxy resin [146].

2.8.3.3 **Adhesive wear**

This wear mechanism entails the formation and rupture of micro-junctions formed as a result of adhesion of polymer unto counter surface during rubbing. The welding between the opposing asperities creates a distinguishing feature on the mating counterpart surfaces in that the localised transfer of wear debris is governed by the bonding between the two contacting surfaces (Figure 2-22). Bely *et al.* [158] explained that the characteristic transfer of wear debris during tribological contacts is a key feature in the adhesive wear mechanism of polymers.

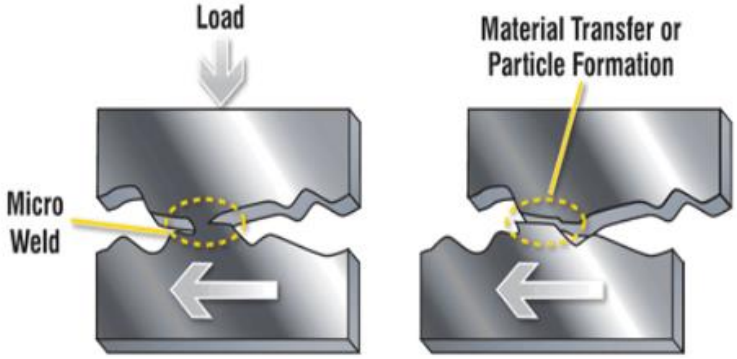

Figure 2-22- Diagram showing a typical adhesive wear process [158].

However, under certain conditions, the thin layer polymer transfer film is continuously carried away from the counterface, thus increasing the wear rate in the process. The fragmentation of transfer polymer may show up in a variety of shapes or form depending on the test conditions and operational environment. Figure 2-23 shows a typical polymer fragmentation pattern shown on varying polymer type surfaces against steel.

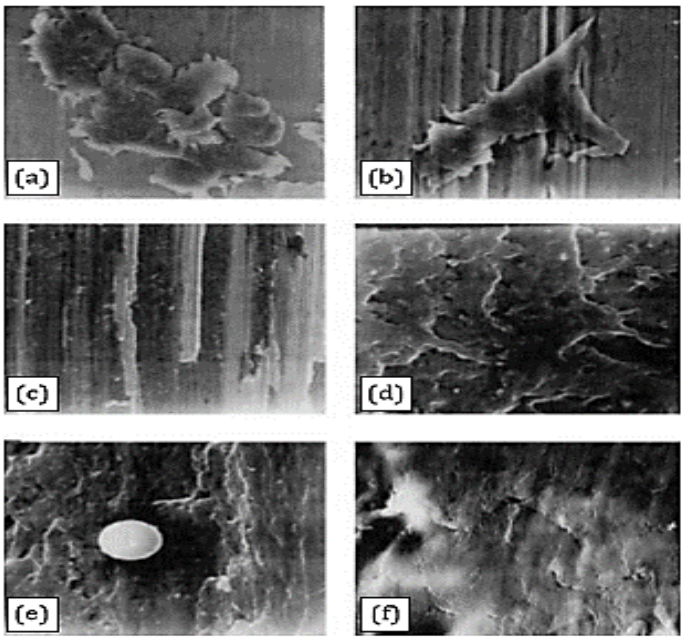

Figure 2-23- Polymer fragmentation transfer film against steel showing the deformation on (a) and (b) HDPE, (c), (d) and (e) PA and (f) PTFE [158]**.**

2.8.4 Tribology of coated polymers

Earlier literature on coatings for tribological applications included work done by Gorlach *et al*. [160], and Kang and Eiss [161] on PI-based copolymers who focused on the development of robust coatings for tribological applications. Carbon-based coatings especially Diamond-like carbon (DLC) has shown an unusual combination with polymer substrates for low friction coefficient, low wear, good adhesion, relatively high hardness and high elastic properties [162]. Kaczorowski *et al.* [163] in the study of the impact of plasma treatment on the tribological properties of DLC/PDMS substrates noted a reduction in the CoF performance between both coated and uncoated substrates. They, however, noted that the most obvious changes were seen when the polymer substrate was pre-treated. Kaczorowski *et al.* [164] in another study to determine the friction coefficient of DLC on PEEK substrate observed that the best tribological performance is seen for coatings with the lowest sp^3 C-C bonds. Similar results were reported by Erdemir and Donnet [165].

Several papers have studied similarly, the possibility of controlling properties of other engineering polymers with DLC film by modifying both material and process parameters to achieve lower friction and improved adhesion [166, 161, 103, 164]. To date, there are many well-known techniques for producing DLC coating [166, 161, 103], with the dominant technique being CVD and PVD [163]. Nevertheless, there are still areas where the current technology for producing DLC using either radiofrequency or micro-wave PECVD technology is still being explored. Such areas include coatings on additively manufactured polymer substrates for enhanced engineering applications. In this case, a significant problem is the limitation caused by the need to deposit at low temperatures (below 40 °C) and the low value of Young's modulus of the 3D printed polymers.

2.8.5 Tribology of additively manufactured polymers

The functional correlation between process parameters and wear have shown that PBM undergoes several modes of wear, including abrasive, corrosive, fatigue and adhesive wear [167, 168]. The most common mechanism, abrasive wear, is self-evident during a steel-on-polymer tribo contact [167]. More often than not, there is no single wear regime characterising a tribo contact involving PBM on steel but a combination of different wear regimes [144].

The frictional response of 3D manufactured PBM provide a different dimension to understanding the role material properties such as hardness [169], surface roughness, and transfer layers play in different tribological regimes. Most recently, a lot of work has been focused essentially on improving dimensional accuracy [170], material strength characterisation [171, 172] and surface roughness refinement [173], all to improve both friction and wear behaviour at the contact interface [171, 172]. Dawuod *et al.* [83], noted an increase in the friction behaviour of 3D-printed acrylonitrile butadiene styrene (ABS) parts manufactured by fused deposition modelling when a positive raster gap was introduced (as shown in Figure 2-24). They defined the raster gap as the gap distance between two adjacent filaments, deposited in the same print plane). They demonstrated that this increase was a result of the independent nature of the deposited filament structure within the filament modelling body contributing separately to elevating the friction coefficient value.

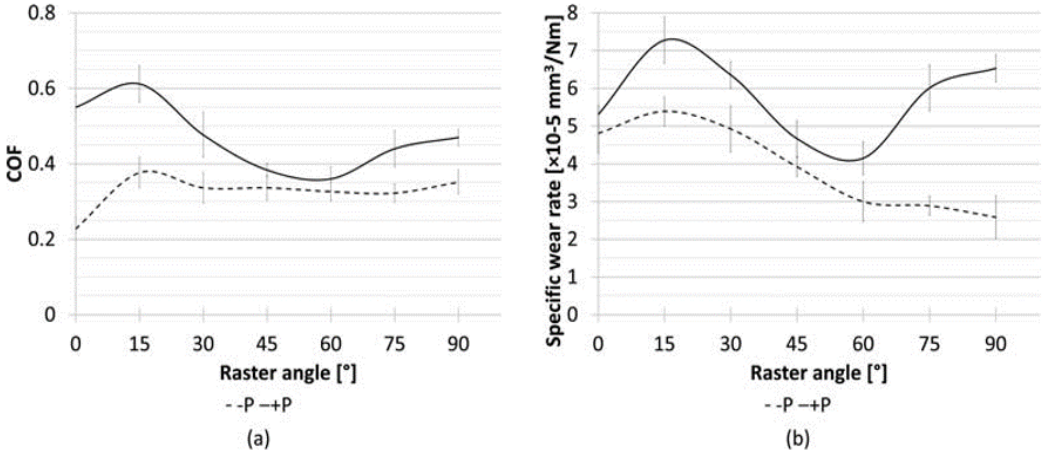

Figure 2-24- Tribological behaviour of pure acrylonitrile butadiene styrene manufactured using fused deposition modelling (FDM) (a)friction coefficient and (b) specific wear rate. * - P is the negative gap width +P is the positive gap width [83].

Sood *et al*. [170], reported similarly an increase in the wear rate when a positive gap is used during manufacturing. The use of positive gap they noted, encourages the creation of pits on the wear surface. Friction heat produced at the steel-polymer interface has a significant role to play on both interfacial and wear adhesion behaviour of films [148]. Generally, thermally conductive metallic counterparts used in tribo pair application involving polymers have shown to promote the formation and adhesion of transfer films on hard metallic counterparts [167].

2.9 Polymer permeability

2.9.1 Introduction

The internal structural complexity of PBMs has shown extensive influence on the permeation of solutes through polymer structure [174, 175]. For instance, polymer chain distribution of amorphous thermoplastics shows extensive irregularity and randomness resulting in free volume or porosity within the polymer structure. This free volume creates tortuous paths allowing gases and hydrate ions to move freely within their pore structures. McKeen [176] recounted a permeability coefficient value twice as much for CO_2 through an amorphous PEEK film in comparison with crystalline samples. Likewise, studies conducted by Cowling and Park [177] on the permeability of CO_2, H_2, Ne and N_2 through a 90 % trans 1,4-polybutadiene described as crystalline and a mixed cis and trans 1,4 butadiene membrane showed that the permeability of all the permeating species was nearly one order of magnitude larger for the amorphous mixed cis and trans 1,4 butadiene membrane than for the crystalline trans 1,4-polybutadiene.

The transition from glassy to a viscoelastic state defined by the T_g of PBMs is very key in providing material bulk properties such as permeability when exposed to heat. When polymers are exposed to an

increasing temperature above its glass transition temperature, T_g, polymer chains within the amorphous region begin to re-orient to provide extra free volume space, hence, the proportional fraction free volume space within the amorphous region increases linearly as temperature increase [178]. The essence of T_g for most engineering polymers is to provide the maximum workable temperature, in particular, the load-bearing and collapse rating exhibit for load-bearing structures. There are, however, some suggestions that the T_g of polymers can be changed during exposure to fluids, which in some cases are considered part of the ageing process. A common example is a change in the crystallisation temperature of some polymers when exposed to supercritical CO_2. Kikic *et al.* [179], noticed a decrease in the crystalline temperature during the plasticization by supercritical CO_2 of poly-2,6 dimethyl phenylene oxide (PPO), poly-acrylic acid (PAA). They later explained this complex phenomenon by attributing the decline in T_g to polymer swelling and the self-lubricating effect possess by the dissolved CO_2 gas acting to facilitate polymer chain movement. Randal [180] in an experiment to determine the water vapour permeability of biodegradable polymers noted similarly, the correlation between polymer crystallinity as a function of T_g.

2.9.2 Mechanism of gas permeation

The fundamental molecular transportation through polymer membrane occurs as a result of indiscriminate molecular motion within the polymer matrix. The driving force which defines molecular sorption, diffusion and permeation through a well-defined polymer membrane is governed by the concentration gradient between the phase-separated by the penetrant and membrane. Fick's first law of diffusion, according to which the total diffusive flux, *J*, defines the amount of penetrants passing through a plane of unit area normal to the direction of flow per unit time is proportional to the concentration gradient.

$$J = -D\left(\frac{\partial c}{\partial x}\right) = DS\,\frac{dp}{dx} \quad \ldots\ldots\ldots (2.3)$$

Where *D,* is the diffusion coefficient (length ^{2}/time,cm^2/s). $\frac{\partial c}{\partial x}$ concentration gradient also known as the solubility, *S*. p is the pressure and x is the material thickness (cm).

On the other hand, as the diffusion process proceeds, the rate of change of the penetrant concentration $\frac{\partial c}{\partial x}$ across the diffusion membrane where x > 0 is described by Fick's second law is:-

$$\frac{\partial c}{\partial x} = D\left(\frac{\partial c^2}{\partial x^2}\right) \quad \ldots\ldots\ldots \quad (2.4)$$

Generally, at unsteady state, where experiments are conducted over a small interval of c, an integral diffusion coefficient function $\overline{D}$ over the concentration range c_1 and c_2 is given as;-

$$\overline{D} = \int_{C_1}^{C_2} D(c)\, dc / c_1 - c_2 \quad \ldots\ldots\ldots \quad (2.5)$$

With c_1 and c_2 being the concentration gradient of the penetrant at the high and low molecular concentration faces of the membrane (Figure 2-25)

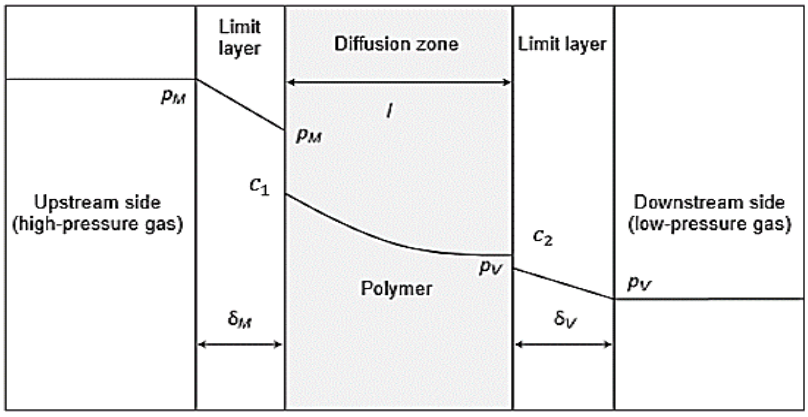

Figure 2-25- Diffusion through polymer membrane showing the different resistance [181]**.**

At a given temperature, the amount of gas dissolved in a material can be related to the partial pressure by Henry's Law;

$$C = s.p \quad \ldots\ldots\ldots (2.6)$$

Where *C,s* and *p* are the concentration, solubility and pressure of the permeant in the film.

At steady-state condition where the diffusion flow is constant throughout the membrane, Fick's first law may be integrated to obtain the following expression

$$J = \frac{D(c_1 - c_2)}{x} \quad \ldots\ldots\ldots \quad (2.7)$$

Assuming the solubility *s* and diffusion coefficient *D* of the permeant is independent of the permeant concentration, then the permeability coefficient, *P* can be defined as:

$$P = D.s \quad \ldots\ldots\ldots \quad (2.8)$$

Therefore, the water vapour transmission rate (wvtr) can be expressed accordingly by the following expression;

$$wvtr = \frac{P.\Delta p}{x}\left(\frac{g}{m^2.day}\right) \quad \ldots\ldots\ldots \quad (2.9)$$

For a multilayer structure, the total permeability, P_T, can be expressed mathematically according to laminate theory;

$$\frac{1}{P_T} = \frac{X_P/_X}{P_P} + \frac{X_C/_X}{P_C} + \frac{X_1/_X}{P_1} \ldots\ldots\ldots \quad (2.10)$$

Where X_P, X_C and X_P are the polymer, inorganic and other layer film thickness. P_P, P_C and P_1 are the permeabilities of the polymer, inorganic material and other layer thickness [181].

2.10 Water sorption

The sorption term usually describes the equilibrium amount of penetrants sorbed within the polymer matrix. This term describes the adsorption, absorption as well as entrapment of penetrants within the free voids of the polymer bulk material.

The governing thermodynamic condition of the polymer-sorbate system, in particular, the force and nature of the said interaction at equilibrium are governed by classes of different sorption modes. Table 2-7 and Figure 2-26 present the sorption models for polymer sorbate interaction at equilibrium [181] as well as the classes of thermodynamic interaction between both polymers and the sorbate.

Table 2-7- Different sorption interaction modes.

Sorption mode	Sorption interaction mechanism
Henry	polymer-polymer
Langmuir	polymer-penetrant
Dual-mode	combination of Henry's and Langmuir modes
Flory-Huggins	penetrant-penetrant
Brunauer–Emmett–Teller (BET)	Combination of Langmuir and Flory-Huggins mode

The simplest sorption phenomenon which is also known as Henry's sorption is considered in an ideal case where a linear relationship exists between an absorbate as a function of pressure.

$$C = k_D p \quad \ldots\ldots\ldots \quad (2.11)$$

k_D also, *S*, the solubility coefficient term of the sorbate in the polymer is defined by the solubility constant term which is independent of sorbate concentration at a constant temperature [181].

The sorption mode is essentially observed for weak low-pressure sorbate-polymer or sorbate-sorbate interaction. In the Langmuir-mode sorption, the predominant interaction is defined by the polymer-sorbate interaction where sorbed molecules occupy free volume fractions sites within the polymer structural voids. At the point of maximum saturation, a tiny fraction of the diffused sorbate may solubilise [181]. In Flory-Huggings mode, the interaction between the molecules of the sorbate is stronger in comparison with the polymer-sorbate interaction resulting in an increased solubility coefficient with pressure. This phenomenon provides two main possible behaviours according to Naylor [182], which is the plasticisation of the polymer by the sorbate or the formation of sorbate clusters in the case of hydrophobic water- polymer interaction. Brunauer–Emmett–Teller (BET) model serves to provide the physical adsorption of sorbate unto highly hydrophilic polymers. The highly sorbed molecules may exist at corresponding polar group sites and later cluster under high pressure.

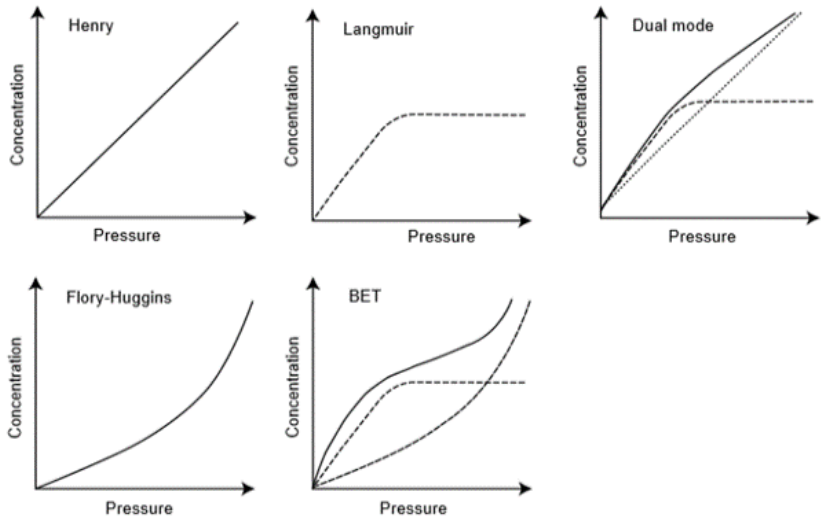

Figure 2-26- Sorption models for polymer sorbate interaction at equilibrium [181].

2.11 Overview of current coatings for improving barrier properties

Surface modification on polymers by thin nano-layers of hard coatings especially DLC has been exploited extensively in the literature for barrier applications, especially in polymer applications. Amongst thin two-dimensional (2D) materials, monolayer graphene produced by CVD technique has been extensively investigated as a gas barrier. However, as a result of the presence of structural defects such as grain boundary variations and point defects in polycrystalline graphene, low gas barrier performance for graphene has been reported [183, 184]. In sputter deposition technique, a great number of research has been focused on inorganic thin film coatings for barrier functionality. Normally, SiO_2 and Al_2O_3 are used for such applications. An overview of the WVTR achieve using inorganic sputter coatings are shown in Table 2-8. These WVTR values are typically a magnitude higher than what is

achieved using evaporation technique. However, for Al_2O_3 and $ZnSnO_x$ coating, Fahlteich observed higher WVTR when running in the transition mode rather than the oxide mode [185].

Table 2-8- WVTR for a single layer thin coating deposited by sputtering.

Coating	Sputtering technique	Substrate	WVTR (MOCON)
SiO_2	Planar RF magnetron	PEN	5 x 10^{-2} g/m^2-day [185]
TiO_2	Planar magnetron, reactive sputtering	PEN	3 x 10^{-1} g/m^2-day [186]
Al_2O_3	Planar magnetron, reactive sputtering	PEN	1 x 10^{-2} g/m^2-day [186, 187]
	Dual magnetron roll-to-roll system	PET	3 x 10^{-2} g/m^2-day [188]
$ZnSnO_X$	Planar magnetron, reactive sputtering	PET	2 x 10^{-2} g/m^2-day [185]
SiZnO	Planar RF magnetron	PI	5 x 10^{-2} g/m^2-day [189]

Besides the formation of metallic oxide coatings, the incorporation of nitrogen into metallic films or oxides containing coatings (metal oxynitrides) has also been investigated as a means of improving the barrier properties. Jin *et al.* [190], Lee *et al.* [191] and Iwamori *et al.* [192] have studied the barrier performance of AlO_x and SiO_X incorporated with N_2. For both films, the barrier properties were significantly improved compared to the pristine metallic oxide film. Erla *et al*. [193] noted that the inclusion of N_2 promotes better interaction with H_2O due to the presence of N-rich active sites. This chemical interaction results in the formation of hydrated compounds which lead to water entrapment and subsequently reduce permeation. Ray *et al.* [126] showed that, the effect of nitrogen doping on a-C:H films has a positive correlation on the WVTR performance. They observed that, by increasing the gas flow rate for nitrogen from 5sccm (standard cubic centimetre per minute) to 20sccm, an ~ 8 and ~12% reduction in the WVTR was observed for the respective DLC coating structures deposited on PET polymers.

Table 2-9- PECVD deposited film for WVTR application

Coating	Technique	Substrate	WVTR (MOCON)
SiON	PECVD – 60 ℃	PET	7.6 x 10^{-2} g/m^2-day [191]
SiOx	PECVD - 150 ℃	High temperature PES	3 x 10^{-1} g/m^2-day [195]
	PECVD – 50 ℃	PET	1.3 x 10^{-1} g/m^2-day [193]
SiCN	Organic catalytic CVD 180 – 190 ℃	High temperature PES	1 x 10^{-3} g/m^2-day [196]

PECVD technique has in recent times shown greater potential in barrier coating applications due to its high deposition rate and conformal coverage. Sekhar *et al.* [194] studied the effect of DLC coatings on the gas barrier performance of PET substrate and saw a 5-10 times improvement in the gas barrier performance. Current works (Table 2-9) have been focused primarily on the synthesis of silicon derivative coatings such as oxides and nitrides with very limited work on DLC coatings synthesised using MW-PECVD technique.

2.12 Surface texturing

The selection of surface engineering techniques for surface modification is an integral tool in designing very adaptive and functioning surfaces for specific engineering purposes. Primarily, the most important requirement involves one that provides one or more functional properties like wear resistance, creep, fatigue, pitting resistance, barrier properties etc. As part of the modification techniques, surface texturing have provided surface finishing roles offering additional independence to produce a specifically defined function. However, the synergetic connection between the ambit of functional material properties, application and engineering technologies are rather very complex. Techniques including photo etching, laser and ion beam texturing, machining and plasma etching have become common in providing a different geometrical pattern to control substrate contact behaviour. By providing the right functionality, specific target application could be achieved. For example, surface adhesion function could be enhanced by carefully controlling substrate surface free energy or wettability through texturing [197]. A unique case is that of superhydrophobic surfaces produced by sub-micron scale surface pattern to provide additional functionality to serve specific purposes, for example, water repellent, self-cleaning and coating adhesion improvement [198]. By this method, Man-Kwan *et al*. [198] demonstrated the effect of surface micro rolling-based texturing in improving the hydrophobicity of aluminium surface. For polymers, considerable prominence is given to surface adhesion improvement using both chemical and physical alteration methods. In tribological applications, this approach has provided improved performance by introducing variation in surface contact mechanics and response during surface contacts. Several authors have shown interesting results in both experimental and computational studies to explain these responsive tribological performances for textured surfaces under dry and lubricated contact regimes [199]. In a hydrodynamic lubrication environment, the introduction of square-pattern dimples has been reported to lower the friction coefficient response due to lubricant retention within the micro-pores and cavities [199]. Jaebong and Cho [199] went further to demonstrate the effect of surface texture density in reducing the friction coefficient of polyoxymethylene.

2.12 Summary

The literature review has provided a comprehensive overview of the subject relating to polymer additive manufacturing principles and how existing vacuum coating technology could be used to improve their functional performance in the areas of tribology and barrier performance. The physics, principles and application of using vacuum technology for the process of deposition coatings on polymer substrates, with great emphasis on the most commonly used techniques such as PVD, CVD and PECVD are discussed. The synthesis, properties and deposition of DLC coatings onto polymers are detailed. As already discussed, the use of PECVD deposition has shown increasing usage in the deposition of DLC coatings structures onto polymer substrates for enhanced functionality, however, the use of MW-PECVD has not been explored in coating additively manufactured polymers. With techniques such as CVD and PVD stilled on the rise, an ideal deposition process for polymers should satisfy the process requirement in achieving a high deposition rate, good step coverage with desired functional properties such as hardness, optical transparency and good adhesion [102].

Thin-film deposition using PVD or PE-CVD is a low to high-temperature deposition process and depending on the coating selection method employed, vacuum deposition temperatures could range from 100 to 500 ℃. These deposition temperatures on average are by far greater than most glass transition temperature (T_g) and melting temperatures (T_m) of essentially many engineering polymers. Moulded ABS for example has a T_g of 105 ℃ as against a Polyjet additively manufactured ABS (3D ABS) of 51 ℃ [69]. This means similar deposition conditions cannot be used for both substrates as this may result in severe structural defects or deformation (through melting, degradation) of the 3D printed polymer. Hence, the first task of any deposition process is to provide a coating method that minimizes the temperature upsurge during the process of thin-film formation. PECVD has shown greater potential in this regard by reducing the thermal load on polymers with low T_g and T_m by allowing deposition at room temperatures whilst maintaining a higher deposition rate throughout the deposition cycle.

This work focuses on providing a well-tailored and bespoke DLC coating produced using the MW-PECVD technique to achieve an advantageous combination of 3D printed polymer bulk properties with the particulate structural properties of a single layer DLC film to improve the functional properties of the underlying AM polymer substrate. In this work, we explored the systematic study on a series of nitrogen-doped DLC films grown under different gas flow regimes. Their microstructure, mechanical properties, and chemical structural composition in relation to adhesion, barrier and tribological functions will be studied and discussed. Both the uncoated and coated film properties (including mechanical, physical and chemical) will be determined using techniques such as nanoindentation, MICP, AFM, X-ray, Raman etc. These characterisation tests are designed to produce the best showcase

of film properties that can be produced on AM polymers using the novel MW-PECVD deposition technique.

Chapter 3

Experimental methodology

3.1 Introduction

This section describes in detail the procedures and methods employed in the characterisation of all the additively manufactured polymers selected for investigation and further outlines the technique used to deposit coatings onto these polymers using MW-PECVD. The analysis in this chapter will focus on three main parts; the first relating to sample preparation and characterisation (pre-coating), the second relating to DLC coating and deposition, and lastly, coating assessment and performance (post-coating analysis). A summary outline describing the experimental methodology is shown in Figure 3-1.

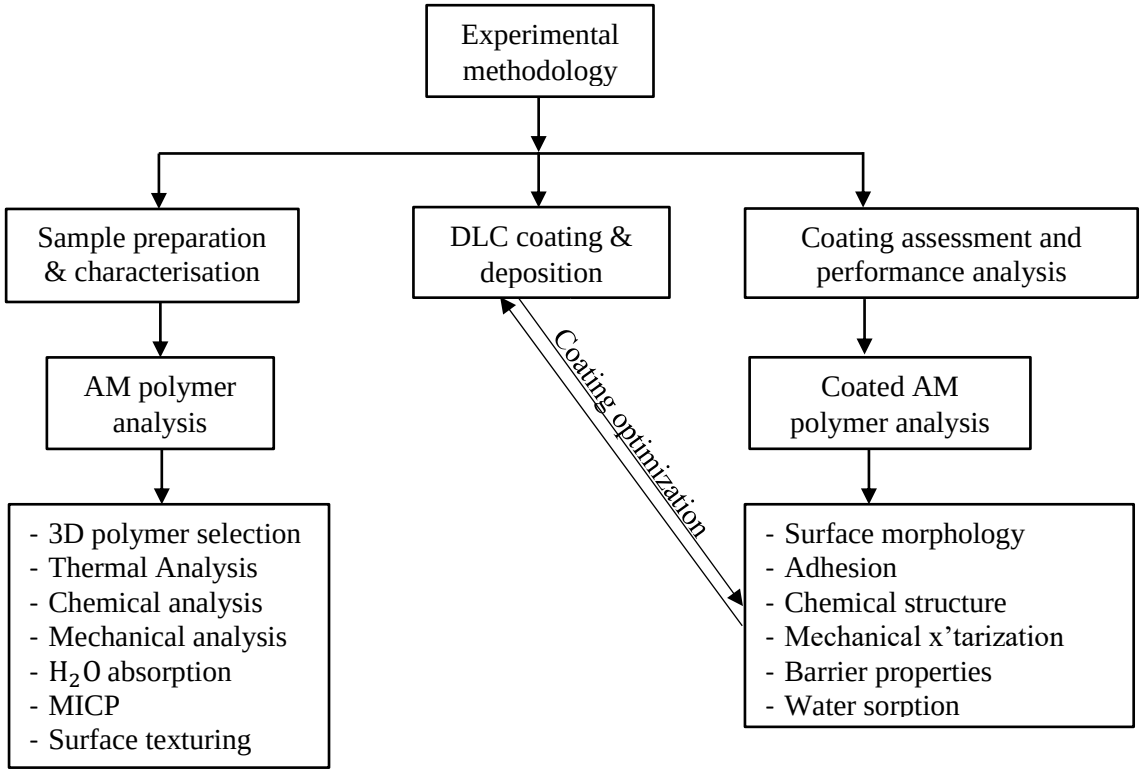

Figure 3-1- Summary outline of the experimental methodology utilised in this study.

3.2 Sample preparation and characterisation

3.2.1 Polymer selection and preparation

This section is aimed at providing a concise outline of the methods and procedures used in the characterisation of all the additively manufactured polymers selected for investigation in this thesis. For this study, a selection of 5 additively manufactured acrylic and epoxy-based resins was made through a consultative study between P&G and the University of Leeds. Properties including Young's modulus, glass transition temperature and water absorption for the individual polymers are presented in Table 3-1. Figure 3-2 shows both AM printers (Polyjet 100 and EnvisionTech^{TM}) utilized in the manufacturing of the 3D polymers. Due to their propriety rights, very little in terms of material properties or characterisations have been reported in the literature. For this reason, this section serves to provide adequate justification for characterising the properties of the individual polymers, such as physical, mechanical, chemical, etc. and to provide the right suitability for use in a MW-PECVD system. These selectivity methods as detailed in each section are presented below.

The liquid photopolymer resins for part manufacturing were supplied by Stratasys USA. A computer-aided design (CAD) drawings for modelling the dimensions and sizes of the required sample to print were created using Solidworks®2017 and printed using Polyjet® 1000 and EvisionTech printers [200] as shown in Figure 3-3. Table 3-2 and Table 3-3 provide detailed parameter settings utilised for the fabrication of both Polyjet® 1000 and EvisionTechTM printers respectively. For this study, two main design options were printed. These were textured or untextured substrates. For the textured surfaces, special design features were added to the substrate surface. Full details are shown in section 3.2.7 of this Chapter. For the untextured surface, no additional features were added. However, as AM polymers inherently possess rougher surfaces due to their method of printing which requires materials to be layered sequentially, substrates printed for this work were of no exception. These design shapes were modelled and printed based on the individual requirement of the equipment and characterisation techniques used in this work [15]. Table 3-4 provides a summary of the additively manufactured parts used in this work and the corresponding tests used in characterising both the uncoated and coated samples.

Table 3-1- General properties of selected additively manufactured polymers [69].

Sample	Glass transition temperature (°C)	Water absorption (%)	Outgassing (<1%weight loss)	Young's modulus (MPa)
3D ABS	61	-	Y	2600-3000
Veroblue	49	1.5	N	2740
Verogray	56	1.1	N	3000
LS600	61	-	N	1800
RCP30	45.08	-	N	N/A

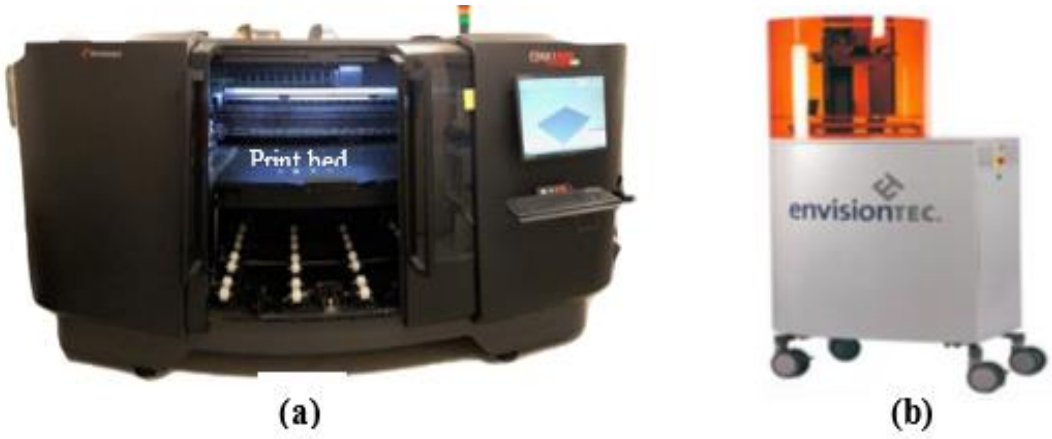

Figure 3-2- Sample diagram of (a) Stratasys® Objet 1000TM 3d printer (b) P3 mini multi lens envisionTech™ P4K series 3d printer [201].

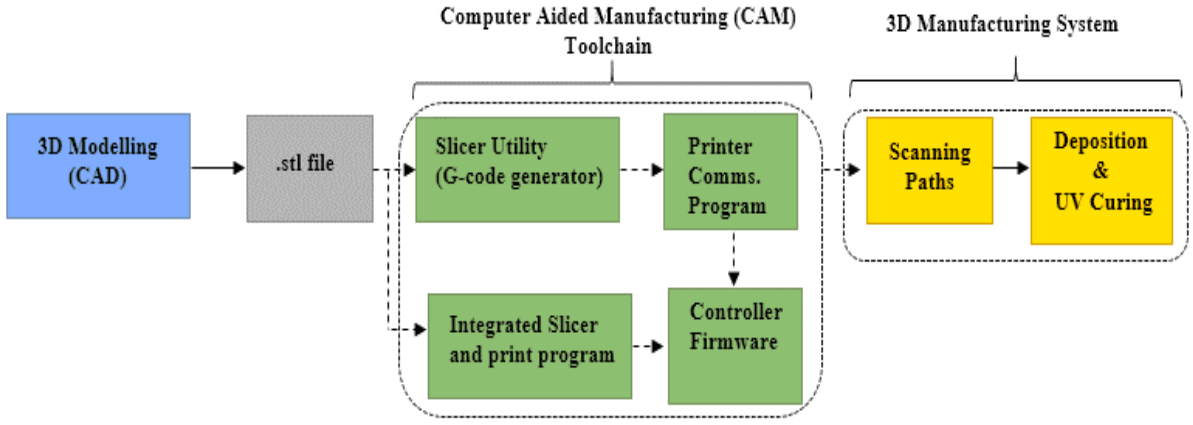

Figure 3-3- Process flow diagram for the development and manufacture of the 3D printed parts for both Polyjet and envisionTech™.

Table 3-2- Polyjet 1000 printer parameters for fabricating 3D polymers.

Polyjet 1000 printing parameters	
Resolution	
X-axis	300dpi
Y-axis	300dpi
Z-axis	1600dpi
Print Accuracy	600µm
Layer thickness	16 µm

Table 3-3- EnvisionTEC™ P4K printer series parameters for fabricating 3D polymers.

EnvisionTEC™ P4K series printing parameters	
Built Envelope	230 x 143.75 x 180 mm
Native Pixel Size XY	35 µm
Pixel Size With ERM	23
Dynamic Voxel Resolution in Z	25 µm
Projector Resolution	2560 x 1600 (WZXGA)

Table 3-4- Substrate design types with dimension and characterisation methods.

Substrate design options	Sample design type	Dimension	Characterisation techniques
Untextured	A [Cirular disc shaped]	25mm (diameter) x 0.28mm (thickness)	WVTR, MICP
	B [Rectangular shaped]	20mm x15mm x 2mm	Nanoindentation, SEM, FTIR, Raman, Tribology
	C [Rectangular shaped]	4.5mm x 5mm x 2mm	AFM, Talysurf profilometry, X-ray, scratch test for adhesion
	*D [Rectangular shaped]-Polished	4.5mm x 5mm x 2mm	Scratch test for adhesion
	ASTM D638	See Figure 3-6	Mechanical test
Textured	E[Circular disc shaped]	25mm (diameter) x 0.28mm (thickness)	WVTR, MICP

3.2.2 Thermal analysis

The purpose of this selective test is to analyse and understand the thermal characteristics of the different 3D printed polymer samples under process control conditions and to further determine their suitability for the coating process. This section describes two of the many thermal analytical methods used in the characterisation of polymers.

3.2.2.1 **Differential scanning calorimetry (DSC)**

Differential scanning calorimetry (DSC) measures the response of polymers to heating. A typical DCS set-up comprises a thermal cell with a sensory unit that registers the temperature variation between two test cells, a thermally inert reference crucible (empty) and a sample filled crucible. The design of a DSC system could either take the form of heat flux or a power compensated DSC module. Although fundamentally different in operation, they have the added advantage of producing comparable data during analysis. The Q20 DSC module works on the heat flux design principle where both sample and reference pans are heated from the same source. The produced signal, which is a measure of the temperature difference between the sample and reference material, is converted to a power differential signal using the calibration sensory thermal unit. The uniqueness of this system relies on the symmetric transfer of thermal energy from the furnace to the sample and reference pans through very conductive materials. Depending on the design method, metals, ceramics or quartz glass can be used.

During the process of heating, heat flows to the sample and reference material to raise the set temperature to produce a differential temperature signal ΔT which is usually transmitted in the form of an electrical potential difference between the heat flow rate of the reference pan and sample. This is given by the expression

$$\Delta T = T_S - T_R \quad \ldots\ldots\ldots \qquad (3.1)$$

Where T_S and T_R are the sample and reference temperatures.

The heat flow rate m, which is calculated by multiplying the differential temperature signal value by the machine constant (factory installed), k' is given by the expression;

$$m = k'x\,\Delta T \quad \ldots\ldots\ldots \qquad (3.2)$$

In most Q20 DSC's, the heat flux is available for temperatures in the range of -1900 ℃ to 1600 ℃ [202]. To determine the T_g of all the 3D samples under study, 8 mg of the individual samples were weighed in a 70µL aluminium pan using a TA microbalance. With a heating and cooling cycle from 35 ℃ to 250 ℃ under N_2 environment, a heating rate of 10 ℃/min was used.

3.2.2.2 **Thermogravimetric analysis**

Thermogravimetric analysis (TGA), unlike the DSC method, detects and measures changes in sample mass as a measure of both physical and chemical properties when exposed to heating. Though many variants in the overall type and design exist, the simplest design which is a basic feature in all TGA

equipment comprises a high precision analytical microbalance to which the sample crucible is attached (Figure 3-4).

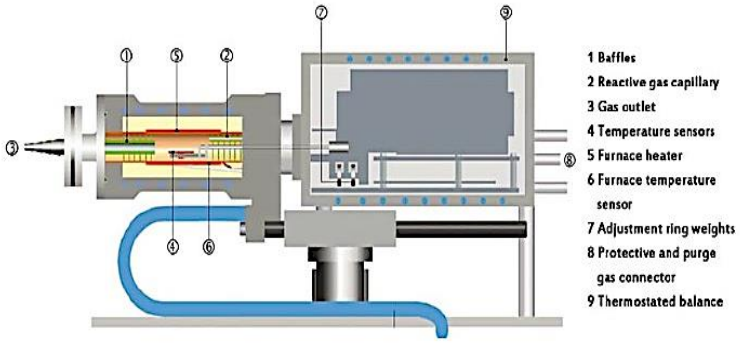

Figure 3-4- Schematic presentation of TGA [203].

In most TGA designs, the equipment control and sample weight balance process are usually influenced by the systems ability to regulate and maintain thermal system equilibrium through dynamic heating and cooling cycles. The process of thermal analysis using TGA methods is an extremely beneficial tool for defining several chemical kinetic processes of liquid and solid material, however, the characterisation of these materials during thermal exposure is key especially during vaporisation, sublimation and decomposition temperatures resulting in material loss.

In this work, the Mettler Toledo TGA/DC1™ equipment was used. Samples weighing 5mg for each additively manufactured polymer were utilised for this analysis. For all tests, a 70µl alumina crucible pan was used. The temperature was cycled between 30 ℃ and 600 ℃ 25 times under both N_2/Air environment. The measured results of total mass change versus temperature for each duty cycle run was noted and plotted to determine the activation energies for the individual polymers under both N_2/Air. Chapter 4 provides a detailed description and analysis of the TGA results.

3.2.4 Mechanical property analysis

It is always very difficult in most cases to classify polymeric material unlike other engineering materials such as metallic or glassy solids, as the majority of their mechanical properties rely strictly on the form of testing, for instance, the rate of application of tensile load, the amount of strain and temperature.

Polymers are usually described as viscoelastic materials, due to their transitional character of acting in one breathe as a viscous liquid and in another as an elastic solid. In most load application measurements, polymers tend to exhibit glass-like properties at high frequencies of measurement or low-temperature conditions. A typical polymer under such conditions may record very high Young's modulus of between 1-10 GPa and at strains greater than 5 %, will experience complete failure or flow. However, the mode

of application of the load is very key in determining the material selection and design parameters. The different physical definitions of polymer behaviour such as creep, necking, fracture, etc., are always considered unique to each polymer material and measurements in that regard are considered separate by comparing different studies of polymer test methods under load tension.

For mechanical tensile testing, the uniaxial tension under load is often characterised by the minuscular response from the material in tension where the strain is measured at the limit of deformation using an extensometer or strain gauge [204, 205]. The outcome of such tests is a plot of a stress-strain curve or equivalently force-displacement curve (Figure 3-5).

To characterise the tensile behaviour of the AM polymers, experimental testing using geometries as specified in ASTM D-638 for Type IV was used. Tensile testing of each specimen was conducted on the INSTRON 5967 universal tensile machine equipped with a 30 kN load cell. The INSTRON wedged grips were displaced at a rate of 5 mm/min with a data (force, strain and grip displacement) capture rate of 100 Hz. An axial clip-on 2630-107 extensometer (25 mm gauge length) was used to measure strain. To ensure reliable and repeatable data, the tensile tests were repeated three times and an average was calculated. The test specimens as shown in Figure 3-6 were all printed with a thickness of 4mm as detailed in ASTM D-638 for the Type IV for polymer tensile testing. The individual STL file generated from solid works were exported to both 3D printers as detailed in Figure 3-3. For this work, the force, displacement and strain values were captured using the BlueHill software as detailed in Chapter 4.

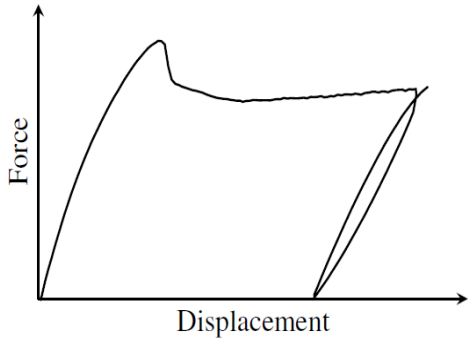

Figure 3-5- Sample plot showing force-displacement cycle curve from a uniaxial tension test [204].

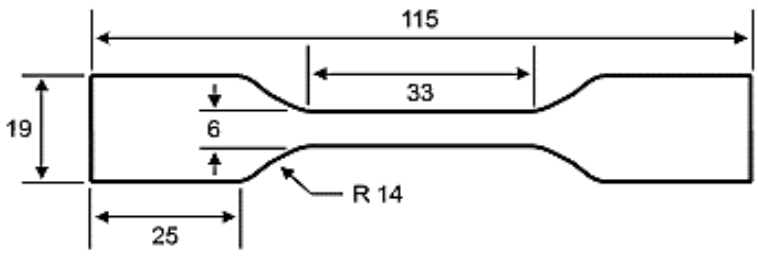

Figure 3-6- Schematic representation of the ASTM D638 Type IV tensile specimen with geometric specification in mm.

3.2.5 Water absorption

The water absorption properties of the 3D printed samples were tested according to the ASTM D570 standard for polymer materials. The rate function for water absorption utilised in this analysis sort to define the portion of water absorbed by the 3D printed polymers where the relationship between moisture absorbed and material performance can be made. In this test, the total amount of water sorbed is determined by using equation 3.12. With the ASTM D570 absorption test as standards, samples to be measured were first dried in an oven for 24hr at 25 ℃ to rid the surface of any adsorbed moisture. At room temperature, samples were first weighed for their dry weight (W_{dry}) and later transferred into a beaker containing distilled water for 24hr. After the end of the test, samples were removed from the distilled water and dabbed gently with a lint-free cloth to remove any excess water. The final wet weight (W_{wet}) was recorded. From equation 3.12, the total percentage (%) water absorbed, $W(\%)$ was computed. A total of 5 samples were measured and an average was taken.

$$W(\%) = \frac{W_{wet} - W_{dry}}{W_{dry}} \quad \dots \dots \dots \quad (3.3)$$

3.2.6 Mercury porosimetry

Mercury porosimetry is an extremely useful technique for characterising pore size and pore distribution functions in porous materials. The scope of characterisation covers a wide range of pores sizes from 3.5 nm to 500 µm [206]. Since mercury is a non-wetting liquid, one of the main limitations is the inability to measure the actual inner size of a pore but rather provide a measure to the pore entrance. The key point defining the geometry for all pore structures defined within the remits of this technique assumes a cylindrical pore geometry using a modified Young-Laplace equation or the Wash burn equation (3.13) [207].

$$\Delta P = \gamma\left(\frac{1}{r_1} + \frac{1}{r_2}\right) = \frac{2\gamma cos\theta}{r_{pore}} \quad \dots \dots \dots \quad (3.4)$$

This equation relates to the pressure difference (ΔP) across the curved mercury interface defined by r_1 and r_2 to the equivalent pore size (r_{pore}) using the surface tension of mercury (γ) and the contact angle (θ) between the mercury and the solid. A Micromeritics AutoporeIV 9520 system was used for this analysis. Samples with 25mm diameter and 0.28 mm thickness were oven-dried at 25 ℃ for 24 hr to remove all free water adsorbed on the surface. Samples were later loaded into a penetrometer and evacuated. This was later followed up by a mercury backfill. The penetrometer pressure was later increased to 25 psi in the low-pressure port and up to 6000 psi in the high-pressure chamber. The

mercury's contact angle is 130 º and the surface tension is 485 dyn/cm. An injection rate of 0.001 µl/g/s of mercury was used for this work.

3.2.7 Surface texturing

Surface modification techniques of polymer materials for enhanced performance, in general, have relied primarily on the addition, removal or deformation of materials from the pristine surface, creating surface modification properties that are either physical or chemical [208]. Techniques, for example, photolithography, focus ion beam machining, micromachining, direct writing techniques among others, have been used in recent times to modify polymer surfaces from the nano to the macro-scale. Nevertheless, the prospect of using these methods involve the utilization of toxic chemicals in some instances or the requirement for a multiplicity of steps, which could later turn cumbersome in the end. Alternatively, a bespoke surface design approach using the Polyjet 1000 printer was utilised to create two surface texture designs (shown in Figure 3-7 and Figure 3-8) to understand the limitations of aspect ratio and feature size/proximity effects on the performance of the coated textured surface for water barrier applications. In this work, aspect ratios (width: height) for textured A and B were 3.5:1 and 7:1 respectively.

Printed textured samples A and B as shown in both Figure 3-7 and Figure 3-8 were further studied for their crack resistance properties under flexural load in a three-point bend test as shown in Figure 3-9.

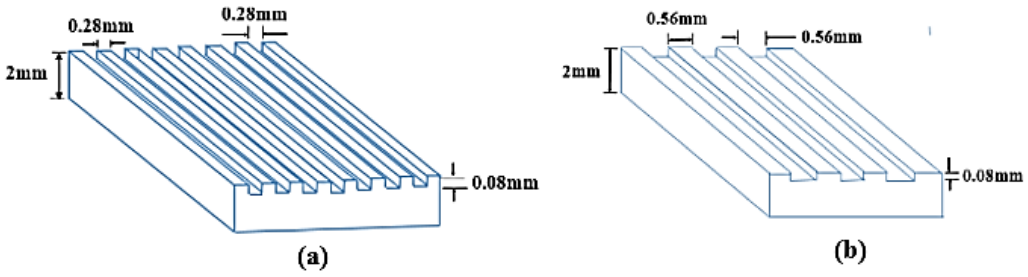

Figure 3-7- Image of the proposed textured surface for (a) texture A and (b) textured B.

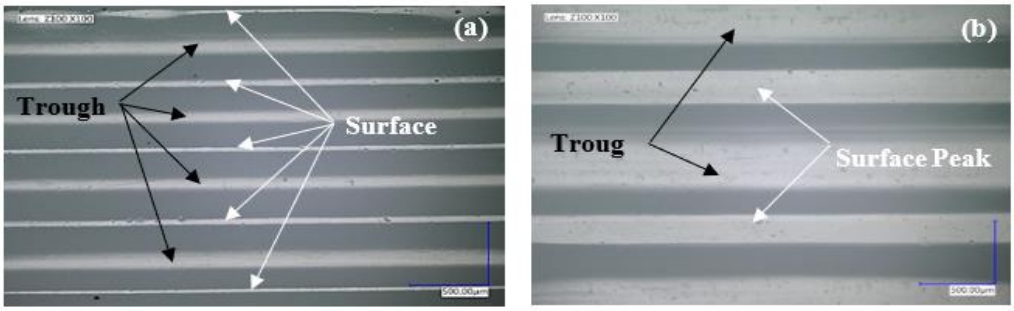

Figure 3-8- Optical image of the Polyjet printed substrate detailing both textured substrates A and B.

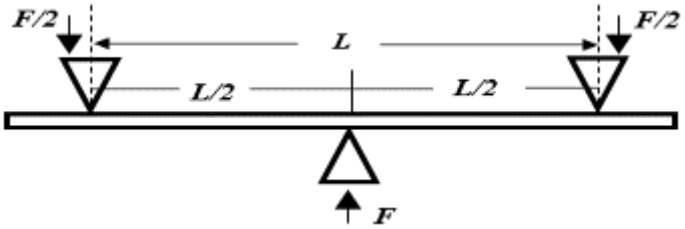

Figure 3-9- Schematic view of the central part of the bending device and definition of direction used for the three-point test.

The test is based on the traditional 3-point bending test as shown in Figure 3-9. During the test, the applied load is continuously increased and recorded by the BlueHill software connected to the Instron test device equipped with a 22 kN load cell. However, due to equipment limitations in the acquisition of real-time in situ data, SEM surface observation of the coating deformation was performed. A maximum set load of 100 N was applied to all samples tested in this experiment. The bending speed was 1mm/min. Further functional analysis to determine the water barrier function for both textured (coated and uncoated) and untextured (coated and uncoated) are detailed in Chapter 8 of this thesis.

3.2.8 Surface roughness measurement

Surface roughness for both uncoated and DLC coated samples was measured using a 2D contact Talysurf PG1800 profilometry scanner. A surface topography scan using a diamond stylus tip with a 2 μm radius was utilised. A defined scan length of 4.7 mm with a Gaussian filter cut-off of 2.5 mm and a bandwidth of 100:1 was utilised. Roughness measurements were repeated five times on each sample surface. Further details are shown in Chapter 5 of this thesis.

3.2.9 Mechanical surface polishing

To further investigate the effect of surface roughness on the adhesion performance of the coated printed substrates, an EcoMet 250 mechanical circular grinder was used to polish the surfaces of the printed substrates (untextured printed substrate) to obtain an Ra value of 38.5 ± 2 nm. The process involved wet grinding each substrate successively with a 320, 600 and 1200 silicon carbide (SiC) grit paper. This method leaves circular grinding layout marks on the substrate surface that may later contribute to poor coating adhesion. Subsequently, samples were later polished with successive fibre polishing cloth (MicroFloc) and polycrystalline diamond suspension until a surface roughness (Ra) value of 38.5 ± 2 nm was attained. Using the MicroFloc further removes the majority of the rough layout patterns on the substrate surface to give a smooth finish. After polishing, samples were rinsed in distilled water and oven-dried for 48hrs at 30 ℃ in a vacuum furnace.

3.3 DLC coating and deposition

3.3.1 Introduction

This section describes in detail the coating methods used in undertaking the experimental work for this thesis. A fundamental understanding of the key processes and equipment describing the coating methodology and recipe design for coating the individual test polymers are described with the focus on PECVD technique. To correctly utilise and interpret the results, a comprehensive analysis of the coated samples using varying coating characterisation techniques are discussed in this chapter.

3.3.2 Coating system

The Hauzer Flexicoat 850 coating system situated in the advanced coatings laboratory at the University of Leeds was used for depositing all coatings in this project. A follow up detailed description of the system is explained.

The Hauzer Flexicoat 850 is an integrated modular coating system with microwave (MW), pulse DC, high power impulse magnetron sputtering (HiPIMS), filtered arc deposition, radio frequency (rf) bias, cold finger, plasma etching capabilities and nano-particle source functions. The configuration detail used in this work comprises two 1200W microwave sources installed in parabolic reflectors, three circular arc evaporation targets, a 600 x 50 mm magnetron target and a remote plasma source comprising of a copper anode and tungsten cathode wire with a 200A maximum current capacity. Schematic representation of the deposition chamber layout in the Hauzer Flexicoat 850 is shown in Figure 3-10.

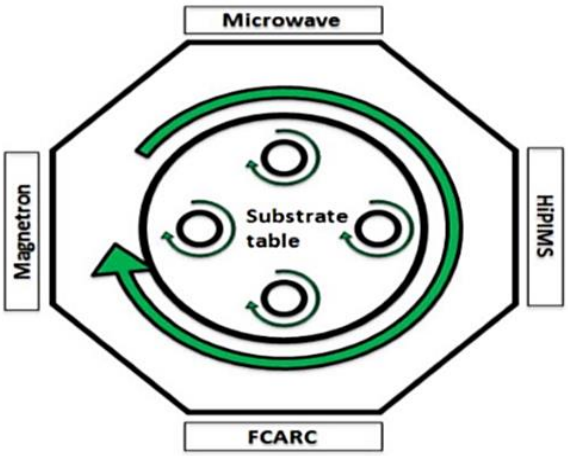

Figure 3-10- Top view deposition chamber of the Hauzer Flexicoater 850.

The filtered arc deposition system (FCARC) shown in Figure 3-10 provides a frontal sectional view which serves as an entry point into the chamber with added functionality for potential target add-on aside from the FARC. The operation of the sputtering targets positioned opposite each other provide added advantage for coating using high power impulse magnetron sputtering (HiPIMS), direct current (DC) or pulsed DC modes. Opposite the FARC is the microwave source function which is built into the rear opening to the chamber as shown in Figure 3-11.

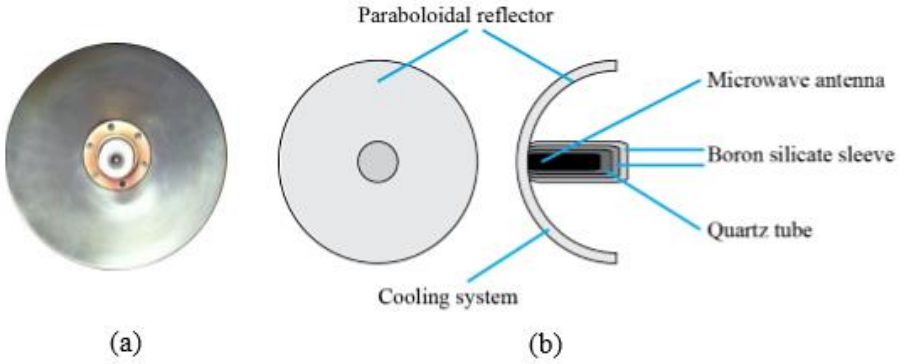

Figure 3-11- Schematic diagram showing the microwave power source antenna (a) frontal view (b) side view.

With two working microwave antennae at 2.4 GHz, the solid stainless-steel mount designed to effectively direct plasma into a quasi-parallel beam using a steel parabolic reflector provides energy input at up to 1.2 kW into the working gas. With two integrated cooling systems found in the centre of the antennae and at the reflectors, overheating during the coating process is controlled using both cold air and water. The Flexicoater 850 also houses within it a detachable cylindrical column which serves as the substrate holder during deposition. The cylindrical column provides added advantage during the coating process by allowing independent rotation of the dummies (substrate holder) from the table in a two-fold rotation mechanism or by allowing independent rotation of the samples to both table and dummies throughout the coating process. To produce high performance and quality coatings, it is a common practice to adopt substrate biasing to have direct control over adatom mobility during coating growth, however, these sputtering options available in the Hauzer Flexicoater were not exploited in this research as this goes beyond the scope of this thesis. Operations involving substrate biasing are achieved through the substrate holder table with DC power supply functions at either constant, pulse or bi-polar pulse. The main coating deposition technique adopted to deposit coatings unto the 3D printed polymer substrates in this work is based on PECVD using microwave-assisted technique.

3.3.3 Substrate preparation

A four-stage sample cleaning procedure was adopted to rid the 3D printed sample surfaces of any potential contamination originating from either the 3D printing process or otherwise through the handling of the samples before deposition. The first step of cleaning involves using pressurised water to remove the bulk of support material left behind on the 3D printed polymer surface after completion of the polymer print. This was followed through with a 30 minutes ultrasonic bath in distilled water to further remove impurities that survived the water blast procedure. Samples were later stored in a controlled vacuum heater oven at 35 ℃ for 48hrs to remove all interfacial and absorbed water molecules. After adequately drying the samples, a suitable solvent with high volatility that causes no chemical abrasion or damage to the surface on all the 3D printed polymers was chosen. Ethanol was used with lint-free tissue to wipe down the surface further before and after mounting them within the deposition chamber. A Kapton heat resistant tape was used to mount all samples onto the substrate table. To further rid the surface of impurities and improve surface functionality and adhesion, a 3 mins plasma surface etching (PSE) stage (Ar flow rate = 50sccm, Pressure = $1.2x10^{-5}$ mbar) was introduced pre-deposition. With a surface heating rate of 1.75 ℃/min, determined by two thermocouples located on the substrate table, the maximum surface temperature attained during the 3min of surface Ar^{+} bombardment was 34 ℃.

3.3.4 Coating deposition using MW-PECVD

As per any PECVD process which utilises a controlled high voltage potential across the working gas to ignite and sustain a plasma, the acceleration of ion species within the plasma body to the substrate material in the case of electrically conductive material promotes increased bombardment and film growth with added functionality. However, polymers generally are non-conductive and by their nature electrically insulating, hence, within the plasma body, the non-electrostatic attraction between the ions and substrate creates a reduced ionisation effect. A phenomenon that leads to lower surface mobility of ions, and the creation of reduced coating properties.

In this work, a design of experiment approach (DOE) was adopted in the design optimisation and characterisation of the coating process to determine the effect of varying deposition conditions on the properties of the resulting coating produced using the MW-PECVD.

For the DOE approach used as a basis for characterising the design space for this work, an initial model was provided for by Procter & Gamble Innovation centre, London for depositing coatings unto polymer substrates i.e. acrylonitrile butadiene styrene (ABS) and Polyetherimide (PEI) served as the basis for all coating design in the deposition of DLC coatings unto the 3D printed samples. Table 3-5 shows the initially proposed DOE parameters used.

Table 3-5- Initially proposed DOE parameters used as the basis for formulating the coating recipe for this thesis.

Leg	Microwave Power Setpoint (W)	Microwave Power (Actual) (W)	Working Pressure (mbar)	Gas flow rates ratio(Ar&C_2H_2) (C_2H_2%)	C_2H_2 Partial Pressure
1	1050	1032	0.012	94	0.0113
2	1100	1087	0.011	92	0.0101
3	1050	1032	0.011	85	0.0094
4	1100	1087	0.009	40	0.0036
5	1200	1178	0.009	74	0.0067
6	1200	1178	0.011	42	0.0046
7	1200	1178	0.011	91	0.0100
8	1050	1032	0.013	43	0.0056
9	1050	1032	0.011	66	0.0073
10	1100	1087	0.013	67	0.0087

In principle, this was found to be the most efficient approach in achieving a more robust and bespoke DOE tailored to the requirements of the 3D printed samples instead of proposing a new design regime using trial and error approach with prolonged modification time.

For the proposed DOE detailed in Table 3-5, greater emphases were placed on the applicability of using similar process conditions for 3D printed polymer parts. Therefore, factors relating to heating rate, starting deposition temperature, coating structure, adhesion and mechanical properties were all considered as the bases for selection. An initial assessment of the coating structure synthesised using the deposition parameters defined in Table 3-6 showed a poorly adhered coating structure. Detailed characterisation of these coating is given in Chapter 5. Hence, there was the need to modify the design to resolve the issue of adhesion and coating cracking resulting from the inherent stresses presented by DLC coatings [117]. To this end, a modified coating design based on the pre-existing DOE (Table 3-6) was adopted, where the effect N_2 was accessed together with C_2H_2 gas. Nitrogen was used as a combined strategy with C_2H_2 gas to improve coating adhesion and coating cracking of the second family of coatings developed (DLC/1 to 5). In total 5 DLCs namely, DLC/1 to DLC/5 are studied and presented as the modified DLC coating (Table 3-7). The 5 DLCs form the bases upon which all further quantitative and qualitative characterisation, as well as properties relating to their functionality, are made. Further details on the modified coating design and structural characterisation are shown in Chapter 5.

Table 3-6 Actual deposition parameters for 3 Leg DOE design deposition.

Leg	Microwave Power Setpoint (W)	Microwave Power (Actual) (W)	Working Pressure (mbar)	Gas flow rates ratio(Ar&C_2H_2) (C_2H_2%)	C_2H_2 Partial Pressure
1	1050	1032	0.012	94	0.0113
3	1050	1032	0.011	85	0.0094
6	1200	1178	0.011	42	0.0046

Table 3-7 Proposed parameters used to deposit the DLC coatings.

DLC	MW Power (W)		Working Pressure (mbar)	C_2H_2 flow rate (sccm)	Ar flow rate (sccm)	N_2
	1	2				
1	1050	1050	0.012	610	50	-
2	1050	1050	0.012	610	50	10
3	1050	1050	0.012	610	50	20
4	1050	1050	0.012	310	50	10
5	1050	1050	0.012	310	50	20

3.3.5 Substrate temperature control

To attain satisfactory coating on polymer substrates, several issues must be addressed. As polymeric substrates have very low Tg and Tm temperatures [129, 179, 209], coatings must be grown at low temperatures, which in some cases may result in low packing density resulting in film porosity [129]. For DLC films, structural transformation has been observed at different temperatures such as the conversion of nano-crystalline graphite at 300 ℃ in atmospheric air or the decrease in hardness and fracture toughness above 400 ℃ [210]. Even though several attempts have been made to deposit DLC films onto various substrates at lower temperatures, its applications in low-temperature polymer substrates (<100 ℃) is still lacking. Carley [122] in his study of the mechanical behaviour of DLC coatings showed that to successfully deposit this coating onto both ABS and PC polymers using MW-PECVD, deposition runs should be split with intermittent cooling steps lasting an hr. Similarly, Sarto *et al*. [131] used this technique of intermittent cool periods totalling an hour in the deposition of hard oxide thin film coating on PC substrates. In this work, a similar technique was adopted for the control of substrate temperature below 40℃ during deposition using four thermocouple heat sensors located on both chamber walls (2 fixed) and the substrate rotation table(2 rotating).

3.4 Coating assessment and performance analysis

3.4.1 Surface morphology

3.4.1.1 **Scanning electron microscopy**

Scanning electron microscope (SEM) scan surfaces using a beam of electrons to produce a true image of the surface under study. In a typical SEM device, electrons are emitted from an electron beam gun under vacuum by either thermionic or field emissions, with the later using a large electric field to create ionization in atomic species whilst the former uses current to discharge electrons in the process.

Electrons emitted from the electron gun are first attracted to the anodic section of the device where they are accelerated and transmitted to the magnetic condenser to be later condensed and focused onto the substrate surface for imaging. At the surface, electrons are either absorbed, reflected or may produce secondary electrons from the excitation of the surface atomic species. Amongst the variety of electron beams produced, the secondary and backscattered electrons are the most utilized sources for surface imaging using specialist instrumentation within the sample chamber.

In the case that there is an imbalance in the proportion of incident to reflected electron beam hitting a polymer surface where the incident electron is greater than the escaping electron species, charging effect is observed on the surface of the polymer due to the negative charge accumulation at the point of incident. This charging phenomenon causes a range of unusual defects in the quality of the image produced by introducing unwanted noise to signal ratio. To solve this problem, polymer samples are always coated with conductive material to mitigate this charging effect problem. A Carl Zeiss EVO MA15 SEM was used to image the 3D polymer substrates. Image tuning was done over a range of accelerating voltages, beam currents, and magnifications. An accelerated voltage of 20kV with backscattered electron imaging was used to acquire surface imaging. Samples were mounted onto metallic holders using a self-adhesive carbon pad with carbon gel applied to the sample edges for good conductivity. Substrates were later coated with a thin conductive layer (~10nm) of iridium to allow surface charge to dissipate through the sample holder. To obtain accurate measurements for each coating thickness, measurements were taken at both centre and edge of each coated sample and the average reported in this work as shown in Chapter 5.

3.4.1.2 **Atomic force microscope (AFM)**

The principal operation of an AFM relies on the accurate detection and measurement of interaction forces acting between a sample surface and a contact probe tip at close proximity. To perform surface high-resolution imaging of a surface, the probe tip is raster-scanned over the defined sample area and defined by the interaction deflection force, F due to weak van der Waals repulsive forces experienced

from the sample surface. An AFM force-distance curve which is defined by a plot of the tip-sample distance against the tip-sample interaction force along the vertical axis (Z-axis) and the cantilever deflection δ_c is given by Hooke's law (3.14):

$$F = -k_c\delta_c \quad \ldots\ldots\ldots \qquad (3.5)$$

A typical AFM (Figure 3-12) has a Z scanner (cantilever) that moves up and down the sample surface based on the repulsive force measure, an additional XY scanner, that moves along the X and Y direction underneath the cantilever and a position reflector that records the displacement and position of the cantilever. The displacement of the cantilever is traced using a laser beam source. Using this detection method, the surface topography of a sample can be imaged by scanning the surface region of interest using the feedback loop method to accurately define surface features. In this study, a contact probe mode was to gain topological information of both DLC coated and uncoated 3D printed polymer surfaces.

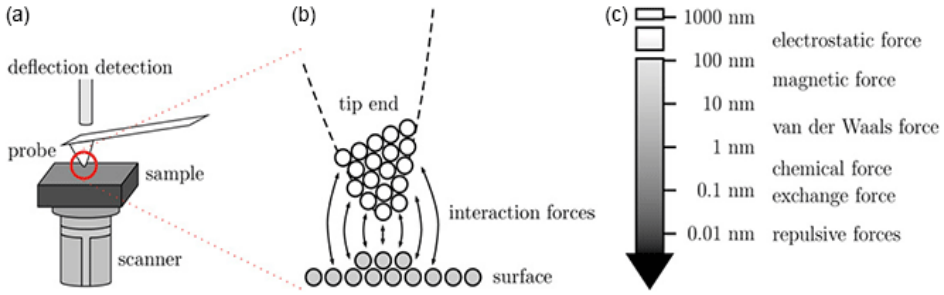

Figure 3-12- (a) Schematic representation of a typical AFM scanner probing a macroscopically flat surface by a sharp contact probe. (b) at very small separation distance, the atomic structure of both surfaces become very important defined by the separation distance (Z). (c) Varying atomic force interactions are determined from different heights in the Z direction [211]**.**

3.4.2 Chemical composition and bonding characterization

3.4.2.1 **Raman spectroscopy**

Raman spectroscopy is a light scattering technique where an incident light from a high-powered laser source is emitted to provide detailed information about chemical structure, phase and polymorphy, molecular interaction and crystallinity of samples. When light is exposed to a surface in a Raman scan, the majority of the scattered light reflected off the surface is unchanged and has the same wavelength as the incident light and does not provide any useful information about the surface being probed, this scatter is termed 'Rayleigh scatter'. However, a minute fraction of the light, typically 1 part in 10million, loses or gain energy in the process and is dissipated in varying wavelengths which are used in the analyte chemical structure capture, this is termed Raman scatter. Where energy is dissipated in the process, the Raman scatter is designated as 'Stoke'; whereas anti-Stoke occurs where energy is gained in the process. The spectrum peak distribution of a typical Stoke Raman scattered light features

the intensity and wavelength position of each corresponding molecular vibration peak including individual bonds such as C-C, C=C, N-O etc. A shift in the molecular polarizability is essential during the molecular vibration for a Raman effect to be realised.

To examine the chemical bonding state of the MW-PECVD DLC films, Raman spectra were acquired from 1000 cm^{-1} to 1800 cm^{-1} Raman shift and fitted by two Gaussian peaks. The coated samples were exposed to a 488 nm laser mounted in a Renishaw InVia Raman microscope. To avoid sample damage, analysis using a fixed maximum laser power output of 0.1mW was used throughout the analysis with a 10 sec exposure time over 5 exposures.

3.4.2.2 **FTIR surface analysis**

To ascertain the chemical structure and surface characteristics such as chemical activity, adhesion, wetness etc. of the surface number atomic layer of the solid-state material. A molecular Infrared spectroscopy technique using Fourier transform infrared spectroscopy (FTIR) was employed to study and analyse the sample surface molecular chemistry. FTIR is a very good example of infra-red (IR) spectroscopy technique but with an added transform function based on Fourier mathematical series for data analysis. This technique as identified by most researchers is particularly useful in identifying polymeric materials and organic compound composites based on their chemical functionality. However, unlike other IR spectroscopy applications, for example, ultraviolet (UV) spectrometry which does have very few distinct peaks in most data peak representations, FTIR has an added advantage of providing a much larger absorption spectrum band to define the chemical structure of a particular molecule under study [212]. In this work, all measurements were taken using the attenuated total reflectance (ATR) accessory coupled to a Perkin Elmer Spectrum 100 FTIR Spectrometer. The spectral data ranged from 600 to 4000 cm^{-1}, with a spectral resolution of 4 cm^{-1}.

3.4.3 Mechanical Properties

3.4.3.1 **Nano Indentation Hardness**

Nanoindentation has provided a useful tool in characterising the mechanical properties of materials at small scales. The most common is the measurement of hardness and elastic modulus of both coated and uncoated samples. Conventionally, this measurement is achieved based on methods proposed by Oliver and Pharr [213] using the classical definition for determining the reduced modulus (E_r) of a material.

$$\frac{1}{E_r} = \frac{(1-v^2)}{E} + \frac{(1-v_i^2)}{E_i} \quad \ldots\ldots\ldots \qquad (3.6)$$

Where E_r is the reduced modulus, v and E are the Poisson's ratio and modulus of the test sample, v_i and E_i are the Poisson's ratio and modulus of the indenter tip.

The hardness (*H*) was calculated using the well-known Meyer hardness relationship which corresponds to the mean contact pressure at full load [214].

$$H = \frac{P}{A} \qquad \ldots\ldots\ldots \qquad (3.7)$$

Where *P* and *A* is the load and projected area of the contact given by the indenter tip.

For this test, a Micromaterial NanoTest platform equipped with a Berkovich indenter tip was used to probe the test substrate to ascertain their mechanical properties for both coated and uncoated DLC coated samples. A depth control experiment was performed for the uncoated samples at a maximum depth of 200nm to determine how the mechanical properties vary with depth. In other to analyse the properties of the coated samples, it is recommended that the tip of the indenter goes no further than 10% of the total coating thickness [214]. For this experiment, a diamond Berkovich indenter tip with modulus (E_i) of 1141GPa and Poisson's ratio (v_i) of 0.07 was assumed [214]. Similarly, the v for both 3D printed ABS and Verogray were assumed to be 0.36 and 0.4. With an initial applied load of 0.05mN, a loading and unloading rate of 0.1mN/min and 0.01mN/min were respectively chosen to mitigate any viscoelastic effect rising from the polymer substrate material. A 20s dwell time was chosen to provide enough time for elastic recovery before unloading commences. Single indents were used for measuring material hardness for all uncoated substrates. For all coated substrates, partial load-unloading were used to measure film properties. A total of 10 indentations were made per coated sample.

3.4.3.2 **Coating adhesion**

The steady progression in the use of nanoindentation test to accurately define material properties such as coating strength and elasticity constant at the nanoscale has necessitated similarly, the idea of scratch resistance to deformation at the contact surface. In using the scratch test technique to access coating adhesion, a load is steadily applied to a coated substrate until the film is debonded from the substrate [257]. Benjamin and Weaver [215] studied the test comprehensively in 1960 and were able to establish a direct linkage between the interfacial shear strength and the critical value at which deformation occur between the film and substrate. They further noted that this plastic formation induces s shearing force equal to the interfacial shear strength, which further causes complete coating removal. Nevertheless, Butler *et al.* [216] noted that the process of scratch formation was very complex and that no absolute value could be deduced from a single scratch test. Following from the dynamic model approach proposed by Benjamin and Weaver [215] in quantifying the critical load of a coated surface, several

attempts have been made to correctly assign the different critical load points on a scratched surface, such as using lower and upper critical loads. In this study, the macro-scratch test was performed to determine the points of critical coating failure which is defined by the appearance of cracks or visible deformation in the contact area. Two separate test parameters were performed to assess the individual coating design failure points defined by their critical load (L_c) of failure. L_{c1} is mostly defined as the critical failure load at which the first plastic deformation of the coating is observed [217]. L_{c2} is the second observed failure point where coating deformation is continuous but not fully debonded from the underlying substrate [217]. L_{c3} further defines the critical load at which the onset of coating detachment occurs [217]. To assess this, a progressive linear load of 0-5N from a Tribotechnic macro scratch Tester (Millennium 200) together with a Rockwell C diamond tip with a 200µm tip radius was used. The scratch length and speed were 10mm and 10mm/min respectively. The second coating design involving DLC/1-5 was similarly tested using the same test parameters. However, a progressive linear load of 0-20N was used. Further results and analysis are detailed in Chapter 5 of this thesis.

3.4.4 Contact angle measurement

Contact angle measurements were performed using the contact angle goniometer to quantify the surface energy of the treated polymer surface bombarded with energetic Ar^+ species during plasma surface etching (PSE) and coating nucleation process using water. For any gas composition used for surface treatment of polymers, there are primarily three surface processes instantaneously transformed depending on the extent of exposure time, process condition and chemistry of the exposed polymer. The transformation results in the ablation, activation and crosslinking of the surface chemistry yielding potential reactive sites from which the so-called “dangling bonds” are created. Upon exposure of the surface to air, the formation of hydrophilic groups typically O-H and CO-OH and other polar groups promote the polarization of the surface. This increase in the surface energy as a result of the polarization would be detected by a contact angle goniometer as a reduction in the surface contact angle measurement due to the hydrophilicity of the surface. In this work, a contact angle goniometry measurement was made to quantify the surface wettability of the plasma-treated polymer surface as a substitution for determining the availability of dangling bonds available to promote strong chemical bonding between the functionalized polymer surface and radicals incident on the polymer surface.

3.4.5 X-ray photoelectron spectroscopy (XPS)

The quantitative determination of surface elemental composition, empirical formula, chemical and electron state existing within a material is crucial in understanding material and coating properties and performance such as hardness, corrosion and friction performance. XPS or electron spectroscopy for chemical analysis (ESCA) is the most commonly utilized surface analysis tool for evaluating surface

chemistry at the nanoscale. It works principally on the photoelectric effect to which soft X-rays (Mg and Al Kα x-ray) are used as the exciting photon [215] to cause excitation and emittance of photoelectrons from the sample surface. When emitted onto a surface, an X-ray photon interacts with the core level electron shell of the sample and transfers its photon energy as a result, thus causing a cascading photoelectron emission from the sample (Figure 3-13).

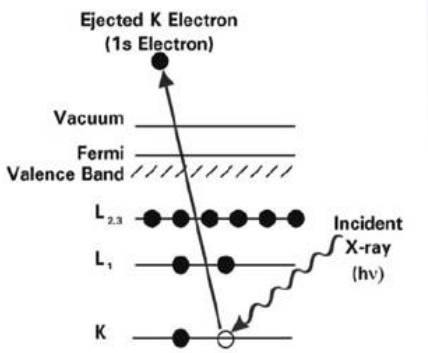

Figure 3-13- Schematic representation of the X-ray photoemission process [215].

The emitted electron has kinetic energy (K.E) given as;

$$KE = hv - BE - \phi_S \quad \ldots\ldots\ldots \quad (3.8)$$

Where hv is the energy of the photon given by Plank's constant (h) and the frequency of the X-ray (v). BE is the binding energy of the core-level electron with ϕ_S being the spectrometer work function. Since the K.E of the photoelectron can be obtained experimentally and that of the X-ray energy is always known, the binding energy of the emitted electron(s) can be easily determined using equation 3.18. With each element possessing a characteristic photoelectron signature emission to X-ray photo impact, specific elemental composition and atoms could be identified as a result.

XPS analysis of the 5 individual coatings was performed using a Thermo NEXSA XPS fitted with a monochromated Al kα X-ray source (1486.7 eV), a spherical sector analyser and 3 multichannel resistive plates, 128 channel delay line detectors. All data were recorded at 19.2W and an X-ray beam size of 200 x 100 µm. Survey steps spot sizes were recorded at pass energy of 160 eV, and high-resolution scans were recorded at pass energy of 20 eV. Electronic charge neutralization was achieved using a Dual-beam low-energy electron/ion source (Thermo Scientific FG-03). Ion gun current = 150 µA. Ion gun voltage = 45 V. All sample data was recorded at a pressure below 10^{-8} Torr and a room temperature of 294 K. Sample etching was performed using a MAGCIS source operating at 4 kV with monotomic Ar^+ ions and rastered over an area of ca 1 × 1 mm. Analysis of the raw spectra began with

the removal of the ubiquitous background present in the core spectra using CasaXPS software. Spectra deconvolution to determine the atomic concentration for C1s and N1s of the individual films were made.

3.4.6 Water sorption

3.4.6.1 **Dynamic vapour sorption (DVS)**

Dynamic vapour sorption or DVS is a gravimetric technique aimed at providing a quantitative measure of how much water is kept in a material as a function of the outside relative humidity. In this technique the mass change as a function of humidity provides useful information about the material under study and provide additional information about the equilibrium moisture content within the material at a set humidity value i.e. the percentage mass change due to moisture absorption or adsorption, material kinetics (how fast moisture permeates into and out of materials), material stability, hydration, diffusion, etc. in defining material stability in their a solid-state form.

For this experiment, DVS Resolution equipment with a dual vapour analyser with key combined ability to measure precisely and control both temperature and relative humidity (RH) whilst recording the highest mass change resolution is used. To generate and maintain the required RH value within the chamber, a nitrogen dry gas stream is bubbled through water at the desired flow rate to produce the expected RH. Two separate tests were performed under different test conditions to determine the effect of varying the control variables such as temperature, time and RH on the water absorption properties of both coated and uncoated samples.

In the first experiment, a time-dependent analysis at constant temperature and RH of 25 ℃ and 80 % respectively were studied for 72hrs. In the second test, the relationship between varying RH and temperature at 25 and 40 ℃ were both determined.

3.4.7 Barrier properties

One of the huge demands placed on most polymer materials is their ability to provide barrier functions against gases and water vapour. However, these properties when compared with other engineering materials such as glass, metals and ceramics are less to be desired in terms of their barrier functionality. In this experiment, the WVTR function of DLC coated and uncoated 3D polymers are assessed using the MOCON PERMATRAN-W model 3/33 equipment according to ASTM F1249 standards. The test samples were first masked using a 100mm diameter Aluminium (Al) foil mask to reduce the size of the test area. In this experiment, the $1cm^2$ Al foil mask was used. The purpose of foil masking is to reduce the area, hence reducing the total amount of gas (water vapour) passing through the sample. This way

we prevent the saturation of the highly sensitive sensors present in this equipment. The fabrication procedure for preparing the samples for testing are explained below.

3.4.7.1 **Aluminium foil masking procedure**

Before testing the samples, masking of the individual samples were performed to reduce the size of the area exposed to testing due to equipment size restriction. An Al foil mask with a $1cm^2$ exposed test part area was used. For each sample, two adhesive Al masks are used, with the first mask placed firmly on the working bench with the adhesive side facing upward. The sample is now placed $50cm^2$ within the test area. Similarly, the second masking foil is lowered onto the exposed polymer surface to make contact and pressed firmly to create an impervious sandwich layer preventing the escape of water vapour and gases from the sides of the test sample. A schematic representation of the masking process is shown below in Figure 3-14 and Figure 3-15.

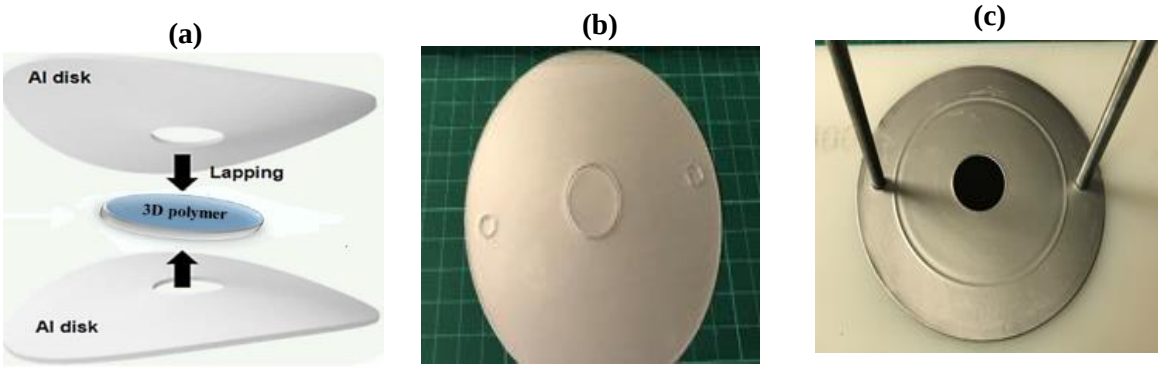

Figure 3-14- Shows the three-stage fabrication procedure for masking the individual test samples for WVTR testing with (a) lapping of the individual test samples using Aluminium mask (b) complete masking procedure (c) test sample showing exposed test area of $1cm^2$.

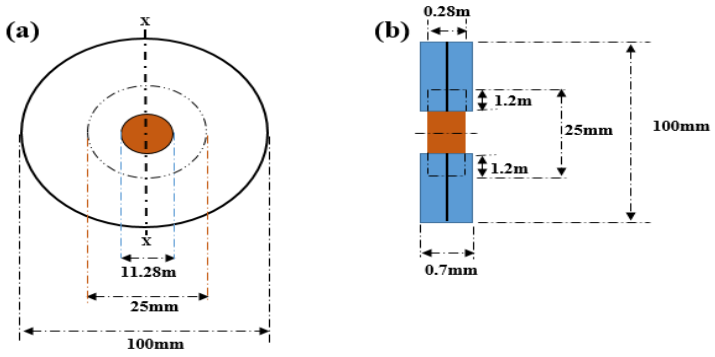

Figure 3-15- Schematic representation showing (a) dimensions of the masked additively manufactured samples (b) cross-sectional view with the corresponding dimension.

3.4.7.2 **WVTR testing**

The operation of the MOCON PERMATRAN-W 3/33 system used for testing the WVTR properties of the additively manufactured polymers is based on a modulated infrared sensing device to detect water vapour transmissivity through the sample (Figure 3-16). Both textured coated and uncoated samples, as well as untextured coated and uncoated polymer samples with a defined thickness of 0.28mm, were tested in this experiment. The masked samples were clamped into the diffusion cell of the test kit followed by a nitrogen gas purge to rid the chamber of any residual moisture before the start of the test. RH was generated by the "two pressure method" and introduced into the outside of the test chamber with the help of a saturated absorbent material capable of providing a 100 % RH at a set temperature of 38 ℃. Water molecules diffusing through the film into the main chamber are detected by the modulated infrared sensor.

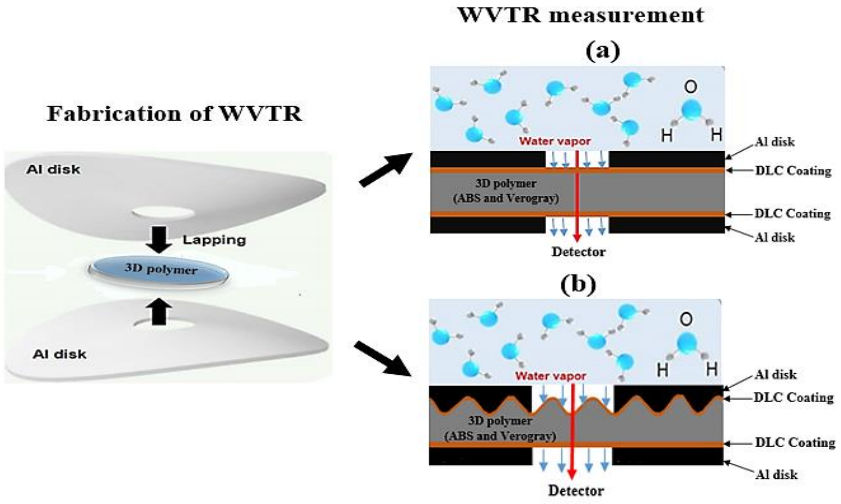

Figure 3-16- Schematic representation of the WVTR test showing both (a) Untextured (b) textured surfaces.

3.4.8 Tribology

Friction and wear loss are important ingredients in material characterisation for the durability of engineered parts using Polyjet technique. However, little work has been accomplished in the characterisation of such 3D printed parts. By investigating the friction and wear response under varying loads, the true sense of their tribological properties could be well understood. To fill this knowledge gap, a comprehensive study of the frictional and wear behaviour of photocurable Polyjet modelled parts namely ABS-digital (3D ABS) and Verogray are investigated. The effect of surface finished defining on both material surface roughness and print orientation on the wear and frictional behaviour of both coated and uncoated polymers are studied. The plane of orientation investigated was the flat (XY plane) represented by the raster orientation of [0/90] which is simplified in Figure 3-17. (The printed raster

direction is the sequential path taken by the printer nozzle or head to the X-axis of the print bed orientation).

3.4.8.1 **Determination of friction**

The frictional performance of 3D ABS and Verogray were carried out using a linear reciprocating universal material test (Bruker UMT) tribo lab equipment. Figure 3-18 shows the contact schematic representation of the frictional couple. At room temperature (23 ± 2 ℃), both the friction and wear test was performed under dry reciprocating sliding conditions. The static body (Counter-body) was an AISI 52100 Chrome Steel bearing with 6.5 mm in diameter. Before the tribological test, all samples (3D ABS, Verogray and Steel ball bearings) were thoroughly cleaned with ethanol to rid the surfaces of all impurities.

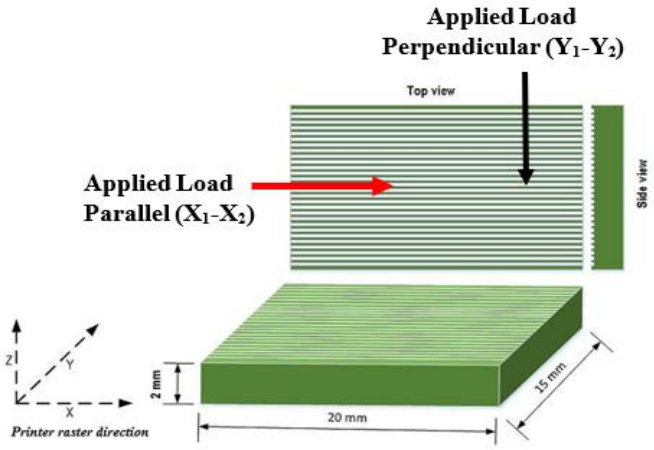

Figure 3-17- Graphic representation of the Polyjet printer bed orientations (flat) and raster angle [0/90] investigated in this experiment.

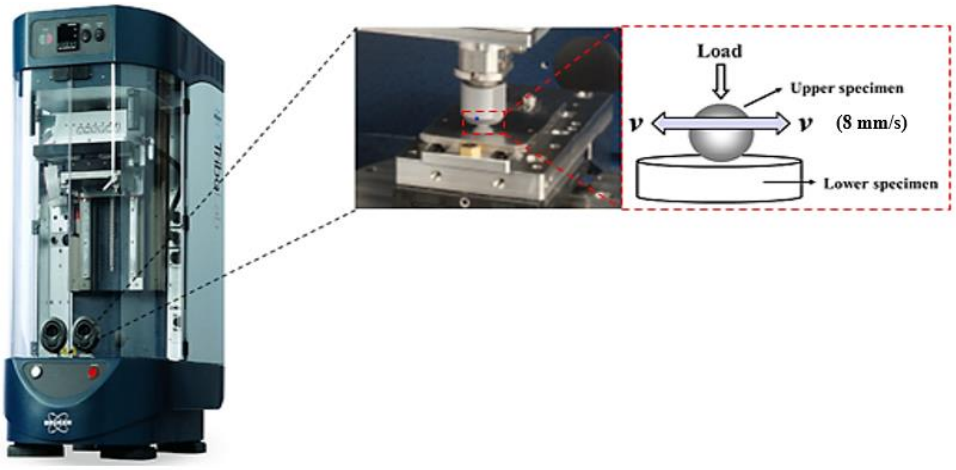

Figure 3-18- Contact schematics used for the friction test.

The friction test was investigated (Figure 3-17) using a Bruker UMT tribo Lab equipped with a linear reciprocating module in a ball-on-plate configuration under dry reciprocating conditions. The test rig consists of an upper assembly unit which comprises a ball sample holder rigidly attached to a pivoted loading cell and a lower reciprocating linear drive which houses the sample holder assembly, a variable speed motor with a maximum speed of 10 mm/s. The upper specimen (ball) was made of 52100 hardened steel with a measured surface roughness (R_a) of 0.07 µm (using a 2D Talysurf equipment as described in Chapter 4.5), a hardness of 65 HRC [216] and a diameter of 6.5 mm. During testing, the room temperature was maintained at 23 ± 2 °C. The maximum sliding speed and distance was 8 mm/s and 2mm respectively. An applied load of 1, 5 and 10N were used throughout the test. For data acquisition, the real-time tangential force, friction coefficient and linear velocity were all recorded in real-time as the test proceeded. In all tests, 36,000 linear oscillation cycles were performed at a frequency of 10Hz for 60 min. For each cycle (10Hz), an average of the recorded friction coefficient values is computed. 10 data points for Both friction and sliding wear data reported in this study are an average of three repetition runs. The maximum Hertzian contact pressures (P_{max}) (equation 3.9) are calculated using the expression given in Equations 3.8 for the contact between a rigid sphere and a flat surface [217].

$$P_{max} = \frac{3W}{2\pi a^2} \quad \ldots\ldots\ldots \quad (3.9)$$

Where W is the applied normal load, a is the contact radius given by the expression:

$$a = \left[3\frac{WR}{8E^*}\right]^{\frac{1}{3}} \quad \ldots\ldots\ldots \quad (3.10)$$

Where R is the ball radius and E^* is the equivalent Young's modulus at the contact given by:

$$\frac{1}{E^*} = \frac{1-v_1^2}{E_1} + \frac{1-v_2^2}{E_2} \quad \ldots\ldots\ldots \quad (3.11)$$

Where v_1 and v_2 are the Poisson's ratio of the 52100-steel ball (0.29) and 3D printed specimen respectively. For the 3D ABS and Verogray, Poisson's ratios of 0.36 and 0.4 were used respectively. E_1 and E_2 are Young's moduli for both 52100 steel ball and 3D printed specimen (Table 4-4). A Young's modulus of 205 GPa was used for the 52100 steel. All data regarding the mechanical properties of the 52100-steel ball was provided by the supplier.

Table 3-8- Calculated maximum contact pressure at each applied load tested.

Applied Load (N)	Sample	P_{max} (MPa)
1	3D ABS	33
	Verogray	36
5	3D ABS	57
	Verogray	62
10	3D ABS	71
	Verogray	78

3.4.8.1 **Wear test**

Wear measurements were quantified by dried polymer mass loss [218], where the mass loss due to wear (ΔM) is given by equation 3.12.

$$\Delta M = (M_1 - M_2) \quad \ldots\ldots\ldots \quad (3.12)$$

Where ΔM is the difference between the final mass M_2 and initial mass M_1 [219, 220]. Materials that exhibit higher resistance to wear will have lower volume and mass loss [220]. All test specimens were weighed before and after the experiment using a single pan Mettler Toledo XPR205 analytical balance with a 0.01mg readability. To accurately compute ΔM, each measurement was taken as the mean of three repeats.

The specific wear rate S_W of the test specimen is given as:

$$S_W = \frac{V_w}{F_N x\, S_d} \quad \ldots\ldots\ldots \quad (3.13)$$

Where F_N is the normal applied load (N), S_d is the total sliding distance (m) and (V_w) is the volume loss (m^3). After completing the tribological test, the crossectional geometry of the individual wear scars was measured using the step scan feature of the Talysurf PG1800 profilometry scanner. The wear volume (V_w) was computed using the geometric profile defined in equation 3.14.

$$V_w = \frac{2\pi\, x\, d\, x\, r}{6b}\,(3d^2 + 4b^2) \ldots\ldots\ldots \quad (3.14)$$

Where d is the wear scare depth (mm), r is the wear track radius (mm), and b is the wear scar width (mm).

Chapter 4

Results & Discussion: 3D Polymer characterisation

4.1 Thermal characterisation

This section focuses primarily on the thermal characterization of the 3D printed polymers produced using both Polyjet and EnvisonTech^{TM} methods of manufacturing as detailed in Chapter 3. The thermal degradation behaviour as a function of temperature and the glass transition temperature of all five 3D printed samples are described in this chapter. The discussion will be covered in two main parts: the first relating to the TGA analysis which will focus on the thermal stability of the 3D printed samples in nitrogen and air decomposition environments and their associated activation energies for the degradation of the AM polymers calculated using both the Murray-White and Coats-Redfern plots. The second, relating to the use of differential scanning calorimetry (DSC) in the determination of the experimental T_g value of the individual polymers understudy.

4.1.1 Thermal stability of additively manufactured polymers using TGA

The effect of using both inert and non-inert gases such as nitrogen and air to study the thermal stability behaviour and characterization of 3D printed polymers was employed as a first attempt to determine the quantitative estimation of the onset of thermal decomposition and degradation of the additively manufactured polymers under study and to mimic the thermal stability of the individually chosen polymers when exposed to vacuum coating environment.

In this method, the weight loss of the sample is constantly observed as the temperature increases from 30 ℃ to 600 ℃. When a material decomposes or degrades at higher temperatures usually above a referenced room temperature, the mass of the material steadily decreases as it loses vital components of the material chemistry due to the combustion process. In all cases, as illustrated in Figure 4-1, each polymer decomposition phase is multifaceted rather than a single-phase process. The different decomposition phases are numbered (1) to (4) and (1) to (5) for both nitrogen and air decomposition environments respectively. Phase1 is characteristic of the loss of moisture of crystallinity, volatiles, monomers and highly volatile solvents [221]. For all 3D printed polymers studied under nitrogen purged conditions, the onset temperature at which phase1 commences is seen as a function of the polymer chemistry. It was observed that for all cases except for LS600, the onset of decomposition relating to

mass loss is delayed when nitrogen is used as the purged gas instead of air. For example, Figure 4-1 shows that, by switching the controlled atmosphere from nitrogen to air using 3D printed ABS, the decomposition onset temperature is lowered from 206 ℃ to 128 ℃. This is also the case with Verogray, Veroblue, and RCP30. Beyler and Hirschler [222] noted that, by swapping from inert gas to air, the level of chemical interaction between polymer samples and the air is promoted with increasing temperature. By so doing, the onset of polymer decomposition temperature is lowered.

In addition to the formation of monomers and volatile products, Peterson *et al.* [223] noted the majority of the degradation product formed during and after the onset of degradation comprises both unsaturated and saturated compounds, mostly dimers and trimers. Staudinger and Steinhofer [224] proposes a chain scission reaction mechanism to explain the formation of these products. Polli *et al.* [225] observed similar degradation mechanisms for ABS of which they also observed radical end-chain and random scission leading to one or multiple phase decomposition stages with multiple kinetic parameters.

The continuous weight loss curve for all the additively manufactured polymers further revealed multiple degradation steps under both nitrogen and air condition. In the presence of nitrogen, all polymers degraded in a 4 stage multiple-step as shown in Figure 4-1. In air, however, there was an additional stage linked to the combustion of carbon due to the presence of oxygen within the air mix fraction. These characteristic step changes as identified in the thermogram plot and the extent to which decomposition or degradation occurs may vary depending on the type of sample been analysed [221].

The total percentage mass loss and their corresponding inert residue after decomposition are shown in Table 4-1. Under nitrogen purge conditions, the Verogray sample showed the highest decomposition percentage of -83.42 % of the initial mass (5.1 mg) with a 17.53 % inert residue left. RCP30, on the other hand, showed the lowest decomposition percentage of -62.62 %.

The combined TGA thermal plot showing the varying percentage mass change as a function of temperature in both nitrogen and air gives a strong indication of the degradation and decomposition tolerance level of each polymer sample when exposed to an elevated temperature above ambient in a controlled environment. It is worth noting from Figure 4-1 that on average, 3D ABS and RCP30 samples showed the highest degradation onset temperature in both nitrogen and air decomposition environments followed by Veroblue, Verogray, and LS600

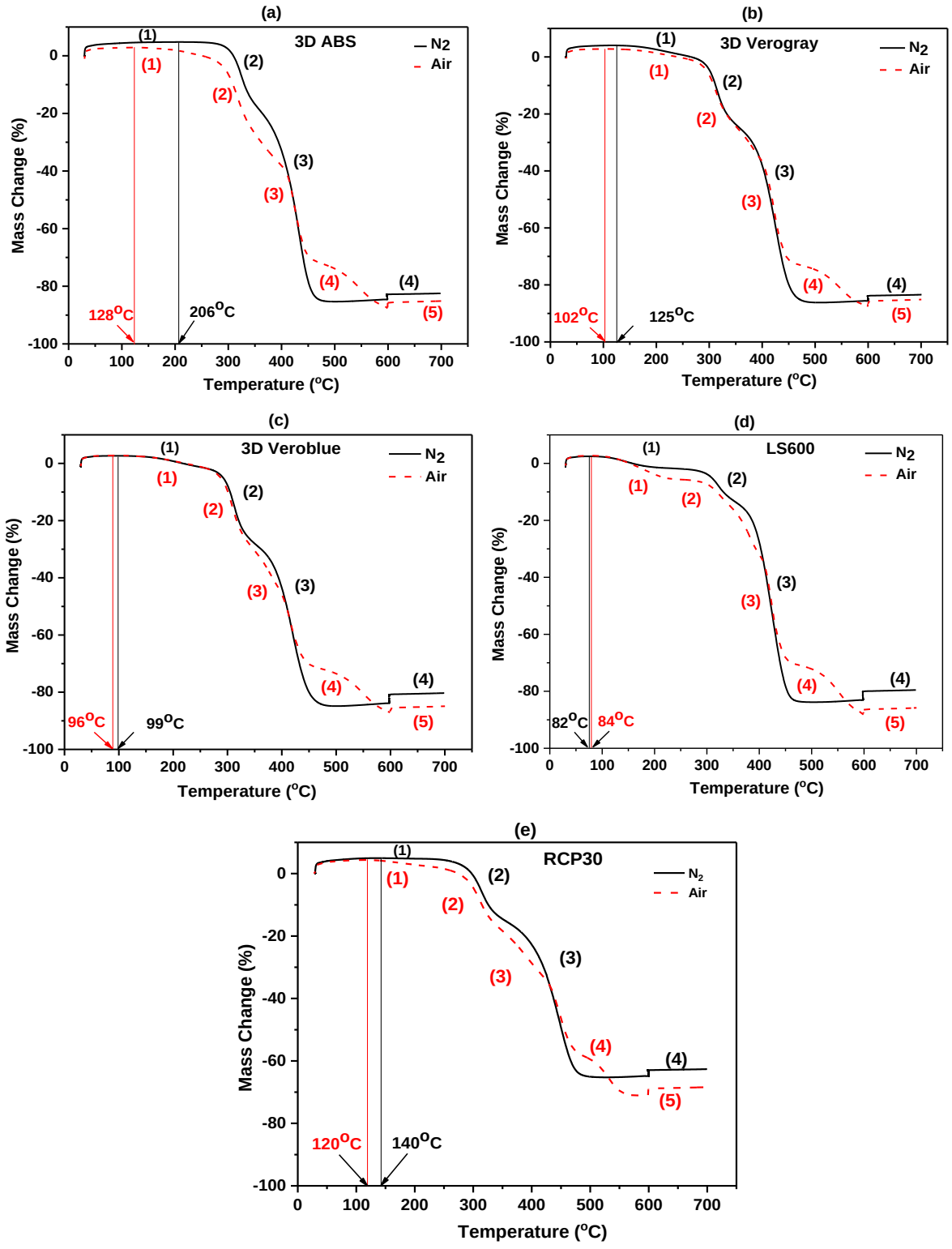

Figure 4-1-TGA Curves showing the percentage mass change (%) of 3D printed (a) ABS (b)Verogray (c) Veroblue (d)LS600 (e) RCPO30 in both air and nitrogen as a function of varying temperature.

Table 4-1- Initial degradation temperature, final decomposition temperature, total mass loss after decomposition and total inert residue left after decomposition.

Decomposition condition	3D Sample	Initial degradation temperature (°C)	Final decom. temperature (°C)	Total mass loss after decom. (%)	Total inert residue left after decom. (%)
N_2	ABS	206 ± 1.5	489	-82.47 ± 0.10	17.53
	Verogray	125 ± 2.1	489	-83.42 ± 0.30	16.58
	Veroblue	99 ± 2.0	489	-80.30 ± 0.25	19.70
	LS600	82 ± 2.5	489	-79.74 ± 0.28	20.26
	RCP30	140 ± 2.8	489	-62.62 ± 0.25	37.38
Air	ABS	128 ± 5.1	600	-85.1 ± 1.10	14.90
	Verogray	102 ± 3.0	600	-84.9 ± 0.87	15.10
	Veroblue	96 ± 4.0	600	-85.15 ± 0.82	14.85
	LS600	84 ± 4.8	600	-85.8 ± 0.60	14.20
	RCP30	120 ± 2.6	600	-68.38 ± 0.33	31.62

- decomp. = decomposition

4.1.2 Activation energies and degradation of additively manufactured polymers

The minimum required energy to initiate atomic or molecular transformation within the polymer structure as defined by the activation energy of the system through the TGA thermal plot were determined using the Murray-White plot [225, 226]. By plotting ln [ln (1-C)]- 2lnT against T^{-1} x 10^{-3} (K^{-1}) a linear correlation is obtained using the Murray-White plot; where C is the conversion and T is the temperature (K). Figure 4-2 shows the Arrhenius plot for the degradation of all additively manufactured polymers studied in the TGA test. The activation energies calculated based on the Murray-White plot for the individual 3D polymers are presented in Table 4-2.

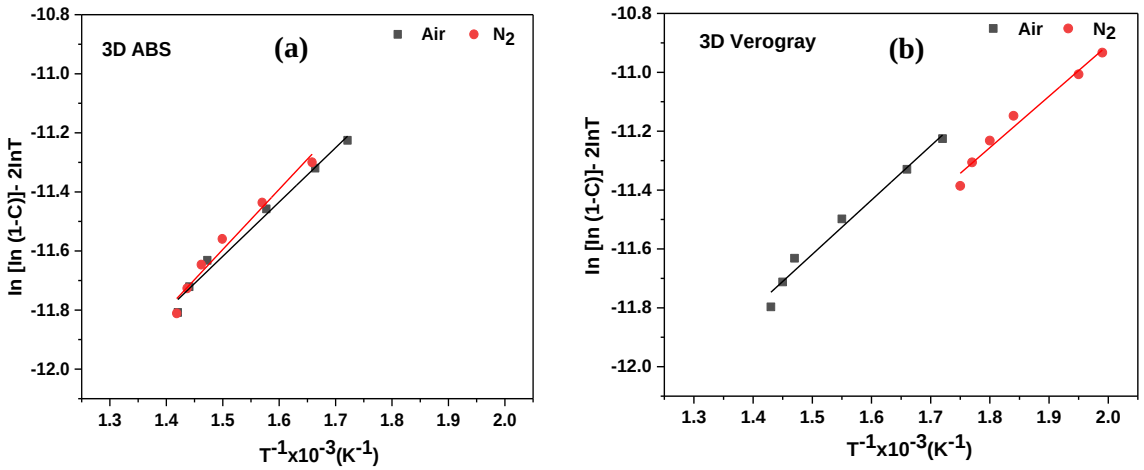

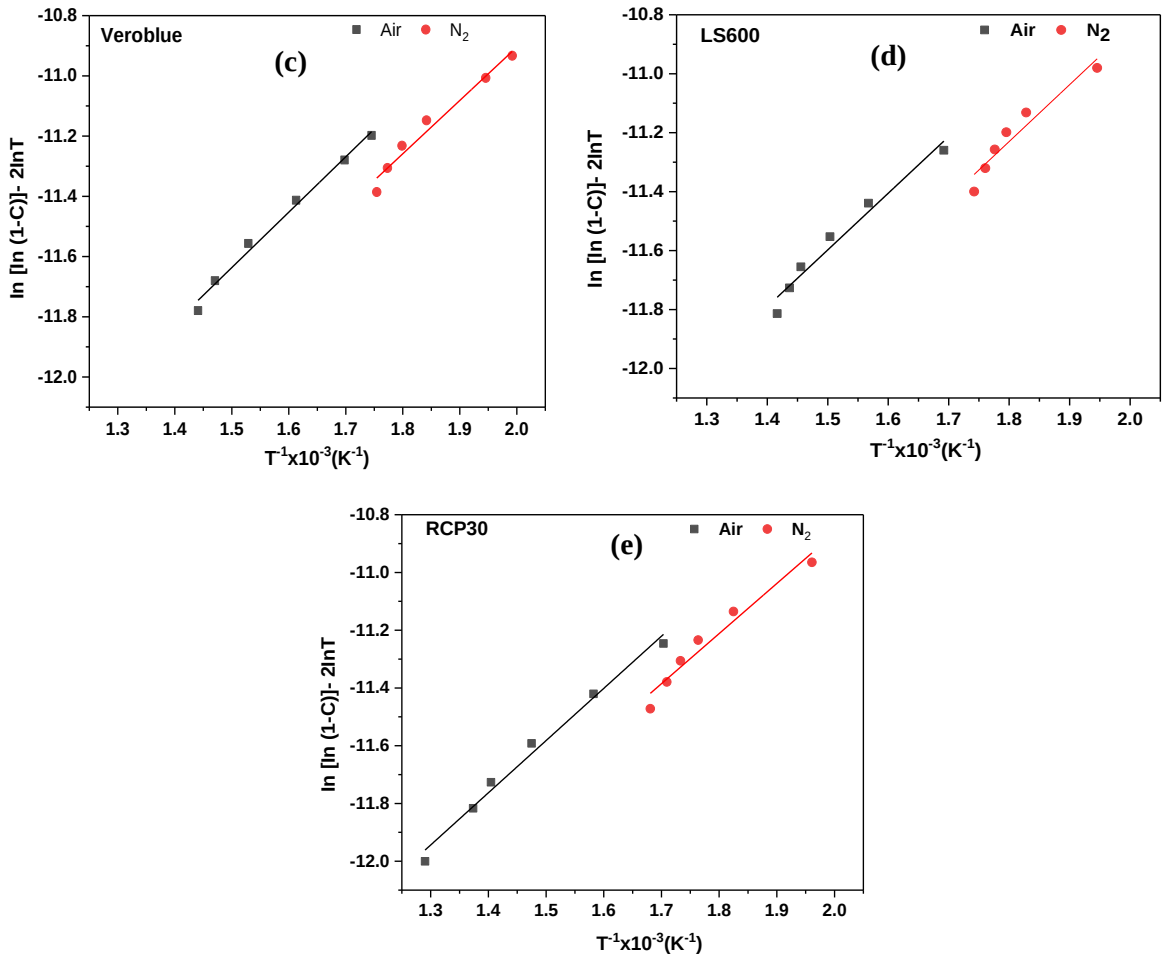

Figure 4-2- Arrhenius plot of degradation for additively manufactured (a) 3D ABS (b) Verogray (c) Veroblue (d) LS600 (e) RCP30 using Murray and White methods.

Table 4-2- Activation energy for the degradation of 3D polymer material.

3D Sample	Activation energy E_a (KJ/mol)	
	Murray-White Method	
	Air	N_2
ABS	15.28 ±0.50	12.42 ± 0.08
Verogray	15.33 ± 0.87	14.72 ± 0.02
Veroblue	15.28 ± 0.80	14.72 ± 0.02
LS600	15.98 ± 0.60	16.04 ± 0.07
RCP30	15.30 ± 0.57	14.43 ± 0.01

From Table 4-2, it was observed that the activation energies for each of the 3D printed polymers varied depending on the degradation environment of exposure. Amongst all the samples studied, LS600 showed the highest activation energies in both air and nitrogen. 3D ABS and Veroblue showed similar activation energies in air, however, in nitrogen, there is a clear distinction between both polymers in terms of their activation energy requirement and thermal threshold. Hence, it could be concluded that LS600 show superior thermally stability in both air and N_2 degradation environments in comparison

with the rest of the 3D printed samples studied. 3D ABS showed the lowest thermal stability as defined by the activation energy value of 15.28 and 12.42 kJ/mol in both air and nitrogen degradation environments respectively. Charles and Ramkumaar [226] both observed similar low activation energies for ABS when compared with polyethylene terephthalate. In PBM's such as ABS and low-density polyethene, definite aspects of their microstructure facilitate degradation, most especially in a thermal oxidation degradation process [227]. Tiganis and Burn [228], noted that tertiary replacement of specific carbon atoms within the microstructure of ABS in an oxidation environment promotes hydrogen abstraction by oxygen, thus making it more thermodynamically favoured in the process. With thermal energy acting as a catalyst to accelerate degradation, the activation energy is reduced especially in a thermo-oxidation environment.

To establish a statistical significance of these data from both tests, results were analysed using a t-test wherein the test statistics are based on a t-distribution. This test offers true test statistics since it's not sensitive to outliers in data. The collected data was analysed using a pair test. The null hypothesis tested was that the use of air or nitrogen does not affect the activation energy of the individual polymers, while the alternate hypothesis was that the activation energy of the individual polymers is affected by either air or nitrogen-containing environment. A p-value of 0.05 corresponding to a confidence interval of 95% was used. From the t-test analysis, a p-value of 0.17 was obtained (Table 4-3). The results support the alternate hypothesis.

Table 4-3- Results of statistical analysis

Concentration	Test	t-value	p-value	Statistical significance?
Low	Paired t-test	1.67	0.17	Yes

4.1.3 Glass transition analysis using DSC

The DSC technique is a quantitative analysis tool that allows the T_g and T_m of a particular sample to be measured. For this test, the additively manufactured polymer samples were analyzed for their glass transition temperature at a heating rate of 10 ℃/min in a Q20 DSC equipment. A summary of the DSC data for all 3D samples analysed is shown in Figure 4-3. From the experimental T_g values, it was shown that RCP30 has the least low limit T_g value of 45 ℃ amongst all the 3D printed samples with 3D ABS having the highest transition at 56 ℃.

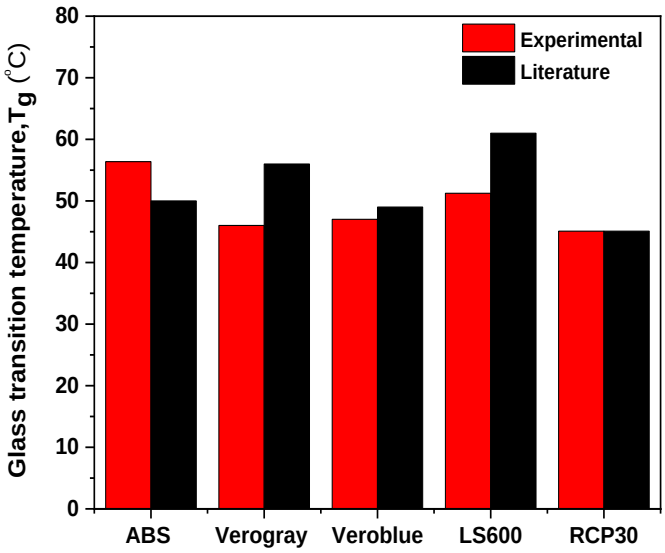

Figure 4-3- DSC plot showing both experimental and literature glass transition temperature for all additively manufactured samples using DSC Q20.

On the same plot, a comparison between the experimental values and literature [69] are made. From the plot, a few variations were observed between the experimental and literature values. For example, the calculated percentage error for Verogray and 3D ABS samples was ~18 % and ~13 % respectively. During the photoinitiation and subsequent polymerization of the activated monomer resin, material properties such as morphology, density etc., may have been affected, thus one would expect some variations in material properties during testing. That being said, the true essence of obtaining the individual T_g values were to provide an accurate prediction of the thermal transition temperature limit to which samples could be exposed within a vacuum deposition chamber without affecting the chemistry and mechanical properties of the substrate in question.

4.2 Mechanical testing

To provide a better understanding of the mechanical and behavioural characteristics of the test samples under tension, material properties such as Young's modulus, E, yield strength, ultimate strength, strain at failure and the strain energy density were all calculated. For easy of clarification, a representation plot showing each of the calculated variables is shown in Figure 4-4.

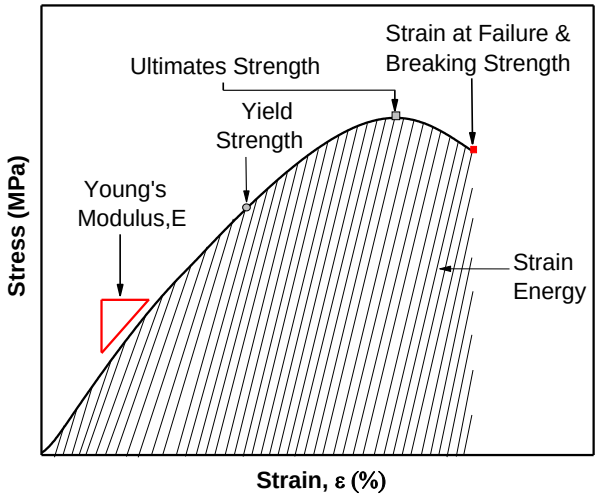

Figure 4-4- Schematic plot showing the relevant tensile stress-strain properties calculated in this study.

The Young's modulus as shown in Figure 4-4 was calculated based on the linear stress-strain relationship curve. Several authors [229, 230, 231, 232] have focused immensely on the mechanical characterization of the additively manufactured parts using varying techniques including fused deposition modelling (FDM) [229], Polyjet [233] and selective laser sintering [230]. They have all shown that the mechanical properties exhibited by 3D printed parts are a function of their printing parameters [234]. Amongst these are the raster direction, layer thickness, gap length, build orientation, printer type, etc [234]. In this experiment, two different techniques (Polyjet and SLA) producing uniquely different additive manufactured materials are mechanically studied. A summary table comprising all calculated properties for the tested samples are shown in Table 4-4.

From the stress-strain plot shown in Figure 4-5, it was observed that the stress distribution becomes relatively homogenous and independent of the strain increase with time until an inflexion point, commonly known as knee-point is attained [235]. For the 3D ABS, the end of the inflexion point is achieved at 0.5% of strain. Similarly, Verogray (V.G), Veroblue (V.B), LS600, and RCP30 show a 1.35, 1.7, 1.8 and 1.8 % strain respectively. Fitoussi *et al.* [235] noted similar strain behaviour when analysing the effect of high strain-rate tensile behaviour of polymer matrix, which they attributed to the Visco–damage behaviour characterizing the deformation regime. Swallowe [236] observed similar stress-strain behaviour in fully amorphous polymers such as PMMA and polymer composites and concluded that generally, the level of polymer crystallinity surges as a result of strain-induced crystallization leading to strain hardening during polymer tensile deformation as polymer chain structure assumes a more symmetrical close packing.

Table 4-4- Mechanical properties of additively manufactured materials.

Process	Material	Modulus (GPa)	Tensile strength at yield (MPa)	Elongation to failure(%)	Strain energy density(MJ/m^3)
3D system/ Polyjet	ABS	1.23 ± 6E-02	53 ± 1E-04	7.6	3.4
3D system/ Polyjet	Verogray	1.35 ± 4E-02	45 ± 4E-03	8.2	2.2
3D system/ Polyjet	Veroblue	1.35 ± 4E-02	36 ± 4E-03	11.39	2.5
3D system/ SLA	LS600	0.87 ± 5E-03	26 ± 5E-04	13.6	2.6
3D system/ SLA	RCP30	0.54 ± 6E-03	22 ± 1E-3	13.7	1.97

Further review of the tensile test results from Table 4-4 and Figure 4-5 revealed that 3D ABS had the highest tensile strength at yield with a modulus of 1.23 GPa. However, at failure, 3D ABS showed the least percentage strain value of 7.6 % as compared to all the additively manufactured tests samples analysed. This serves to indicates that, 3D ABS is by far the strongest material in terms of mechanical performance compared to the other materials tested with RCP30 being the weakest. However, since the modulus of a material is directly related to its stiffness, Verogray (V.G) and blue with similar modulus was adjudge the stiffest amongst all the samples tested. This is exemplified in Figure 4-5 where the multiple failure points are exhibited by Verogray in comparison with the other additively manufactured polymers tested. The strain energy density which is given by the area under the curve (A.U.C) for the stress-strain plot is summarized in Table 4-4. The results go further to confirm the total stored energy function per unit volume samples and provide a better estimation of the material toughness. It is shown that ABS has the highest strain energy density of 3.3MJ/m3 with the least being RCP30 with a value of 1.97MJ/m3.

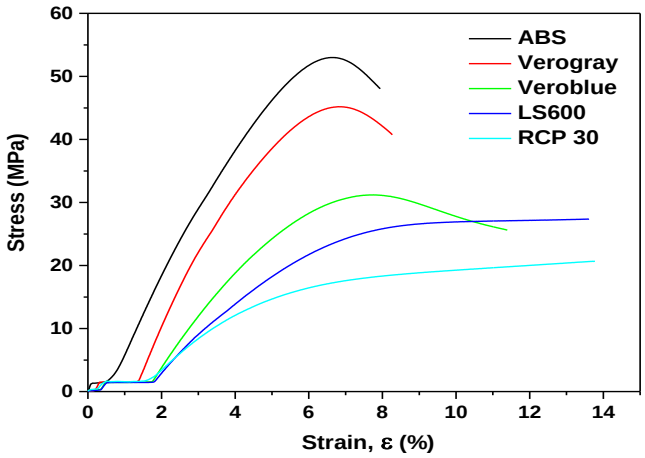

Figure 4-5- Plot showing the stress-strain properties of all 3D printed polymers (ABS, Verogray, Veroblue, LS600 and RCP30) using an INSTRON close-loop axial loading system.

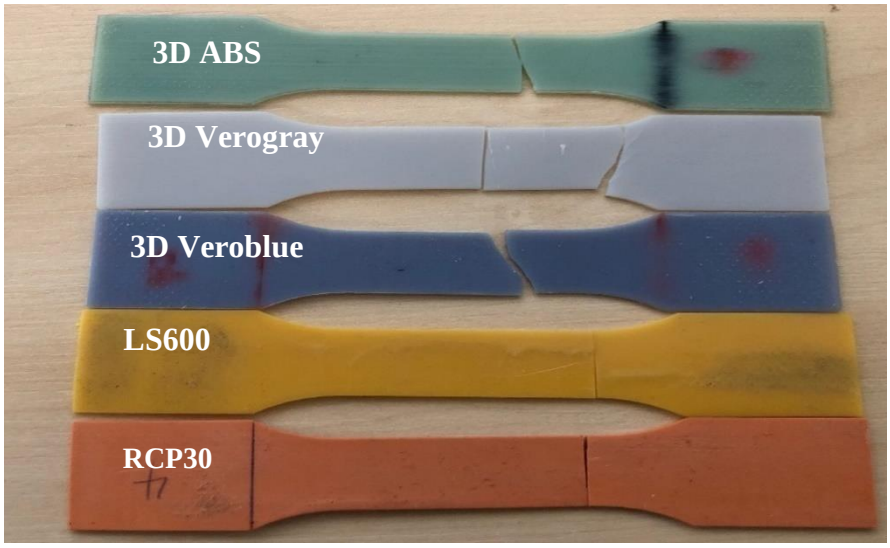

Figure 4-6- A photograph of the gage section of all tested 3D printed polymers showing the common failure modes.

Based on the results obtained, it was shown that RCP30 polymer exhibited the highest flexibility in comparison with the rest of the polymers tested. In most examples of stress-strain curve plots, there is always a clear distinction between the linear elastic region and the transition into plasticity [234, 235]. However, in some cases, materials may not always show these distinctive regions under tensile load as can be seen in the stress-strain curve for RCP30 and LS600. This, however, makes it very difficult to estimate the modulus of elasticity of such materials. Further analysis of the stress-strain curve for RCP30 shows an observable transition from an elastic to a plastic regime where a small increase in stress results in a huge strain increase until complete failure occurs. At this point, as we increase the strength by strain hardening, we lose material ductility

This phenomenon, known as strain hardening, could also be seen in LS600. Nonetheless, the stress-strain relation for 3D ABS, Verogray, and Veroblue shown in the same plot indicates an extended elastic region where the relationship is almost linear until the proportional limit is reached. 3D ABS and Verogray showed very small plastic deformation region before breaking, thus making it very brittle as already stated. In all cases, none of the polymers showed necking as observed for most thermoplastic materials processed by extrusion or injection moulding [237].

Additionally, the fractured surfaces of the tensile specimen were assessed for their deformation patterns as shown in Figure 4-6. LS600 and RCP30 all exhibited similar fracture patterns at the point of fracture where each of the samples appears to fracture cleanly and perpendicular to the loading direction. The printed polymers produced using the Polyjet technique in the case of ABS, Verogray, and Veroblue showed irregular and jagged deformation patterns as a result of their brittleness nature when compared with both LS600 and RCP30 materials (Figure 4-6).

4.3 ASTM D570 water absorption test

An understanding of the water absorption performance of all test samples was key in determining the most suitable polymer type to be targeted for selection and coating. In this experiment, a water absorption test was performed following the recommendations set out in ASTM D570. It was noted that the percentage of water absorbed at room temperature varied significantly between the individual samples, with 3D ABS recording the highest percentage of water absorbed. RCP30, on the other hand, was the most hydrophobic amongst the five individual samples. The following hydrophobicity ranking for each of the polymers at 25 ℃ is presented as follows; RCP30(0.33%)> LS600(0.63%)> V.B (1.16%)> V.G(2.15%)> 3D ABS(2.86%). Ayrilmis *et al.* [238] in a study looking at the effect of printing layer thickness on water absorption properties of 3D printed wood/PLA composite material noted the influence surface chemistry and mechanical properties play in the water absorption process and reported varying water absorption rates of between 0.19 % to 0.72 % for the print layer thickness of 0.05 mm to 0.3 mm. They further confirmed that not only does layer thickness play an important role in the absorption phenomenon but also the presence of surface free hydroxyl bonds makes polar covalent bonding with hydrogen ions from water more easily. Carlos [239] reported a 1.13 % moisture absorption for 3D ABS printed using FDM technique and attributed this increase to the non-uniformity of the polymer layer orientation structure during both the printing and curing surface.

A comparison with similar research conducted by Stratasys [69] shows the percentage of water absorption could vary from 1.1-1.5 % and 1.5-2.2 % for Verogray and Veroblue polymers respectively. However, due to the proprietary nature of these polymers, detailed material properties are sometimes withheld by the manufactures and are not made public. As a consequence, only V.G and V.B samples could be compared.

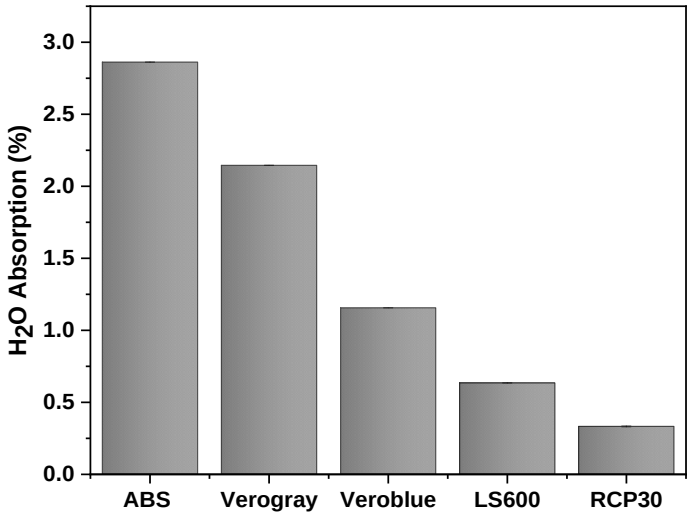

Figure 4-7- ASTMD570 water absorption plot showing the percentage of water absorbed after 24hrs of testing for the individual 3D printed polymers.

4.4 Surface chemistry analysis

FTIR spectroscopy has been fully exploited for the identification and characterization of the basic chemical structural units presented in all the additively manufactured polymers under study. The comprehensive vibration band assigned to each of the polymers is presented for the selected infrared (IR) peak for easy confirmation of their molecular structure [240]. The characteristic large singlet –OH absorption peak which occurs at wavenumbers between 3550-3200 cm^{-1} [241] is seen in all polymers with a much stronger peak % transmittance observed with the Verogray sample. The yield of this large singlet –OH absorption peak could be attributed to the surface interaction with moisture in the air as the sample is exposed to the atmosphere. Except for the IR peak intensity variations observed for the –OH band, similar vibrations patterns were observed from wavenumbers 3000-500 cm^{-1} for all samples studied. Amongst the major peaks observed were the sp^3-CH stretching observed between 3000-2800 cm^{-1} wavenumbers which are characteristic of aliphatic compounds [242]. As seen from Figure 4-8, the principal transmission signal observed between 2000-1500 cm^{-1} is due to C=O and C=C stretching, with C=C occurring around 1650 cm^{-1} due to its weak absorption properties [241]. Table 4-5 shows the vibrational frequency of all the fundamental bands along with their corresponding intensities for all 3D polymers. It was observed that except for the spectra vibration bands at 1156 cm^{-1} for LS600 and RCP30, similar vibration wavelengths were observed for all five 3D polymers studied.

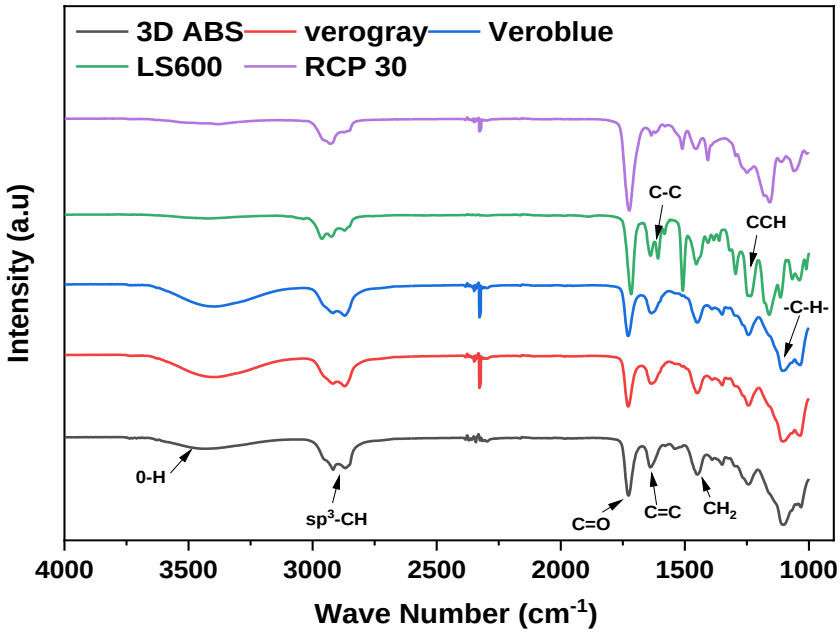

Figure 4-8- FTIR spectra showing the transmittance(%) for the individual 3D polymers studied.

Table 4-5- FTIR plot summary showing the corresponding individual wave numbers and functional groups present in each of the 3D samples analysed.

3D Samples	Wavenumber (cm^{-1})	Functional group	Vibration mode
3D ABS,Verogray,Veroblue LS600 and RCP30	3700-3000	O-H	Symmetric stretching
3D ABS,Verogray,Veroblue LS600 and RCP30	2919	CH_2	Asymmetric stretching
3D ABS,Verogray,Veroblue LS600 and RCP30	2860	CH_2	Symmetric stretching
3D ABS,Verogray,Veroblue LS600 and RCP30	1721	C=O	Stretching
3D ABS,Verogray,Veroblue LS600 and RCP30	1635	C=C	Stretching
LS600 and RCP30	1603	C-C	Ring stretching
3D ABS,Verogray,Veroblue LS600 and RCP30	1454	CH_2	Scissoring
3D ABS,Verogray,Veroblue LS600	1352	CH_2	Wagging
3D ABS,Verogray,Veroblue LS600 and RCP30	1261	CCH	Asymmetric bending
LS600 and RCP30	1156	CCH	Symmetric bending/CH_2 twisting
3D ABS,Verogray,Veroblue LS600 and RCP30	1097	-C-H-	-CH bending vibrations of fatty acid

4.5 Roughness measurement

The two proposed 3D printing techniques (Polyjet and SLA) are used in this work for the evaluation of the surface roughness Ra parameters. Figure 4-9 shows a talysurf example scan of the measured surface profile of each of the substrates post-cleaning.

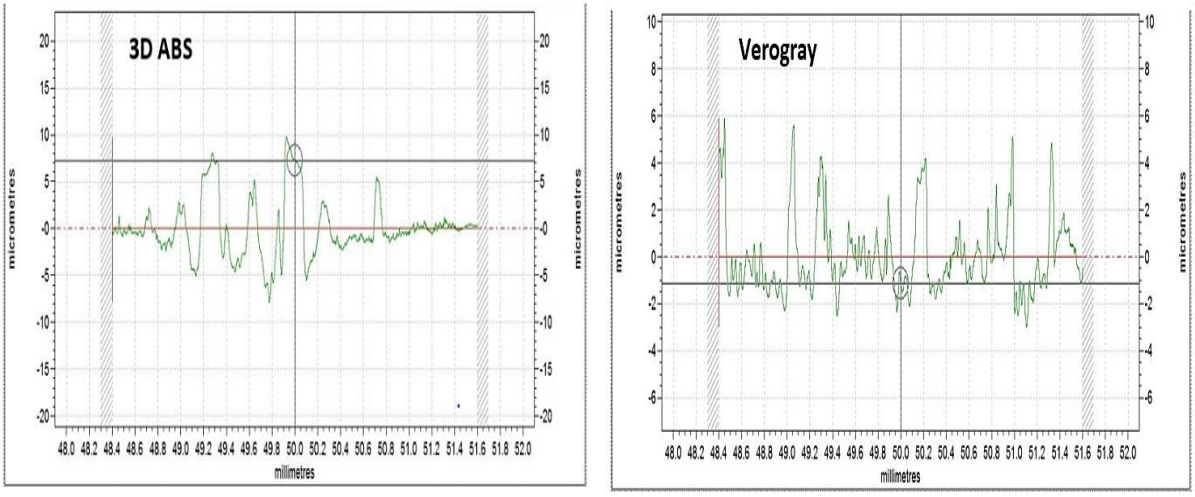

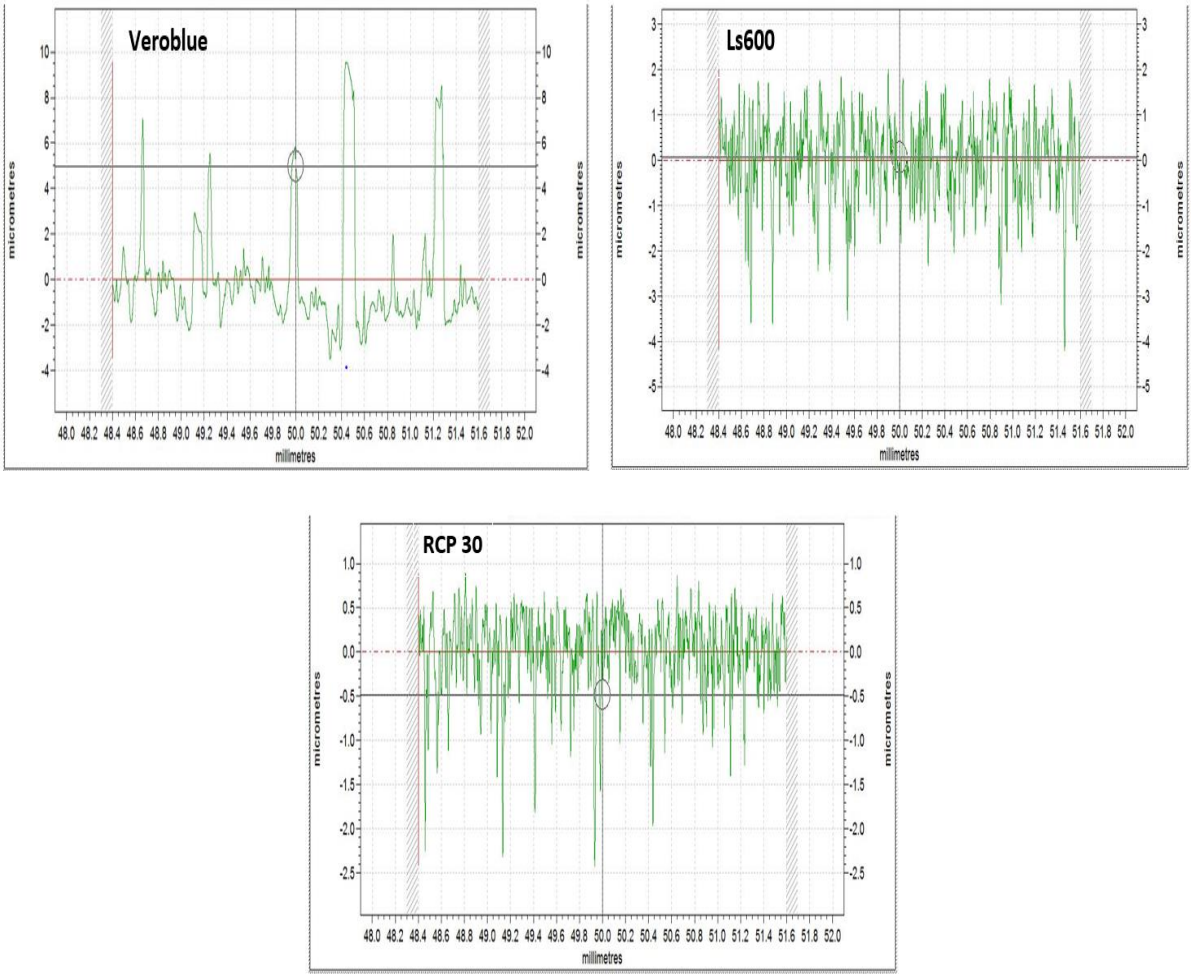

Figure 4-9- Surface roughness profile of 3D printed substrates.

An average plot of the individual surface roughness (R_a) is also presented in Figure 4-10. For each of the two methods presented and their impact on surface roughness, it was shown that the average roughness of the substrates is highly dependent on the printing technique used. For the Polyjet technology, the average surface roughness value ranged from 1.35 ± 0.28 to 1.55 ± 0.21µm. The SLA technique showed values between 0.23 ± 0.12 to 0.49 ± 0.13 µm. Vidakis *et al.* [243] explained that 3D printing quality is affected by factors such as layer thickness, part orientation, deposition mechanism and finish methodology. Considering that Polyjet materials are built layer by layer, Chryssolouris *et al.* [244] noted that in Polyjet printing, a typical classic staircase error is created when the layer shape does not align perfectly with the printing orientation. Vidakis *et al.* [243] measured an average Ra of 2.77 µm for his study of Polyjet printed substrates. Even though different authors have measured variable Ra values for SLA printed parts [243, 245], this work showed lower Ra values for SLA printed parts

compared with Polyjet printed parts. It was concluded that for both techniques, a lower R_a value is highly achievable with the SLA technique as the classic staircase effect is minimised in this case.

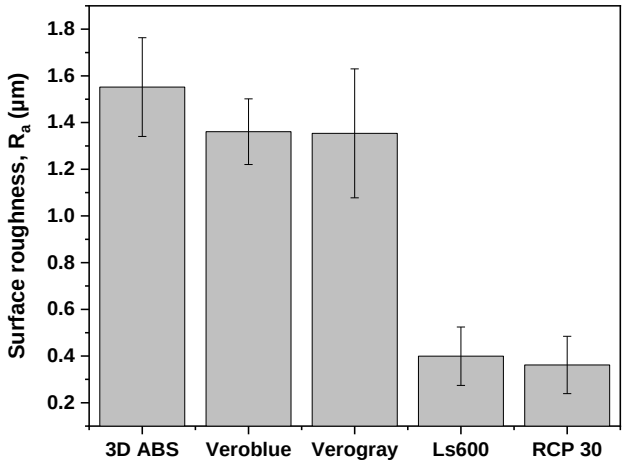

Figure 4-10- Average surface roughness of all printed substrates

4.6 Pore size distribution

Mercury Intrusion capillary pressure (MICP) measurement was employed as a first attempt to determine and characterize pore features, particularly pore throat size distribution in both 3D printed 3D ABS and V.G within the nano (< 1-3 nm) and microscale (up to 350 µm) pore size range. For this test, only 3D ABS and Verogray were selected due to the project specification and polymer property characterisation.

Not only is MICP very fundamental in characterizing pore size distribution with great accuracy but a resourceful tool for revealing in great detail the physical properties of the solid material. In addition to the pore size information provided by this method, polymer density, porosity, void volume, and material volume data could all be obtained through the process. In a typical MICP plot showing the capillary pressure (psi) against saturation fraction as shown in Figure 4-11 for 3D ABS and Verogray, the volume of mercury injected into the available voids is shown to increase as pressure injected into the sample increases regardless of the pore geometry. Figure 4-11 further reveals that the saturation of mercury injected into pore structures is not attained until such a point that the pressure applied to the system is sufficient enough to cause the migration of mercury into the pore network. This illustrates that increasing the pressure allows mercury to access the majority of the voids within the polymer matrix structure. For both 3D ABS and Verogray samples tested, this pressure corresponds to 25 psi (172.4kPa) and 69.3psi (477.8kPa) respectively. This is followed by a steady-state increase in the pressure until a maximum saturation point of 100% is attained for both polymer samples. Verogray showing high capillary pressure suggests a high-pressure injection requirement to access the pores structure, demonstrating poor connectivity or accessibility. In contrast, a significant proportion of the saturation fraction volume ($8.6x10^{-4}$) of the 3D ABS pore structure was filled before exhibiting comparable

behaviour to the Verogray sample towards high injection pressures. The general shape of the two curves are comparable, signifying similar pore size properties after both threshold capillary and saturation fractions are achieved.

An investigation into the pore size distribution of both 3D ABS and Verogray as shown in Figure 4-12 reveals varying pore size radius present within the polymer matrix. For both samples, the minimum pore radius recorded was 0.0015µm but with varying pore size distribution function. For 3D ABS, the pore size distribution function was calculated as 0.0285 whereas that of V.G was 0.0156. It was observed that the pore size distribution for 3D ABS ranges from a minimum of 0.0015 - 3.62 µm whilst Verogray had a maximum pore size radius of 0.93 µm. For both samples, it is observed that the pore size distribution lies between the meso (1-25 nm) and macropore (>25 nm) size characterization range. This, however, is very much reflective of the inherent porosity for both samples as 3D ABS showed higher porosity of 7.7% as against a 6.6% porosity value for Verogray. For LS600 and RCP30 samples, the MICP technique was deemed unsuitable as the pore sizes were too small to be accurate measured, hence, no measurements were taken.

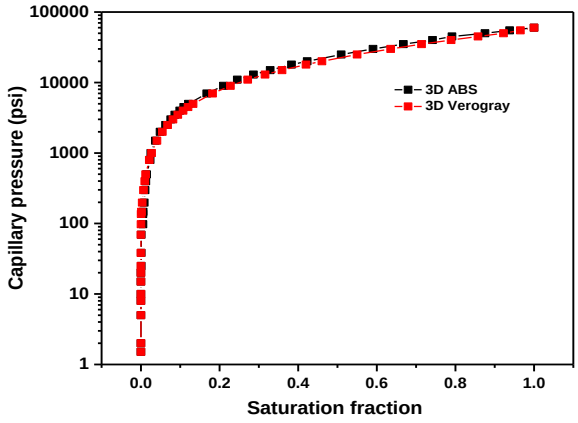

Figure 4-11- MICP plot for both 3D ABS and Verogray showing the capillary pressure variation against saturation fraction for mercury.

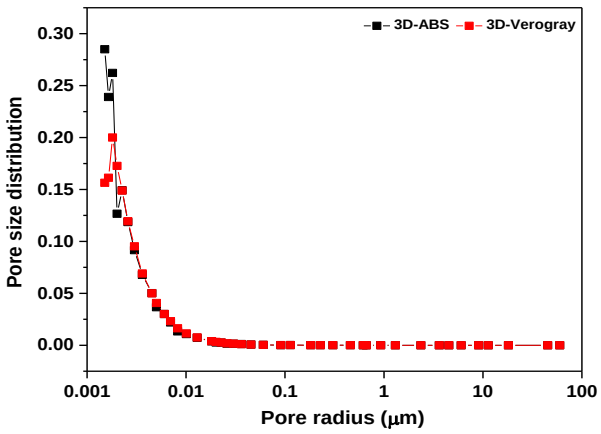

Figure 4-12- MICP plot showing the pore size distribution function against pore size radius for both 3D ABS and Verogray samples.

4.7 Material selection

In summary, the physical, chemical and thermal properties of five different 3D-printed polymers have been investigated. From the individual characterization test results obtained, the following conclusions are drawn and summarised using a material performance ranking index proforma (Table 4-6). The suitability for functionalization using MW-PECVD was introduced to effectively grade each 3D-polymer sample based on their performance under each test condition. With consultation from Proctor and Gamble as the industrial sponsor for this project, 3D ABS and Verogray samples were chosen for enhanced functionalization using the MW-PECVD technique due to characteristic properties elucidated in Chapter 4.

Table 4-6- Show a summarised material ranking proforma for the individual 3D-printed materials. The numerical grading assigned to each polymer indicates the performance of each polymer to the other. The final grading provides the overall performance of the individual samples studied under thermal, water and tensile testing properties.

	Thermal Analysis			Water absorption		Tensile Testing				
Samples	Average (Tg)	DSC(Nitrogen)	DSC(Air)	25°C	50°C	Modulus	Tensile Stress at Yield	Toughness	Stiffness	Final Tally
ABS	5	5	5	1	4	3	5	5	3	36
LS600	4	4	1	4	5	2	2	4	2	28
VeroBlue	3	3	2	3	2	5	3	3	4	28
VeroGrey	2	2	3	2	3	4	4	2	5	27
RCP30	1	1	4	5	1	1	1	1	1	16

Fair (1),Satisfactory(2),Good(3),VeryGood(4),Excellent(5)

4.8 Summary

The results presented in this chapter show the characterisation of five different AM polymers used in this study. The thermal, mechanical, water absorption, surface chemistry and pore size structure are discussed. The activation energy during thermal decomposition shows the degradation of the individual polymers is highly dependent on the deposition gas environment used. It was noted further that except for LS600 samples, the thermal decomposition onset temperature and mass loss was enhanced under atmospheric air rather than in nitrogen. The highest experimental T_g was observed for 3D ABS at 56 °C. In terms of the mechanical property performance of the individual AM polymers, 3D ABS was adjudged the strongest amongst all the materials tested with RCP30 being the weakest at yield. Similar modulus of 1.35 GPa for both Verogray and Veroblue were calculated and shown to be the stiffest amongst all the five polymers studied. Water absorption measurement using ASTM D570 standard showed increased hydrophilicity in the case of 3D ABS where the highest percentage water absorption

of 2.86% was calculated. Further analysis using MICP showed the presence of highly dominated mesopore size range pore structures accounting for 99.75 % of the total void fraction.

Chapter 5

Results & Discussion: DLC film deposition and characterisation

5.1 Introduction

This chapter presents the DLC films deposited using the MW-PECVD technique by the design of experiment approach. Results of the substrate thermal heating and temperature evolution, as well as the characterization of the DLC films, are presented in this chapter.

5.2 Process recipe characterisation

By using a design of experiment approach, the deposition environment space definition was based on the initially proposed design parameters needed to sustain a stable plasma body. By this, the setpoint parameters for each of the initial DOEs was seen to deviate from the initially planned deposition conditions. The chosen experimental parameters for a 3 leg experimental design for the proposed and actual recipes used as the bases for the initial deposition steps are shown in Table 5-1and Table 5-2 respectively.

Table 5-1- Proposed parameters used to deposit the initial DLC coating.

	Proposed				
DOE Leg	MW Power (W)		Working Pressure (mbar)	C_2H_2 flow rate (sccm)	Ar flow rate (sccm)
	1	2			
1	1050	1050	0.012	722	50
2	1050	1050	0.011	610	110
3	1200	1200	0.011	250	350

Table 5-2- Actual parameters used to deposit the initial DLC coating.

	Actual				
DOE Leg	MW Power (W)		Working Pressure (mbar)	C_2H_2 flow rate (sccm)	Ar flow rate (sccm)
	1	2			
1	1027	942	0.011	568	43
2	1050	885	0.011	610	101
3	1172	1181	0.0097	250	350

During the initial test run phase, it became apparent that the proposed deposition setpoint parameters were not achievable in their current form and all DOE runs had to be carefully tuned to match the processes and hardware restrictions variability posed by the equipment tolerance. For example, to maintain constant MW power as defined in each of the design deposition steps on both microwave sources, manual adjustments are required during the deposition stages to maintain stable glow discharge.

5.3 Substrate heating

Low-temperature plasma deposition in vacuum using MW-PECVD like any other deposition method is subjected to the generation of heat as a result of the K.E transfer between the energetic ions, molecules and reactive species with the substrate solid surface, as the structure and morphology of the thin film depend strongly on the energetic flux density of the reactive species. By suitable variation of the experimental parameters, the different contributions to substrate surface heating during deposition can be separated and the resulting temperature build-up during deposition studied independently.
To achieve coating uniformity and consistency throughout the deposition cycle without damaging the 3D printed substrate, adequate steps were taken to ensure the coating deposition chamber was controlled and maintained below the glass transition temperature of the most sensitive polymer been coated, i.e. Verogrey with a T_g of 46 °C. Shimbo [246] noted that the stress build-up in epoxies and resins due to higher temperatures exposure above the glass transition temperature is commonly negligible, however, when cooled below the glass transition temperature, stresses begin to build up within the polymer structure. These stresses were further noted to be linearly proportioned to the change in temperature below the T_g value. Riande *et al.* [247] in the quest to determine the viscous response of epoxies to temperature change at the glass transition temperature using the time-temperature correspondence principle, noted that the deformation due to viscous flow is generally constant at the glass transition temperature. However, with increasing temperature above the T_g value, they noted that the unrecoverable contribution to the shear deformation (viscous deformation) was extremely high. As a consequence, 4 different thermocouples located on both the chamber walls (2 fixed) and substrate rotation tables (2) were utilized in this regard to control the temperatures within the deposition chamber from exceeding the maximum temperature threshold defined by the most sensitive 3D polymer substrate to be coated.

Figure 5-1 shows the temperature evolution with time for each of the coating deposition DOEs steps utilized in the initial deposition phase of this work. To allow for sufficient coating thickness to be deposited, several deposition steps were implemented within a DOE cycle with a complimentary off duty cycle lasting an hour between each deposition step to minimize the sudden effect of temperature build-up due to the direct thermal heat flux from the micro-wave sources, particle ionization and

bombardment during each deposition cycle. The heating rates for each of the deposition cycles were mostly linear through the deposition steps, however, few deviations were observed in the case of some deposition steps. This phenomenon was solely attributed to the difficulty of igniting the plasma at some stage during the deposition cycle.

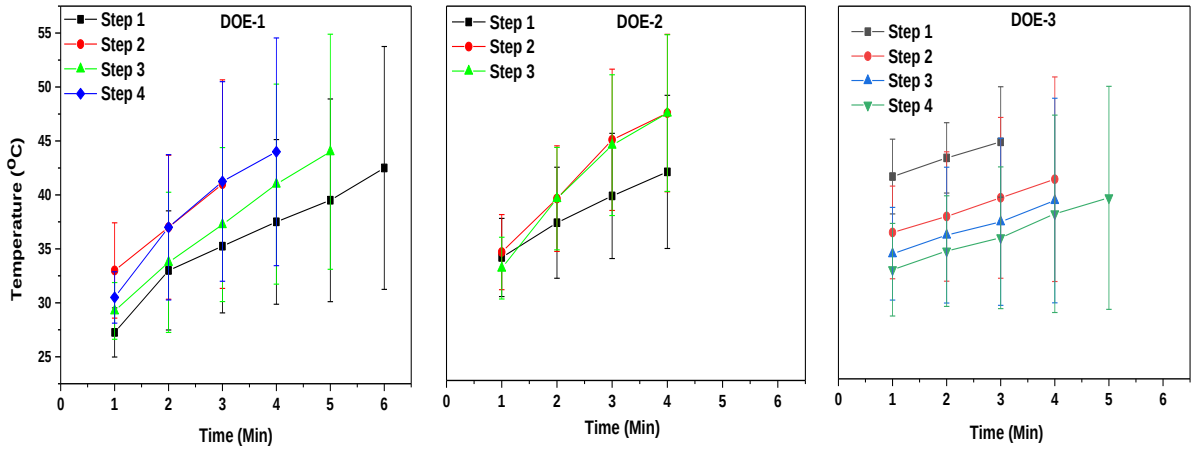

Figure 5-1- Temperature evolution during deposition leg for DOE-1,2 and 3 with plots showing each deposition step made to deposit the DLC coating.

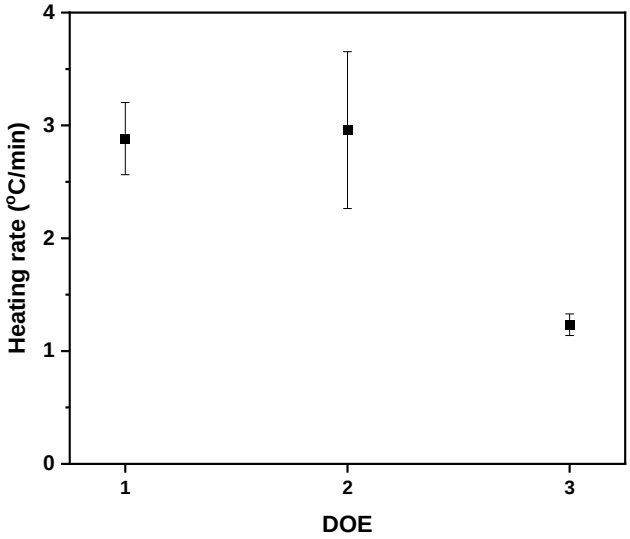

Figure 5-2- Plot of the average heating rate of DLC deposition step for each deposition Leg determined from individual rotating thermocouples located at the same working distance as the substrate during.

The heating rate for the individual deposition legs is presented in Figure 5-2, where the maximum average heating rate for the three DOEs was found to be 2.95 °C/min for DOE 2. The lowest calculated rate was observed in DOE 3 at 1.23 °C/min with DOE 1 having a 2.54 % reduction in the heating rate compared with DOE1. This means for each DOE, the time at which the thermal threshold within the chamber will be attained (at 46 °C) will vary. Therefore if we assume an average starting temperature

range (consisting of the minimum and maximum starting temperature points obtained during the deposition individual deposition steps) of 35.8 ℃ - 38.2 ℃ with a maximum allowable temperature of 46 ℃, then we would expect to have on average 2.5 mins of deposition time before overheating occurs. Similarly, for DOE 2 and 3 at temperatures of 38.25 ℃ – 41.13 ℃ and 36.10 ℃ – 43.10 ℃, a heating rate of 2.98 ℃/min and 1.23 ℃/min respectively was recorded. This means it will take between 1.7 – 2.65 mins and 4 – 8 mins for DOE2 and 3 to attain the maximum allowable temperature of 46 ℃. A review of the process parameters as they affect the heating rate shows a corresponding increasing gas flow for both Ar and C_2H_2 as shown in Figure 5-2. This means more energetic particles can transfer their K.E to the substrate surfaces, thus increasing the heating rate as a result. Since the process parameters used for each DOE was different, the time leg for which the maximum temperature threshold is attained will vary. As a result, the deposition time in reaching the maximum temperature for each leg in other to prevent overheating of the substrate was different.

5.1.4 Deposition rate

The deposition rates for the various DOE's were determined by measuring the step height change from an area on the surface of the coating to that of the uncoated surface masked during the deposition stage with a Kapton tape using a 2D contact Talysurf PG1800 profilometry scanner. The average coating thickness (µm) of the three DOE DLC's produced with their corresponding deposition rates on both 3D ABS and Verogray are presented in Figure 5-3. The deposition rate is a measure based on the coating thickness and total deposition time (mins) determined in each deposition step for a total 5 samples.

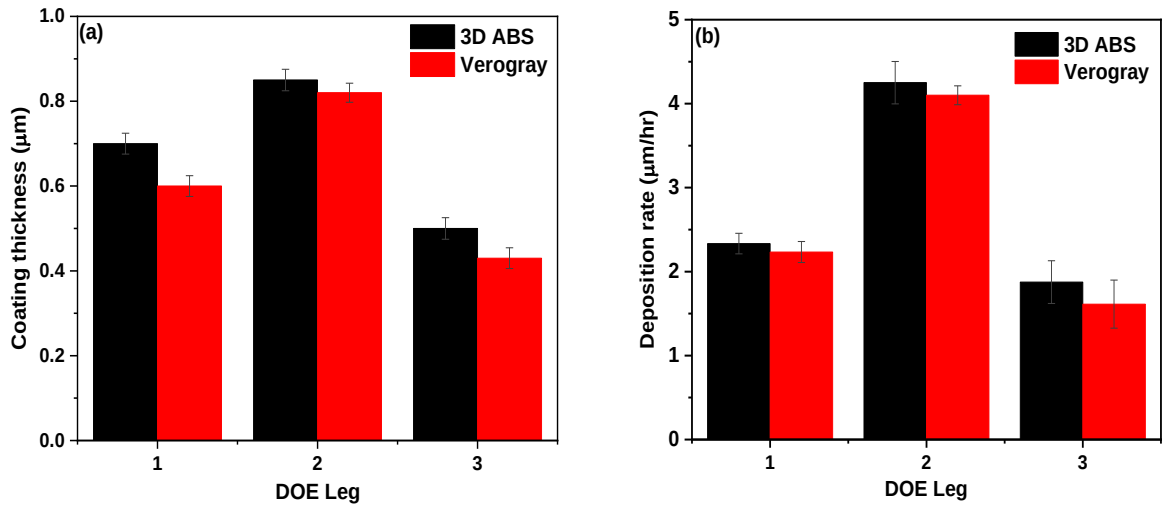

Figure 5-3- Variation of (a) coating thickness and (b) deposition rate for all DOE Legs studied on both 3D ABS and Verogray samples.

It was observed that the coating thickness varied from roughly 0.44 to 0.75 µm in the case of 3D ABS for DOE 1-3 and 0.42 to 0.7 µm for similar deposition steps on Verogray samples. The effect of the gas flow in both coating thickness measure and deposition rate calculation shows a positive relationship between the two parameters determined as the increase in the process gas flow increases deposition rate [248]. The highest coating thickness and deposition rate were observed for DOE2. A comparison between both substrates in terms of coating thickness and deposition rate show that under the same deposition condition, film growth through atomic nucleation is enhanced in all cases for 3D ABS polymers compared with Verogray.

5.4 Surface roughness

The relationship between the surface roughness of both coated and uncoated substrates roughness is shown in Figure 5-4. It is observed that in all cases for 3D ABS, the surface roughness of the underlying substrate material is always higher than their coated counterpart and similar could be said for Verogray samples. Significant differences were observed for all Verogray coated samples with DOE 3 coating providing a 97 % reduction in the surface roughness of the pristine surface. Even though 3D ABS showed some reduction in their R_a values, deposition under DOE 2 for 3D ABS showed no significant differences between both coated and uncoated samples. It is apparent from both R_a values that the surface roughness and topography definition for the uncoated polymer played an important role in creating a conformal coating structure on the already existing surface.

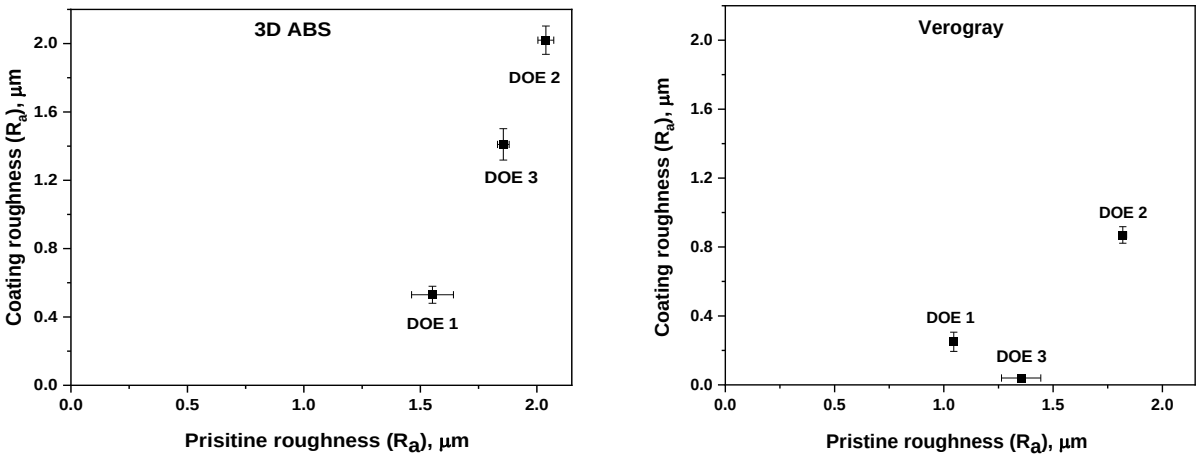

Figure 5-4- The relationship between the roughness of the DLC coated surfaces and that of the pristine substrate surface for (a) 3D ABS and Verogray(b).

Further analysis of both coated and uncoated surfaces reveal detailed surface coating cracking and irregular abrasive marks created as a result of the post surface treatment methods after printing. A summary representation is shown in Figure 5-5 for both 3D ABS and Verogray samples for DOE 1. It is evident from the SEM image shown in Figure 5-5 that, the coating damage resulting from the extensive cracking exhibited by the coated surface may have led to the increased surface roughness.

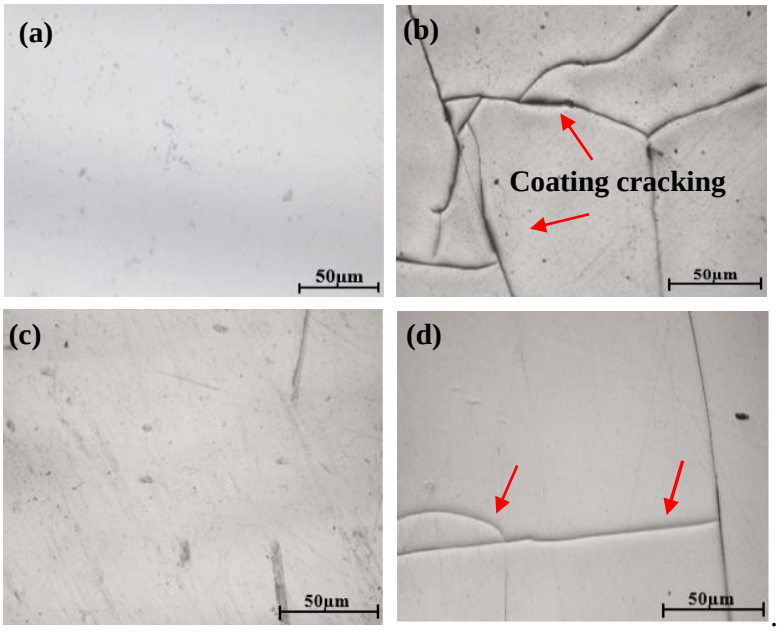

Figure 5-5- SEM Image showing the surface morphology for both uncoated and coated 3D ABS (shown as (a) and (b) for coated and uncoated 3D ABS respectively) and Verogray (shown as (c) and (d) for uncoated and coated Verogray respectively) for DOE 1.

Even though the above conclusion on the role of surface roughness provides some evidence in support of the relationship between surface feature definition and coating roughness, the evidence, however, provides some exceptions which are multifaceted.

5.5 Coating adhesion

A progressive load scratch test to assess the coating adhesion was performed using a 200µm conical diamond tip with a sliding speed of 10mm/min along the coated surface with a linearly increasing load of 0-5N until coating failure occurs. The failure event is examined by an optical microscope to determine the extent of deformation on the surface. Figure 5-6 shows a representative deformation response of the coated 3D ABS for DOE 1-3. In all cases, the test results show complete coating failure characterized by varying degrees of adhesive failure. For DOE 1 it was observed that the coated 3D ABS showed gross spallation of the coating from the substrate surface at the start to the completion of the test at 5N as large detached regions are seen completely spalled in the process. However, for DOE

2 and 3, the deformation observed was characteristic of buckling spallation failure where coating damage is seen ahead of the stylus tip with irregular chevron-like cracking extending beyond the scratch grove.

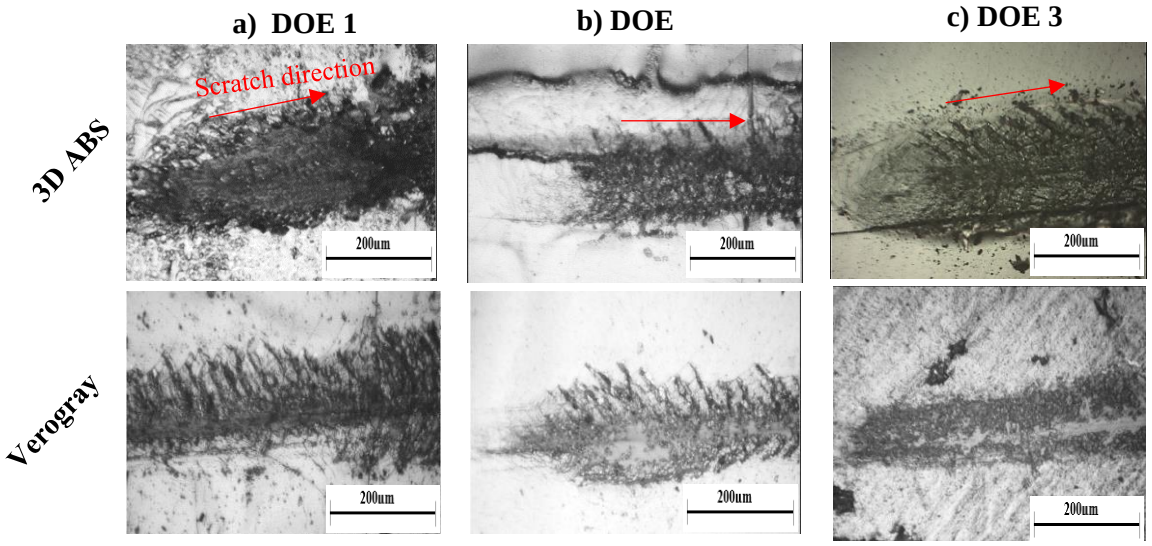

Figure 5-6- Coating adhesion response to progressive load scratch test from 0-5N on 3D ABS and Verogray for DOE1 (a), DOE2 (b) and DOE3 (c).

Similarly, the performance of Verogray to the applied tensile and shear stress provided similar deformation characterization where complete failure was observed in all DOEs. It is self-evident from the SEM image from Figure 5-5 that, the highly-stressed coating structure showing extensive cracking being acted upon by both tensile and shear stress from the macro-scratch test is as important a contributing factor in the coating delamination process as both the tensile and shear stresses acting on the surface. By extension, it was concluded that to obtain satisfactory coating-substrate adhesion, the individual DOE's must be reviewed to account for the stress build-up developed during the coating process resulting in the coating deformation through cracking. A typical characteristic property associated with DLC coating on polymer substrate [249, 126].

5.6 Modification of DLC coating

DLC films, in general, have been constrained in their application as a result of the large internal compressive stress generated during film deposition which could be up to 10 GPa under certain deposition conditions [250]. This is shown to greatly limit the adhesive strength between the DLC films and substrate, resulting in the deformation of the coating at the substrate-film interface through cracking and or peeling-off of the coating from the surface [251, 252]. To solve the problem of high internal stress and poor adhesion, several methods including the use of interlayers and elemental doping using

Ti, Cr, W, N, and Si are regularly used in the process [250]. Bootkul *et al.* [253] compared the scratch critical load performance of both ta-C and ta-C:N DLC films and noted that the critical load for the nitrogen-doped ta-C film increased by about two folds even for the lowest partial pressure of 9 x 10^{-5} Torr (N< 0.001%) and showed an upward increase in the scratch resistance with increasing nitrogen partial pressure. This is because the use of nitrogen dopant serves to increase the adhesion strength of DLC films by prompting the clustering of sp^2 sites, thus enhancing the graphitization of the film owing to the preferential π bonding of nitrogen in the film [254]. As C=C bonds have shorter bond lengths than C-C bonds, the surge in the formation and clustering of C=C yields to decrease the strain in the film [253]. However, with further inclusion of nitrogen in the film, the formation of C=N bonds having shorter bond lengths in comparison with both C=C and C-C bonds occurs as a result, thus promoting further the reduction of strain in the film and increasing adhesion as a result.

As a consequence, a new design of experiment was proposed based on the addition of varying amounts of nitrogen content in the amorphous hydrogenated carbon (a-C:H) to form a nitrogen-doped amorphous hydrogenated carbon (a-C:N:H). Table 5-3 and Table 5-4 provide details of both the proposed and actual coating parameters used for the deposition. In the new proposal, the gas flow rates of N_2 and C_2H_2 are varied at constant micro-wave input power, Ar gas flow rate, and working pressure. In total, five different DLCs were studied based on the initial proposed design discussed earlier. The nitrogen gas flow rates used in relation to a constant Ar flow rate (sccm) of 50sccm were 10 and 20sccm as detailed in the proposed design table. Similarly, the gas flow rate of C_2H_2 to Ar gas flow of 50 sccm used were 610 and 310. The resulting coating performance is discussed further in this chapter and shall act as the basis for all coating design and discussion in subsequent chapters.

Table 5-3- Proposed parameters used to deposit the modified DLC coating.

	Proposed					
DLC	MW Power (W)		Working Pressure (mbar)	C_2H_2 flow rate (sccm)	Ar flow rate (sccm)	N_2
	1	2				
1	1050	1050	0.012	610	50	-
2	1050	1050	0.012	610	50	10
3	1050	1050	0.012	610	50	20
4	1050	1050	0.012	310	50	10
5	1050	1050	0.012	310	50	20

Table 5-4- Actual parameters used to deposit the modified DLC Coating.

	Actual					
DLC	MW Power (W)		Working Pressure (mbar)	C_2H_2 flow rate (sccm)	Ar flow rate (sccm)	N_2
	1	2				
1	1034	1044	0.011	610	50	-
2	1050	1050	0.014	608	50	10
3	1027	1042	0.012	600	50	20
4	1043	1050	0.012	298	50	10
5	1050	1050	0.010	310	50	20

5.6.1 Substrate heating

The heating rate for the modified new design for all DLCs deposited is presented in Figure 5-7 and Appendix I where individual DLC deposition legs are shown. Similarly, as detailed in the previous discussion in this chapter, the majority of the heating rate curves show a positive linear correlation between the temperature build-up on the substrate with time. The average maximum and minimum heating temperatures attained for each deposition leg are also detailed in Figure 5-7 (b). Data presented in Figure 5-7 are an average of 3 individual runs. It was revealed that, for all the five DLCs deposited, the highest maximum average temperature attained was at 41.6 ℃ for DLC/2 with a corresponding heating rate of 2 ℃/min (Figure 5-8)

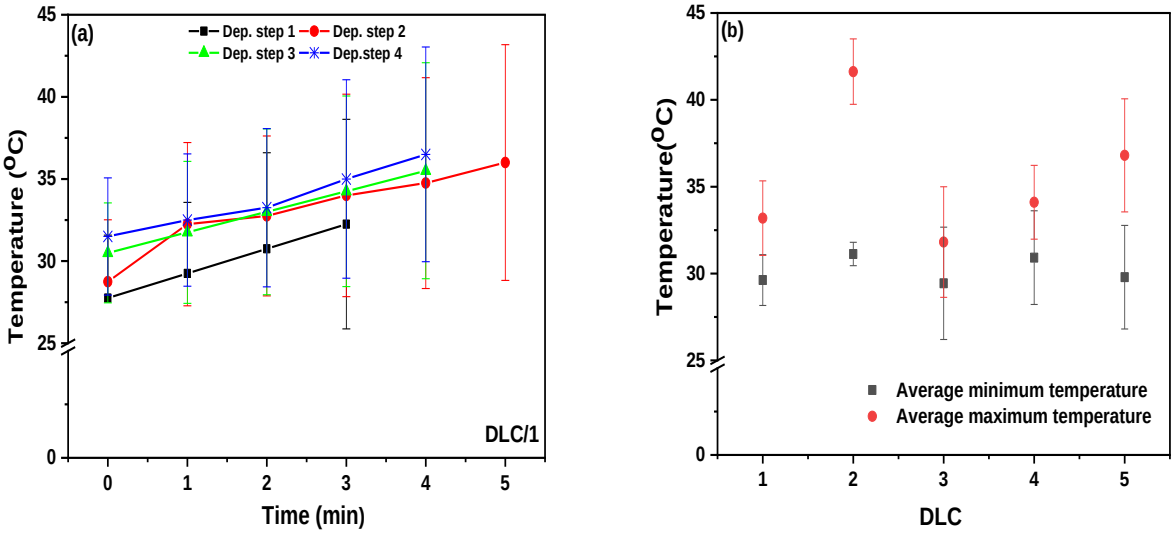

Figure 5-7- Plot showing the (a) temperature evolution during deposition leg for DLC/1 with plots showing each deposition step made to deposit the DLC coating (b) combine average minimum and maximum temperature attained for each DLC coating during coating.

Thus, considering the difference between the maximum and minimum temperature of about 10 ℃ and a heating rate of 2 ℃/min, it will take between 7-8 mins to attain the maximum permissible temperature

of 46 ℃. The highest heating rate of 4.62 ℃/min was recorded for DLC/5. This could be partly due to the micro-wave source working at full power (1050W), thus emitting maximum thermal radiation flux to the substrate or through ion particle flux to the substrate.

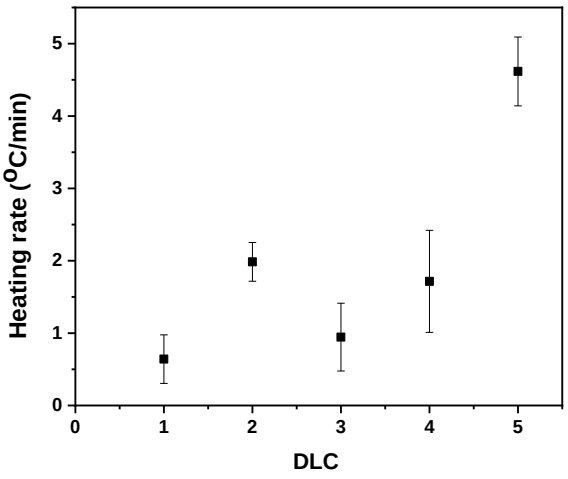

Figure 5-8- Plot showing the average heating rates for DLCs 1-5

5.6.2 Deposition rate

The deposition rate for the modified DLC coating was similarly measured using the step height technique described in Chapter 3 with the 2D contact Talysurf PG1800 profilometry scanner. However, further validation of the coating thickness was performed using an SEM. The deposition rates for each of the five individual DLCs and their corresponding coating thickness are detailed in Figure 5-9 and Figure 5-10 respectively. To access accurately the deposition rates and total thickness on each sample for the different DLC films, 5 individual substrates from both 3D ABS and Verogray were measured for their thicknesses.

To prevent the samples from overheating, the individual deposition times were varied based on the response to the temperature build-up on the substrate, hence the individual rates do not exactly match the coating thickness in some cases. The highest deposition rate recorded for all five DLCs was 7.4µm/hr for DLC/1 with the lowest being DLC/5 at 1.8 µm/hr. For a similar deposition time of 15mins, recorded for both DLC/5 and 3, the deposition rate was seen to almost have doubled from 1.84 to 4.2 µm/hr.

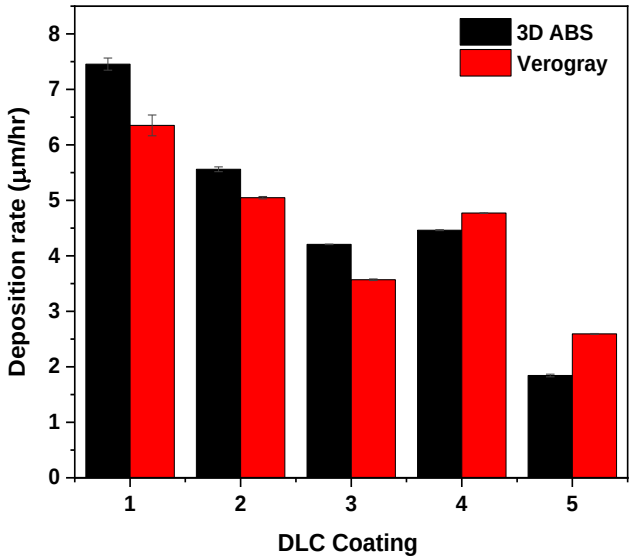

Figure 5-9- Deposition rate for modified DLC coatings.

The corresponding coating thicknesses for all DLCs are summarized in Figure 5-10. The thickness measured varies from 0.5 - 2 µm for 3D ABS and 0.8 – 1.7 µm for Verogray using similar deposition steps and rates for each deposition cycle. The variation observed between coating thickness and substrate material shows limited variation in measured error for most of the DLCs deposited in this study. It is interesting to note that, in all cases except for DLC/4 and 5 where the opposite was the case, the coating thickness increases on 3D abs when both substrates are compared under similar deposition conditions.

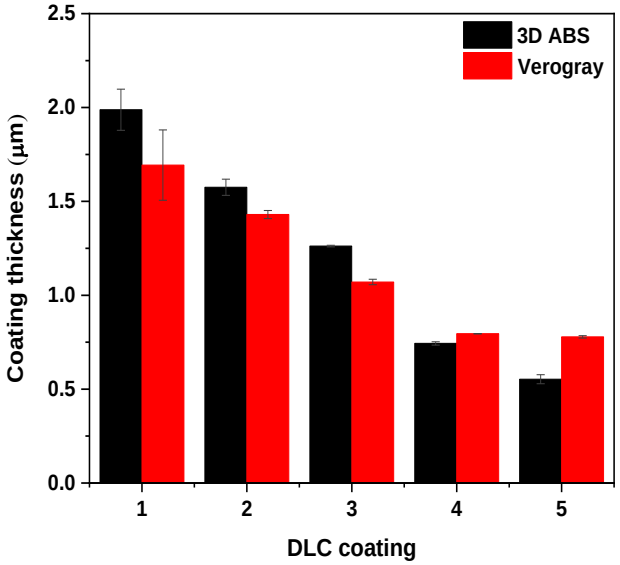

Figure 5-10- Coating thickness for modified DLC coatings.

5.7 Modified DLC coating adhesion

The adhesion of the modified DLC coatings is assessed for their critical loads (L_c) of failure using the Tribotechnic macro scratch tester as detailed in Chapter 3. The experimentally observed modes of failure in the scratch test are described in this section.

5.7.1 Surface energy and wetting

Surface energy is a useful characterisation tool for defining the adhesion properties at the surface compared to the bulk material. When adhesion of polymers with other forms of organic and inorganic coating structures become necessary, chemical interaction between the bonding species at the interface resulting in covalent bonding is essential. This means it is necessary to have the presence of highly reactive functional group sites on the polymer surface during the build-up of coating on the surface. Surface wettability based on the measurement of the polymer surface contact angle response to drop shape was conducted to quantify the surface energy of the polymer surface. Surface treatment using Ar^+ plasma on polymer surface like any other plasma treatment has shown to promote surface ablation, crosslinking and activation. The yield of these so-called dangling bonds resulting from the surface treatment is defined by the exposure time and plasma power. Figure 5-11 shows the measured contact angle for both pristine and plasma surface etched polymer surface after 3mins of exposure to Ar^+ plasma. As can be seen, the water contact angle measurement for the untreated pristine surfaces for both 3D ABS and Verogray was 40 ° and 58 ° respectively. However, after 3mins of Ar^+ plasma exposure, the respective contact angles (c.a) of both samples were further reduced to 22 ° and 17 ° for both 3D ABS and Verogray.

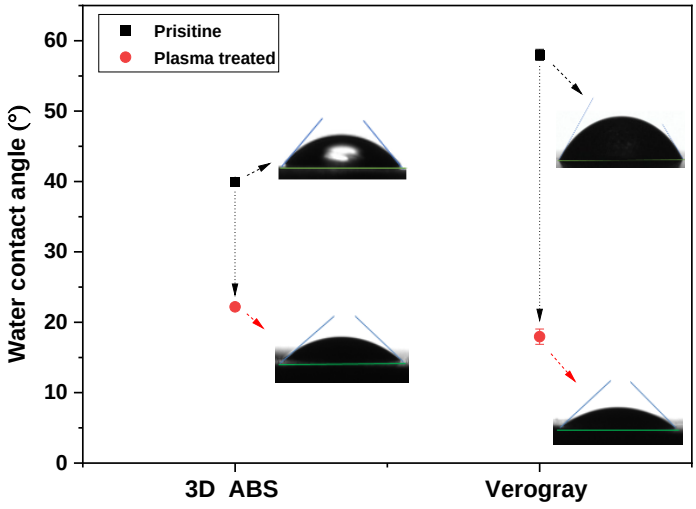

Figure 5-11- Water contact angle measurement for both pristine and plasma surface etched after 3mins for 3d printed ABS and Verogray.

Polymers, in general, have low surface energy, poor wettability and coating adhesion on surfaces are extremely poor after printing. Apart from the advantageous removal of surface contaminants through Ar bombardments, several authors have shown that surface treatment of polymer may lead to the increase in OH functional group which upon exposure to the atmosphere may react with air and water [122, 249, 255]. Carley [122] noted that this change may result from the OH group concentration on the polymer surface and would be traceable by measuring the contact angle of deionised water on the surface. He later observed a decrease in the c.a on virgin ABS when treated with Ar^+ plasma. Jeon et al. [255] in the metallization of PET polymer with Cu showed that pre-treatment is a condition for attaining stronger adhesion. Lambare et al. [256] also explained that the combination of chemical and topographic modification of polymer surface using PSE treatment pre-coating enhances adhesion and mechanical anchoring to the functionalised polymer surface after Ar^+ plasma treatment. They further noticed a positive correlation between surface wettability and adhesion strength when ABS, ABS/PC and PEEK polymers were treated in an argon plasma for 2 min. This is self-evident in the c.a results obtained before and after PSE treatment that after the PSE treatment, surfaces possess much higher surface energy as a result of their improved hydrophilicity.

5.7.2 Scratch test

Coating failure on polymer systems has often been used to explain surface conditions underpinning the mechanisms characterizing the failure modes for polymer-coating systems. The outcome of the individual scratch test for all five DLCs deposited onto both 3D ABS and Verogray are shown in Figure 5-12 to Figure 5-16 and Appendix II. The 200 µm Rockwell diamond tip radius test comes with the series of multiple failure mechanisms observed as critical failure points of the coating on the substrate. As Ollivier & Matthews [257] noted, coatings failure occurs at different modes owing to the substrate and coating properties. They further defined these coating failure points along the scratch length as critical loads (L_c). For this work, the critical coating failure points observed along the scratched length are defined by L_c1, L_c2 and L_c3 (where L_c1, L_c2 and L_c3 are the initial, second and final critical loads respectively.). A representation of some typical failure modes is presented in Figure 5-12 and Figure 5-13. All scratch tests data presented in this study are an average of three repeats.

In all cases resulting in coating failure, the applied progressive load scratch direction was from left to right, resulting in the plastic deformation of the coating and substrate as a result. The majority of the shape and failure produce suggest a predominantly tensile control damage regime with coating failure occurring on the leading edge of the scratch tip. As load is increased from 0-20N, the frequency of cracks developing on the coating surface increases and are defined by their critical load points of failure until complete deformation is attained defined by cross spallation at the region with maximum shear stress. From Figure 5-14, the critical loads of the individual DLCs are shown. Despite all coated DLC

samples undergoing similar test conditions, they performed differently. With the introduction of nitrogen gas, the initial critical loads of failure defined by L_c1 was lowered for all coating except DCL/1.

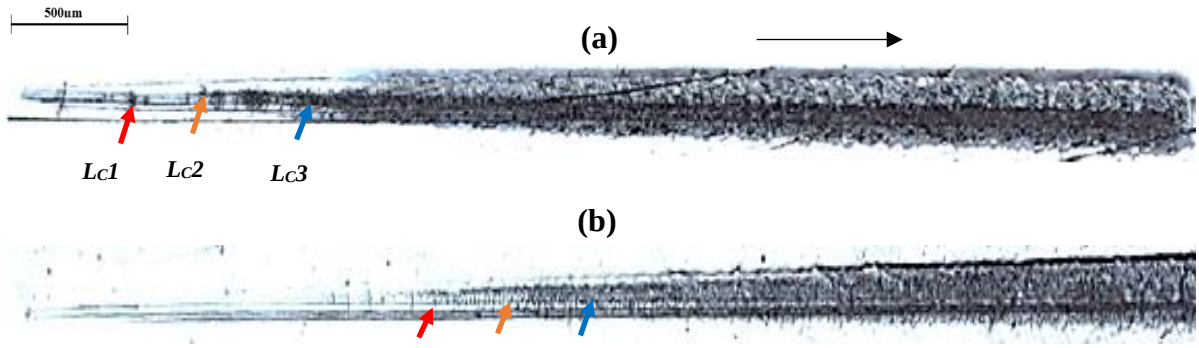

Figure 5-12- Typical failure mode of DLC/1 coatings on pristine additively manufactured (a) ABS (b) Verogray. Black arrow shows scratch direction.

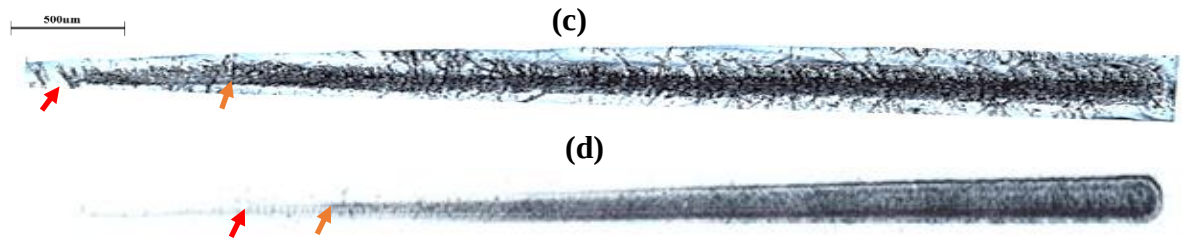

Figure 5-13- Typical failure of DLC/2 coating on pristine additively manufactured (c) ABS and(d) Verogray.

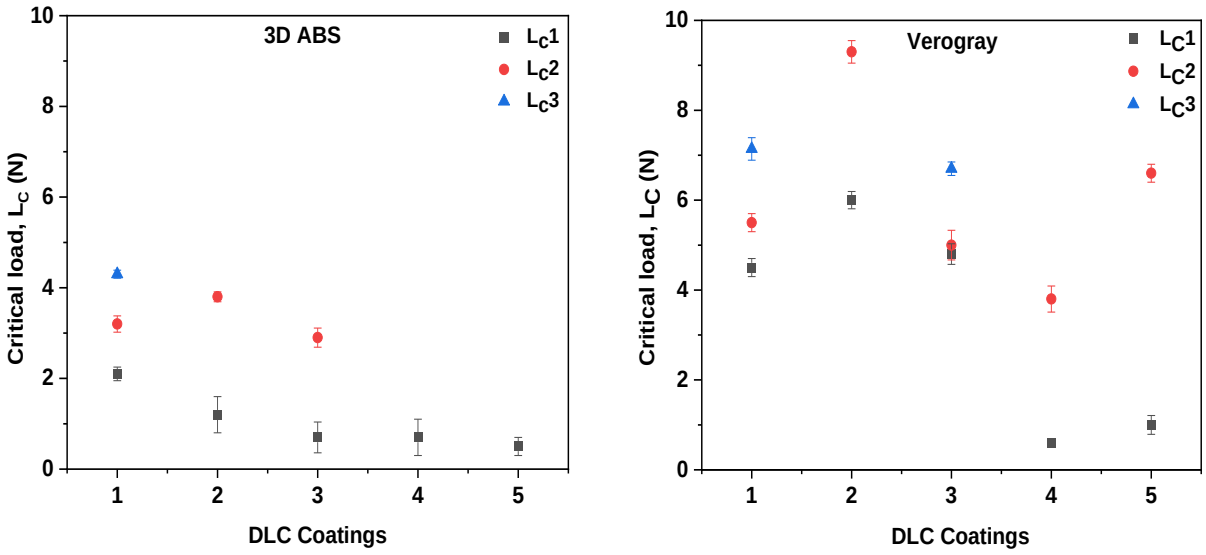

Figure 5-14- Shows the Individual critical loads defining the coating deformation regimes for DLC/1-5 for unpolished 3D ABS (a) and Verogray (b).

For 3D ABS, the sequence of reduction for DLC/1- 5 for L_c1 was 2.1>1.2>0.7=0.7>0.5N respectively. However, even though similar trends were observed for 3D Verogray except for DLC/2, the initial critical loads for DLC/1-3 were the highest when compared with 3D ABS. The sequence observed for 3D Verogray for L_c1 was 4.5<6>4.85>0.6<1N for DLC/1 to 5 respectively. Olliver and Matthews [257] noted that, when a compressive load was applied on both hard and soft surfaces, the resulting pressure at the contact is consequently low if the contact surface is soft as compared with a harder surface. Hence, if a certain pressure is needed at the contact area between the coating and film to induce a shear stress large enough to cause coating failure, then this yield pressure will be attained at lower loads for harder coatings than for the softer coating; as a consequence, the critical load for softer coating will be greater than that of the harder coating. Therefore, on average, it is right to say, DLC/1 produces the softest coating in the entire design based on the adhesion performance on both polymers.

To understand the effect and limitations surface roughness play in the adhesion performance of both 3D ABS and Verogray samples, all samples were polished to attain an R_a of 38.5±2nm surface roughness as detailed in Chapter 3. Similar coatings were deposited, and their failure modes assessed in Figure 5-15 for DLC/1 and 2 and Appendix II for DLC/3-5.

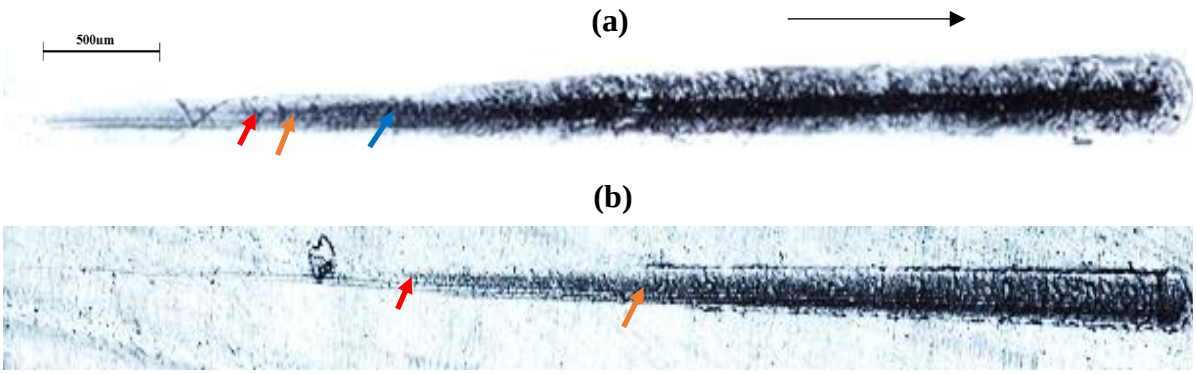

Figure 5-15- Typical failure mode of DLC/1 coatings on polished 3D printed (a) ABS (b) Verogray. The black arrow shows scratch direction.

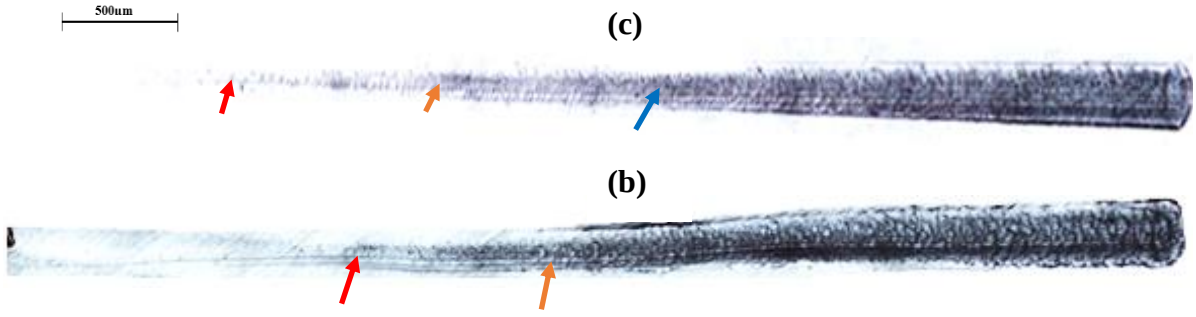

Figure 5-16- Typical failure mode of DLC/2 coatings on polished 3D printed (c) ABS (d) Verogray. The black arrow shows scratch direction.

It was noted that the overall adhesion performance for both polished 3D ABS and Verogray coated samples were improved in comparison with their pristine unpolished counterpart. The observation of the fracture damage behaviour even though delayed in some cases show similar plastic tensile deformation with coating failure occurring also on the leading edges of the Rockwell diamond tip. The critical loads of failure are presented in Figure 5-17 for both 3D ABS and Verogray. DLC/1 coating on polished 3D ABS showed improved response to shear load damage from a 2.1N to 4N. For the same coating, there was an improvement of 37 % for Verogray from 4.5N to 7.14N. The highest critical load observed for DLC/1 coating for both samples was at 11N. This represents the second critical load after which complete deformation of the coated substrate is attained for Verogray polished samples. As discussed previously, it can be seen that for the introduction of nitrogen, there is a downward decline in the performance of the DLC coatings on polished Verogray. In comparison with ABS polished samples, there was a marginal increase of 1N for DLC/2 from a starting L_c1 of 4N for DLC/1, but this however declined further for DLC/3 and 4. That notwithstanding, it can be seen that Verogray provide better adhesion for both cases of polish and unpolished substrates.

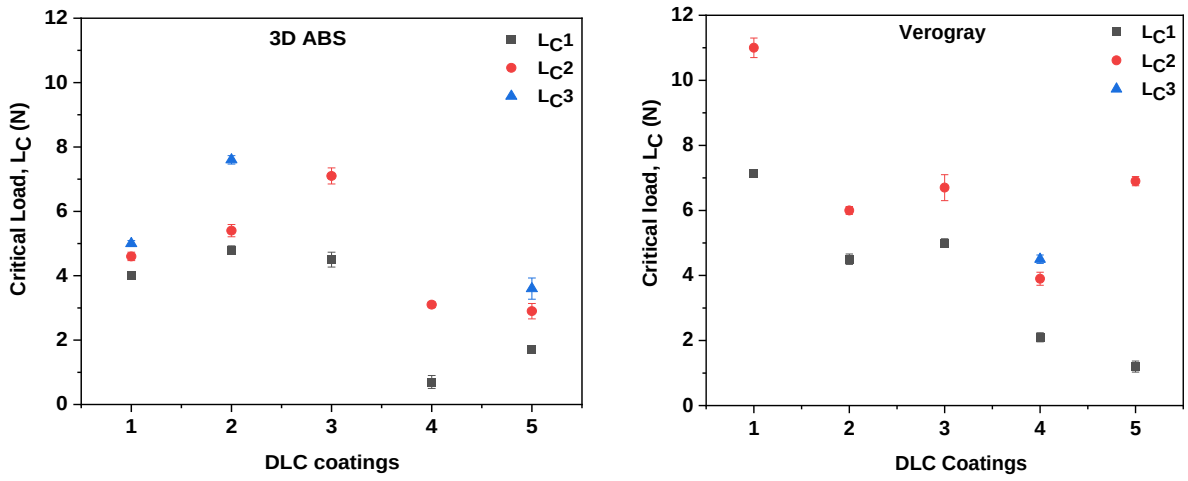

Figure 5-17- Shows the Individual critical loads defining the coating deformation regimes for DLC/1-5 for polished 3D ABS (a) and Verogray (b).

5.8 Coating fracture toughness

The resistance to coating failure during bending through the initiation and propagation of cracks within highly stressed coating for both textured and untextured coated polymers is morphologically examined. By using a 3-point bend test as described in Chapter 3, the coating failure detailed response for the different textured surfaces, namely textured A and B are presented.

5.8.2 Coating failure

In this technique, the progression of crack patterns during the 3-point bending is monitored as a function of the applied load to the individual coated surfaces. Figure 5-18 shows a typical flexural curve of the 3D printed polymer-coated surface under flexural load where the distribution of bending observed at first hand is linear as predicted by the linear theory, however, as the curvature increases, the polymer is seen to kink, thus localizing the bending. Wiggins *et al.* [258] attributed this behaviour to the signature of non-linearity softening at high curvature.

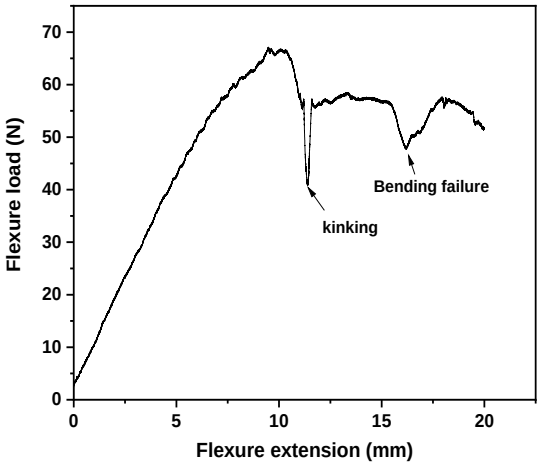

Figure 5-18- A typical flexure curve of 3D- polymer showing the kinking and bending failure of the crack during its propagation.

To reveal the extent of coating damage amongst the individual coated substrates during bending, the failure mechanism is discussed through observing the cracked morphology after bending by using a 4K Ultra-High Accuracy VHX-7000 series digital microscope, which is shown in Figure 5-19 to Figure 5-22 and Appendix III. It can be observed that in all cases regarding the Verogray samples, the in-situ optical micrograph shows no coating deformation in the form of cracking regardless of the coating thickness, DLC coating type and surface texture variation used. This, in turn, indicates a strong adhesion bonding in the coating-substrate interface. This means the energy released during the transverse loading or 3-point bending of the individual coated samples is significantly less than the fracture toughness of the individual coated DLCs and hence no fracture is formed as a result.

In the case of the coated 3D ABS substrates, the predominant failure regime was characterised by coating cracking at the polymer-coating interface. As can be seen, the deformation and crack propagation through both textured and untextured surfaces at the saturation of the fragmentation test, show varying coating responses to the applied flexural load. It was observed that for DLC/1 coating, the fracture formed were characteristically continuous with uninterrupted propagative crack pattern terminating at specific intersection junctions defined by other levels of surface crack irregularities. It is

very telling to note that, these termination points are preferentially nucleated at specific sites where there is a change in the surface morphology or contouring as seen in both textured surfaces defined in Figure 5-19 (b) and (c).

In DLC/2, the characteristic deformation pattern observed after the test shows a highly stressed coating with a mixture of surface buckling and crack deformation patterns. For textured surface A and B coated substrates for 3D ABS, a clear distinction could be made regarding the coating deformation regime. Figure 5-21 (b) show limited surface fragmentation in the form of coating cracking, however, surface regions primarily restricted to the trough areas (denoted as 'a' on Figure 5-21 (b)) of the corresponding peaks, show a rather highly stressed section in comparison with the peak textured areas on the surface. However, for the textured B surface, the coating damage is seen to be dominated by surface cracking with sections of the cracked region showing complete spallation.

Similarly, the comparative morphological study of DLC/3 on 3D ABS show similar surface coating deformation to DLC/2, but with a far-reaching deformation pattern extending to the peak heights of the textured surface. However, it was observed that for the same coating on 3D ABS textured B surface, only limited regions of the coated surface showed a crack deformation pattern where crack formation run perpendicular to the transverse load.

For DLC/4, it was shown that for the untextured surface, extensive 'brick-like crack surface patterns were distributed along the entire substrate surface with high-stress regions shown as surface wrinkles and coating buckling. On both textured surfaces A and B, similar deformation patterns in the form of micro-cracks oriented parallel to the transverse load are observed. However, for DLC/5 the deformation was seen to be randomly distributed and highly chaotic with interspersed cracking patterns. A detailed surface scan of both 3D ABS and Verogray surfaces of which is extensively discussed in Chapter 6 show widespread coating defects in the form of nano and micro pit-like structure present on the surfaces of 3D ABS of which can be attributed to the coating failure when under severe flexural extension. Additionally, it can be seen that for most cases involving textured surface A for 3D ABS, the primary deformation pattern observed after bending was the presence of highly stressed thin-film showing extensive residual stress state formed due to the imbalance of the bending moment from the minimal stress state of the coated surface after deposition. This stress state produces extensive buckling and surface wrinkling of the coated surface consequently as a result of the highly deformed surface. For textured surface B, it was largely seen that the predominant surface deformation condition was limited to the development of cracks. However, in all cases showing coating failure amongst the individual textured and untextured surfaces, no coating delamination failure was observed after bending.

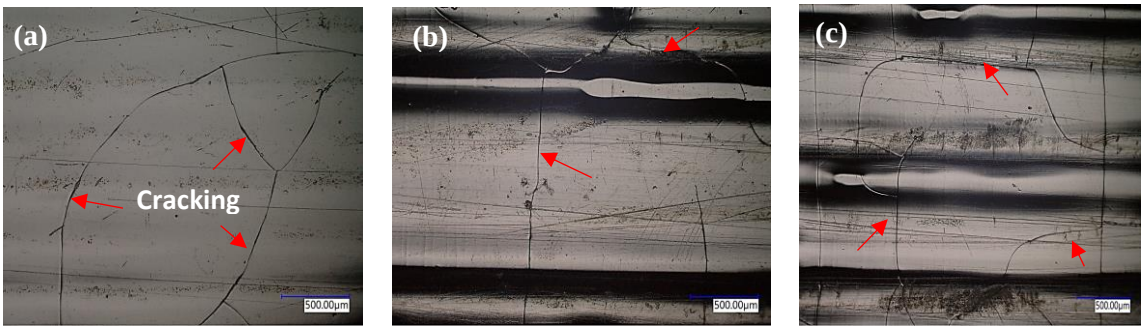

Figure 5-19- Cracking behaviour of DLC/1 coating on 3D ABS after bending showing coating deformation pattern on all three surfaces defined as (a) untextured coated surface (b) textured type A (c) textured type B.

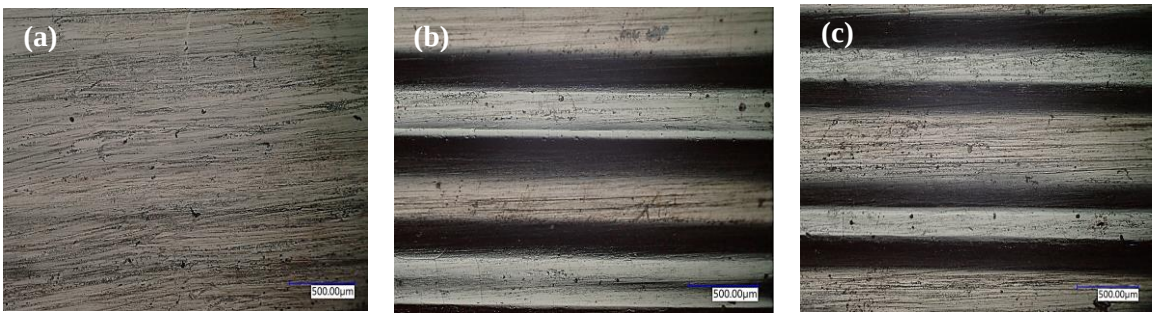

Figure 5-20- Morphology of DLC/1 coating on 3D Verogray showing no surface deformation after bending on all three surfaces defined as (a) untextured coated surface (b) textured type A (c) textured type B.

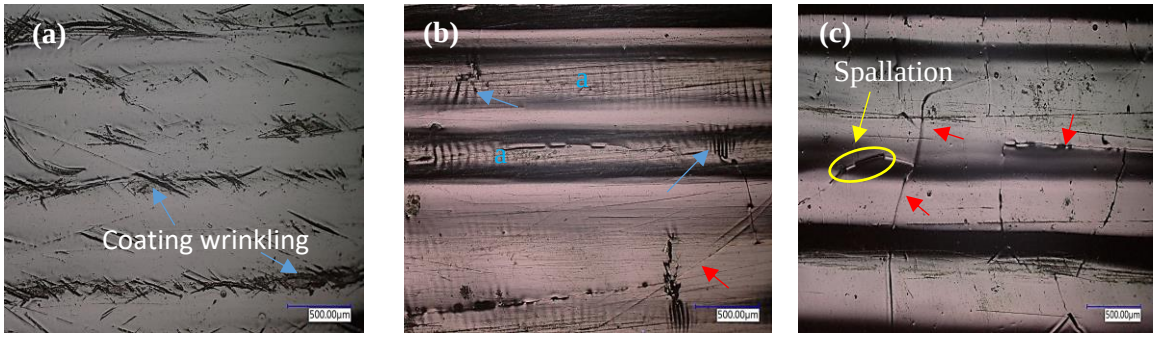

Figure 5-21- Coating deformation behaviour exhibited by DLC/2 coating on 3D ABS after bending showing coating deformation pattern on all three surfaces defined as (a) untextured coated surface (b) textured type A (c) textured type B.

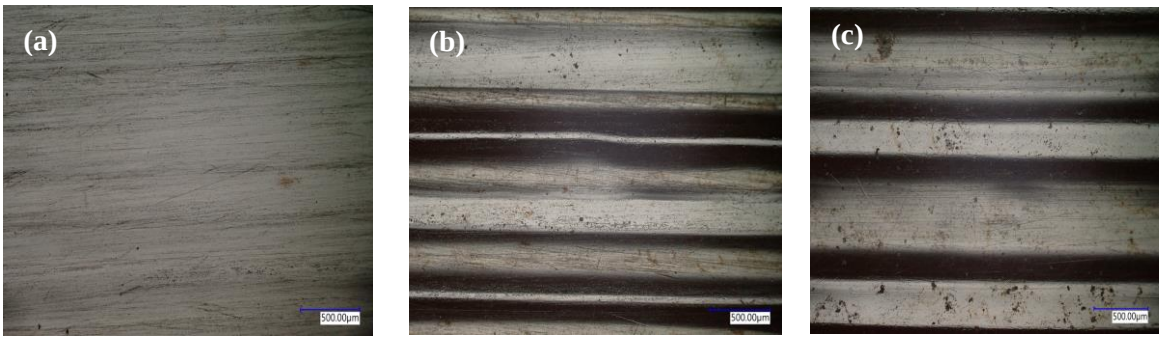

Figure 5-22- Morphology of DLC/2 coating on 3D Verogray showing no surface deformation after bending on all three surfaces defined as (a) untextured coated surface (b) textured type A (c) textured type B.

5.8 Summary

Low-temperature MW-PECVD technique has been successfully used in the deposition of DLC films below 46 ℃. To allow sufficient coating thickness to develop, several deposition steps with complimentary off duty cooling cycles lasting an hour were implemented to minimise the thermal heat load within the deposition chamber. The qualitative surface morphology analysis of the initial DLC coatings reveal the presence of highly stressed surfaces characterised by the presence of irregularly dispersed coating crack patterns on all coated substrates. In analysing the adhesion property of the individual coatings using scratch testing, complete coatings failures were observed for progressive loads of 0-5N. For some DLC coatings, compressive stress generated after coating could reach up to 10GPa [250] resulting in poor adhesion and coating delamination through cracking. To mitigate this problem, interlayers and elemental doping using nitrogen are regularly used [250] to increase the adhesion strength by promoting sp^2 clustering sites. With a modified DLC coating structure, the gas flow rates of nitrogen and C_2H_2 were varied at constant micro-wave input power. For this modified coating design, 5 different DLC coatings were synthesized and deposited onto both 3D ABS and Verogray. Further adhesion tests with the modified coating showed improved coating adhesion performance under 0-20N.

Chapter 6

Results & Discussion: Coating structure and composition

6.1 Introduction

This chapter presents a detailed analysis of the 5 individual coating structures produced using the MW-PECVD technique as described in Chapter 3. A cross-section analysis of the coating using SEM imaging is presented. Further correlation between the compositional, structural and mechanical properties of all coatings is made.

6.2 Coating structure

The 5 individual coatings analysed were cast in resin and polished to mirror finish after curing to expose the cross-section view of the coating. The cross-sectional view of the coated samples obtained using the Hitachi SEM is shown in Figure 6-1, with each coating structure sandwiched between the polymer substrate at the bottom and resin at the top. As the resin dries and begins to set around the coated polymer, it is expected that the adhesion between the resin and DLC coating may produce some form of tensile stress at both interfaces, especially between the resin and coating.

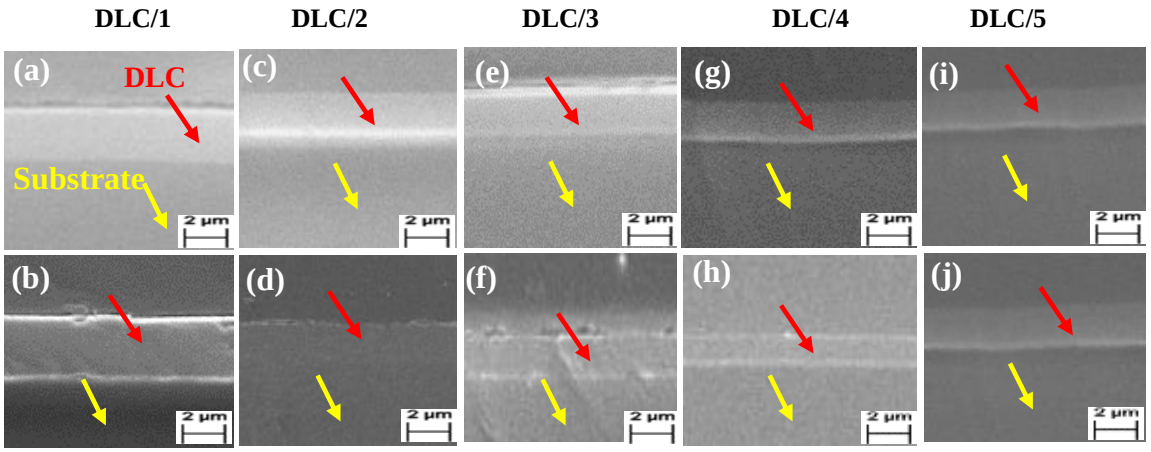

Figure 6-1- Cross sectional SEM image showing coating thickness properties on both 3D ABS and Verogray substrates. Cross section shown as (a),(c),(d),(e),(g),(i) represents 3D ABS samples coated under DLC/1-5 respectively. Samples (b),(d),(f),(h),(j) represents Verogray coated samples for DLC/1-5 respectively.

These stress accumulation at the interface may be large enough to overcome the adhesive strength of the coating with the polymer, however, the scratch test results show adequate adhesion of the coating of which the impact from the resin is assumed to be less than the adhesion between the coating and polymer. The respective images show a uniform and well-distributed DLC coating with good adhesion on the polymer substrate.

6.3 Atomic force microscopy (AFM)

The surface characterization at the nanoscale, using an atomic force microscope (AFM) has proven to be a useful tool in offering both quantitative and qualitative information about material surface properties. Material quantitative properties such as height and surface roughness can easily be probed without damaging the fibrillar architecture of the surface [259]. Figure 6-2 to Figure 6-5 provide a detailed surface qualitative morphological description of both uncoated and coated surfaces for both 3D ABS and Verogray. For all figures presented, the detailed comparative AFM surface scan showing the material surface properties pre and post coating is made evident. The 3D topography image reveals a more homogeneous surface with very low colour variation and contrast, which reveals the uniformity of surface features on both substrates. However, as a general observation, for the coated 3D ABS sample in (a), Figure 6-4 (a) and Figure 6-5 (a), the distinction depicted by the colour contrast is self-evident to prove the variation in the surface feature [260]. An important surface feature observed typically with the 3D ABS is the presence of macro and micro pit like defects structures shown in Figure 6-2 for both uncoated and coated samples respectively [261, 262]. It was evident for the DLC/1 coated 3D ABS sample that similar surface features were still visible after coating the surfaces. This shows the coating coverage on the substrate is controlled by the surface feature to which the coating mirrors the exact surface contours of the pristine surface. As further observed, the differences in peak height values and spread over the entire surface of the Verogray sample for both coated and uncoated samples show a more heterogeneous surface compared with 3D ABS when coated with functional DLC film.

A summary plot showing the quantitative depth-sensing profile for both coated samples are presented in Figure 6-6. Figure 6-6 further captures the percentage depth distribution for each substrate studied from the micro to nanoscale range before and after coating. For this analysis, a 10µm x 10µm scan area was analysed using the NanoScope AFM software. A comparison of the individual depth profile distribution for both pristine and DLC/1 coated substrates show observable changes in the micro and nano-cavities range where a shift from a predominantly high depth to a lower depth range distribution. However, DLC/2 coated substrate showed a significantly broader range of microcavities range after deposition. For all DLC/3 coated substrates, there was a shift in the peak positions band for the depth profile distribution, where 3D Verogray showed a higher proportion depth band distribution. A similar analysis for both DLC/4 and DLC/5 samples was attempted, but for poor resolution from the raster scan, no results for the two coatings were presented.

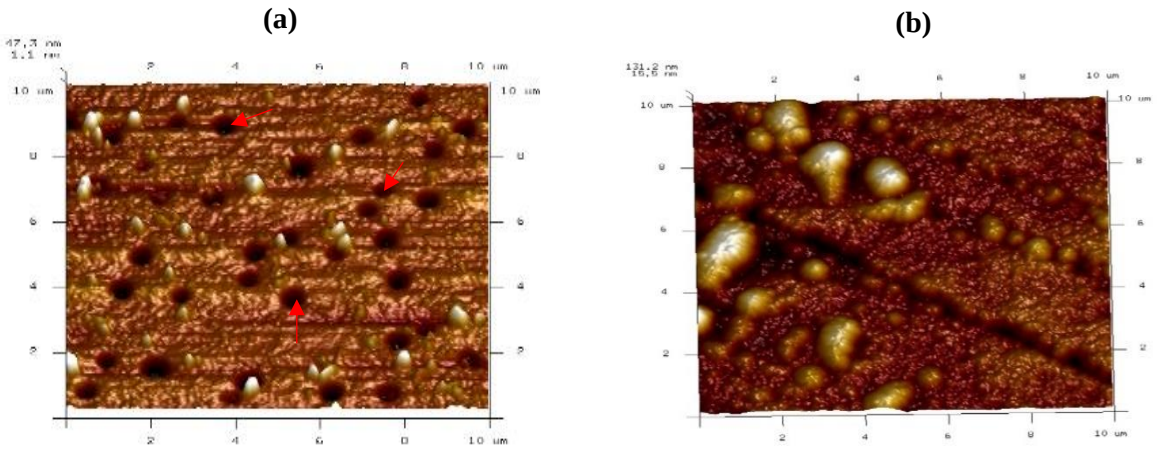

Figure 6-2- AFM Image of uncoated samples showing 3D printed ABS (a) and Verogray (b). Red arrows indicate surface defects in the form of micro and macro-pits on polymer surfaces.

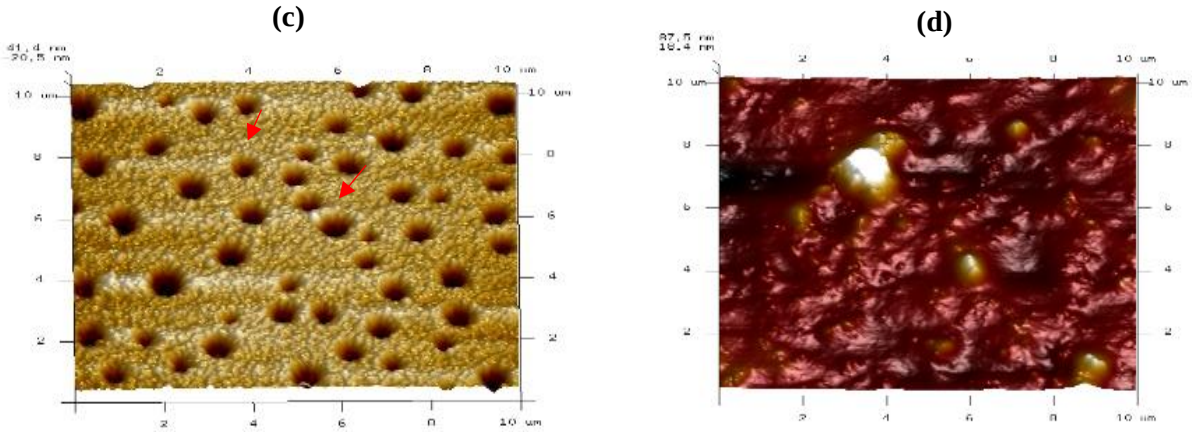

Figure 6-3- AFM image of DLC/1 films deposited on (c) 3D ABS and (d) Verogray.

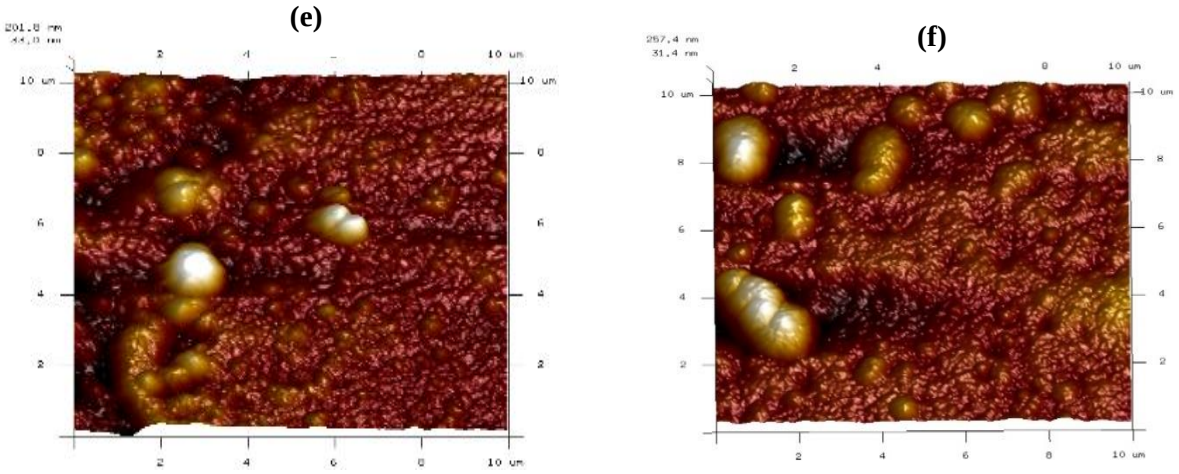

Figure 6-4- AFM image of DLC/2 film deposited on 3D ABS (e) and Verogray (f).

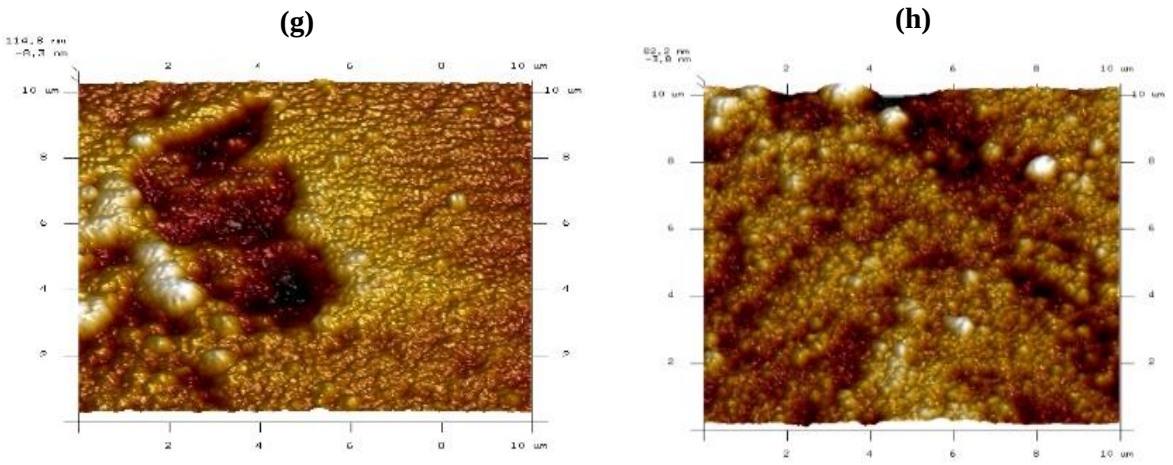

Figure 6-5- AFM image of DLC/3 film deposited on 3D ABS (g) and Verogray (h).

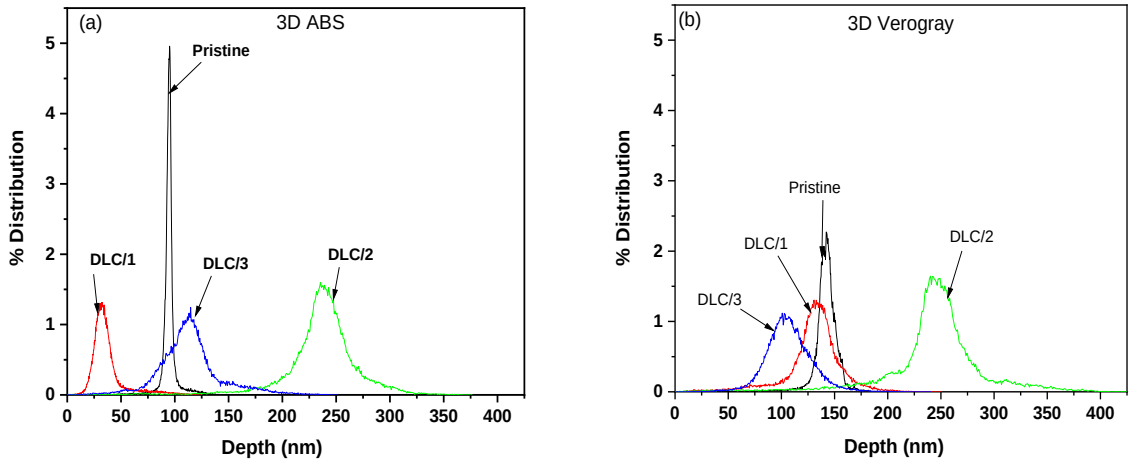

Figure 6-6- AFM surface scan showing quantitative depth-sensing of substrate nanoscale cavities for 3D printed ABS (a) and Verogray(b) for all coated and uncoated samples.

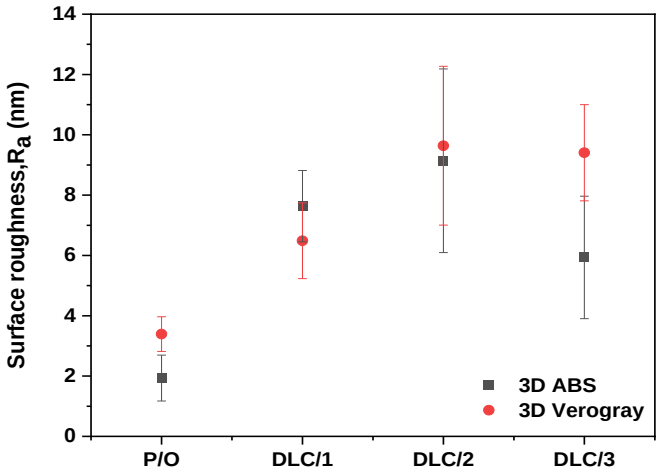

Figure 6-7- Surface roughness quantification using AFM scan of the individual surfaces. P/O is the pristine uncoated 3D printed samples. DLC/1, DLC/2, and DLC/3 are the coated samples deposited with 0, 10 and 20sccm of nitrogen flow.

The average surface roughnesses of both coated and uncoated surfaces are presented in Figure 6-7. For all samples studied, the average surface roughness value of the uncoated substrates was much lower than their coated counterparts. The average surface roughness on the uncoated 3D ABS and Verogray samples were 1.9 and 3.4 nm respectively. However, by the application of functional DLC coating films onto the 3D polymer surfaces, the average surface roughness increased sharply. With the increment of nitrogen incorporation from 0 to 10sccm for DLC/2, the average roughness increased from 7.63 to 9.13nm for 3D ABS and 6.48 to 9.63 nm for Verogary.

Commonly, it has been noted that surface morphology variation arising from surface roughness in DLC coatings are affected by the surface species migration, graphitic crystallization, surface bombardment of energetic particles and surface temperature [263]. Most prominently are the molecular ion and neutral species incident at the film surface which breaks into atomic ions and energy on impact [260]. These neutrals consist of an undissociated precursor gas, mono-radicals, for instance, CH_3, di-radicals and others contribute to the mass growth of the film rather than the molecular ions alone [260]. Several authors have noted that the growth rate of a-C:H films decrease with temperature increase [260, 264, 265]. The initial research conclusion was that this was as a result of the weakly adsorbed neutral species which would desorb from the film at higher temperatures [264, 265] but Kessels *et al.* [266], von Keudell and Jacob [267, 268] noted that contrary to the desorption theory of atomic neutrals exclusion at higher temperatures, dependence in film growth at higher temperatures is as a consequence of atomic hydrogen etching effect. The atomistic growth of film in itself is independent of temperature [260]. Aarão Reis and Franceschini [269] in a study of the deposition and erosion model feature of carbon-nitrogen film growth under PECVD observed an increase in surface roughness of the a-C:N:H film with increasing nitrogen content. They further noted that this increment in surface roughness was a consequence of the erosion driven behaviour facilitated by N_2^+ ion bombardment. Similarly, Silva *et al.* [270] observed an increase in surface roughness with increasing nitrogen incorporation, which is shown to be related to the film growth kinetics during deposition [270]. Prioli *et al.* [271] in an investigation of both the friction coefficient and surface roughness of an a-C:N:H using an AFM showed a similar increment in the surface roughness value by a factor of two for an 11% nitrogen content increase.

6.4 Nano-Indentation

The mechanical properties of both uncoated and coated substrates are studied using nanoindentation technique to determine the properties of both 3D ABS and Verogray substrates before and after coating. The nanoindentation response for as-deposited DLC coatings and the corresponding pristine substrate are shown in Figure 6-8 and Figure 6-10. For both conditions, the depth dependence on hardness is shown.

6.4.1 Polymer hardness properties

Figure 6-8 shows the hardness profile as a function of indentation depth (nm) for both substrates. At all measured depth between 100 and 600 nm, Verogray showed higher material hardness properties as compared with 3D ABS. As the indentation depth increases, both substrates recorded lower hardness values with Verogray showing the most significant reduction with depth whereas 3D ABS showed a relatively consistent hardness value across the entire indentation depth profile with reduced standard deviation (shown as error bars). These responses in hardness measure are mostly attributed to the roughness effect possessed by the individual substrate surfaces. With the hardness depth profile response shown, typically, for the Verogray samples, it is very difficult to define the precise length scale-dependent deformation, since the explanation for such ordered decline could be complex in certain polymers and may be related to heterogeneity in the material properties with depth, friction and surface effect properties.

Similarly, by monitoring the length scale deformation of the polymer substrate, the Young's modulus for the pristine substrates were all determined using the Berkovich diamond tip nanoindenter as detailed in Chapter 3. It was observed that at all depths, Young's modulus for Verogray was larger than the 3D ABS sample (Figure 6-9). However, exceptions could be made also at 600 nm depth where both materials exhibit similar elastic modulus properties. As with the hardness measure for the two 3D polymers (Figure 6-8), Verogray measurement at different depth are within the measured 1σ value with depth. Meaning, for the two substrates studied, the indentation substrate effect (ISE) on the two coated polymers should perform similar at indentation depths where their 1σ value remains same.

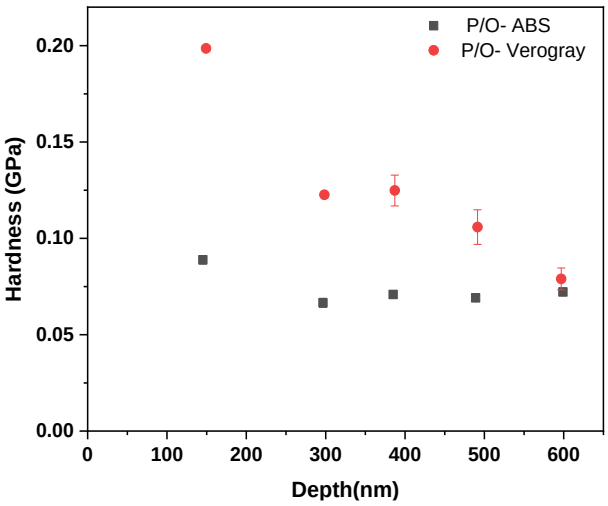

Figure 6-8- Hardness of pristine (P/0) 3D ABS and Verogray at different indentation depths.

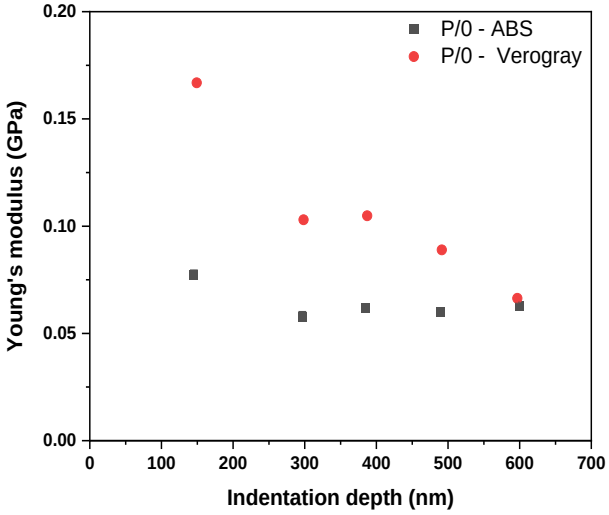

Figure 6-9- Young's modulus for pristine (P/0) 3D ABS and Verogray polymers measured at different depths.

6.4.2 DLC composite hardness

Figure 6-10 shows the hardness measured for all DLCs coatings produced on both 3D ABS and Verogray substrates at depths equivalent to 10% of the coating thickness. The normalised indentation depth of 10 % coating thickness was used to minimize the substrate effect [272]. Both coated substrates characteristically showed a similar surface hardness trend in all but one of the DLC coatings where the hardness for Verogray exceeded that of 3D ABS in the case of DLC/5. On both substrates, the hardest coating was produced for DLC/3 coating structure. By comparing both coated substrates for DLC/3, it was observed that 3D ABS showed the highest coating hardness of 4.1 GPa compared to 3.1 GPa measured for Verogray. The softest coating produced was DLC/5 with a corresponding hardness of 2.0 GPa and 2.3 GPa for 3D ABS and Verogray respectively. It was observed that, as the nitrogen gas flow rate increases from 0 sccm in DLC/1 to 10sccm in DLC/2 and finally to 20 sccm in DLC/3, the coating hardness increases as a result. However, as the acetylene gas flow rate was reduced by 50 % to 310sccm (Chapter 5) with similar nitrogen gas flow rates at 10 and 20 sccm for DLC/4 and 5, a reduction in the coating hardness was observed for all 3D coated samples. For DLC/2 and 3 coated samples for Verogray, the coating hardness measure was seemingly close in value at 3.1 GPa and 3.2 GPa for DLC/2 and 3 respectively. Similarly, the corresponding Young's modulus for the individual coated substrates are presented in Figure 6-11. For the coated substrates, it is evident that similar trends could be observed for the individual Young's modulus value experimentally determine

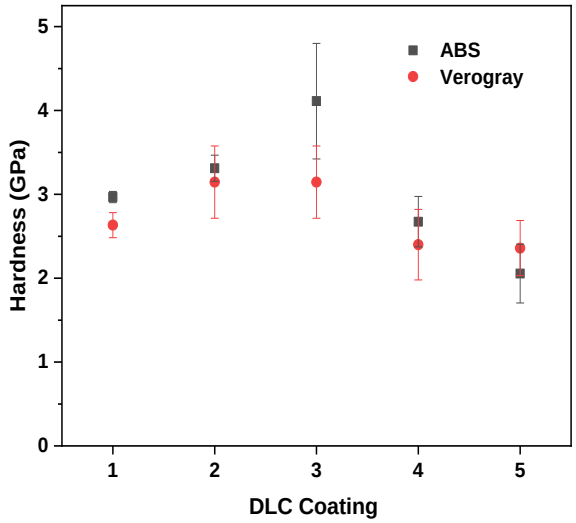

Figure 6-10- Hardness values of DLC coating structures on both 3D ABS and Verogray substrate.

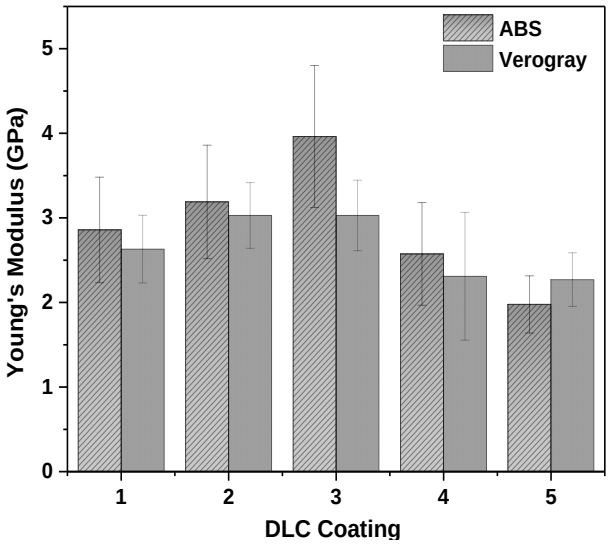

Figure 6-11- Young's modulus of MW-DLC coated samples.

6.5 Raman spectroscopy

The central focal point of any amorphous carbon film is the hybridization of the carbon atom. For a large fraction of sp^3 dominated carbon atom in a well cross-linked a-C:H film, an improvement in the film hardness is achieved as a result. However, the main concern arises with the hybridization state of carbon atoms when the structure is incorporated with nitrogen. Several authors have reported a decline of the sp^3 C atomic fraction when nitrogen is incorporated as a precursor during deposition [273, 274, 275]. Raman spectroscopy as among other useful structural characterization tools provides useful information about the structural quality of diamond, graphite, DLCs and carbon nanotubes. For this work, Raman spectroscopy was used to characterize the film quality produced by the MW-PECVD

technique (Figure 6-12). As in a-C:H and a-C:N:H films, the main structural features are the broad peaks shown as the 'D' and 'G' bands present in the non-crystalline graphitic carbon material. Both 'D' and 'G' peak modes correspond to the fundamental breathing modes of sp^2 -C atoms in rings (A_{1g} mode) and E_{2g} mode of graphite in the bond disordered chain structure stretch [274, 275]. Figure 6-12 shows the Raman spectra of the DLC films grown at different nitrogen and acetylene flow rates. In the spectrum of carbon film with no nitrogen gas flow (DLC/1), a strong peak centred at approximately 1533cm^{-1} and a broad peak at 1320cm^{-1} are observed for ABS coated substrates and similarly, a 1531 cm^{-1} and 1319 cm^{-1}, referring to the so-called 'G' and 'D' peak modes respectively was recorded for Verogray coated samples. With the introduction of nitrogen gas, for example, in the case of DLC/2, the spectra intensities for both G and D peaks remained fairly similar to that of DLC/1 for Verogray, where both peak band responses showed a positive shift in the Raman intensities from 1531 cm^{-1} to 1533 cm^{-1} for the G peak and 1319 cm^{-1} to 1320 cm^{-1} for the D peak band respectively. However, for 3D ABS, the spectra shift for the D peak was slightly intensified from 1320 cm^{-1} to 1329 cm^{-1}. Tables 6-1 and 6-2 show the summary Raman shifts intensities for all DLCs coated on both 3D ABS and Verogray. The shift in both 'D' and 'G' bands corresponds to the changes in the film structure towards a more sp^2 clustering C atom [249]. Menegazzo *et al.* [166], noted similarly a variation and decrease of the full width at half maximum (FWHM) of the G-band upon the addition of nitrogen to a DLC structure. Figure 6-12, is indicative of the broadening feature band manifestation of the D-peak between 1100 cm^{-1} and 1600 cm^{-1} for DLC films incorporated with nitrogen flow during the deposition process. Schwan *et al.* [276] and Stan *et al.* [260] both noted that this broadening feature observed between these wave limits is a result of the manifestation of the presence of monocrystalline diamond-like cluster of sp^3-C atomic bonding.

Table 6-1- Raman data showing 'D' and 'G' peak intensities for DLC films 1 to 5 produced using MW-PECVD technique on 3D ABS.

DLC/1	D-peak position	G-peak position	I_D/I_G
1	1320	1533	0.43
2	1329	1534	0.33
3	1327	1534	0.31
4	1336	1537	0.17
5	1322	1531	0.28

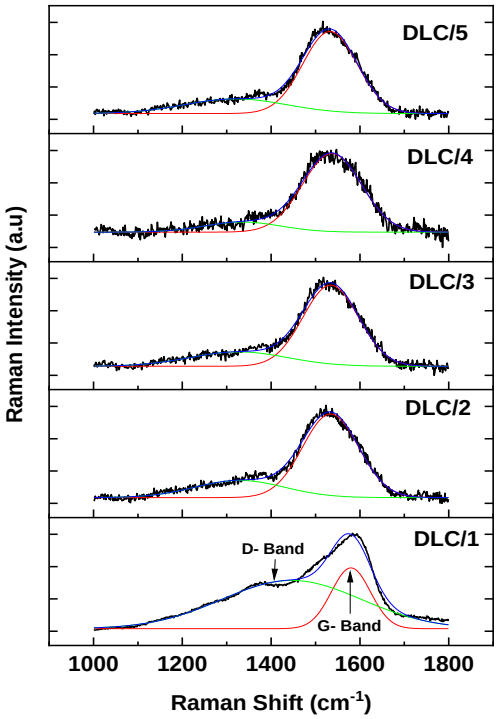

Figure 6-12- Raman spectra of DLC films grown at different nitrogen and acetylene gas flow rates.

The position and width of both D and G band ratios also known as I_D/I_G ratio after spectra deconvolution fitting of the integrated areas under both peaks provides a useful correlation between the sp^3 and sp^2 bonding ratios within the amorphous film [260, 277]. In both Table 6-1 and Table 6-2, the calculated I_D/I_G ratios are presented. I_D/I_G ratios were calculated as a ratio of the D to G peak after spectra fitting. A decrease in the I_D/I_G was observed as the gas flow of nitrogen changes with that of the acetylene gas flow rate suggesting an increase in the ordering of the sp^2 bonded graphitic domain. However, for a higher sp^3 content, the opposite is observed in the I_D/I_G ratio, which should be noticeable in the form of a harder coating.

Table 6-2 - Raman data showing 'D' and 'G' peak intensities for DLC films 1 to 5 produced using MW-PECVD technique on Verogray.

DLC	D-peak position	G-peak position	I_D/I_G
1	1319	1531	0.27
2	1320	1533	0.28
3	1326	1534	0.20
4	1317	1536	0.13
5	1317	1532	0.33

6.5.1 Correlation between coating hardness and I_D/I_G

To determine the accuracy of the I_D/I_G ratio as a measurable quantification of the DLC coating film hardness, a correlation of the hardness measured using nanoindentation and I_D/I_G ratio which is a measure of the sp^3/sp^2 bonding ratio [260] are presented. As shown in Table 6-1 and Table 6-2, increasing the nitrogen gas flow rate from 0 to 10 sccm is shown to decrease the I_D/I_G ratio for the nitrogen-doped DLC with a corresponding increase in the DLC film hardness from 3 to 3.3 GPa for 3D ABS and 2.6 to 3.2 GPa for Verogray samples (Figure 6-13). With a further increase in the nitrogen gas flow rate from 10 sccm to 20 sccm, a reduction in the I_D/I_G ratios were recorded for the DLC/2 coating on both substrates. As further detailed in Figure 6-13, the I_D/I_G ratio and hardness are weakly interrelated. Nevertheless, the correlation suggests that the increase in coating hardness is a result of the increased sp^3 content of the film.

Although a greater number of authors have observed decreases in the stress release for most DLC films by the incorporation of nitrogen, the observable mechanical hardness behaviour has shown a widespread performance due to the sp^3 and sp^2 cluster function [273].

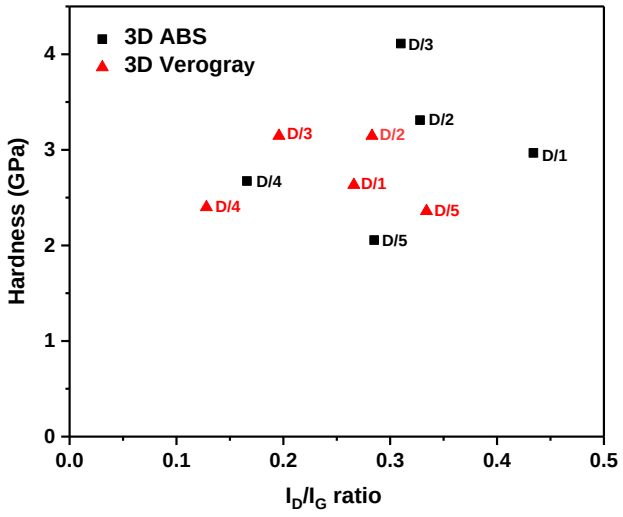

Figure 6-13- Correlation between I_D/I_G and hardness.

Albeit, on the simple phase of increasing nitrogen flow into the deposition chamber, one would expect a decrease in the mechanical hardness of the thin film [273, 249, 278], however, the reverse was observed when the nitrogen gas flow rate was increased. Thus, further investigation of the coating to confirm doping and quantification of nitrogen in the DLC film to be able to validate the relationship between the I_D/I_G ratio and the hardness were required.

6.6 X-ray photoelectron spectrum (XPS)

To validate the I_D/I_G ratio to hardness claim presented in the fore mentioned section (6.5.1), it was necessary to perform an elemental composition analysis using XPS spectroscopy to determine the

presence or otherwise of N1s within the DLC thin films and their binding state. Figure 6-14 shows the percentage atomic concentration of both C1s and N1s binding states as a function of coating depth. In addition to the surface scan, two different scans corresponding to coating depths of 10 nm and 100 nm were performed. The atomic concentration of C1s was found to increase with depth until a maximum peak is attained at 100 nm. For DLC/1 and 2, this concentration was seen to be lower compared with DLC/3 and 4. Most importantly is the N1s atomic percentage concentration plot shown in Figure 6-14 (b). It was observed that for both DLC/1 and 2 films, the atomic concentration for N1s binding state was unchanged even at a higher flow rate. The higher atomic percentage fraction observed in DLC/1 could only be possible due to the precursor gas used for the deposition. Acetylene gas possesses enormous advantages over other precursor gases utilised in plasma deposition such as benzene, butane and methane. Acetylene, however, has high ionisation potential at low pressures, simple dissociation paths given $C_2H_n^+$ off mainly ions and less polymerisation [279]. However, one of the biggest disadvantages identified with the use of acetylene is the possession of high nitrogen impurity content [102, 107]. Weiler *et al.* [280] after depositing ta-C:H using acetylene gas noted a 4 % atomic N_2 content present within the acetylene based DLC film which they attributed to impurities in the acetylene gas. By increasing the nitrogen gas flow rate from 10sccm in DLC/1 to 20 sccm in DLC/2, significant changes in the percentage nitrogen concentration were observed for DLC/3 film. This change was the lowest atomic concentration for N1s in all the DLCs synthesized for this work. Even though internal stress reduction has always been observed upon nitrogen incorporation in an amorphous DLC coating, its hardness has shown a considerable spread in experimentally determined behaviour. Even though some authors have shown stable mechanical hardness properties for nitrogen-doped DLCs [279, 281], different authors have reported decreases in the mechanical hardness behaviour with increasing nitrogen incorporation in an a-C:N:H film [102, 282]. Booktul *et al.* [253] noted that the doping of nitrogen in DLC film tends to reduce the sp^3 content and promote the clustering of sp^3 bonding sites, thus decreasing the mechanical properties of the film. This means the hardness decreases with increasing nitrogen content as shown in the I_D/I_G ratio versus hardness plot (Figure 6-13) [253, 279, 283].

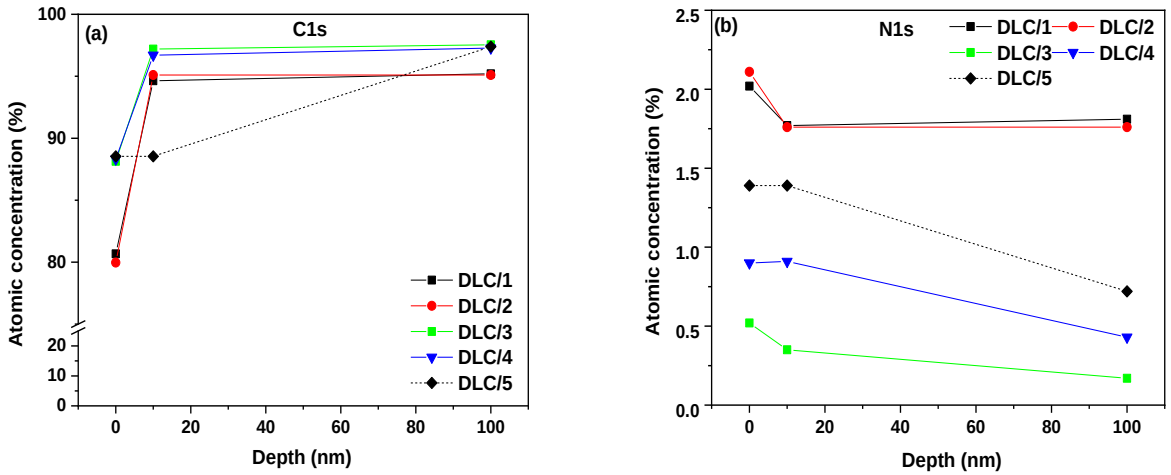

Figure 6-14- C1s and N1s atomic concentration as a function of depth for (a) Carbon and (b) Nitrogen.

6.7 Summary

In this chapter, the coating structure and composition are assessed. A cross-sectional view through the individual coatings showed a well bonded and uniformly distributed coating structure on the polymer structure. An AFM surface scan for the uncoated substrate showed varying observable surface irregularities with the most prominent feature being the presence of pit-like defect structures present on the 3D ABS polymer surface. These observable surface defect structures were shown to remain persistent on DLC/1 coated 3D ABS. However, in the case involving DLC/2 and DLC/3 coatings, a more uniform surface structure with no observable pit-like surface defects were shown. The hardness measure of the uncoated samples showed decreasing hardness profile with depth due to the complex heterogeneity in the material properties due to factors such as friction, surface effect properties etc. The highest coating hardness was observed for DLC/3 coatings deposited on 3D ABS. Raman analysis of the individual coatings provided key quantification of the effect of nitrogen gas flow rates on the I_D/I_G ratio in relation to coating hardness performance.

Chapter 7

Results & Discussion: Friction and wear

7.1 Introduction

Friction and wear are important ingredients in material characterisation for the durability of engineered parts using the Polyjet technique, however, little work has been accomplished in the characterisation of such additively manufactured parts. By investigating their friction and wear response under varying loads, the true sense of their tribological properties could be well understood. In this chapter, a comprehensive study of the frictional and wear behaviour of photocurable Polyjet modelled parts namely ABS-digital (3D ABS) and Verogray are investigated. The effect of surface finished defining on both material surface roughness and print orientation on the wear and frictional behaviour for both coated and uncoated substrates are studied. This study may be beneficial where sliding mating contact between two surfaces composed of either polymer-on-polymer or a non-polymer-on-polymer are involved.

7.2 Friction

7.2.1 Time frictional response for uncoated additively manufactured polymers

As detailed in the experimental methodology (Chapter 3), the friction tests were performed under compressive loads in a reciprocating unidirectional plane parallel (X_1-X_2) and perpendicular (Y_1-Y_2) to the print orientation axis. All friction data presented are an average of three repeats as shown in Appendix VI. From the individual imposed velocity and normal applied load, the coefficient of friction (μ) as a function of time has been computed. The time frictional response for both 3D ABS and Verogray at constant applied normal loads of 1, 5 and 10N are shown in Figure 7-1.

On the macroscopic scale, the friction coefficient behaviour of both parallel and perpendicular orientations shows varying friction responses. In Figure 7-1 (a) and (b), it can be observed that the friction coefficient behaviour for 3D printed ABS show an extended running-in period for both parallel and perpendicular orientations where in both cases the friction coefficient value increases with time before reaching a steady-state value. At this stage the self-lubricating property of the polymer becomes apparent. Sood *et al.* [170] in a similar study using FDM additively manufactured ABS part, identified

a similar coefficient of friction response with time. They further noticed that the surface asperities of the test samples contributed significantly to the initial variation and sudden increase in the coefficient of friction value during the start of the test. However, as the surface asperities progressively become plastically deformed and are removed from the contact surface, the variation in the coefficient of friction becomes stable over time. Recent work by Wang *et al.* [284] also provides similar evidence in support of this phenomenon for PTFE, PR, UHMWPE, and PEEK at a constant load of 10 N. By comparing the frictional response for 3D ABS at different applied loads (Figure 7-1 (a) and (b)), it can be observed that both parallel and perpendicular orientations showed progressively decreasing overall coefficient of friction value with increasing load. The large fluctuations and drastic increase in the coefficient of friction value with time as observed in Figure 7-1 (b) for the perpendicular orientation correlate with the viscoelastic deformation of the surface asperities. For the perpendicular to print orientation coefficient values, a maximum peak value of 1.48 was attained as against a reduced value 0.96 for the parallel to print orientation at 1N. The running-in period where the lowest coefficient of friction value is obtained is self-evident for both parallel and perpendicular orientations to the applied load wherein in both cases, there is clear evidence of change in friction performance to material orientation. Similar distinctions were observed in the case of Verogray material, however, the effect of surface anisotropy was self-evident when a 1N load was applied perpendicular to the print orientation.

It was observed that by changing the surface orientation to the applied normal load from parallel to perpendicular at 1N, the coefficient of friction value for both Verogray and 3D ABS were both altered from 0.87 ± 0.13 to 0.91 ± 0.29 and 0.95 ± 0.02 to 1.23 ± 0.07 respectively. This shows a positive correlation between surface texture density, surface roughness and frictional performance at lower loads where plastic deformation is seen to play a dominant role in the CoF value as compared to a flat surface where little or no resistance to motion is encountered.

It is a common phenomenon in polymer tribology to see a direct proportionality between frictional force and applied load as defined by Amonton's law of friction [147], however, at certain loads, this proportionality breaks down [148]. For the 1N case, it was shown that the sequence of the coefficient of friction evolution with time (as shown in Figure 7-1 (c) and (d) for Verogray produced a characteristic delayed pattern followed by a sudden spike in the coefficient of friction value before reaching a steady-state regime. This delayed phenomenon was highly pronounced within the first 10 mins of the test when the orientation to applied load was perpendicular to the raster direction (Figure 7-1 (d)). Larsen [285] has shown that a higher coefficient of friction may be observed as a result of stronger interfacial adhesion or high elastic and plastic deformation of surface asperities.

At moderate loads of 0.02 to 1N, Larsen [285] again noted that the friction coefficient decreases with increasing load as a result of the elastic deformation of surface asperities. Myshkin *et al.* [148], however, explained that contrary to the elastic deformation of the surface asperities at lower loads, on the other

side of the proportionality range lies the plastic deformation region where the coefficient of friction increases with increasing load. This was further explained by Kragelskii [152], where he demonstrated that at higher loads i.e. above 1N the friction coefficient passes the minimum elastic deformation point into the plastic zone where the friction coefficient increases with increasing applied load.

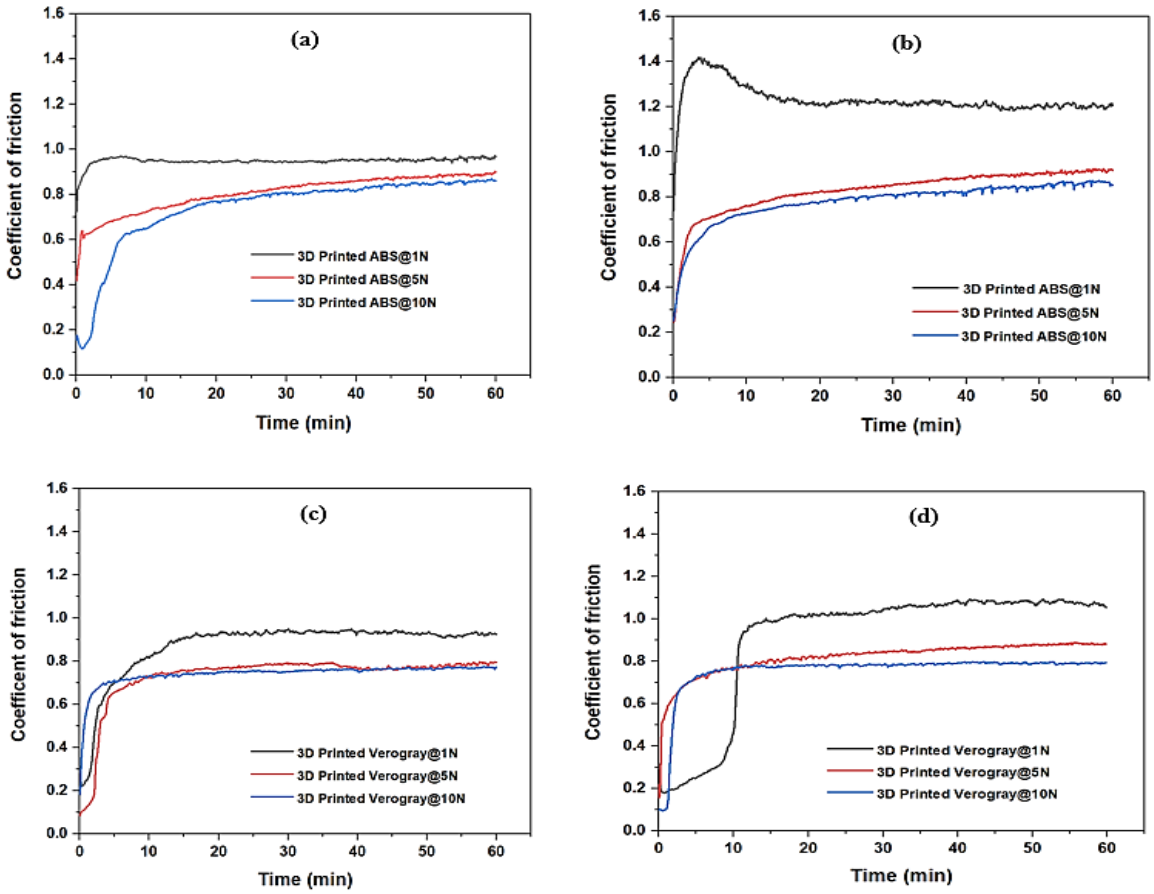

Figure 7-1- A comparative plot showing the variation of friction coefficient behaviour under varying contact load and print orientation: (a) parallel to print for 3D ABS (b) perpendicular to print orientation for 3D ABS (c) parallel to print orientation for 3D Verogray (d) perpendicular to print orientation for 3D Verogray.

At higher loads (i.e. 5N and 10N), the gradual progressive response was seen to be less dominant in both parallel and perpendicular print orientations for the Verogray samples. 3D ABS, on the other hand, showed a more pronounced and distinctive delayed separation CoF plot at 5 and 10N under parallel to print orientation until a steady-state regime is attained. Both plots show a similar CoF value after 20 mins into the test. The phenomenon was less visible under perpendicular to print orientation where there was no apparent distinction between the CoF value at 5 and 10N. Sooter and Tabor [149] observed that at constant loads of 10 to 100N, the CoF value remain constant after the running-in period where for instance in the case of polyvinyl chloride (PVC), the CoF was measured at 0.35-0.45. Similar conclusions were made in a tribo contact between a 6.5 mm radius steel ball bearing, polyethylene (PE)

and polyvinylchloride (PVC) under applied compressive loads from 2 to 15N [150, 286]. This suggests that the applied load is sufficient to cause maximum plastic deformation of the surface asperities, thus shifting the deformation mechanism from predominantly adhesive friction controlled to deformation friction-controlled regime. Larsen [285] also showed a good correlation between the coefficient of friction and interfacial adhesion resulting from high elastic and plastic deformation of surface asperities.

Thus, it is justified to conclude that because of the plastic deformation of the surface asperities at higher loads (5 and 10N), the friction coefficient is independent of surface orientation but material bulk property.

7.2.2 Time frictional response for DLC coated additively manufactured polymers

Similarly, the time-dependent frictional response for the coated polymers substrates was evaluated to ascertain their performance under 1 and 5N loads in both parallel and perpendicular orientations to the print direction. Three DLCs were tested, namely DLC/1, 2 and 3. Figure 7-2 shows the contact response for both 3D ABS and Verogray substrates with respect to DLC/1 coating. Similarly, each experiment was repeated thrice to ensure good repeatability of results. For the CoF response to both parallel and perpendicular orientation plots for 3D ABS (Figure 7-2 (a) and (b)), the frictional response was seen to be highly dependent on the orientation to the applied loads. For the perpendicular orientation at 1N load, the running-in period showed a progressively increasing CoF response with irregular fluctuations until a maximum peak was attained at 0.55. This was followed by a progressive drop in the CoF until a stabilised regime is attained at around 0.37. In comparison with the parallel to print orientation shows a more stable CoF regime throughout the test duration. From the 5N Load plot, it was evident that both orientations showed similar CoF responses over the entire test duration. However, at the commencement of the tests, it was shown that the CoF was uniformly stable and independent of time until such a point where it begins to progressively increase to a stable maximum regime. For the Verogray DLC/1 coated samples (Figure 7-1 (c) and (d)), the plots show a relatively uniform CoF regime for both parallel and perpendicular orientations at 1 and 5N. However, at 1N the perpendicular to print orientation plot showed a slight increase in the CoF trend which later become stable.

It was further observed that, by changing the coating structure from DLC/1 to DLC/2 (Figure 7-3), the CoF response at 1 and 5N loads for 3D ABS in the perpendicular orientation followed a similar trend with time. By changing the surface orientation from perpendicular to parallel, no significant differences were observed between the CoF performance at 1 and 5N loads. Similar distinctions were observed in the case for Verogray sample under both loads and surface orientations.

The DLC/3 frictional response for both coated 3D printed ABS and Verogray are presented also in Figure 7-4.

For the perpendicular to print orientation for 3D ABS, a progressively increasing CoF trend was observed for both 1 and 5N plots where at 5N, a higher CoF response was observed. At 1N load, however, the CoF response was seen to be progressively less dominant as compared to the applied load at 5N. For the parallel orientation, similar trends were observed for the 5N load with less progressively stable trend observed for the 1N load. In the case involving 3D coated Verogray, the CoF response for both applied loads (1 and 5N) showed distinctive responses with time, where at 1N, the CoF was seen to be fairly stable after an initial rise. This, however, was followed by a second peak rise in the CoF trend until a stable regime was attained at about 0.6. A comparison with the 5N load shows a much higher CoF response with an uninterrupted progressive rise in the CoF value. However, in comparison with the parallel orientation plot, the CoF for the perpendicular orientation plot showed greater frictional force instability, characterised by the unstable depiction in the CoF trend with time (Figure 7-4).

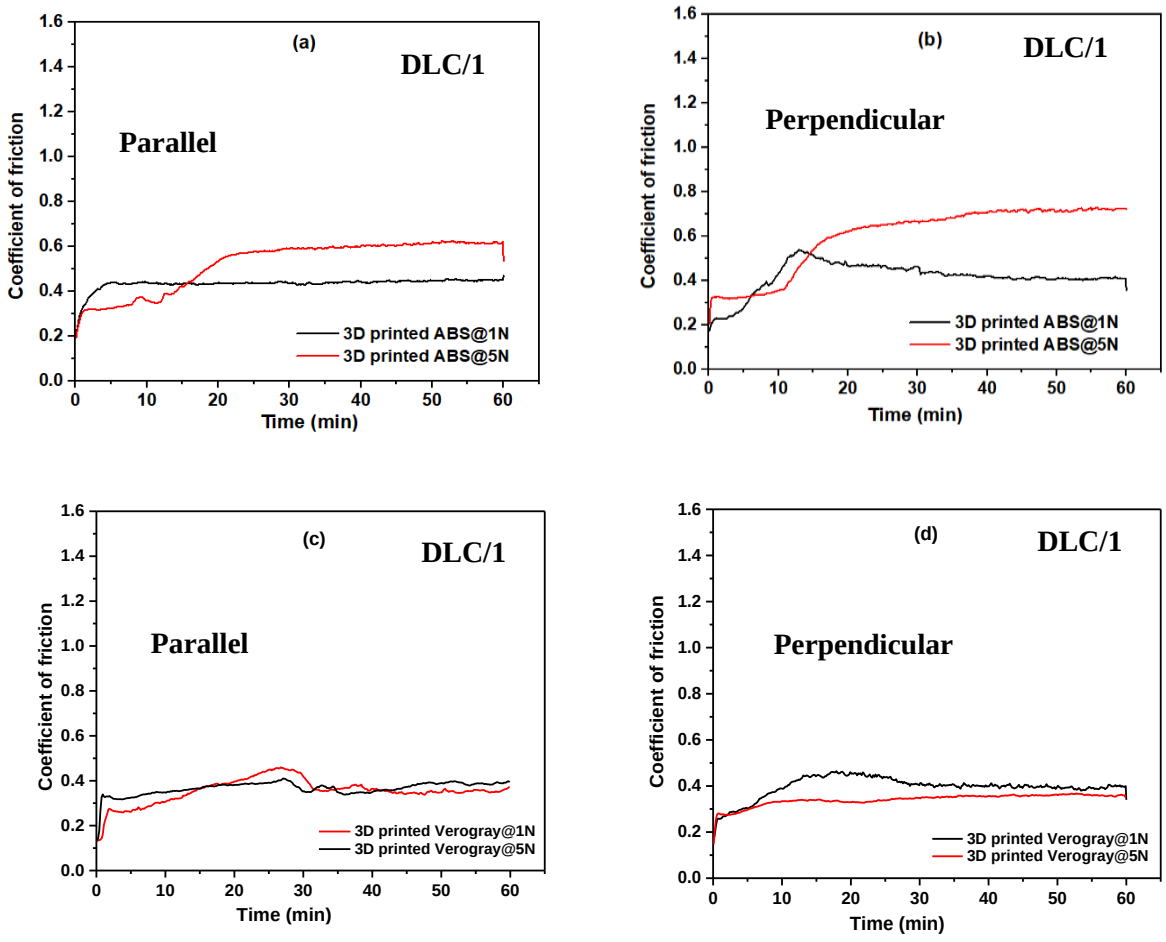

Figure 7-2- A comparative plot showing the variation of friction coefficient behaviour under varying contact load and print orientation for DLC/1 coated polymers: (a) parallel and (b) perpendicular to print orientation for 3D printed ABS, (c) parallel and (d) perpendicular to print orientation for 3D printed Verogray.

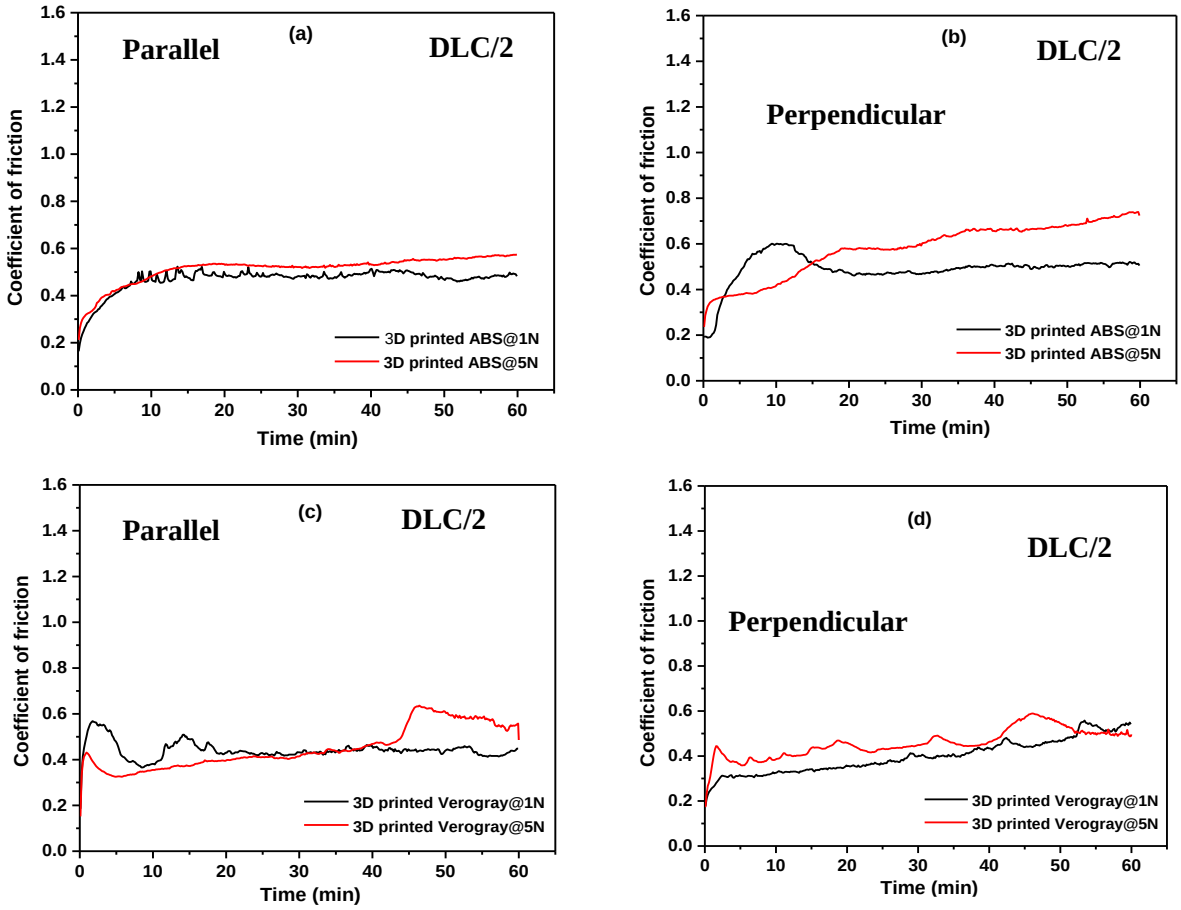

Figure 7-3- A comparative plot showing the variation of friction coefficient behaviour under varying contact load and print orientation for DLC/2 coated polymers: (a) parallel and (b) perpendicular to print orientation for 3D printed ABS, (c) parallel and (d) perpendicular to print orientation for 3D printed Verogray.

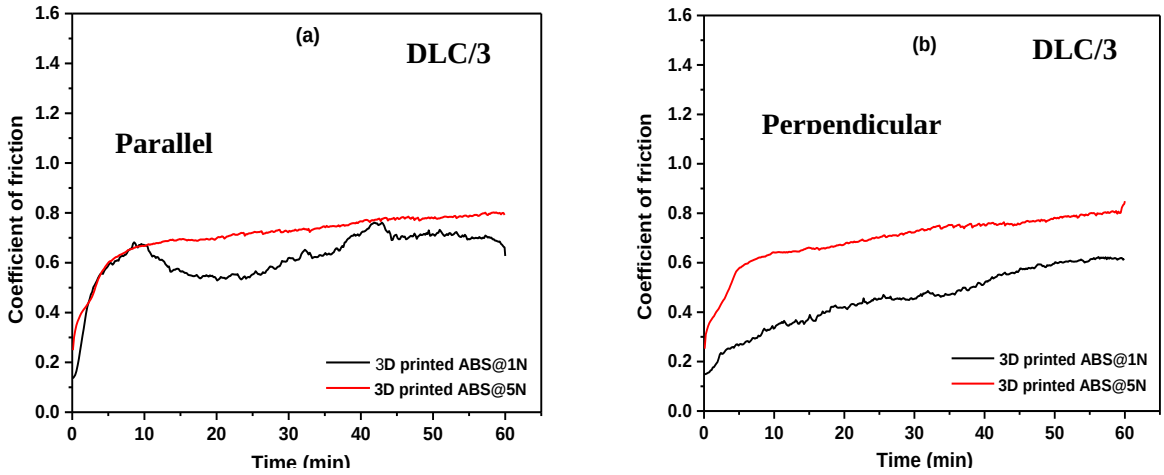

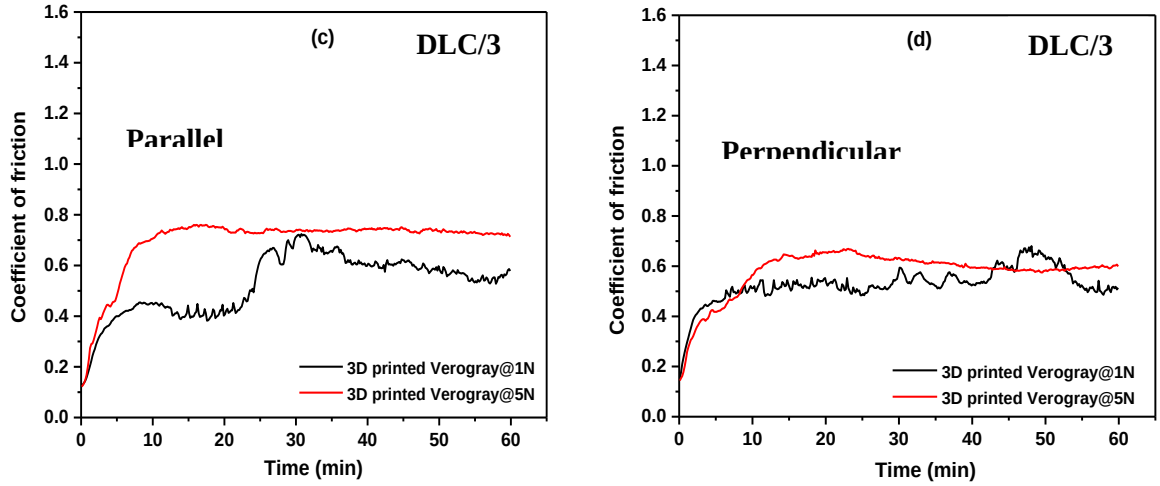

Figure 7-4- A comparative plot showing the variation of friction coefficient behaviour under varying contact load and print orientation for DLC/3 coated polymers: (a) parallel and (b) perpendicular to print orientation for 3D printed ABS, (c) parallel and (d) perpendicular to print orientation for 3D printed Verogray.

7.2.3 Steady-state friction response

The steady-state frictional response for both uncoated and coated substrates tests are summarised and presented in Figure 7-5 and Figure 7-6. In this test, the steady-state was defined by the last 20 min of the test where the CoF remained stable. For the uncoated 3D ABS, it was observed that the highest frictional response was observed at 1N where the contact orientation was perpendicular to the applied load. That notwithstanding, the parallel orientation to the applied load also showed a much higher CoF response at 0.95 even though this value was ~26 % less than the CoF value recorded for the perpendicular orientation. In the case of Verogray, similar trends were observed for both the parallel and perpendicular orientations where the average CoF value observed were 0.93 and 1.01 respectively. Other than in the case of 1N load, there were no significant changes observed in the CoF values under both 5 and 10N loads for the parallel and perpendicular print orientation.

For the coated samples, the steady-state friction response is presented in Figure 7-6. The combined effect of surface orientation and coating performance is made evident, where at 1N, DLC/1 coated 3D ABS showed similar CoF performance regardless of the orientation to the applied load. However, the opposite was observed for the parallel and perpendicular orientation where higher CoF values were recorded for the Verogray material. It can be shown that by changing from DLC/1 to 2 and finally to DLC/3, the CoF response increases progressively even under the same load regardless of the orientation. Similarly, at higher loads of 5N, the CoF increases as the DLC coated samples change from 1 to 3. By comparing the performances of both coated samples under 1N load, it can be concluded that the Verogray samples on average performed better at all levels in comparison with their 3D ABS coated counterparts. Similarly, the same could be said for Verogray at 5N for all DLC coated samples.

By comparing the frictional performance of both coated and uncoated samples at 1 and 5N loads, it is evident that the effect of surface coating provided a significant reduction in the CoF values for all coated samples regardless of both orientations and applied load. However, for the uncoated and coated 3D ABS samples, variations were observed in the CoF performance at 1N. Under the uncoated regime of 1N load, the average CoF for both parallel and perpendicular orientations were 0.95 and 1.2 respectively. For the DLC/1, 2 and 3 coated samples, the parallel and perpendicular orientations recorded a 0.43 and 0.44 average CoF value for DLC/1, 0.52 and 0.55 for DLC/2, and 0.67 and 0.63 for DLC/3 respectively. At 5N load, both the parallel and perpendicular orientations showed 0.85 and 0.88 CoF values respectively as compared to 0.67 and 0.60 for DLC1, 0.60 and 0.68 for DLC 2, and 0.76 and 0.77 for DLC/3 respectively for 3D ABS.

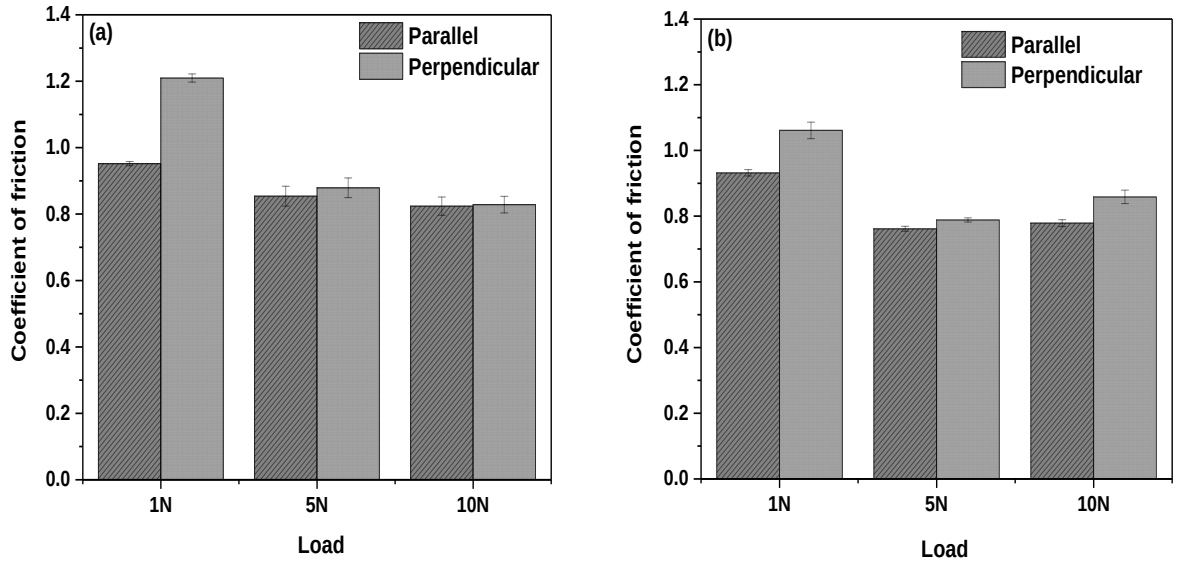

Figure 7-5- Steady-state summary result showing the coefficient of friction result for the uncoated 3D printed (a) ABS and (b) Verogray.

For the Verogray uncoated samples at 1N load, the CoF for both parallel and perpendicular orientations were 0.93 and 1.06 respectively. However, for the same load, the coated samples showed a reduced CoF value in both orientations as shown in Figure 7-6. For both parallel and perpendicular orientations, the corresponding average CoF for DLC/1, 2 and 3 coatings were 0.37 and 0.52, 0.44 and 0.44, and 0.60 and 0.55 respectively (Figure 7-6). For the 5N load, the CoF values for the uncoated samples were 0.76 and 0.79 for the parallel and perpendicular orientations. Correspondingly, the DLC coated samples for DLC/1 showed 0.37 and 0.35 CoF values for both parallel and perpendicular orientations. A 0.5 and 0.55 CoF values were recorded for DLC/2 whilst DLC/3 recorded a 0.73 and 0.61 CoF value for both parallel and perpendicular orientations to the applied load.

It can be observed that, in all cases of the test, the role of coating thickness and resistance to mechanical damage under both tensile and shear stress cannot be underrated and their contribution in effecting tribological changes is key in the performance of the coated 3D samples.

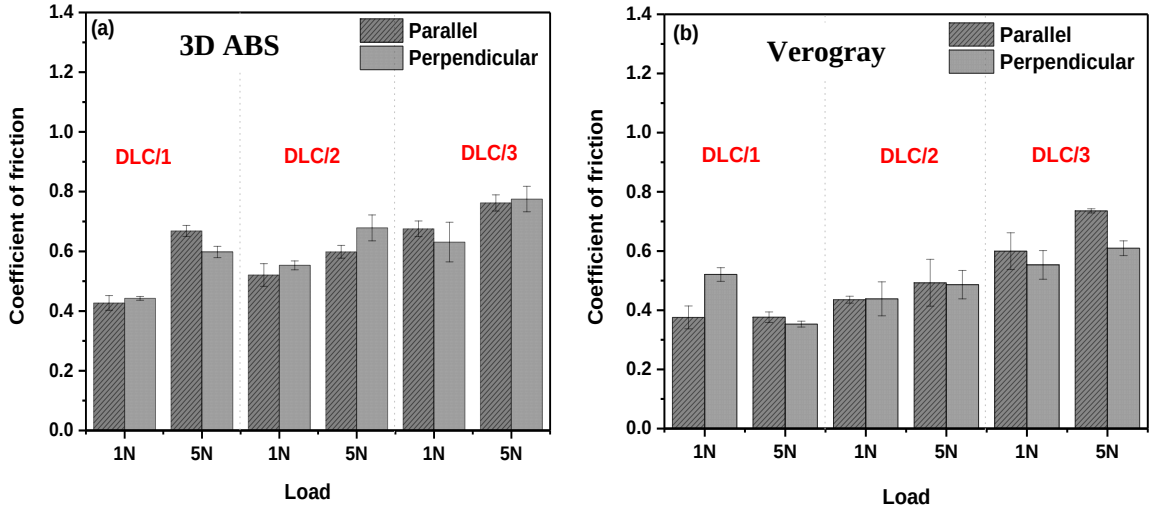

Figure 7-6- Steady-state summary result showing the coefficient of friction results for the coated 3D printed (a) ABS and (b) Verogray.

7.2.4 Wear analysis and mechanism

The wear of polymers may be variously characterised and quantitatively defined based on the volume and mass loss in a tribological contact. The sequence of events leading to surface debris generation as a consequence of both mechanical and contact fatigue stress encourages surface deformation in the contact area. From Figure 7-7, it was observed that the wear resistance of both 3D printed polymers understudy was greatly dependent on the surface orientation at which the contact load was applied. For all applied loads the surface orientation effect on debris generation is self-evident. However, it was observed that the level of wear generation is not only dependent on the surface orientation but also the bulk material property resistance to deformation. 3D ABS under 1N showed better resistance to wear in comparison with Verogray in all orientations. However, at higher loads of 10N, the reverse phenomenon of wear generation is observed for all print orientations where Verogray demonstrated higher resistance to wear than the 3D ABS counterpart. At 5N load, the highest resistance to wear for Verogray was observed when the parallel orientation was used rather than the perpendicular. Both 3D ABS and Verogray showed relatively similar material loss and specific wear rate values even though the later showed slightly higher resilience to wear.

Similarly, the specific wear rates of both coated 3D ABS and Verogray are summarized in Figure 7-8. In all cases involving the 1N load, no specific wear volume data were obtained as a result of the coatings resilience to deformation at the applied load of 1N. However, at 5N, the deformation at the contact area

is self-evident in the plot describing the different coated materials under both parallel and perpendicular orientations to the applied load. It was observed that at a constant load of 5N in all cases, the parallel orientation encourages greater wear generation in comparison with perpendicular orientation. For the parallel orientation, DLC coated Verogray samples exhibited the highest resistance to wear in comparison with the coated ABS sample. By way of comparison with all the DLCs examined, DLC/2 coated Verogray on average demonstrated higher resistance to wear followed up by DLC/1 and DLC/3 for the parallel orientation. Similarly, for the 3D ABS coated substrate, the highest resistance to wear was observed for the DLC/2 coated substrate followed by DLC/1 and DLC/3.

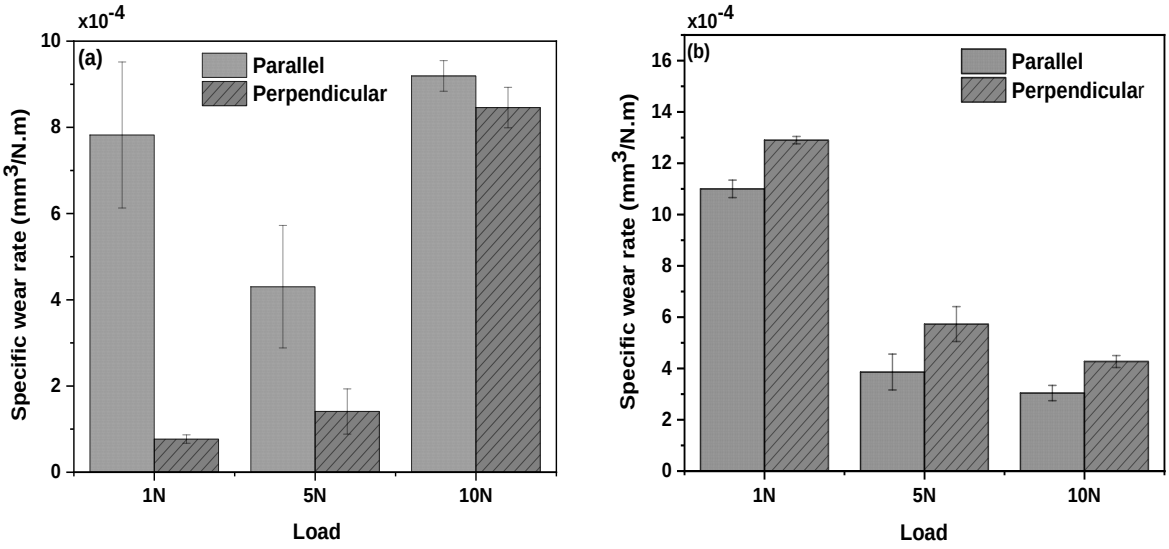

Figure 7-7- Specific wear rate at 1, 5 and 10N for (a) 3D ABS (b) Verogray.

The morphological study of the wear scar for both 3D ABS and Verogray uncoated surfaces are presented in Figure 7-9 to Figure 7-12. Figure 7-9 and Figure 7-10 compares the SEM images of the wear scars of both parallel and perpendicular orientations to the applied loads respectively. It can be observed that at lower loads, the most prominent surface deformation was due to the overlapping compaction effect of the individual raster surface features. Dawoud *et al*. [83] observed a similar phenomenon when they tested fused deposited ABS polymers under a 35N load for 60 mins at 8.4m/s. Even though different loads were applied in both cases, the deformation pattern and trend observed were very similar. Further, increase in load from 1 to 5N show a transition from a more layer compacted layer regime to a mixed regime characterised by layer detachment and compaction for both parallel and perpendicular orientations. As noticed from both Figure 7-9 (c) and Figure 7-10 (c) under an applied load of 10N, there is a further increase in surface layer detachment resulting from both abrasive and adhesive wear damage. Additionally, further inspection of the worn surface indicated severe plastic deformation.

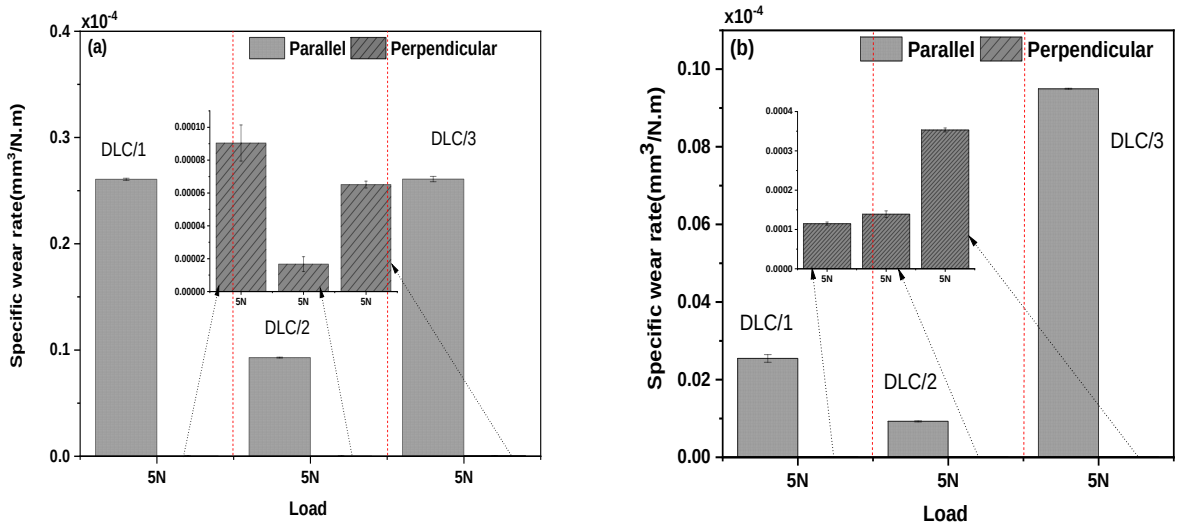

Figure 7-8- Specific wear rate of DLC coated 3D printed (a) ABS (b) Verogray at 5N load.

Further analysis of the 3D printed Verogray sample showed varying surface deformation patterns characterised by irrevocable changes, giving rise to the initiation and development of surface crack. A phenomenon termed friction fatigue [148]. At 1N load it was observed that Verogray showed varying surface deformation when the applied load is parallel to the print orientation. The loss of polymer material from the dry contact between the steel counterpart surface and polymer owing to friction fatigue is mostly termed fatigue wear [148]. As observed in Figure 7-12 (a) the special wave-like deformation phenomenon created as a result of the compressive deformation and subsequent buckling giving rise to layer detachment can be observed on the worn surface of Verogray similar to the well-known Schallamach pattern [287]. At higher loads, the deformation caused as a result of friction fatigue is highly intensified in both parallel and perpendicular to print orientations leading to further layer detachment in the case of applied load parallel to the print orientation. The initiation of extensive crack formation on Verogray sample is visible at 10N applied load perpendicular to the print orientation of the test sample.

The morphological study of the wear scar for both coated 3D ABS and Verogray for the three individual DLCs are presented in Figure 7-13 to Figure 7-18. Figure 7-13 and Figure 7-14 compares the surface deformation regime of the 1N load for both coated 3D ABS and Verogray for DLC/1. Further SEM images are shown in Appendix IV describing the surface deformation regimes and wear scars of the individual DLC coatings. It can be observed that in the case of 3D ABS, severe coating damage characterised by irregular fracturing along the wear track are observed for both orientations to the applied load of 1N.

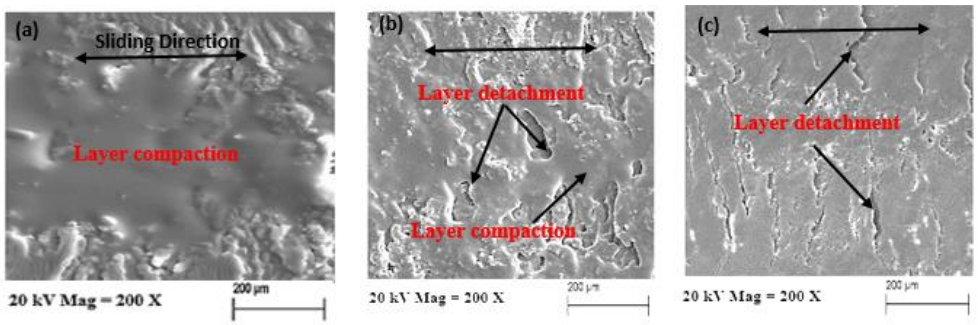

Figure 7-9- SEM images of 3D-printed ABS showing the influence of polymer print orientation on wear under dry reciprocating sliding condition oriented parallel to the sliding direction at varying applied load for (a) 1N (b) 5N (c) 10N.

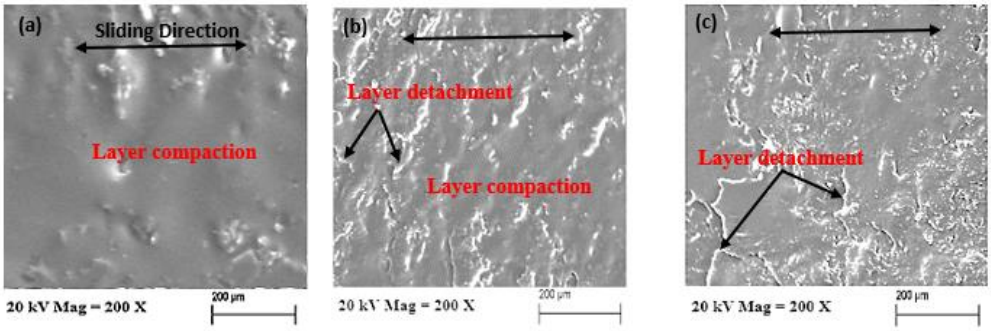

Figure 7-10- SEM images of 3D-printed ABS showing the influence of polymer print orientation on wear under dry reciprocating sliding condition oriented perpendicular to the sliding direction at varying applied load for (a) 1N (b) 5N (c) 10N

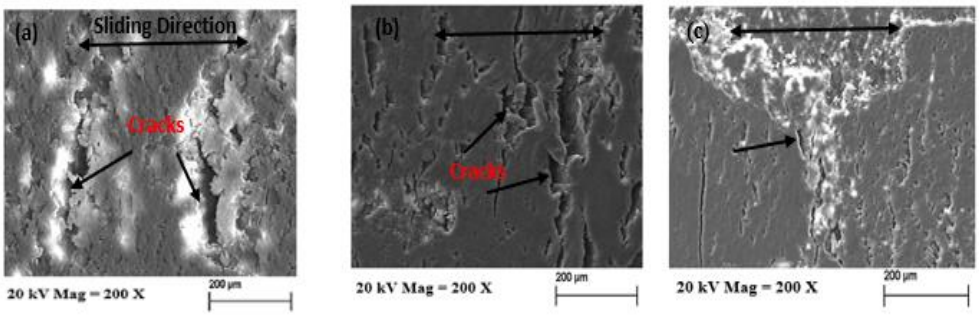

Figure 7-11- SEM images of 3D-printed Verogray showing fatigue damage under dry reciprocating sliding condition oriented parallel to the sliding direction at varying applied load for (a) 1N (b) 5N (c) 10N.

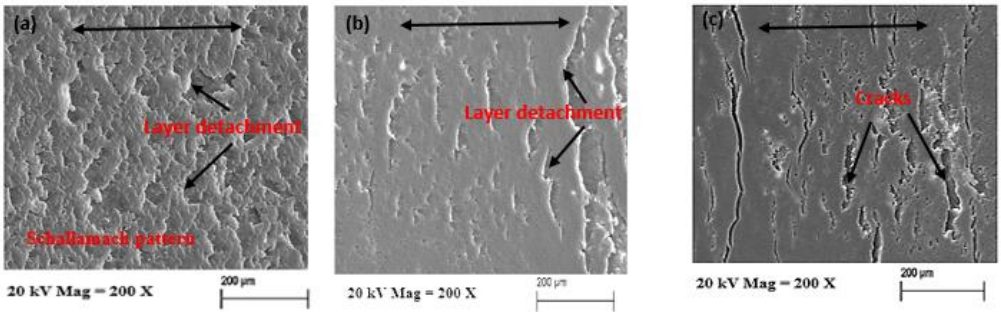

Figure 7-12- SEM images of 3D-printed Verogray showing the influence of polymer print orientation on wear under dry reciprocating sliding condition oriented perpendicular to the sliding direction at varying applied load for (a) 1N (b) 5N (c) 10N.

However, for the same coating deposited on 3D Verogray, no visible coating fracture failure was observed. It was further noted that several localised nucleation of decohesive areas causing spallation of the coating at the interface between the coating and substrate had developed. The most visible wear mechanism dominating the surface was sliding abrasion as a result of the solid-solid frictional interaction between the two surfaces. For the coated samples of DLC/2 and 3, similar deformation mechanisms were observed, however, the extent of deformation was observed to be pronounced in DLC/2 followed up by DLC/3 where in the latter, significant coating damage is observed. These shifts in coating response to deformation at 1N for all DLCs could be attributed to the better adhesion observed for the DLC-Verogray interaction compared to the 3D ABS, surface hardness and coating thickness.

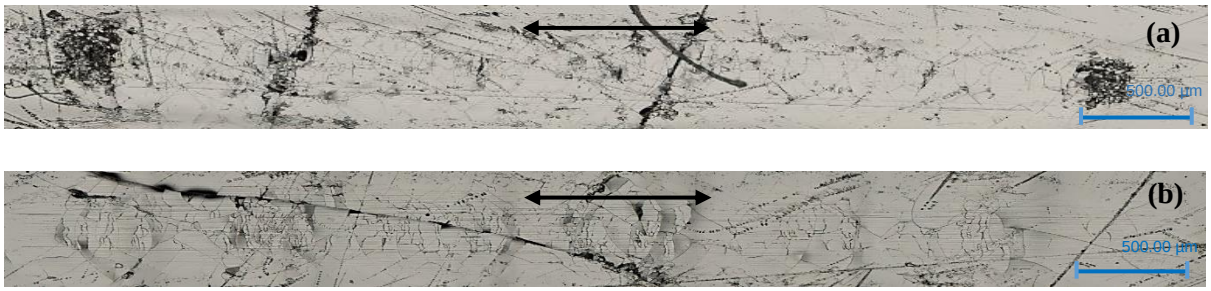

Figure7-13- DLC/1 coated ABS substrate showing the deformation on (a) parallel (b) perpendicular orientation to the applied load of 1N.

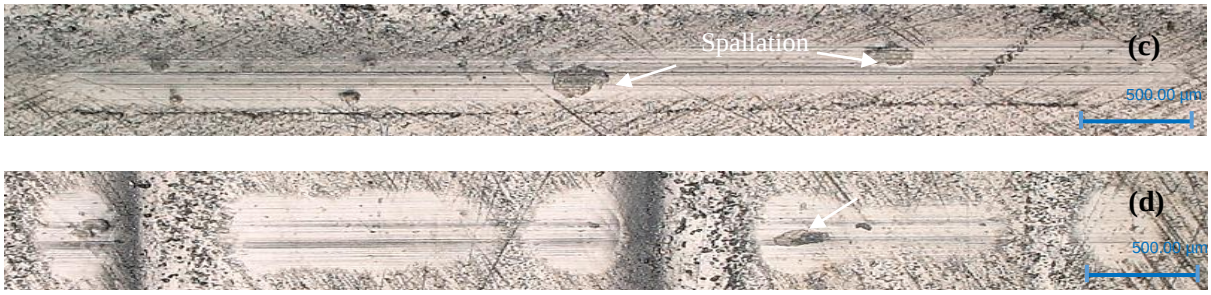

Figure7-14- DLC/1 coated Verogray substrate showing the deformation on (c) parallel (d) perpendicular orientation to the applied load of 1N.

By considering the wear response for both 3D ABS and Verogray samples, the orientation of the test surfaces along (parallel) and across (perpendicular) the applied load of 5N is shown in Figure 7-15 to Figure 7-18. As noticed from both Figure 7-15 and Figure 7-16 for all DLC coating types under 5N load for 3D ABS, it can be seen that there is an increasing trend in the plastic deformation of both coating and polymer where the resistance to both abrasive and adhesive damage is intensified as one moves from DLC/1 through to 3. At a similar load at 5N, the performance of Verogray sample as shown in Figure 7-17 and Figure 7-18 exhibits a more robust coating structure in all orientations when compared with the 3D ABS substrates. For both parallel and perpendicular orientations for DLC/1

(Figure 7-17 (a) and Figure 7-18 (a)), the primary observable feature defining the wear track is the presence of abrasive wear marks resulting from the dry solid-solid interaction. By changing from DLC/1 to DLC/2 coating, a brittle delamination mode is observed with spallation extending over the side of the wear track for the parallel orientation (Figure 7-17 (b)). When considering the perpendicular to print orientation, the deformation regime as observed in Figure 7-18 (b) is more pronounced and characterised by a combination of abrasive and fatigue wear leading to spallation of the coating. The complete removal of coating along the wear tracks under intense abrasion from the polymer-coating interface is made evident in Figure 7-17 (c) and Figure 7-18 (b) for DLC/3. In comparison, the parallel orientation was seen to promote excessive wear as the surface provided minimal resistance to deformation during the solid-solid contact in the dry reciprocating tribo contact.

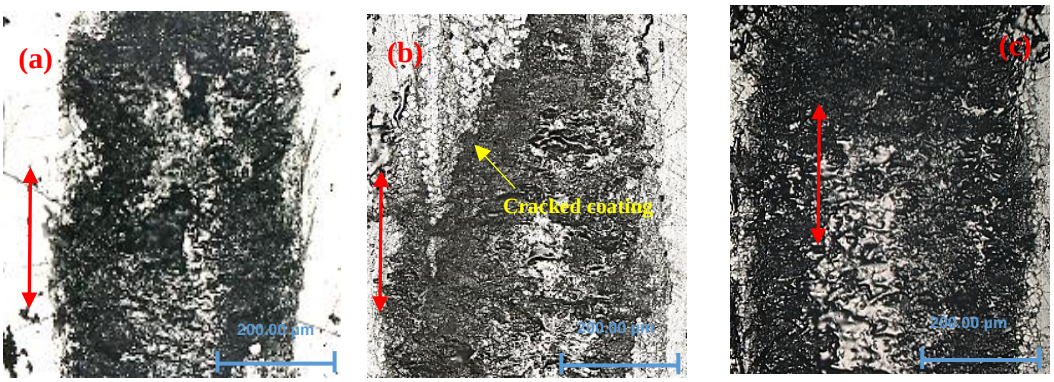

Figure 7-15- Wear track showing coating damage on 3D ABS for (a) DLC/1 (b) DLC/2 (c) DLC/3 for dry reciprocating sliding at 5N load for parallel orientation. Red arrow shows the sliding direction

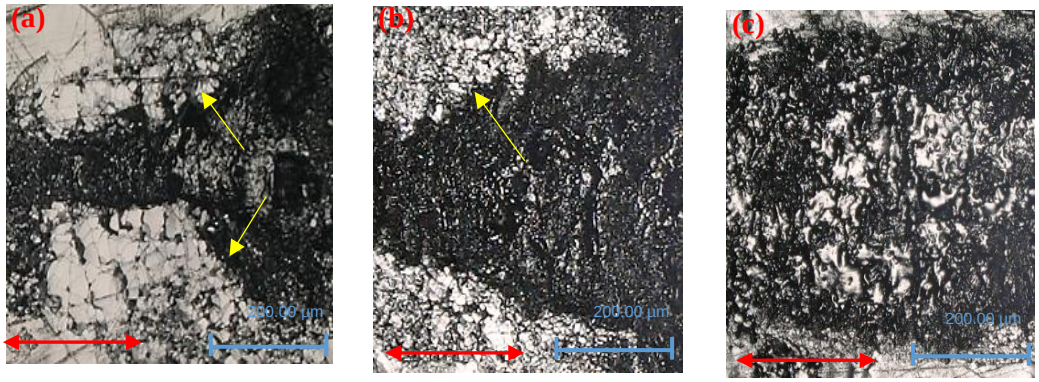

Figure 7-16- Wear track showing coating damage on 3D ABS for (a) DLC/1 (b) DLC/2 (c) DLC/3 for dry reciprocating sliding at 5N load for perpendicular orientation. Red arrow shows the sliding direction.

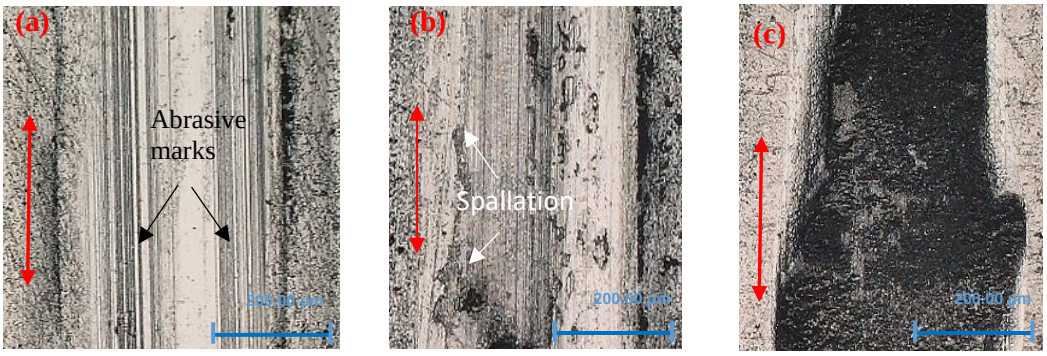

Figure 7-17- Wear track showing coating performance on Verogray for (a) DLC/1 (b) DLC/2 (c) DLC/3 for dry reciprocating sliding at 5N load for parallel orientation. The red arrow shows the sliding direction.

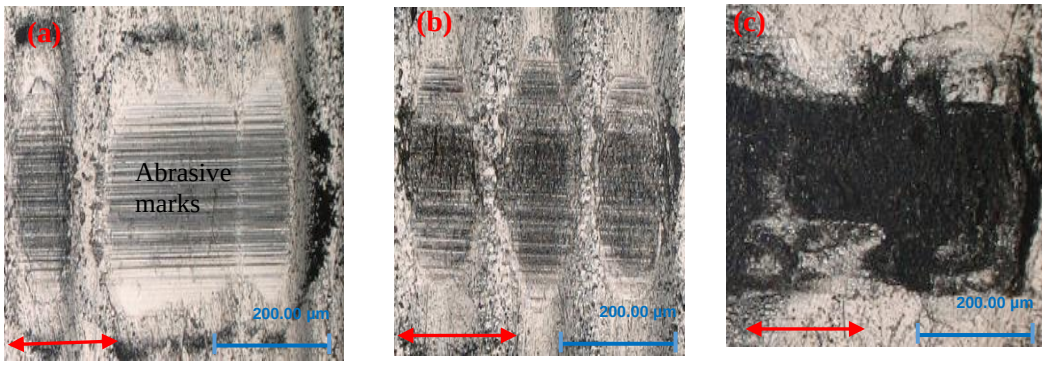

Figure 7-18- Wear track showing coating performance on Verogray for (a) DLC/1 (b) DLC/2 (c) DLC/3 for dry reciprocating sliding at 5N load for parallel orientation. The red arrow shows the sliding direction.

7.2 Summary

In this chapter, the tribological performance of both coated and uncoated substrates are accessed under parallel and perpendicular orientations to applied loads of 1, 5 and 10N. The evolution of friction coefficient over time shows the varying response for all the different cases of loading and orientation for both 3D printed materials tested. For the two print orientations tested, the frictional performance was strongly reliant on the surface finishing properties. Other than in the case of 1N load, there were no significant changes observed in the coefficient of friction value under both 5 and 10N loads for the parallel and perpendicular orientations, being in these occasions the friction dominated by the bulk properties of the materials involved in the contact for the uncoated polymers. For the coated sample, the frictional performance for both orientations was seen to be significantly lower than their uncoated counterpart at 1N load, with DLC/1 showing the least CoF response compared with both DLC/2 and DLC/3 due to the ductile nature of the coating. As the load increases to 5N, a higher CoF response is observed for all coated samples with the highest observed for DLC/3. Similarly, it was observed that the wear resistance of both 3D printed polymers was very dependent on the surface orientation at which

the contact load was applied. 3D printed ABS under 1N showed better resistance to wear in comparison with Verogray in all print orientations. At higher loads of 10N, the reverse phenomenon of wear generation is observed for all print orientations where 3D Verogray demonstrate higher resistance to wear than the 3D ABS for the uncoated surface. By investigating the results of the wear performance in relation to their coating structure and orientation, it was seen that even though no coating removal was observed for both polymers at 1N load, excessive localised surface deformation in the form of tensile cracking was seen along with the wear scare for both surface orientations in the case of for 3D ABS. For the Verogray sample, the deformation regime characterising the wear scar was dominated by the presence of abrasive wear. At 5N load, it was observed that as the coating transitions from a ductile to a more brittle like coating structure, the trend in plastic deformation intensifies. It was further shown that for both orientations studied under 1 and 5N, the parallel orientation promoted excessive wear as a result of the minimal surface resistance during the solid-solid tribo-contact. In future, the role of adhesive layer transfer onto counter steel surfaces in defining the tribological regime could be explored further.

Chapter 8

Results & Discussion: Barrier and water absorption function

8.1 Introduction

The barrier and protective function of DLC coatings can be quantitatively measured by determining the water vapour transmission rate (WVTR) and absorption properties of the coated substrate material. This functionality is achieved through the quantitative measure of the steady-state rate function at which water vapour molecules pass through the sample per unit area at a pre-determined time, usually measured in gm/m^2-day or absorbed at equilibrium. Currently, there is no reported literature on the deposition of amorphous DLC coatings on AM polymers to provide barrier functionality for specific household and industrial applications. This work studies the advantageous combination of Polyjet AM parts (3D ABS and Verogray) with the particulate structural properties of a single layer amorphous DLC film to improve the water vapour barrier function of the underlying AM substrate. Further studies of the water vapour transmissivity and absorption functions of the textured surfaces (Chapter 3) are also studied.

8.2 WVTR of barrier films

By using the standard MOCON PERMATRAN-W model 3/33 equipment, the WVTR function of the DLC coated substrates and uncoated substrate (pristine textured and untextured) are assessed according to ASTM F1249 standards. Chapter 3 provide a detailed design description of the methodology utilised in this work.

8.2.1 Effect of nitrogen gas flow rate on the WVTR function

In this study, two DLC films with varying nitrogen ratios were deposited on both substrates. The effect of nitrogen gas flow rate at 0 and 20 sccm (represented by DLC/1 and DLC/3 respectively) on the coating barrier performance is shown in Figure 8-1. The WVTR function curve for both uncoated (P/0) and coated samples versus time are also detailed. For the 3D ABS plot, it was observed that the WVTR function increases sharply with time before reaching a steady-state peak where the maximum limit is attained for all coated and uncoated samples. As expected, the maximum WVTR function was observed

for the uncoated 3D ABS with an average WVTR of 73.31 gm/m^2-day. It was found that the DLC/1 and DLC/3 films provided improved barrier functions at 55.68 and 61.51 gm/m^2-day (Figure 8-1) corresponding to a 24 and ~16% reduction in the WVTR function. This could be partly due to the role film thickness play in the reduction of WVTR by increasing the migration path through which water molecules migrate before reaching the detector. Ray *et al.* [126] noted that thicker a-C:H films provide a better barrier option for water vapour and oxygen transmission function but cautioned that after a certain thickness, adhesion becomes poor and so does WVTR.

The increased WVTR function for the Verogray pristine sample can be seen when compared with both coated samples as shown in Figure 8-1 and Figure 8-2. The rate determined transmissivity of water vapour through both coated and uncoated substrates show the general trend observed for most uncoated substrates where higher transmissivity of water vapour is observed compared with their coated counterpart. At steady state, the uncoated pristine Verogray is seen to have the highest WVTR of 28.8 gm/m^2-day. For both samples coated with DLC/1 and DLC/3 for Verogray, a WVTR of 11.25 and 8.5 gm/m^2-day was measured (Figure 8-2). This corresponds to a 60 and ~70.4 % reduction in the WVTR function respectively. This decreased trend observed for both coated Verogray samples could be attributed to the robustness of the DLC structure present on the Verogray substrate. The surface morphology study reported in Chapter 6 shows that Verogray samples possess improved nucleation compared with 3D ABS and as a result, provide a limited pathway or defect structure through which water vapour could penetrate. The MICP pore analysis show for both uncoated polymers, the main driving force contributing to the increase in the WVTR was the presence of higher porosity and pore size distribution function present within the 3D ABS bulk, thus providing greater access for water vapour transmissivity. The variation in the surface morphology as described by the AFM surface scan (Chapter 6) show greater detail in material property and pore structure variation in both polymers.

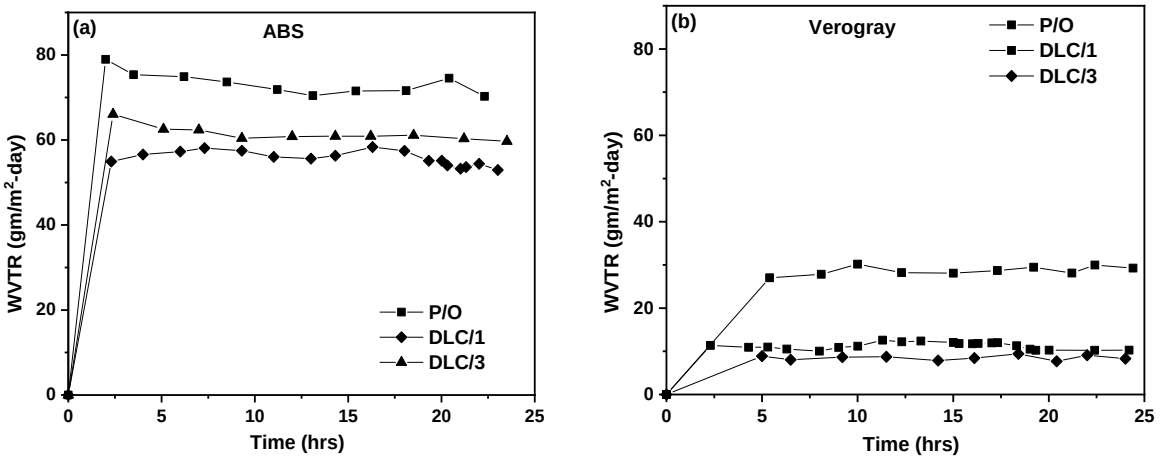

Figure 8-1- MOCON WVTR rate curve showing the WVTR function with time for both 3D printed ABS and Verogray.

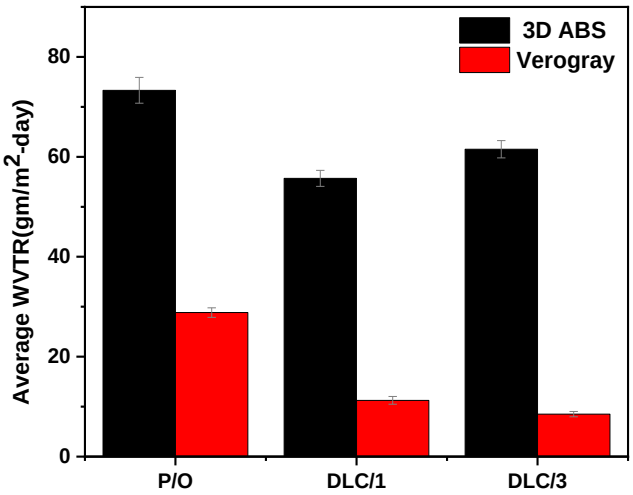

Figure 8-2- A comparative plot showing the average WVTR rate function for both 3D ABS and Verogray.

8.2.2 Surface texturing effect on the WVTR

8.2.2.1 **Uncoated additively manufactured polymers**

This test presents a single MOCON rate curve showing the effect of surface texturing on the WVTR function for both 3D ABS and Verogray (Figure 8-3). From both plots as presented in Figure 8-3, the WVTR function with time is shown to be dependent on the surface texturing used. The use of textured surfaces in comparison with the untextured substrate simplifies the comparison between both substrates pre-deposition and shows the obvious variation with WVTR as a function of time wherein all cases, different WVTR was observed. Textured substrates A and B for 3D ABS showed the highest WVT at 91.56 and 77.7 gm/m^2-day respectively with the lowest rate recorded for the untextured substrate at 73.32 gm/m^2-day. It was similarly noted for the Verogray sample that, both textured A and B substrates showed higher WVTR at 36.89 and 39.31 gm/m^2-day in comparison with a 28.68 gm/m^2-day for the pristine Verogray sample. As the number of repeats conducted equals 2, the use of predictive models to provide statistical interpretation for the data presented may become inadequate, however, one could conclude that, for both textured surfaces for Verogray, no significant differences were observed for their WVTR. However, this was not the case when 3D ABS is considered. Even though there is a marginal increase in the WVTR of ~7 % for using textured B instead of the untextured surface for Verogray, the greatest rise in the WVTR was observed for textured A for 3D ABS which stood at ~20 % in comparison with the pristine untextured surface.

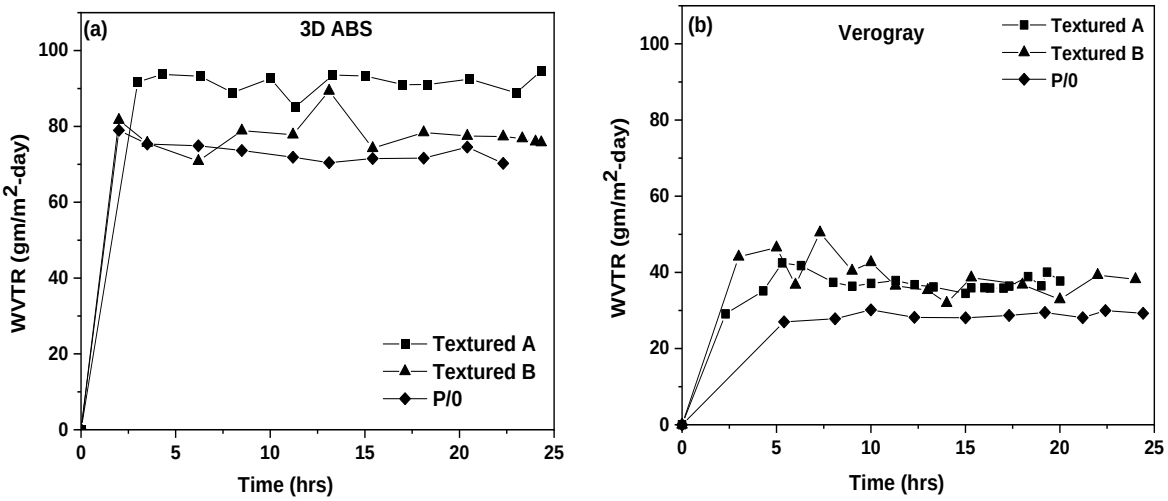

Figure 8-3- MOCON WVTR rate curve showing the WVTR function with time for both 3D printed ABS and Verogray for textured surface A and B.

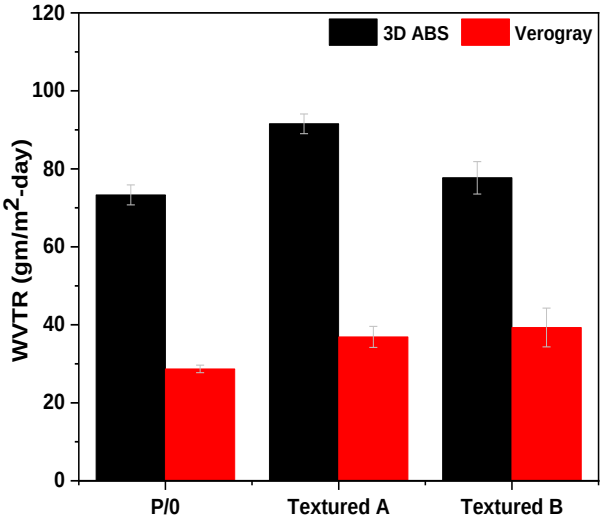

Figure 8-4- A comparative plot showing the average WVTR rate function for both ABS and Verogray.

8.2.2.2 **Coated additive manufactured polymers**

The WVTR function of the individual coated samples is assessed to determine the role surface feature (s) play in the permeation of water vapour through 3D printed polymers. In this study, both textured substrates (A and B) for 3D ABS and Verogray are coated and discussed. With both substrates coated with DLC/2 (C_2H_2= 610 sccm, N_2= 10 sccm) and DLC/5 (C_2H_2= 310 sccm, N_2= 20 sccm) the individual WVTR function is assessed. The two sets of coatings were chosen to study the limitations for each of the textured samples when coated with DLC/2 and DLC/5. In Figure 8-5 the WVTR function for 3D ABS is presented. The individual rate function plots for both DLC/2 and DL/5 coatings are also shown in Figure 8-5 (a) and (b) respectively for surface texturing types A and B having an aspect ratio

(width: height) of 3.5:1 and 7:1 respectively. It can be noted that DLC/2 coating on both textured substrates for 3D ABS showed a similar linearity trend until a steady-state regime is attained. For all cases involving both coated substrates, the WVTR was shown to increase linearly with time until a maximum steady-state regime is attained. For both textured substrates A and B shown in Figure 8-5 (a) for 3D ABS, an average rate of 77.87 and 36.12 gm/m^2-day were obtained. Similarly, both textured substrates A and B for DLC/5 coating are shown in Figure 8-5 (b), where the average WVTR for both textured surfaces A and B were 82.68 and 69.83 gm/m^2-day. In terms of the percentage change in the WVTR between the two coatings, it was seen that DLC/2 provided a 53.61 % reduction in the WVTR function compared with a 15.54 % in DLC/5 coatings when the two textured surfaces are compared. This was thought to be a result of the total area of exposure for WVTR. As more surface area is exposed for contact, one would expect a higher rate of transmissivity across the test film. Hashmi [288] noted that increasing surface area is the most obvious trend for increasing gas permeation performance through a porous nanostructure.

Similarly, the WVTR function tests for 3D Verogray samples have been studied (Figure 8-6 (a)). The WVTR function for the DLC/2 coated and textured substrates A and B were 20.61 and 15.45 gm/m^2-day respectively. For similarly textured surfaces as shown in Figure 8-6 (b), the WVTR function curve was again seen to be highly reliant on the surface features present. For the same coating type deposited (i.e. DLC/5), it can be shown that by using textured A instead of B, the WVTR was reduced by as much as 49 %. However, a comparison between both DLC/2 and DLC/5 coated samples for Verogray with similar textured surface features exhibited different barrier properties. For textured A samples, it was seen that by switching from DLC/2 to DLC/5, there was a 19.3 % reduction in the WVTR performance.

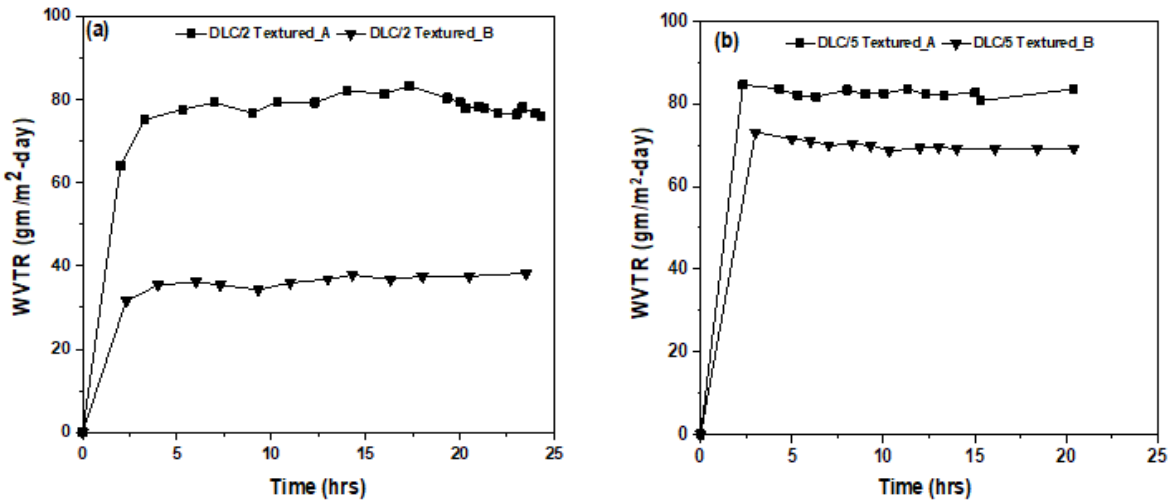

Figure 8-5- A comparative plot showing the effect of surface texturing on the WVTR function of 3D printed ABS polymer for (a) DLC/2 and (b) DLC/5.

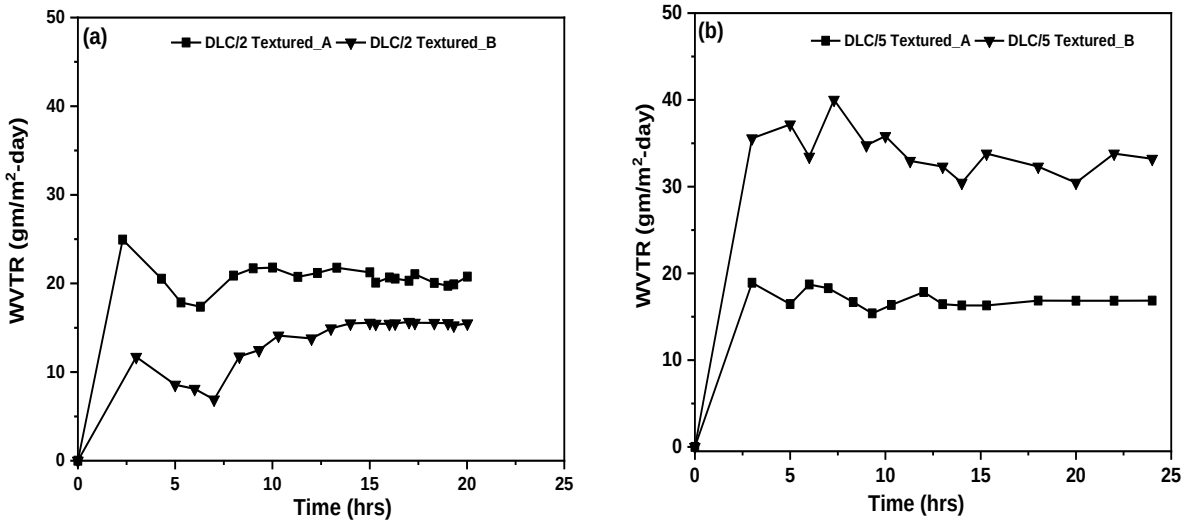

Figure 8-6- A comparative plot showing the effect of surface texturing on the WVTR function of 3D printed Verogray polymer for (a) DLC/2 and (b) DLC/5.

Nevertheless, as we consider the performance of both textured B surfaces for the DLC/2 and DLC/5 coating, it was seen that the WVTR performance increased by as much as 52 %. A comparison between the textured uncoated (P/0*) and textured coated samples show the variation in performance of the two surfaces under consideration. From Figure 8-7, it can be deduced that the introduction of surface texturing on both 3D ABS and Verogray provide some level of change in the WVTR function in comparison with the pristine non-textured surfaces shown in Figure 8-1 and Figure 8-2, where an average WVTR of 73.31 and 28.8gm/m^2-day were recorded for 3D ABS and Verogray respectively. This in comparison with both textured uncoated surfaces for 3D ABS and Verogray shows an increase in the WVTR function for all substrates studied. It can be concluded that the use of surface texturing has a positive effect on the WVTR function. The introduction of DLC coating on both textured surfaces for 3D ABS and Verogray, on the other hand, has shown varying degree of barrier responses where in all cases the WVT is lowered. For both DLC/2 and DLC/3 coated samples, it was observed that the highest WVTR reduction was achieved in the case of textured B DLC/2 coated substrates for both cases involving Verogray and 3D ABS. The highest reduction of 65 % compared to 53 % was recorded for Verogray and 3D ABS textured B substrates. Even though a similar reduction of ~53 % was recorded for textured A Verogray substrate coated with DLC/5, the average WVTR for the remaining coated substrates was 10.9 % compared with an average of 54 % reduction in the WVTR function for samples coated with DLC/2.

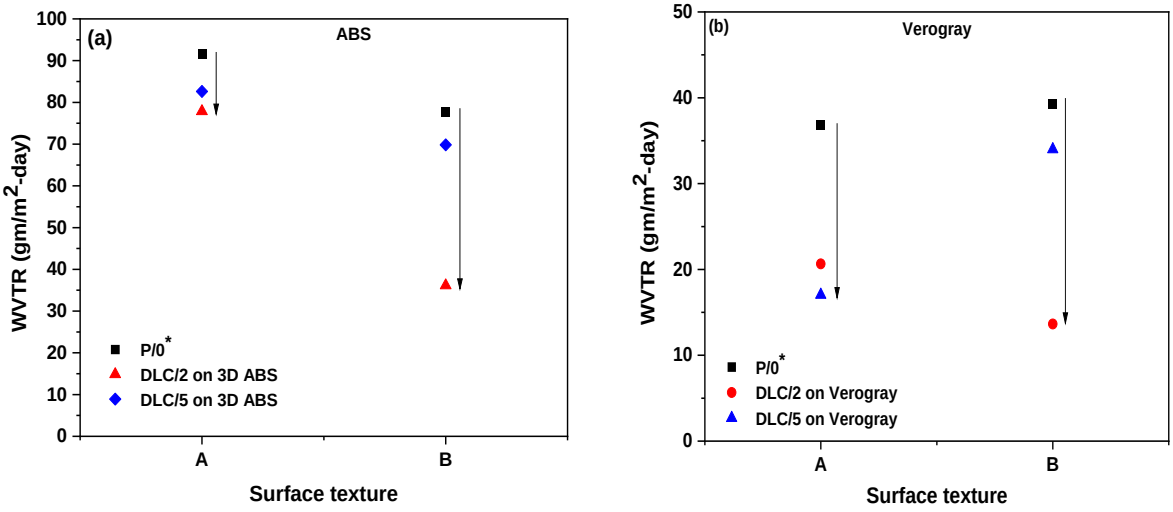

Figure 8-7- A comparative plot showing the change in WVTR for textured surface A and B deposited with DLC/2 and DLC/5 on 3D ABS (a) and Verogray (b).

8.2.2.3 **Effect of acetylene gas flow ratio on the WVTR function**

The observed WVTR function plots with time for DLC/3 and DLC/5 are shown in Figure 8-8 where the performance of the two individual coatings are assessed on textured B substrates as detailed in Chapter 3 for both 3D ABS and Verogray. Figure 8-8 (a) shows the water rate function curve for the water vapour transmissivity through 3D ABS at steady state using DLC/3 and DLC/5 coating. At a steady-state, the rate function for the water vapour transmissivity was ~70 gm/m^2-day for DLC/5. In comparison with the DLC/3 plot, it was observed that the level of water vapour transmissivity is much reduced when 3D ABS are coated with DLC/3. At steady state, the average WVTR for the coated 3D ABS was 18.4 gm/m^2-day. This accounted for a ~74 % reduction in the WVTR even though DLC/3 had a much thicker coating of 1.26 µm compared with DLC/5 coating of 0.55 µm.

The WVTR function of the Verogray coated samples are shown in Figure 8-8 (b) wherein in both plots, similar permeation trends are observed. However, due to the pore size restriction to flow of permeants through the micro and nanopore structures of the polymer matrix with the added advantage of a protective DLC coating, lower WVTR was observed as a result. For the DLC/3 coated sample, the average WVTR was 5.7 gm/m^2-day compared with 32.34 gm/m^2-day recorded for DLC/5.

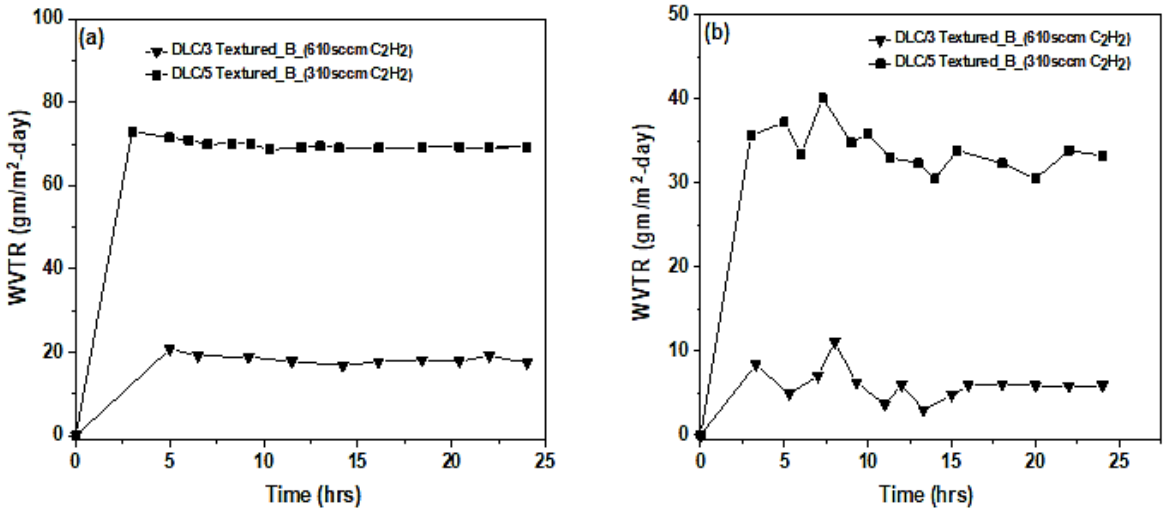

Figure 8-8- A comparative plot showing the WVTR function with time for both 3D ABS (a) and Verogray (b) coated with DLC/3 and DLC/5.

8.3 Dynamic water vapour sorption (DVS)

8.3.1 Water sorption at constant temperature and relative humidity

A comparative saturation water vapour sorption curve at a constant temperature of 25 ℃ and RH of 80 % is presented in Figure 8-9 (a) for all uncoated samples. As can be seen, very different water uptake patterns were observed for all samples studied. As it is expected from the pore size distribution curve and porosity measurements from the MICP test detailed in Chapter 4, 3D ABS in response to its higher porosity value of 7.7 % as against a 6.6 % for Verogray will have a much higher water vapour sorbed in comparison with Verogray and ABS moulded. The total moisture sorbed per mg sample tested also showed a similar trend with 3D ABS having the highest water vapour sorbed in comparison with both Verogray and moulded ABS (Figure 8-9 (b)). The moisture sorption properties of all coatings at constant temperature and relative humidity are similarly assessed to understand the limitations of their saturation water sorption properties at equilibrium. Figure 8-10 also shows a summary plot of the individual sample plot performance. It was observed that as the coating on the polymer surface changes, the rate and total water vapour sorbed changes in response. The biggest decline was observed for 3D ABS samples whereby introducing a protective DLC coating layer, the total amount of water sorbed decreases until a minimum is achieved for DLC/3. For both Verogray and moulded ABS, the comparative plot shows a relatively well distribution of data points corresponding to the individual total water vapour sorbed at 25 ºC and 80 % RH for the individual coatings. For all 3D ABS samples coated in Figure 8-10, DLC/3 provided the lowest water vapour sorbed, however, this reduction remained high in comparison with both Verogray and moulded ABS. For both Verogray and ABS moulded samples,

similar trends were observed in the sorption function, however, lower water sorption values were obtained for moulded ABS as a consequence.

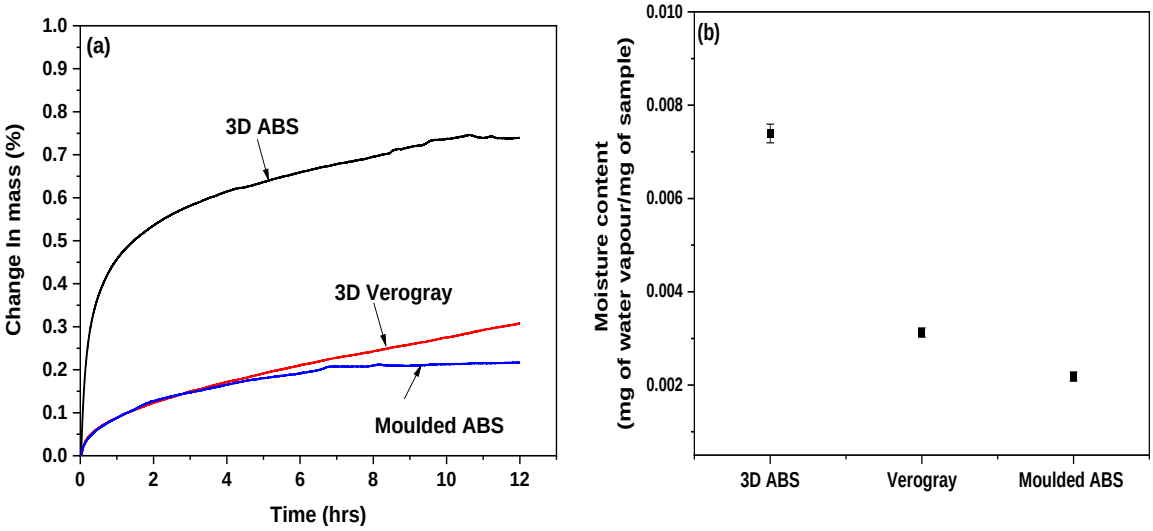

Figure 8-9- (a) Sorption isotherm plot for uncoated 3d printed ABS, Verogray and moulded ABS showing the percentage mass change with time. (b) Total average moisture absorbed (mg) per mg sample mass (mg).

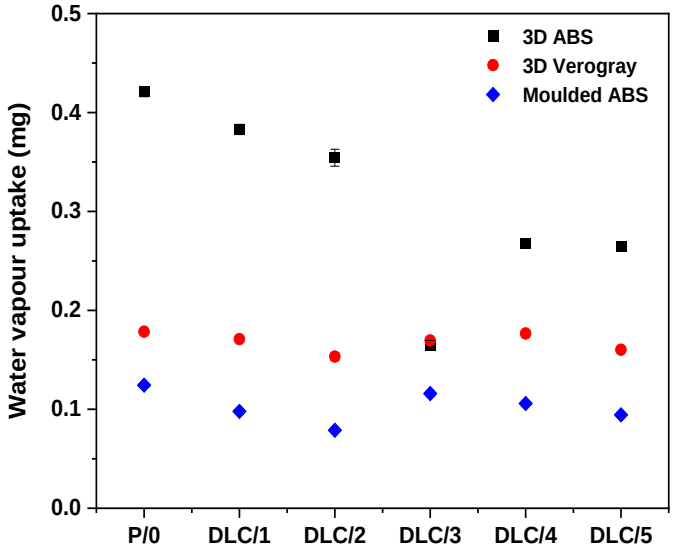

Figure 8-10- Summary plot showing the individual total gravimetric water sorbed for both coated and uncoated polymers analysed using the Dynamic Vapour Sorption at 25 ℃ and 80 % RH.

8.3.2 Temperature dependence water vapour sorption properties

Based on the moisture isotherm plot of the absorption-desorption curve and temperature at varying RH, the dynamic vapour sorption method was used to characterize both the coated and uncoated polymer samples. Full cycle moisture sorption isotherm of individual samples (coated and uncoated) from 0 to 90 % at temperatures of 25 ℃ and 40 ℃ are presented in Figure 8-11, Figure 8-12 and Appendix V. In

Figure 8-11 the adsorption and desorption isotherm plots for the uncoated samples are presented. At 25 ℃, it can be noticed that the level of water uptake was gradual in all cases for both substrates. In the case shown in Figure 8-11, bulk sorption becomes very dominant for 3D ABS after 20 % P/Po followed up by a sharp water uptake until a maximum is attained at 90 % P/Po. However, Verogray and moulded ABS both show slower water uptake for all P/Po exposures. The total amount of water sorbed is characteristic of the desorption curve and in all cases involving the individual polymers show a reversible isotherm where both sorption and desorption lines converge at the origin. At 40 ℃, the isotherm plots for both sorption and desorption lines showed an increasing shift in the total moisture sorbed at each P/Po, as the amount of moisture absorbed by a polymer is highly dependent on the temperature, relative humidity and chemical composition of the material [289]. In general, the water activity changes with temperature and as a result, properties such as barrier and material strength are compromised. It is well known that water activity usually increases with temperature and pressure increase, as described by an Arrhenius-type equation [290, 291]. For the 3D ABS sample, it was shown that both equilibrium plots showing the sorption and desorption plots were reversible and similar observations were seen for the moulded ABS. However, for the Verogray sample, the hysteresis gap between the sorption and desorption plot shows an irreversible state where moisture is firmly held into the polymer structure even after the desorption phase.

The hysteresis plots describing the difference in the total moisture adsorbed between the sorption and desorption isotherms for both coated and uncoated samples are shown in Figure 8-13 to Figure 8-15. For the 3D ABS hysteresis plot shown for both 25 ℃ and 40 ℃ (Figure 8-13), the percentage of water vapour isotherm hysteresis increases as the test temperature increases. It could be observed that at 25 ℃, there is an increasing upward shift in the total moisture adsorbed by the coated 3D ABS. The highest was seen for the DLC/2 coated substrates. A similar observation was made at 40 ℃ where the highest hysteresis was observed at 60 % P/Po with a 0.38 % water sorbed compared to 0.26 % at similar P/Po for the 25 ℃. For the 3D Verogray sample at 25 ℃, cluster isotherm plots of less than 0.1 % were observed for all coated substrates with the highest sorption P/Po occurring at 0.078 %. Bley *et al.* [292] noted that these characteristic kinetic changes resulting in the increased water uptake could be attributed to the change in the hydrophilicity and swelling capacities of the polymer as multilayers are formed on the substrate. As a result, the heat of liquefaction becomes greater than the heat of absorption of the first monolayer where typically condensation and cluster formation dominate at the surface rather than to the bulk material. The moulded ABS, on the other hand, showed similar characteristics to the Verogray at 25 ℃ and 40 ℃ but with fewer data spread and peak height isotherm jump at each corresponding P/Po (Figure 8-11).

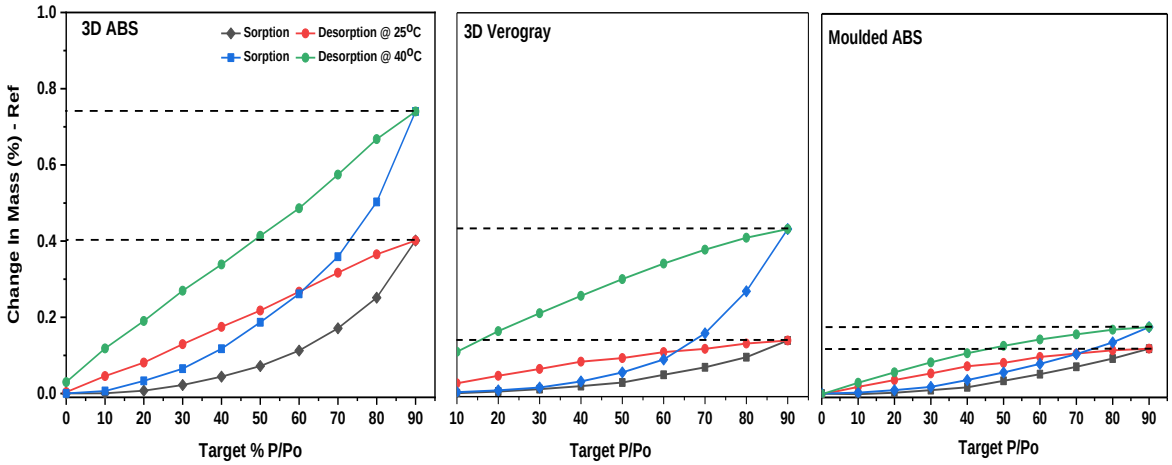

Figure 8-11- Typical isotherm plot for uncoated 3D ABS, Verogray and moulded ABS showing both sorption and desorption curves at 25 °C and 40 °C.

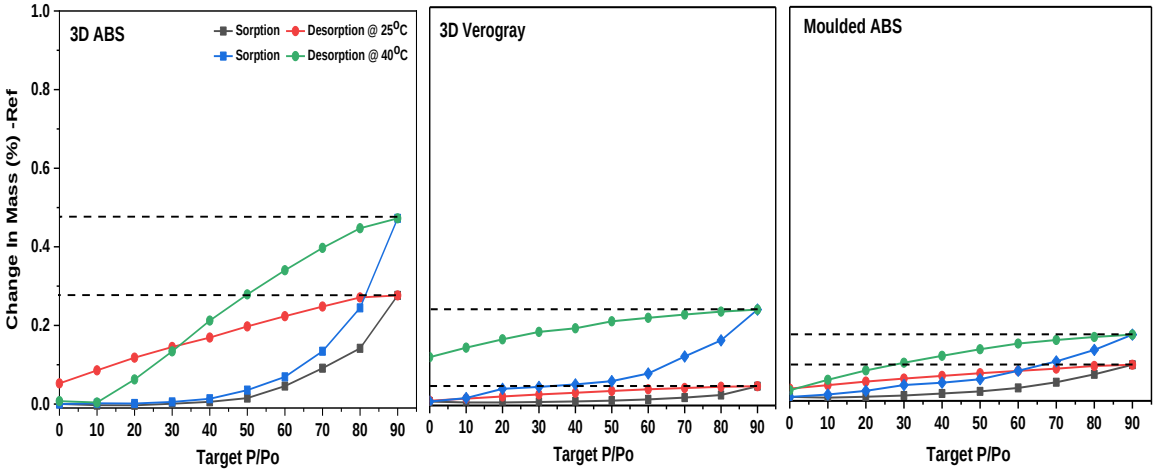

Figure 8-12- Typical isotherm plot for DLC/1 coated 3D ABS, Verogray and moulded ABS showing both sorption and desorption curves at 25 °C and 40 °C.

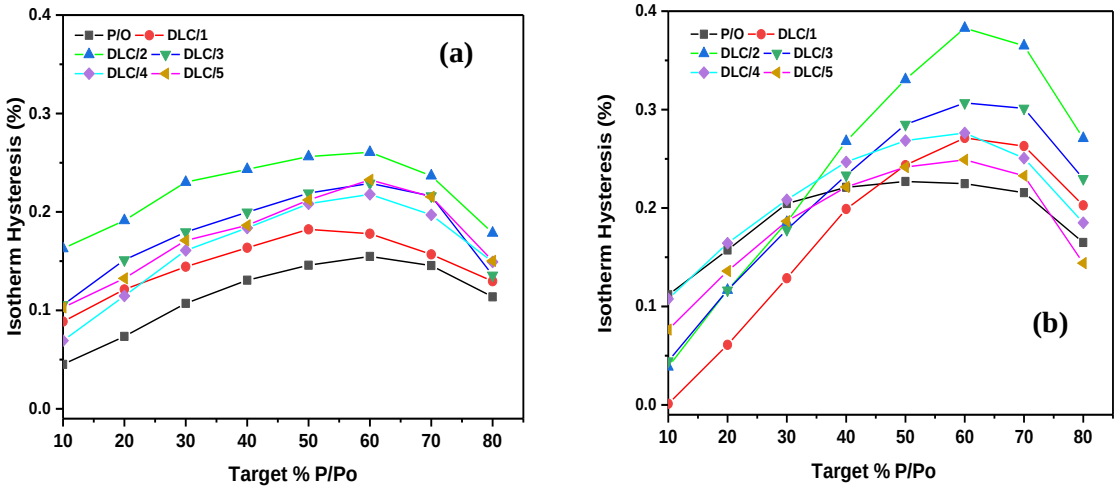

Figure 8-13- Hysteresis of the isotherm plot for 3D ABS at (a) 25 °C and (b) 40 °C.

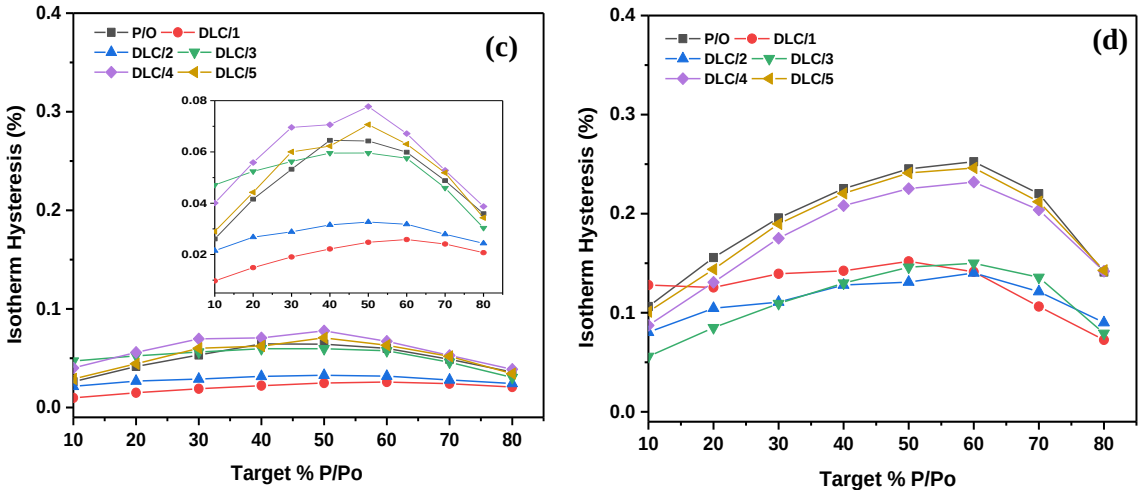

Figure 8-14- Hysteresis of the isotherm plot for Verogray at (c) 25 °C and (d) 40 °C.

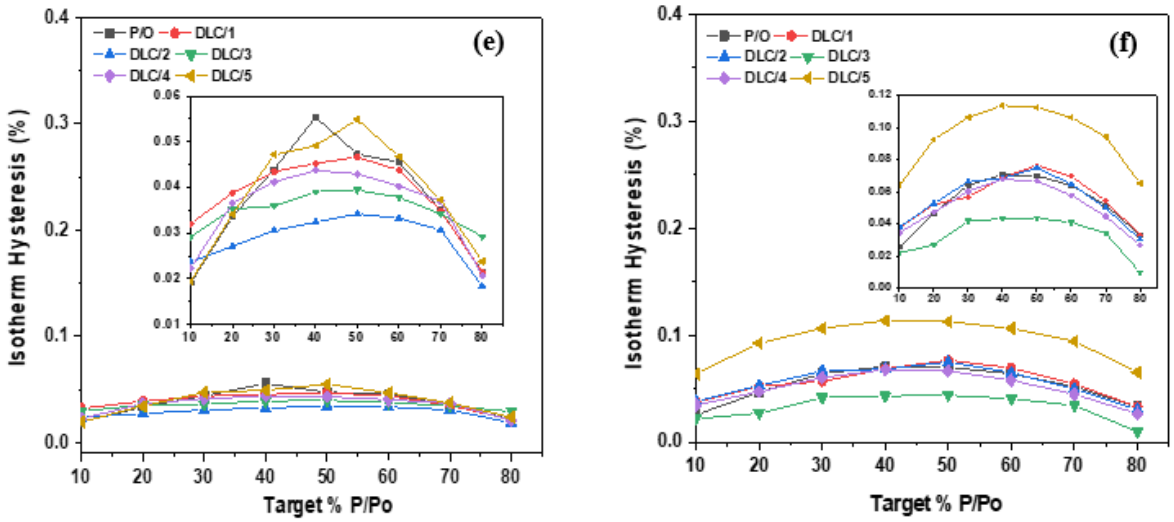

Figure 8-15- Hysteresis of the isotherm plot for moulded ABS (e) 25 °C and (f) 40 °C.

8.4 Summary

In this chapter, the correlation between the polymer and coating properties on the water barrier performance has been studied. The WVTR function for the uncoated polymers showed a highly permeable 3D ABS film with an average WVTR of 73.31gm/m^2-day as opposed to 28.8gm/m^2/-day for Verogray. The detected porosity and pore size distribution function from the MICP analysis confirms these findings as well as the AFM study, where 3D ABS was shown to possess higher porosity than its Verogary counterpart [293]. In literature, the best WVTR reported for pristine uncoated polymers are the PET films with a WVTR of 0.1 – 2 g/m^2-day [294]. However, it is important to note that these polymers (moulded or extruded polymers) perform differently due to their unique properties. They possess different chemistry [23] and their process of manufacturing differs from AM processes. As several studies have been conducted in the past to understand the WVTR limitations for moulded or

extruded polymer-based material, but, none accomplished in the study of AM parts, this work, therefore, seeks to originate the study of these materials for engineering applications.

The MOCON permeation test was further utilised to determine if the influence of nitrogen gas flow would affect the WVTR function of DLC films deposited on both 3D ABS and Verogray samples. In this study, both DLC/1 and DLC/3 films were studied. Data from the test showed an improvement in barrier performance for both coated 3D substrates as a result of the film thickness and improved nucleation of the DLC film on the individual substrates. Further tests using textured coated surfaces were compared to both untextured and pristine uncoated substrates to understand the limitations of aspect ratio on the barrier performance of both 3D ABS and Verogray substrates. A comparison between both textures and untextured surfaces for the uncoated polymers show higher water transmissivity for all cases involving the textured surface. However, with the introduction of DLC coating on the textured surfaces studied, varying degrees of barrier responses were achieved, wherein in all cases, the WVTR was lowered in comparison with their uncoated counterpart. The effect of C_2H_2 gas flow ratio on the WVTR function show a highly pervious coating structure when the C_2H_2 gas flow is increased.

Even though the lowest WVTR of 0.5 - 3.7 g/m^2-day has been reported in the literature for a Si-DLC coating [315], the use of the MW-PECVD technique for depositing N-doped DLC under 40 ℃ may provide an additional tool for exploring DLC coating for improving coating performance.

The water absorption properties using dynamic vapour sorption showed characteristic variation in the sorption properties for both coated and uncoated samples under constant and varying temperatures at a set humidity exposure. It was observed that at a constant temperature, bulk sorption become very dominant for 3D ABS after 20 % P/P_o (relative humidity), whilst that of Verogray was seen to be gradual. It was further revealed that at higher temperatures, the rate of sorption increases as the P/P_o increases.

Chapter 9

General Discussion

9.1 Introduction

In this chapter, the experimental result sections are discussed, highlighting the key findings, and how they compared with literature. The novelty of this work brings to the realization of the complex interaction between additively manufactured polymers and DLC coatings in the creation of robust functional surfaces for applied applications.

This work has explored the viability of using plasma-enhanced technology, more specifically MW-PECVD in the synthesis and deposition of a:C:N:H DLC coating unto 3D printed polymers manufactured using photocurable resins. Two photocurable polymer types namely, 3D ABS and Verogray have been successfully coated and characterised using DLC coating. By this technique, the advantage of generating microwave-assisted plasma and their sustainability thereof without using substrate biasing in the creating of uniform and functional coating at temperatures below 45 °C is made possible.

The polymers 3D ABS and Verogray, produced using Polyjet additive manufacturing technologies have been fully characterised to understand their performance limitations in terms of their thermal, mechanical, structural chemistry etc., and their suitability for coating using MW-PECVD systems. Post coating assessment of the coating towards more specific mechanical and physical functional applications to increase material robustness for specific project applications are discussed.

The thesis focuses on three key areas namely, sample preparation and characterisation, DLC coating and deposition, and coating assessment and performance analysis. Wherein the former, the additively manufactured polymers are assessed for their material performance before DLC deposition, the latter provides a comprehensive assessment and characterisation of individual coated samples produced.

9.2 Effect of the 3D substrate

Exploring the advantages of thermal analysis for establishing a connection between temperature and specific material properties in vacuum was deemed essential for this study, most especially in plasma vacuum deposition. In the study of the thermal degradation behaviour of the individual substrates, the

quantitative mass loss or gain for all samples showed characteristic changes to mass loss based on the decomposition environment. In a nitrogen-controlled environment, the decomposition was seen to be much delayed, where for the 3D ABS, the onset of decomposition (T_1) was reached at 206 ℃ as against 128 ℃ for air. Similar trends regarding the individual decomposition onset temperatures were seen to be evident in the case of Verogray samples wherein nitrogen rather than air, an initial decomposition temperature of 125 ℃ instead of 102 ℃ was observed. As similarly observed by Sarac *et al*. [294] and Gu & Liang [295], polymer decomposition in nitrogen occurs at higher temperature in comparison with decomposition in air, as the path required for the phase transition is usually controlled by lower activation energy in an air controlled environment compared with random chain incision polymer decomposition in nitrogen [294]. By exposing polymers, especially ABS at higher temperatures under an oxygen-containing environment, the abstraction of hydrogen by oxygen is shown to be thermodynamically favoured because of the presence of tertiary substituted C atom within the polybutadiene phase. Following on from the reaction regime proposed by Shimada and Kabuki [296], certain degradation by-products may further decompose to create polymer radicals to promote crosslinking which may create microstructural incoherence on the surface acting as stress concentration sites at higher temperatures. Hence, the determination of the minimum energy required to initiate atomic or molecular chain movement within the polymer structure. This is usually defined by the activation energy of the PBM and is key in understanding the thermodynamic state of the polymer phase during decomposition.

For both polymers, the activation energies were determined using the Murray-White plot from the TGA data (Table 4.1). In both cases involving N_2 and air, the activation energies for the individual samples show observable differences between their thermodynamic state wherein the case involving N_2, the calculated mean activation energy is seen to be less than in air. Further statistical analysis using the t-test confirms the null hypothesis under a nitrogen-controlled environment wherein both cases involving 3D ABS and Verogray, a calculated p-value of 2.2E-4 was made. The alternate hypothesis was the case under the air-controlled environment where a p-value of 0.89 was calculated.

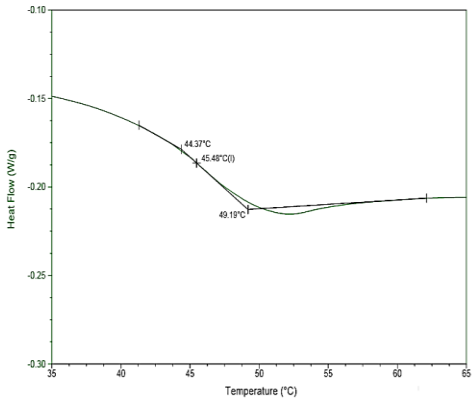

Figure 9-1- Heat flow versus temperature plot for the determination of T_g for Verogray sample.

Polymeric based materials could further be understood in terms of their structural transition when heated or cooled below their T_g temperature. To provide greater emphasis on the quantitative liquid-glass transition phenomenon for 3D ABS and Verogray samples analysed, a graphical representation of a typical glass transition plot shown as heat flux versus temperature plot is given in Figure 9-1. From the heat flux versus temperature curves, the T_g calculated for both 3D ABS and Verogray were 56 ℃ and 46 ℃ respectively. From the heat flux curve, a typical amorphous-like structure was observed for both substrates as no crystallisation phase change was observed when heated or cooled [247]. Kuzman et *al.* [209] conducted a study on the viscoelastic behaviour of 3D printed ABS and PLA polymers using an FDM printer and noted a Tg of 115 ℃ for pure ABS and 70 ℃ for pure PLA polymers. As polymer chemistry and architecture differ in their thermodynamic state when heated or cooled, substrate response in their glassy state may show varying Tg values especially if their chemical structure is altered [179].

The tensile property characterisation of both 3D ABS and Verogray summarises the mechanical properties of the two Polyjet AM polymer parts according to ASTM D-638 for the Type IV testing. In this work, the ultimate tensile strength and modulus have been presented in Table 9-1 for both substrates. A modulus of 1.35 GPa was measured for Verogray with 3D ABS measuring 1.23 GPa. The measured ultimate strength for 3D ABS and Verogray were 53 and 45 MPa respectively.

For the majority of 3D printed parts, several authors have focused primarily on the yield strength, ultimate strength, elasticity and elongation at break [234] where parameters such as raster print orientation, layer thickness etc., have been shown to greatly influence material mechanical properties. In the Fused deposition modelling (FDM) technique, the majority of the literature [297, 298, 234] have reported that the mechanical properties rely on the printing parameters used. The best tensile properties are observed when filaments are aligned parallel and longitudinally to the printing axis, and the worse observed along the build directionality only. Letcher and Waytashek [297] showed that PLA printed parts could have as much as 64 MPa ultimate tensile strength at 45 ° raster. At 0 ° and 90 °, they recorded the lowest ultimate tensile strength at 58 MPa and 54 MPa respectively. Dizon et *al.* [234] recorded 26 MPa tensile strength and 2.2 GPa modulus for FDM printed 3D ABS parts, although for Polyjet manufactured parts, Dizon et *al.* [234] noted a 50 MPa ultimate strength and a 2.2 GPa modulus for Veroclear RGD810.

Even though greater anisotropy in material print behaviour have been reported extensively in the literature where statistical studies have shown greater dependency of material mechanical characteristics to print parameters [234], for this work, the effect of varying key process parameters such as print orientation, speed of print, raster spacing etc. was not explored as a greater number of publications, have shown no or minimal statistical variations in mechanical isotropicity [82, 299].

Table 9-1- Mechanical properties of 3D printed materials.

Process	Material	Modulus (GPa)	Tensile strength at yield (MPa)	Elongation to failure (%)	Strain energy density (MJ/m^3)
3D system/ Polyjet	ABS	1.23±6E-02	53±1E-02	7.6	3.4
3D system/ Polyjet	Verogray	1.35±4E-02	45±4E-02	8.2	2.2

Nanoindentation was used to characterise both hardness and Young's modulus of the coated and pristine test samples. A depth profile showing the variation in hardness and Young's modulus was ascertained wherein the case of Verogray, Young's modulus was seen to decrease with indentation depth until a stable modulus regime was attained at 600 nm. The Young's modulus at the polymer surface was shown to be ~55 % higher than that of ABS at 0.17 GPa as against 0.077 GPa for 3D ABS. However, at an increasing indentation depth of 600 nm, the modulus for both substrates was seen to converge at a minimum, where the calculated modulus for Verogray was 5 % higher than that of 3D ABS at 0.066 as against 0.063 GPa for 3D ABS. These variations were seen to be positively linked to the inhomogeneity in the polymer contact geometry resulting from surface roughness variation necessitated by the inherent surface morphological effect, nanoindentation size effect and polymer structure or chain alignment. Further statistical analysis using t-test showed no significant differences between both samples at a 95% confidence interval.

9.3 Coating deposition & characterisation

Five DLC coatings were synthesised using MW-PECVD technology. For all 5-coating designs, the gas flow rates of Ar, C_2H_2, and N_2 were varied whilst maintaining constant vacuum pressure at 0.012 mbar. The hardness measurements for the individual DLC films up to the depth of 10 % coating thickness is summarised in Table 9-2. Further results are shown in Chapter 6 of this thesis. It was shown that by varying both C_2H_2 and N_2 content within the amorphous DLC film, film mechanical properties such as hardness could be altered for specific functional performance.

Franceschini [273] noted that the aspect of nitrogen incorporation produces achievable limitations in the uptake of nitrogen in an a-C:N:H film where no more than 20 atomic percentage compositions could be achieved in any plasma deposition. He also went further to explain that, the incorporation of nitrogen results in a strong decline in the sp^3 C atomic fraction which dictates a-C:N:H rigidity. As detailed in Table 9-2, the coating hardness was seen to increase as the nitrogen flow rate increased from 0 to 10 sccm and then to 20 sccm for similar C_2H_2 gas flow rates for DLC/1, DL/2 and DLC/3 respectively. It is interesting to also note that as the flow rates for C_2H_2 was reduced by half with the flow rates of N_2 maintained at 10 and 20 sccm for DLC/4 and DLC/5 respectively, both corresponding films exhibited

a gradual reduction in the film hardness. This occurs due to the doping effect of nitrogen, which has been widely used to relieve the internal compressive stress build-up during deposition [273].

Similar to Franceschini [273] observation, it was interesting to note that the maximum nitrogen atomic percentage uptake was not directly related to the N_2 incorporation yield of the deposition environment. By comparing the XPS scan results at the film surface, the true relationship between the coating mechanical properties vis-à-vis nitrogen doping effect on the hardness properties is made known. It was noted that as the flow of N_2 into the chamber increases at constant C_2H_2 flow of 600 sccm for DLC/1, 2 and 3, a disproportionate decrease in the nitrogen content within the individual films were observed. The lowest was seen for DLC/3 which had between 0.52 - 0.17 % atomic N1s composition. Although the role of hydrogen in the stabilisation of sp^3 bonding state has well been established, the addition of nitrogen to the hydrocarbon precursor gas is shown to encourage C sp^2 bonding. This modification in the chemical bonding state is shown in the Raman spectroscopy analysis, where an increased nitrogen content results in a disordered DLC structure towards a more sp^2 bonded graphitic domain, exhibited by decreasing in coating hardness as the ratio of the I_D/I_G decreases.

Table 9-2- Hardness of DLC coating measure at 10% coating thickness on 3D ABS and Verogray.

	Hardness (GPa)				
DLC	1	2	3	4	5
3D ABS	2.97	3.31	4.11	2.67	2.05
Verogray	2.63	3.15	3.15	2.40	2.36

The outcome of the individual scratch test for all five DLC films as coated on both 3D ABS and Verogray (Chapter 5) have been comparatively assessed. Both samples exhibited a larger variation in adhesion strength compared to cracking properties as both polished and unpolished surfaces are evaluated. The test results provide a series of multiple failure mechanisms observed as critical failure points of the individual coatings on both 3D ABS and Verogray samples. It was shown that the variation in surface roughness played an important role in the yield load. Though yielding was seen at lesser loads for coatings with higher hardness for the unpolished substrates, DLC/1, 2 and 3 is seen to be very scratch resistant with higher loads when polished. The increase in surface roughness causing failure at lower yield was also noted by Weidner et *al.* [301] on glass soda-lime coated with DCL. The increase in surface roughness resulted in the lateral cracking and severe sub-interfacial damage of the coating. The substrate effect on the observed coating failure mechanisms establishes that the changes in coating adhesion as observed for both substrates is due to the differences in surface viscoelastic properties mismatch as well as surface roughness variation as observed by Fujisawa *et al.* [302] who noted that coating delamination occurs when there is an elastic modulus mismatch at the substrate/film interface. They further observed that substrate surface roughness below $R_a <$ 0.05µm improves mechanical bonding between the coating and substrate

9.4 Tribology

The tribological function of both DLC coated and uncoated 3D ABS and Verogray substrates have been extensively studied where the effects of surface orientation to applied loads of 1,5 and 10N have been studied. It was shown that other than in the case of 1N load for the uncoated substrates, there were no significant changes observed in the CoF value under both 5 and 10N loads for the parallel and perpendicular print orientations. Similar tests were performed to understand the frictional behaviour for the coated DLC samples under 1 and 5N loads. The 10N load test was excluded as the study on the uncoated sample showed no significant variations in the performance under both print orientations for the 5 and 10N loads. DLC/1, DLC/2 and DLC/3 were studied, and the steady-state time friction response showed that the effect of surface coating provides a significant reduction in the CoF time trend behaviour. By comparing the frictional performance under 1N load for the 3D ABS coated samples, it was seen that DLC/1 showed the highest CoF reduction regardless of orientation to the applied load in comparison with the other coatings tested on the same sample. An average CoF of 0.43 was observed for both orientations under 1N load for DLC/1. However, as the nitrogen incorporation within the film decreases creating harder coating as a result, the CoF is seen to progressively increase for DLC/2 and 3 as the coating deforms under repetitive shear stress (Figure 9-2 (a)).

A comparison made with Verogray using a similar coating, i.e. DLC/1, produced a CoF response of 0.37 and 0.52 for the parallel and perpendicular orientations. Similarly, increasing CoF responses were observed as DLC/2 and 3 coated samples were tested for their tribological function. On average, lower CoF values were recorded for all Verogray samples coated using the different DLCs studied in this work. To probe further on the correlation between the coating adhesion performance and frictional response at the different test loads at 1 and 5N, an SEM surface morphology study was made. The results show an observable relationship between the coating structure and their corresponding tribological performance. DLC/1 coated substrate under 1N shows limited coating failure on the Verogray sample compared with its 3D ABS counterpart where severe tensile coating damage is observed for both parallel and perpendicular print orientations.

It is shown that for all DLC/1 coated surfaces involving 3D ABS, the resulting coating damage does not affect any coating removal from the coated surfaces. As the coating hardness increases, the corresponding surface damage is shown to increase accordingly where the shear strength is large enough to cause severe coating damage due to the brittle nature of the coating. For the coated surface involving Verogray, the deformation regime showed similar increasing trends where coating damage is seen to be most pronounced in the case where the orientation is parallel instead of perpendicular. The coating performance under 5N load exhibited increased resistance to deformation as the transition from a more brittle-like coating to a ductile structured regime is made in the case of DLC/1. Jiang and Arnell [303]

noted that, where the interface between the coating and substrate undergo minimal damage as a result of mild loading, wear performance is subjected to the coating bulk properties. However, as stress build-up within the coating interface and substrate due to high load, the fragmentation and removal of the coating will become apparent resulting from the plastic or fatigue deformation due to the continuous repetitive sliding action of both coating and substrate. Changes in the wear mode arise as both contact pressure and the number of repetitive cycles increases. The principles of contact adhesion defined by Bowden and Tabor on the fundamentals of adhesive friction provide greater insight into the coefficient of friction performance with increasing applied load, where according to this law, the friction force (F) is directly related to the real contact area (A_r) and shear strength (τ) [304] in equation 8.1.

$$F = A_r\tau \ldots\ldots\ldots \quad (9.1)$$

Liu *et al*. [305], in their earlier report on the microscale contact characterisation, proposed that the friction force could be estimated on DLC thin films using the Hertzian theory which gives the contact area (A_r) estimation according to the Hertzian model given by equation 8.2 [306].

$$A_r = \pi[RF_n/K]^{2/3} \ldots\ldots\ldots \quad (9.2)$$

Where K is the effective modulus, F_n is the normal applied load and R is the ball radius. From equation 8.2 it is obvious that the real contact area (A_r) is highly dependent on the applied load and ball size radius. Therefore, it is expected that as the surface area increases with increasing load or ball size, the resulting friction force will increase as a result. This model explains further why the observable friction force increases as the normal load increases. The increase in the coefficient of friction thus is consistent with what was observed by Bowden and Tabor concerning the law of friction. As it is widely known, the friction force encompasses two components which are the adhesive and ploughing friction [304]. The adhesive friction expression is defined in equation 8.1. The ploughing friction (F_P) is given in equation 8.3. Where S is the shear contribution to the total friction force.

$$F = F_P + S \ldots\ldots\ldots \quad (9.3)$$

From this equation, it is seen that the ploughing friction is directly related to the mean pressure (P) required to displace the surface material at the solid-solid contact interface and as such as the surface contact pressure increases with increasing applied load, the friction component defined by ploughing increases. From Figure 9-2 and Figure 9-3, as well as, the complementary morphological study of the individual coated surfaces post friction test detailed in Chapter 7, it can be seen that these surfaces have

undergone wear. The morphology of these surfaces shows some evidence of ploughing and deformation as detailed in Chapter 7 for similar DLC with different load regimes.

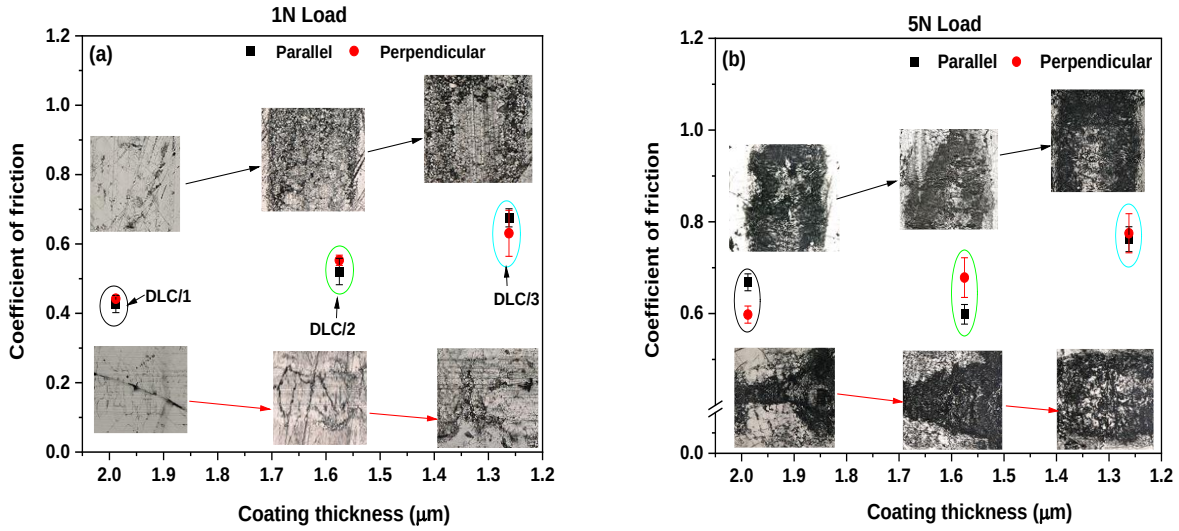

Figure 9-2- Coefficient of friction with coating thickness for 3D ABS for 1N (a) and 5N (b) loads showing the friction performance for each DLC coating.

The morphology shows no wear debris present on the wear track when considering both coated and uncoated surfaces. It is obvious to note that, the pressure at the contact is high enough to initiate ploughing and deformation. Several authors in the study of interfacial sliding have demonstrated the mechanism of film transfer in the study of DLC coatings and have observed that, in all cases, the material removal arise as a result of tribochemical mixed and compact layer transfer owing to the third body material transfer in the form of rolled up debris [306, 307]. In the present case involving both 1 and 5N loads for Verogray and 3D ABS, there is no visible rolled debris at the tribo contact surface indicating the absence of a tribolayer. It is worth noting that, for a chosen value of the applied load, the friction trend with film thickness variation defined by the coating type plays a limiting role in the friction performance but primarily anchored on the mechanical properties of the coating and orientation to the applied load [306, 307]. As previously mentioned, the friction force arising from the sliding contact between two independent bodies is said to be an amalgamation of both the ploughing and adhesive component of the friction force [304]. That notwithstanding, even though there is a continuous interaction between the adhesive and ploughing component of the friction force, the frictional behaviour is not solely dependent on the material property but on also the contact condition [306]. Meaning, depending on the tribological contact, there could be a primary determinant factor in the friction force build-up on the surface which could be exclusive to a single component or a mixture. Yoon *et al.* [308] noted that, for surface making contacts with multiple asperities, the ploughing force term decreases with increasing contact points for similar loads. Therefore, as the orientation to applied load is varied it could

be seen from both Figure 9-2 and that, the ploughing effect is minimal as compared to the parallel orientation.

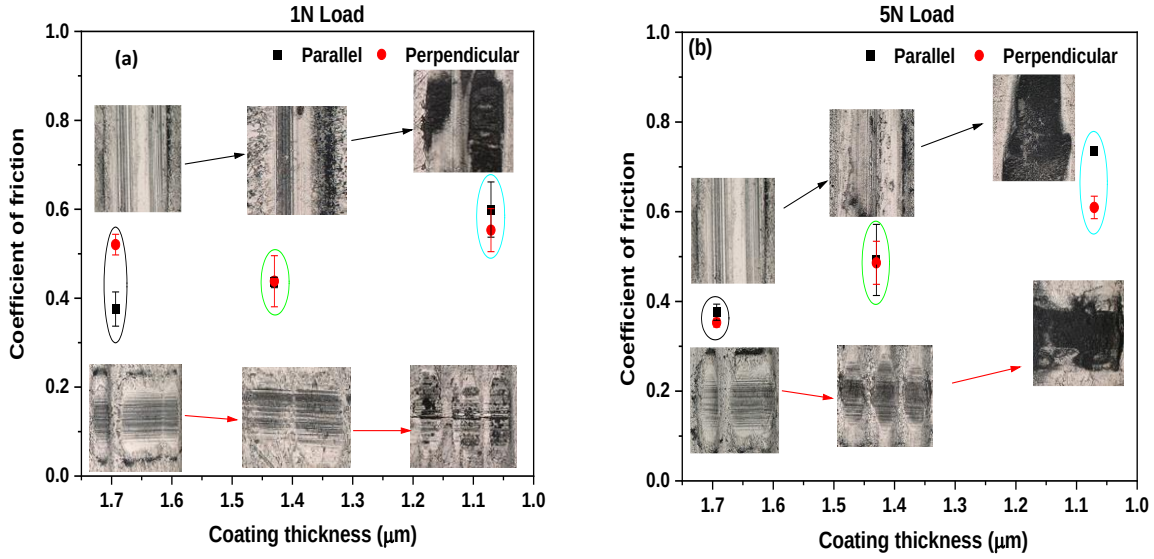

Figure 9-3- Coefficient of friction with coating thickness for Verogray for 1N (a) and 5N (b) loads showing the friction performance for each DLC coating.

9.5 Barrier function

To understand the barrier function and water sorption properties of both coated and uncoated samples, the water vapour transmission rate and sorption mechanism have been studied using both the MOCON PERMATRAN-W model 3/33 equipment and dynamic vapour sorption (DVS) analyser. The effect of gas flow rate on the structural composition and architecture of the resulting DLC are assessed based on their WVTR function. Additionally, the interaction effect in the use of both surface texturing and coating in the optimisation of water vapour transfer through the individual polymers have been well established and extensively discussed in Chapter 8. For both pristine uncoated substrates, the WVTR corresponding to 73.31 and 28.83 gm/m^2-day for 3D ABS and Verogray have been reported. These differences in the WVTR performance show that the factors controlling individual barrier performance could be attributed to the defects owing from the polymer printing technique which is seen to control the polymer WVTR function through the pore distribution structure and function, and surface defect. By using a mercury porosimetry technique through MICP, the detailed pore size distribution and porosity function of both substrates showed varying pore size range from the meso to the macropore characterisation range with detailed analysis shown in Chapter 4. It was shown that for both samples, the minimum pore size radius recorded was at 0.0015 µm with 3D-ABS showing the maximum pore size radius of 3.62 µm in comparison with 0.93 µm for Verogray. This, however, was seen to promote increasing porosity in the 3D ABS sample when compared with its Verogray counterpart. For the 3D ABS, a porosity of 7.7 % was observed with Verogray having a porosity of 6.6 %. Jarvis *et al.* [124]

noted that polymers in general typically have a WVTR of between 0.1-100 g/m^2-day. In a similar investigation, Jarvis *et al.* observed a 2.22 g/m^2-day WVTR for PET films when they compared different test methods. Even though different rate functions were observed for the different tests, they concluded that the validity of the equal rate assumption may have not been met due to material permeability variability.

In the same test, Jarvis *et al.* [124] observed that the WVTR is highly dependent on the relative humidity and further showed that the WVTR of PET could be double from 1.22 to 2.26 g/m^2-day if the RH is also doubled. In a similar study using a much thicker substrate of 100 µm, Zhang *et al.* [127] noted an increase of 48.76 g/m^2-day in the WVTR. However, the use of surface modification to promote suitable barrier function has not been explored in greater detail especially with amorphous diamond-like coatings for 3D printed polymers.

The effect of varying nitrogen gas flow rate in the provision of suitable barrier property function for both substrates is determined. For this study, both DLC/1 and DLC/3 are assessed. The results show a reduction of 24 and ~16 % in the WVTR for 3D ABS when coated with DLC/1 and 3. For Verogray, a reduction corresponding to 60 and ~70.4 % was observed for similar coatings type. It was shown that for the 3D ABS, the barrier performance was highly reliant on the coating thickness and subsequently it's WTR [126]. This theory was confirmed by Ray *et al.* in a similar study to determine the WVTR function of both Si and N doped DLC where he showed the linkage between coating thickness, mechanical properties and WVTR. For coating thicknesses of 1.03 and 1.01µm. They observed a WVTR of 45.98 and 43.70g/m^2-day respectively [126]. For the Verogray sample. It was observed that the reduction in the WVTR was independent of the coating thickness but dependent on the improved coating structure and adhesion, thus providing limited pathways through which water vapour could permeate.

The exploitation of surface texturing effect on the WVTR performance for both substrates (coated and uncoated) have been studied. The effect of aspect ratio size features (defined by textured surfaces A and B) and acetylene gas flow rate variations are studied (Chapter 5). It was shown that samples coated with DLC/5 measured higher WVTR values when compared with similar substrates coated with DLC/3. A morphological study of both surfaces shows clearly the presence of surface crack propagation along the defective plane of the textured trough feature for DLC/5. These cracks upon exposure to water vapour could act as an easy migration path for the diffusion process, thus compromising the integrity of the coating to effectively act as a barrier coating. Similar observations were seen for Verogray samples

It was shown that, by combing textured B and DLC/3 coating, the water WVTR could be reduced by as much as ~74 % when compared with the pristine 3D ABS. A similar comparison with the untextured coated surface shows a 70 % reduction in the WVTR function. However, no measurable differences

were observed for both textured B and untextured coated DLC/3 Verogray substrate in comparison with its 3D ABS counterpart.

Table 9-3- Interaction effect of both surface texturing and DLC single layer coating on the water vapour barrier performance for both coated 3D ABS and Verogray samples.

		WVTR (gm/m^2-day)	
		3D ABS	**Verogray**
Coating	**Textured Surface**		
DLC/2	A	77.86	20.61
	B	36.14	15.45
DLC/5	A	82.68	16.63
	B	69.82	32.34

The interaction effect between surface texturing and DLC coating type has been explored further to understand the limitations surface texturing effect has on the WVTR function for both 3D ABS and Verogray coated samples. In this work both DLC/2 and DLC/5 have been accessed on both textured surfaces A and B as detailed in Chapter 3. For the first part of the WVTR analysis using DLC/2 coating as shown in Figure 8-5, the performance of both textured A and B surfaces show a stable and uniform WVTR function with time. This was also evident in the case of DLC/5 for both textured surfaces. The average WVTR is shown in Table 9-3. From the summary table, it was observed that the highest WVTR is seen in DLC/5 with textured A surface. The lowest WVTR of 15.45 gm/m^2-day was exhibited by the Verogray sample with textured surface B. Further comparison under similar deposition environment for both textured surfaces show for DLC/2 coating on 3D ABS, a reduction of 53.57 % in the WVTR function is achieved when textured B is used rather than A. For Verogray, a 25 % reduction was attained as a result.

An in-depth understanding of the water adsorption and sorption behaviour of both coated and uncoated test substrates using the dynamic vapour sorption technique is studied in this work to complement further, the absorption kinetics of the additively manufactured parts. Depending on the physicochemical properties, polymer materials may provide a greater or less efficient barrier performance against humidity [309]. At a constant temperature of 25 ℃ and relative humidity of 80 %, the water absorption isotherm behaviour of both coated and uncoated substrates behaviour in the form of total water vapour uptake are shown in Figure 8-9 and Figure 8-10 in Chapter 8. As expected in all cases, the highest total weight gain for all three polymers tested was the 3D ABS sample, followed by the Verogray and then moulded ABS. A temperature dependence water vapour sorption isotherm of the sorption-desorption curves at 25 and 40 ℃ at varying RH of 0 to 90 % have shown that for most cases involving each of the three polymers studied, the influence of increasing temperature on the sorption process can not be

underestimated even after providing sufficient barrier layer protection in the form of coating. As the temperature increases from 25 to 40 °C, the hysteresis isotherm response for all samples shows some level of increasing water activity, thus, pushing the percentage of water sorbed to a much higher sorption peak.

Bley *et al.* [158] noted that, when polymers are exposed to higher RH and temperature, water initially form a monolayer on the substrate surface. This is characterised by stronger interaction with the polar group present on the surface acting as a backbone for subsequent multi-layered systems to be formed through hydrogen bonding. For both coated and uncoated polymers, the multi-layer structure could be held up as an adsorbed multi-layer complex or sorbed into the bulk polymer through the diffusion process. It is shown from the isotherm sorption plot for all substrate studied, that, the pressure versus the amount of water adsorbed increases as the saturation pressure increases. This phenomenon is shown as a typical type III adsorption isotherm plot [182], where on the adsorbent surface, several molecules are adsorbed to form a monolayer. The subsequent molecules may either take up the free space available or form a multi-layer structure. As the heat of liquefaction becomes greater than the heat of absorption, a direct multi-layer molecular structure held together by weak van der Waals forces is formed. It is shown in all isotherm plots for the three coated substrates that, as the partial saturation pressure increases, the rate of water sorbed is minimal as weak interaction between adsorbate and adsorbent becomes dominant. At higher saturation pressure, the rate of adsorption increases as there is a strong interaction between the adsorbent and adsorbate molecules. Therefore we can assume that the most important contributing factor to the weight increase as seen in the isotherm plot is as a result of the formation of adsorbed multi-layer molecules of water which may be further absorbed into the polymer matrix as and when a diffusion path is available or created within the coating structure.

9.6 Uniqueness of this coating system

The Hauzer Flexi coating system used in this research boast of an industrial scale deposit chamber with additional multiscale functionality using MW-PECVD technique capable of depositing DLC coating structure at a temperature below 50 °C. Previous work using the same equipment [112, 310] have been used in the deposition of DLC by MW-PECVD onto metallic [310] and polymer substrates [112]. An estimation of the plasma density distribution during deposition by comparing the deposition rates on metallic substrates mounted at different locations with the chamber using one or two MW sources is shown in Figure 9-4. It would seem that by using two MW sources during coating synthesis, lower coating thickness is achieved in comparison with using one MW source (from Figure 9-4). However, for this work, two MW sources were used rather than one, as this is shown to promote uniform plasma density resulting in unvarying coating distribution over the entire substrate surface. MW-PECVD has shown greater potential in producing quicker and faster coating thickness through its enhanced

deposition rate cycle and reduced reliance on substrate biasing to maintain conductivity on the anode to sustain a plasma.

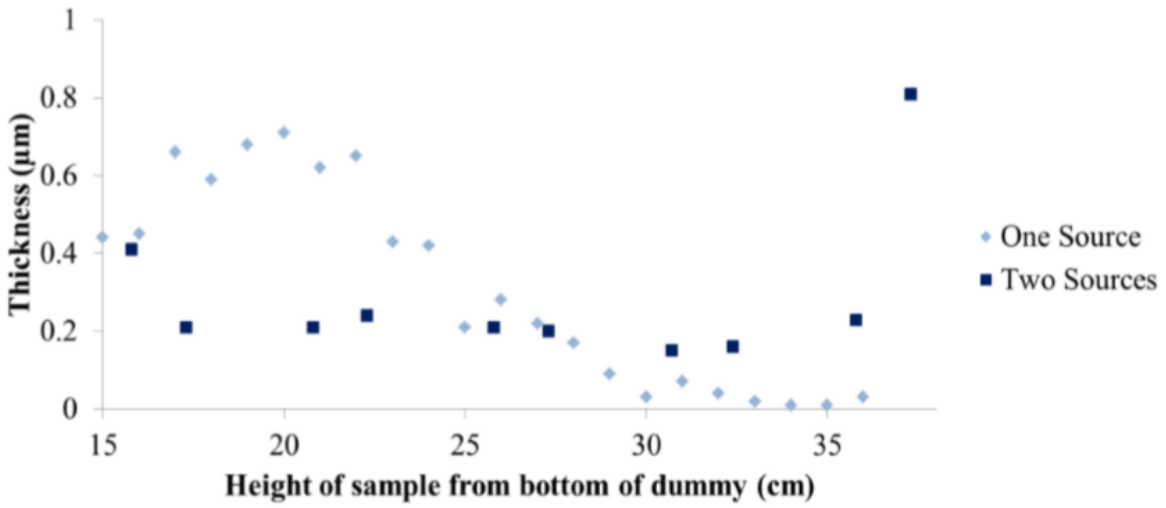

Figure 9-4- Coating thickness plot using one and two microwave sources at different heights from the bottom along with the substrate holder [310]**.**

As can be seen in most conventional deposition systems where the use of large voltage potential difference is created across the working gas to ignite and sustain a plasma body, the Hauzer Flexi Coater is no exception. To maximize the use of this potential, especially in the deposition of conductive substrates like metals, a large negative voltage is often applied to the substrate holder to influence the directionality and energy of the arriving ions to influence generally, the mechanical properties of the coating. This method of deposition throws a greater challenge where non-conductive coatings are synthesized within the deposition chamber. With the constant exposure of the anodic section to the deposition chamber, coating eventually is accumulated on the anode, leading to increased resistivity. A phenomenon known as 'disappearing anode' is created as the coating thickness on the anode increases. This as a consequence, produces plasma instability as a large potential difference cannot be sustained during deposition. As an alternative, the use of MW source during plasma generation and deposition acts to de-couples the bias-circuitry to ensure continuous plasma sustainability to maintain uniform coating deposition and increase deposition rate during coating synthesis. For the work presented in this thesis, the use of substrate biasing was not investigated as the only bias modes available for the FlexiCoater were the DC and DC pulse, which are both known to increase deposition temperatures from ion bombardments.

Regardless of the issues surrounding substrate biasing, especially for insulating and temperature-sensitive substrates such as polymers, the use of RF biasing has proved useful in this regard. However, in large scale designs, where RF biasing technique have been employed, the technical problem with respect to non-uniformity in coating build-up on substrate surfaces have been identified as a drawback.

That notwithstanding, the use of this technique was not exploited as the facility was not available as part of the bias options for the FlexiCoater.

The outcome of this work in terms of coating performance is compared with other works investigated by different authors in the literature to show how the coating synthesised in this work compare with others in terms of both mechanical and water barrier function. In terms of the coating mechanical property shown as coating hardness in Table 9-4, it could be seen that similar measure has been reported by several authors with a marginal magnitude of errors with regards to coating hardness. However, the reported values in this work were generally low.

Table 9-4 - Hardness properties of diamond-like coatings deposited on polymer substrates from the literature

Substrate	Coating	Deposition Technique	Thickness (µm)	Hardness (GPa)	Ref.
PA	DLC	PECVD	-	17.46	[311]
PA	a-C	Sputtering	-	12.75	[311]
PA/PPE	DLC	RF-plasma based	1	2.14 - 3.45	[312]
PMMA	DLC	RF-sputtering	1	4.25 - 6	[313]
PMMA/PET	DLC	Pulse PECVD	~1	1.2 - 15	[314]
PET	a-C:H	PECVD	0.5 – 3.7	2	[315]
PET	ta-C	FCVA	0.5 – 3.7	8	[315]
ABS/PEI	a-C:H	MW-PECVD	~2 - 5	~2 - 5	[112]
3D ABS/Verogray	a-C:N:H	MW-PECVD	~0.5 - 2	2.05 – 4.11	This work

Since the advent of 3D printing of polymers, material manufacturing and testing has been on the ascendency but for most of the work reported in the literature, the use of 3D printed materials have been limited with significant focus around the traditional polymers such as PC, PET, PMMA and PE for their excellent performance in friction control and general application such as optical and scratch resistance. The concept for understanding the limitations in coating 3D printed polymers and their subsequent application in providing barrier performance against water for both textured and untextured substrates have been compared with similar coatings produced in literature. Even though this research is one of its kinds in the development of additively manufactured parts for barrier function application, a comparison in terms of performance to the more traditional polymers is very promising as seen in Table 9-5. The WVTR study proposed in this thesis show an interesting comparison with those reported in the literature where in some cases a significant reduction in the WVTR function are observed.

Table 9-5- WVTR performance properties of carbon coating deposited on polymer from the literature

Substrate	Coating	Deposition Technique	Thickness (µm)	WVTR (gm/m^2-day)	Ref.
PET	a-C:H	PECVD	0.5 – 3.7	0.56	[315]
PET	a-C:H:Si	PECVD	0.5 -3.7	0.03	[315]
PET	a-C:H:N N-flow: 5 sccm	RF PECVD	1.29	45.98	[126]
PET	a-C:H:N N-flow: 20 sccm	RF PECVD	1.28	43.70	[289]
3D ABS **untextured** **textured** **3D Verogray** **untextured** **textured**	a-C:N:H	MW-PECVD	~0.5 – 2 ~0.8 – 1.7	 55.68 18.4 – 82.68 11.41 5.7 – 32.34	This work

Chapter 10

Conclusions

This study has provided a thorough insight into the characterisation and performance of additively manufactured Polyjet polymers, namely 3D ABS and Verogray. The study provides three basic characterisation tools in understanding the physical, structural and chemical limitations possessed by the AM substrate with their coated counterpart. By using a MW-PECVD technique in the synthesis and deposition of hard diamond-like carbon coatings unto the polymer substrate, the creation of a robust functional coating defined by their mechanical, chemical, tribological and barrier performance function are summarised in this chapter along with recommendations for future work. For the first time, an efficient coating structure has been synthesised and deposited onto additively manufactured polymers with acceptable coating adhesion and improved surface properties.

10.1 Sample preparation and characterisation

To understand the limitations and practicality of using AM polymers rather than the more traditional PBMs such as PET, PMMA, PE etc. An investigation into properties such as mechanical, thermal, chemical, porosity and pore size distribution were deemed necessary to establish a solid framework upon which all future coating methods and characterisation shall be based. The following conclusions were drawn:

- For the thermal characterisation of the glass transition state and its associate molecular chain mobility temperature described as T_g for all tested samples, it was shown that 3D ABS and Verogray exhibited typical amorphous behaviour as opposed to either crystalline or semi-crystalline polymer. For both 3D ABS and Verogray samples, a T_g of 56 ℃ and 46 ℃ was obtained.
- The quantitative mass loss or gain due to decomposition for all test samples in both air and the nitrogen-controlled environment was shown to vary as the decomposition temperature was approached. For all cases involving nitrogen, the onset of decomposition was seen to much lower than in air.

- A calculation of the activation energy for the individual samples using Murray-White plot show observable differences between the thermodynamic state wherein nitrogen, the calculated activation energy is seen to be less than in air
- For both samples, the mechanical property characterisation defined by material properties such as modulus, tensile strength and yield, elongation to failure and strain energy density is made. The calculated Young's modulus shows a much stiffer material for Verogray than 3D ABS.
- By using nano-indentation, a correlation was made between Young's modulus and hardness of both materials as defined in the tensile testing. The Young's modulus for Verogray was shown to be ~55 % higher than that of 3D ABS at 0.17 GPa as against 0.077 GPa for 3D ABS
- The frictional performance of the uncoated substrates was shown to be strongly dependent on the surface orientation at 1 N load where surface asperities are seen to play a major role during the reciprocating sliding. However, at higher loads of 5 and 10 N, the bulk mechanical properties affect the coefficient of friction rather to a greater degree than surface roughness.

10.2 DLC coating and deposition

- The MW-PECVD technique used in this work has shown great applicability in the depositing of robust DLC structure that conforms to the substrate surface with good adherence to the polymer surface under scratch testing.
- The method of deposition using MW remote source was made possible using the necessary deposition steps and intermitted cooling periods to achieve a low heating rate and deposition temperature. An achievable deposition temperature of < 45 ℃ has been presented in this work which is made possible due to the lack of substrate bias as a consequence leading to reduced ion flux on the polymer surface.
- For the initial coating recipes deposited, it was seen that coating adhesion on both substrates was fundamentally flawed owing to the high internal and interfacial stress leading to coating delamination through extensive cracking. A revised coating taking advantage of N_2 was introduced to mitigate against this shortfall in adhesion performance.

10.3 Coating assessment and performance analysis

- The adhesion of the modified DLC coating investigated through scratch testing showed great adhesion performance with an increasing progressive load of 0–20N. By assessing their mechanical performance through nano-indentation, a correlation between the coating mechanical properties and coating adhesion property was determined.

- A correlation between the coating hardness and XPS measurement show decreasing atomic N1s percentage within the coating structure as the amount of nitrogen gas flow increases within the deposition chamber.
- Raman analysis of the individual coating shows observable I_D/I_G ratio change as the nitrogen: acetylene gas flow rate changes. The results further suggest a re-ordering of the sp^2 bonded graphitic domain. A good correlation between Raman spectroscopy and XPS further confirmed the DLC film hardness obtained for both 3D ABS and Verogray.
- For the coated sample, the steady-state time frictional response showed that the effect of surface coating provided a significant reduction in the CoF time trend behaviour compared with the uncoated surfaces.
- A morphological analysis of both coated and uncoated worn surfaces show that the friction and wear responses for 3D printed ABS and Verogray at both orientations to the normal applied loads are controlled by different deformation regimes with characteristic evidence of surface coating ploughing and visible fracture failure for 3D coated substrates, whereas, for similar loads, Verogray showed minimal coating deformation characterised by localised spallation and abrasive wear.
- By exploring the water barrier performance of both coated and uncoated samples, it was shown that; for the uncoated polymers, 3D ABS had the highest WVTR function compared to its Verogray counterpart owing to the pore structure present within the polymer matrix, thus contributing to the overall WVTR performance of the material.
- A correlation between coating thickness, adhesion and mechanical properties have shown a positive synergy in the reduction of WVTR.
- The use of surface texturing as a tool in improving the WVTR performance has also shown some positive correlation in the reduction of WVTR for both samples when coated with DLC.
- From the individual absorption isotherm plot, it was concluded that the primary contributing factor to the change in mass is a result of the formation of adsorbed multi-layer molecules of water which may be further absorbed into the polymer matrix as and when diffusion paths are available or created within the coating structure.

10.4 Further work

The work presented in this thesis has shown great potential in the development of improved coating structures for varying functional applications for 3D printed polymers in summary. As the future of 3D printing evolves and its usage in practical mechanical and tribological applications increases, a reliable knowledge base platform shall be required to define and characterise suitable coating recipes to optimise and complement the material performance. As such, an exhaustive study into the limitations of coating

design, adhesion and surface interaction at the atomic scale will help guide this interesting research path.

Hence, these are some further opportunities identified for further studies from this research.

- The exploitation of substrate biasing in improving coating performance and structure for varied functionality.
- The use of Inductively coupled plasma mass spectrometry (ICP-MS) as an added tool in the study of the ion dissociation and charge particle flux in a nitrogen-doped deposition environment.
- An investigation into the stress build-up dynamics of DLCs on 3D polymers and understanding the limitations of doping effect in the control of substrate coating interaction at the near-surface in the reduction of coating failure on polymers especially, 3D printed polymer
- The development of an inhouse permeability kit to study the behaviour and limitations of gas flux through 3D printed polymers and other polymer materials in general
- Understand the role surface roughness play in adhesion optimization in 3D printed polymers.
- Develop a bespoke nanoindentation technique for probing further coating mechanical properties on soft polymer materials, especially 3D printed polymers.
- The exploitation for coating complex features with micron-size features to determine their functional performance to understand the limitations in terms of feature size and aspect ratio could be studied.

References

[1] **S. K. Ghosh, "Functional coatings and microencapsulation: A general perspective," in *Functional Coating,* Weinheim, WILEY-VCH Verlag GmbH & Co, 2006, pp. 1-28.**

[2] **S. T. Douglas and W. G. Stanley, "Costs and cost effectiveness of additive manufacturing: A literature review and discussion," December 2014. [Online]. Available: https://www.slideshare.net/devkambhampati/costs-cost-effectiveness-of-additive-manufacturing. [Accessed 01 July 2019].**

[3] **R. Liu, Z. Wang, T. E. Sparks, F. W. Liou and J. W. Newkirk, "Aerospace applications of laser additive manufacturing," in *Mechanical and aerospace engineering faculty research & creative works,* Elsevier, 2016, pp. 351-371.**

[4] **S. Tranchard and V. Rojas, "Manufacturing our 3D future," 05 May 2015. [Online]. Available: https://www.iso.org/news/2015/05/Ref1956.html. [Accessed 01 December 2019].**

[5] **F. P. Melchels, J. Feijen and D. W. Grijpm, "A review on stereolithography and its applications in biomedical engineering," *Biomaterials,* vol. 31, no. 24, pp. 6121-6130, August 2010.**

[6] **G.-H. Wu and S.-h. Hsu, "Review: Polymeric-based 3D printing for tissue engineering," *Journal of medical and biological engineering,* vol. 35, no. 3, pp. 285-292, 2015.**

[7] **F. Thewihse, S. Karevska, A. Czok, C. Pateman-Jone and D. Kraus, "If 3D printing has changed the industries of tomorrow, how can your organization get ready today?," 2016. [Online]. Available: https://www.ey.com/Publication/vwLUAssets/ey-3d-printing-report/$FILE/ey-3d-printing-report.pdf. [Accessed 01 December 2019].**

[8] **K. Wong, "Wohlers 2017 report on 3D printing Industry points to softened growth," 11 April 2017. [Online]. Available: https://www.digitalengineering247.com/article/wohlers-2017-report-on-3d-printing-industry-points-to-softened-growth/.%5b. [Accessed 01 December 2019].**

[9] **E. Macdonald, R. Salas, D. Espalin, M. Perez, E. Aguilera, M. Dan and R. B. Wicker, "3D Printing for the rapid prototyping of structural electronics," *IEEE,* vol. 242, pp. 234-242, 2014.**

[10] **D. Briggs, Surface analysis of polymers by XPS and static SIMS, Cambridge: Cambridge University Press, 1998, pp. 1-10.**

[11] **I. Kolev, "Coatings on plastics — Technology designed for a wide range of solutions," *SVC Bulletin,* pp. 42-43, 2013.**

[12] **Kruss-scientific, "Kruss-scientific. Adhesion on polymers," [Online]. Available: https://www.kruss-scientific.com/fileadmin/user_upload/website/brochures/kruss-bro-appl-adhesion-polymers-en.pdf. [Accessed 01 December 2019].**

[13] **I. Corporation, "Chemical vapour deposition vs. Physical vapour deposition," 01 December 2015. [Online]. Available: https://www.scribd.com/document/291744475/Cvd-vs-Pvd-Advantages-and-Disadvantages-98752-r0. [Accessed 01 December 2019].**

[14] **Ionbond, "PVD technology," IHI Ionbond AG, 2020. [Online]. Available: https://www.ionbond.com/technology/pvd/. [Accessed 01 December 2019].**

[15] M. Konuma, Konuma. Film deposition by plasma techniques, Berlin: Springer Heidelberg, 1991.

[16] B. Zhang, W. Huang, J. Wang and X. Wang, "Comparison of the effects of surface texture on the surfaces of steel and UHMWPE," *Tribology International* , vol. 65, pp. 138-145, 2013.

[17] Z. Rymuza, "Tribology of polymers," *Archives of civil and mechanical engineering,* vol. 7, no. 4, pp. 177-184, 2007.

[18] W. A. Glaeser, Materials of tribology, Amsterdam: Elsevier, 1992, pp. 651-662.

[19] B. Aldousiri, A. Shalwan and C. W. Chin, "A Review on tribological behaviour of polymeric composites and future reinforcements," *Advances in material science and engineering,* vol. 2013, pp. 1-9, 2013.

[20] U. Petterson and S. Jacobson, "Friction and wear properties of micro-textured DLC coated surface in boundary lubricated sliding," *Tribology Letter,* vol. 17, pp. 553-558, 2004.

[21] H.-G. Elias, An Introduction to polymer science, New York: Weinheim, 1997.

[22] F. W. Billmeyer Jr, Textbook of polymer science, New York: Wiley–Interscience, 1997.

[23] D. W. Van Krevelen and K. Te Nijenhuis, Properties Of polymers: Their correlation with chemical structure; Their numerical estimation and prediction from additive group contributions, Amsterdam: Elsevier, 2009.

[24] J. Izdebska-Podsiadły and S. Thomas, Printing on polymers: Fundamentals and applications, Oxford: Mattew Dean, 2015.

[25] F. J. Davis, Polymer chemistry, New York: Oxford University Press Inc., 2004.

[26] P. J. Flory, Principles of polymer chemistry, New York: Cornell University Press, 1995.

[27] G. Odian, Principles of polymerization, Jersey: Wiley International, 2004.

[28] M. Morbidelli, "Polymerization processes," [Online]. Available: http://www.treccani.it/export/sites/default/Portale/sito/altre_aree/Tecnologia_e_Scienze_applicate/enciclopedia/inglese/inglese_vol_5/369_388_ing.pdf. [Accessed 02 December 2019].

[29] V. R. Gowariker, Polymer science, New York: John Wiley & Sons, 1986.

[30] G. Moad and D. Solomon, The chemistry of free radical polymerization, Oxford: Pergamon, 1995.

[31] J. Brandrup and E. H. Immergut, Polymer handbook, NewYork: Wiley, 1989.

[32] F. R. J. Mayo, *Journal of American chemical society,* vol. 90, pp. 1289-1295, 1968.

[33] K. S. Khuong, W. H. Jones, W. A. Pryor and K. N. Houk, "The mechanism of the self-Initiated thermal polymerization of styrene. Theoretical solution of a classic problem," *American chemical society,* pp. 1265-1277, 2004.

[34] P. J. J. Flory, "Mechanism of vinyl polymerization," *American chemical society,* pp. 241-253, 1937.

[35] **G. Premamoy, "Polymer science: Fundamentals of polymer science," 21 September 2006. [Online]. Available: http://www.scientificspectator.com/documents/polymer%20spectator/Polymer%20Chemistry%20Basic%20concepts.pdf. [Accessed 02 December 2019].**

[36] **J. M. G. Cowie and V. Arrighi, Polymers: Chemistry and physics of modern materials, NewYork: CRC Press, 2007.**

[37] **J. Gu, X. Yang, Z. Lv, N. Li, C. Liang and Q. Zhang, "Functionalized graphite nanoplatelets/epoxy resin nanocomposites with high thermal conductivity," *International Journal of Heat and Mass Transfer,* vol. 92, pp. 15-22, 2016.**

[38] **M. A. Boyle, C. J. Martin and J. D. Neuner, Epoxy resins, 2001.**

[39] **E. c. agency, "Guidance for monomers and polymers," 02 April 2012. [Online]. Available: https://echa.europa.eu/documents/10162/23036412/polymers_en.pdf/9a74545f-05be-4e10-8555-4d7cf051bbed. [Accessed 20 December 2019].**

[40] **N. Buhler and D. Bellug, "Photopolymers as a powerful tool in modern technology," *Pure & Applied chemistry,* vol. 1, pp. 25-31, 1995.**

[41] **additive3d.com, "How Do Photopolymers Work?," 2 August 2016. [Online]. Available: https://additive3d.com/how-do-photopolymers-work/. [Accessed 2019 December 02].**

[42] **"Photopolymers," 2013. [Online]. Available: http://www.photopolymer.com/index.htm. [Accessed 12 September 2013].**

[43] **T. Brock, M. Groteklaes and P. Mischke, European coatings handbook, Hannover: Vincentz Network, 2010.**

[44] **K. Takemoto and K. Kondo, "Synthetic applications of polymer-bound purine and pyrimidine bases," *Reactive polymers, Ion exchangers, sorbents,* vol. 9, no. 1, pp. 71-79, 1988.**

[45] **M. Cho, H. Yoon, D. Feng, H. Yoon and D. Choi, "Photopolymer composed of a photosensitive polymer binder bearing a chalcone moiety in the repeating unit," *Journal of Information display,* vol. 7, no. 2, pp. 6-11, 2006.**

[46] **N. S. Allen, Photopolymerisation and photoimaging science and technology, NewYork: Elsevier Science Publishers Ltd, 1989.**

[47] **BASF, "Photoinitiators," BASF, 2017. [Online]. Available: https://www.dispersions-pigments.basf.com/portal/basf/ien/dt.jsp?setCursor=1_556340. [Accessed 03 December 2019 02].**

[48] **A. D. McNaught and A. Wilkinson, "IUPAC Gold book," 2013. [Online]. Available: http://goldbook.iupac.org/O04286.html. [Accessed 2019 December 02].**

[49] **R. J. Mondschein, A. Kanitkar, C. B. Williams, S. S. Verbridge and T. E. Long, "Polymer Structure-Property Requirements for Stereolithographic 3D Printing of Soft Tissue Engineering Scaffolds," *Biomaterials,* vol. 140, pp. 170-188, 2017.**

[50] **C. Decker, D. Decker and F. Morel, "Light Intensity and temperature effect in photoinitiated polymerization," *American Chemical Society,* pp. 63-80, 1997.**

[51] **J. Fouassier, X. Allonas and D. Burget, "Photopolymerization reactions under visible lights: principle, mechanisms and examples of application," *Progress in Organic Coatings,* vol. 47, pp. 16-36, 2003.**

[52] **A. Calhoun and A. J. Peacoc, "Polymer Chemistry," Hanser, [Online]. Available: http://files.hanser.de/Files/Article/ARTK_LPR_9783446222830_0001.pdf. [Accessed 03 December 2019].**

[53] **A. Bagheri and J. Jin, "Photopolymerization in 3D printing," *ACS Appl. Polym. Mater.,* vol. 1, no. 4, pp. 593-611, 2019.**

[54] **K. S. Lim, B. S. Schon, N. V. Mekhileri, G. C. J. Brown, C. M. Chia, S. Prabakar, G. J. Hooper and T. B. F. Woodfield, "New visible light photoinitiating system for Improved print fidelity in gelatin based bioinks," *ACS Biomater. Sci. Eng.,* vol. 2, no. 10, pp. 1752-1762, 2016.**

[55] **C. P. Kabb, C. S. O'Bryan, C. C. Deng, T. E. Angelini and B. S. Sumerlin, "Photoreversible Covalent Hydrogels for Soft-Matter Additive Manufacturing," *ACS Appl. Mater. Interfaces,* vol. 10, no. 19, pp. 16793-16801, 2018.**

[56] **J. P. Fouassier, X. Allonas, J. Lalevée and C. Dietlin, Photoinitiators for Free Radical Polymerization Reactions. In Photochemistry and Photophysics of Polymer Materials, New Jersey: Wiley, 2010.**

[57] **A. Al Mousawi, F. Dumur, P. Garra, J. Toufaily, T. Hamieh, F. Goubard, T. T. Bui, B. Graff, D. Gigmes, J. Pierre Fouassier and J. Lalevée, "Azahelicenes as visible light photoinitiators for cationic and radical polymerization: Preparation of photoluminescent polymers and use in high performance LED projector 3D printing resins," *Inc. J. Polym. Sci., Part A: Polym. Chem.,* vol. 55, p. 1189–1199, 2012.**

[58] **J. Zhang, F. Dumur, P. Xiao, B. Graff, D. Gigmes, J. Pierre Fouassier and J. Lalevée, "Aminothiazonaphthalic anhydride derivatives as photoinitiators for violet/Blue LED-Induced cationic and radical photopolymerizations and 3D-printing resins," *J. Polym. Sci., Part A: Polym. Chem.,* vol. 54, pp. 1189-1196, 2016.**

[59] **A. Al Mousawi, D. M. Lara, G. Noirbent, F. Dumur, J. Toufaily, T. Hamieh, T. T. Bui, F. Goubard, B. Graff, D. Gigmes, J. P. Fouassier and J. Lalevée, "Carbazole scaffold based photoinitiator/photoredox catalysts: Toward new high performance photoinitiating systems and application in LED projector 3D printing resins," *Macromolecules,* vol. 50, no. 7, pp. 2747-2758, 2017.**

[60] **B. Steinmann, J. Wolf, A. Schulthess and M. Hunziker, "Photosensitive Compositions". USA Patent 5,476,748, 19 December 1995.**

[61] **J. Xu, "Photo-curable resin composition". USA Patent 9090020, 2015.**

[62] **T. Yamamura, T. Watanabe, A. Takeuchi and T. Ukachi, "Photo-curable resin composition used for photo fabcation Of three-dimensional objects". USA Patent 5,981,616, 9 November 1999.**

[63] **Y. Cai and J. L. P. Jessop, "Decreased Oxygen Inhibition in Photopolymerized Acrylate/Epoxide Hybrid Polymer Coatings as Demonstrated by Raman Spectroscopy," *Polymer* , vol. 47, pp. 6560-6566, 2006.**

[64] **A. Bagheri and J. Jin, "Photopolymerization in 3D Printing," *ACS Appl. Polym. Mater.*, vol. 1, no. 4, pp. 593-611, 2019.**

[65] **C. Hull, "Apparatus for production of three-dimensional objects by stereolithography". USA Patent 5,556,590, 17 September 1996.**

[66] **R. Pandey, "Photopolymers in 3D printing application," ARCADA, 2014. [Online]. Available: https://core.ac.uk/download/pdf/38109995.pdf. [Accessed 02 December 2019].**

[67] **ALL3DP, "Stereolithography (SLA) 3D Printing – Simply Explained," ALL3DP, 01 August 2019. [Online]. Available: https://all3dp.com/2/stereolithography-3d-printing-simply-explained/. [Accessed 2020 May 13].**

[68] **RS, "3D Printing Materials," RS , [Online]. Available: https://www.mcad.com/3d-printing/3d-printing-materials/polyjet-materials/. [Accessed 03 December 2019].**

[69] **Stratasys, "PolyJet 3D printers systems and materials," 2018. [Online]. Available: https://www.stratasys.com/polyjet-technology. [Accessed 03 March 2019].**

[70] **J. Koo, R. Ortiz, B. Ong and H. Wu, "Polymer nanocomposites for laser additive manufacturing," *Laser Additive Manufacturing,* pp. 205-235, 2017.**

[71] **H. Bikas, P. Stavropoulos and G. Chryssolouris, "Additive manufacturing methods and modelling approaches: a critical review," *Int J Adv Manuf Technol,* p. 389–405, 2016.**

[72] **K. V. Wong and A. Hernandez, "A Review of Additive Manufacturing," *Mechanical Engineering,* vol. 2012, pp. 1-10, 2012.**

[73] **A. C. Abbott, G. P. Tandon, R. L. Bradford, H. Koerner and J. W. Baur, "Process-structure-property effects on ABS bond strength in fused filament fabrication," *Additive Manufacturing,* vol. 19, pp. 29-38, 2018.**

[74] **X. Wang, M. Jiang, Z. Zhou, J. Gou and D. Hui, "3D printing of polymer matrix composites: A review and prospective," *Composites Part B,* vol. 110, pp. 442-458, 2017.**

[75] **C.-C. Kuo, L.-C. Liu, W.-F. Teng, H.-Y. Chang, F.-M. Chien, S.-J. Liao, W.-F. Kuo and C.-M. Chen, "Preparation of starch/acrylonitrile-butadiene-styrene copolymers(ABS) biomass alloys and their feasible evaluation for 3D printingapplications," *Composites Part B,* vol. 86, pp. 36-39, 2016.**

[76] **Y. Song, Y. Li, W. Song, K. Yee, K.-Y. Lee and V. L. Tagarielli, "Measurements of the mechanical response of unidirectional3D-printed PLA," *Materials and Design,* vol. 123, pp. 154-164, 2017.**

[77] **O. Abdulhameed, A. Al-Ahmari1, W. Ameen and S. H. Mian, "Additive manufacturing: Challenge, trends, and applications," *Advances in Mechanical Engineering,* vol. 11, no. 2, pp. 1-27, 2019.**

[78] **T. D. Ngo, A. Kashani, G. Imbalzano, K. T. Q. Nguyen and D. Hui, "Additive manufacturing (3D printing): A review of materials, methods, applications and challenges,," *Composites Part B: Engineering,* vol. 143, pp. 172-196, 2018.**

[79] **G. Gibbons, R. Williams, P. Purnell and E. Farahi, "3D Printing of cement composites," *Advances in Applied Ceramics,* vol. 109, no. 5, pp. 287-290, 2010.**

[80] **A. L. Duigou, M. Castro, R. Bevan and N. Martin, "3D printing of wood fibre biocomposites: from mechanical to actuation functionality," *Mater Des,* vol. 96, pp. 106-114, 2016.**

[81] **B. E. Carroll, T. A. Palmer and A. M. Beese, "Anisotropic tensile behavior of Ti–6Al–4V components fabricated with directed energy deposition additive manufacturing," *Acta Mater,* vol. 87, pp. 309-320, 2015.**

[82] **A. Sood, O. R.K and S. Mahapatra, "Parametric appraisal of fused deposition modelling process using the grey Taguchi method," *Journal of Engineering Manufacture,* vol. 224, pp. 135-144, 2009.**

[83] **M. Dawoud, I. Taha and S. J. Ebeid, "Effect of processing parameters and graphite content on the tribological behaviour of 3D printed acrylonitrile butadiene styrene," *Mat.-wiss. u. Werkstofftech,* vol. 46, no. 12, pp. 1185-1195, 2015.**

[84] **H. Xiao, Xiao, Hong. (2012). Introduction to Semiconductor Manufacturing Technology (2nd Edition). SPIE, Washington, USA. pp.237-263, Washington: SPIE Press, 2002.**

[85] **D. M. Mattox, Handbook of physical vapour deposition (PVD) processing, New York: Elsevier, 2010.**

[86] **G. N. Strauss and H. K. Pulker, "Process and analysis of different PVD technologies," 2008. [Online]. Available: http://www.phystech-coating.com/pdf/Strauss-Plasma%20analysis%20of%20PVD%20processes.pdf. [Accessed 2017 March 10].**

[87] **R. J. Goldston and P. H. Rutherford, Introduction to Plasma Physics, New York: Taylor & Francis Group, 2000.**

[88] **O. O. Abegunde, E. T. Akinlabi, O. P. Oladijo, S. Akinlabi and A. U. Ude, "Overview of thin film deposition techniques," *AIMS Materials Science,* vol. 6, no. 2, pp. 174-199, 2019.**

[89] **J. E. Mahan, Physical vapor deposition of thin films, New Jersey: Wiley, 2000.**

[90] **D. Depla and S. Mahieu, Reactive Sputter Deposition, Gent: Springer, 2008.**

[91] **A. De Lodyguine, "Illuminant for incandescent lamps". USA Patent 572,002, 12 01 1893.**

[92] **W. A. Bryant, "The fundamentals of chemical vapour deposition," *Journal of Material Science,* vol. 12, pp. 1285-1306, 1977.**

[93] **Indium, "Chemical Vapor Deposition Vs. Physical Vapor Deposition," 2008. [Online]. Available: file:///C:/Users/franx/AppData/Local/Packages/Microsoft.MicrosoftEdge_8wekyb3d8bbwe/TempState/Downloads/cvd_vs_pvd_advantages_and_disadvantages_98752_r0%20(1).pdf. [Accessed 20 December 2019].**

[94] **C. A. Bishop, Vacuum deposition onto webs, films and foils, New York: Elsevier, 2015.**

[95] **H. W. Kroto, J. R. Heath, S. C. O'Brien, R. F. Curl and R. E. Smalley, "C60: Buckminsterfullerene," *Nature,* vol. 318, pp. 162-163, 1985.**

[96] **S. Iijima, "Helical microtubules of graphitic carbon," *Nature,* vol. 354, pp. 56-58, 1991.**

[97] **K. S. Novoselov, A. K. Geim, S. V. Morozov, D. Jiang, Y. Zhang, S. V. Dubonos, I. V. Grigorieva and A. A. Firsov, "Electric field effect in atomically thin carbon films," *Science,* vol. 306, no. 5696, pp. 666-669, 204.**

[98] **J. C. Angus, "Empirical categorization and naming of "diamond-like" carbon films," *Thin Solid Films,* vol. 142, no. 1, pp. 145-151, 1986.**

[99] **S. V. Hainsworth and N. J. Uhure, "Diamond-like carbon coating for Tribology: Production technique, characterization methods and appliation," *International Materials Reviews,* vol. 52, no. 3, pp. 153-174, 2007.**

[100] **H. Moriguchi, H. Ohara and M. Tsujioka, "History and applications of diamond-like carbon manufacturing processes," *Science technical review,* vol. 82, pp. 52-58, 2016.**

[101] **J. Robertson, "Amorphous carbon," *Advances in Physics,* vol. 35, no. 4, pp. 317-374, 1986.**

[102] **J. Robertson, "Diamond-Like amorphous carbon," *Material science and engineering,* vol. 37, pp. 129-281, 2002.**

[103] **A. Erdemir and C. Donnet, "Tribology of diamond-like carbon films: recent progress and future prospects," *Journal of Physics D: Applied Physics,* vol. 39, pp. 2518-2524, 2005.**

[104] **D. R. McKenzie, "Tetrahedral bonding in amorphous carbon," *Report on Progress in Physics,* vol. 59, no. 12, pp. 1611-1664, 1996.**

[105] **S. Matsumoto, Y. Sato and N. S. Mutsukazu Kamo, "The Japan Society of Applied Physics, find out more," *Japanese Journal of Applied Physics,* vol. 21, no. 4A, pp. L183-L185, 1982.**

[106] **M. Ohring, Materials science of thin films, San Diego: Accademic Press, 2002.**

[107] **N. M. J. Conway, A. C. Ferrari, A. J. Flewitt, J. Robertson, W. I. Milne, A. Tagliaferro and W. Beyer, "Defect and disorder reduction by annealing in hydrogenated tetrahedral amorphous carbon," *Diamond and related materials,* vol. 9, pp. 765-770, 20000.**

[108] **Y. Pei, X. .. Bui, X. Zhou and J. De Hosson, "Tribological behavior of W-DLC coated rubber seals," *Surface and Coatings Technology,* vol. 202, no. 9, pp. 1869-1875, 2008.**

[109] **T. Nakahigashi, Y. Tanaka, K. Miyake and H. Oohara, "roperties of flexible DLC film deposited by amplitude-modulatedRF P-CVD," *Tribology International* , vol. 37, pp. 907-912, 2004.**

[110] **N. K. Cuong, M. Tahara, N. Yamauchi and N. Sone, "Diamond-like carbon films deposited on polymers by plasma-enhancedchemical vapor deposition," *Surface and Coatings Technology,* vol. 174–175, p. 1024–1028, 2003.**

[111] **K. Donnelly, D. P. Dowling, M. L. McConnell and R. V. Flood, "Diamond and Related Material," *The effectt of refractive index on the friction coefficient of DLC coated polymer substrates,* vol. 8, pp. 538-540, 1999.**

[112] **S. Carley, "Diamond-like carbon coatings for Improved mechanical performance of polymer materials," University of Leeds, 2017.**

[113] **T. Fu, Z. F. Zhou, Y. M. Zhou, X. D. Zhu, Q. F. Zeng, C. P. Wang, K. Y. Li and J. Lu, "Mechanical properties of DLC coating sputter deposited on surface nanocrystallized 304 stainless steel," *Surface and Coating Technology,* vol. 207, pp. 555-564, 2007.**

[114] Y. Liu, A. Erdemir and E. I. Meletis, "An investigation of the relationship between graphitization and frictional behavior of DLC coatings," *Surface and Coating Technology,* Vols. 86-87, pp. 564-568, 1996.

[115] A. C. Ferrari and J. Robertson, "Interpretation of Raman spectra of disordered and amorphous carbon," *Physical Review,* vol. 61, no. 20, pp. 14095-14107, 2000.

[116] J. Damasceno, S. Camargo Jr, F. Freire and R. Carius, "Deposition of Si-DLC films with high hardness, low stress and high deposition rates," *Surface and Coatings Technology,* Vols. 133-134, pp. 247-252, 2000.

[117] M. S. Kabir, Z. Zhou, Z. Xie and P. Munroe, "Designing multilayer diamond like carbon coatings for improved mechanical properties," *Journal of Material Science & Technology,* vol. 65, pp. 108-117, 2021.

[118] R. Asakawa, S. Nagashima, Y. Nakamura, T. Hasebe, T. Suzuki and A. Hotta, "Combining polymers with diamond-like carbon (DLC) for highly functionalized materials," *Surface and Coatings Technology,* vol. 206, no. 4, pp. 676-685, 2011.

[119] B. D. Beake, "Evaluation of the fracture resistance of DLC coatings on tool steel underdynamic loading," *Surface & Coatings Technology,* vol. 198, pp. 90-93, 2005.

[120] S. Baek and C.-S. Seok, "Fracture characteristics of DLC on silicon using nano-indentation and FEA," *International Journal of Modern Physics B,* vol. 20, no. 25-27, pp. 4213 - 4218, 2006.

[121] D. Bull, *THE LANCET,* vol. 344, no. 8930, pp. 1159-1160, 1994.

[122] S. Carley, "Diamond-like Carbon Coatings for Improved Mechanical Performance of Polymer Materials," University of Leeds, 2017.

[123] B. Ollivier, S. J. Dowey, Y. S. J and A. Mattew, "Adhesion assessment of DLC films on PET using a simple tensile tester: Comparison of different theories," *Journal of Adhesion Science and Tech.,* vol. 9, no. 6, pp. 769 - 784, 2017.

[124] K. L. Jarvisa, P. J. Evansa, N. A. Cooling, B. Vaughanb, J. Habsudac, W. J. Belcherb, C. Bilenb, G. Griffithsa, P. C. Dastoorb and G. Trian, "Comparing three techniques to determine the water vapour transmission rates of polymers and barrier films," *Surfaces and Interface,* vol. 9, pp. 182-188, 2017.

[125] G. Dennler, C. Lungenschmied, H. Neugebauer, N. S. Sariciftci and A. Labouret, "Flexible, conjugated polymer-fullerene-based bulk-heterojunction solar cells: Basics, encapsulation, and integration," *Journal of Materials Research,* vol. 20, no. 12, p. 3224–3233, 2005.

[126] S. C. Ray, D. Mukherjeeb, S. Sarmaa, G. Bhattacharyac, A. Mathurd, S. S. Royc and J. A. McLaughlin, "Functional diamond like carbon (DLC) coatings on polymer for improved gas barrier performance," *Diamond & Related Materials,* vol. 80, p. 59–63, 2017.

[127] Z. Zhang, R. Song, G. Li, G. Hu and Y. Sun, "Improving barrier properties of PET by depositing a Layer of DLC films on surface," *Advances in materials science and engineering,* 2013.

[128] M. Ohring, Materials Science of Thin Films, San Diego: Accademic Press , 2002.

[129] U. Schulz, "Review of modern techniques to generate anti-reflective properties on thermoplastic polymers," *Applied Optics,* vol. 45, no. 7, pp. 1610-1618, 2006.

[130] K. Yamamoto, T. Harada, N. Tomikawa, H. Uyama, S.-C. Yang and H. Fujiyama, "Temperature measurement of polymer substrates during plasma irradiation," *Thin Solid Films,* vol. 345, no. 1, pp. 94-98, 1999.

[131] F. Sarto, M. Alvisi, E. Melissano, A. Rizzo, S. Scaglione and L. Vasanelli, "Adhesion enhancement of optical coatings on plastic substrate via ion treatment," *Thin Solid Films,* vol. 346, no. 1, pp. 196-201, 199.

[132] P. Vasconcelos, F. Lino, R. Neto and H. P., " Contribution of the phase–matrix interface to the behaviour of aluminium filled epoxies," *Materials Science Forum,* vol. 635, p. 455–456, 2004.

[133] O. Dos Santos Ferreira, A. Stevens and C. Schrauwen, "Quantitative comparison of adhesion in metal-to-plastic systems.," *Thin Solid Films,* vol. 517, pp. 3070-3074, 2009.

[134] E. Occhiello, M. Morra, Morini, G., F. Garbassi and P. Humphrey, "Oxygen-plasma-treated polypropylene interfaces with air, water, and epoxy resins," *Journal of Applied Polymer Science,* vol. 42, no. 2, p. 551–560, 1991.

[135] C. K. Jung, I. S. Bae, S. B. Lee, J. H. Cho, E. S. Shin and S. C. Choi, "Development of painting technology using plasma surface technology for automobile parts," *Thin Solid Films,* Vols. 506-507, pp. 316-322, 2006.

[136] F. Awaja, M. Gilbert, G. Kelly, B. Fox and P. J. Pigram, "Adhesion of polymers," *Progress in Polymer Science,* vol. 34, no. 9, pp. 948-968, 2009.

[137] C. Muhlhan, S. T. Weidner, J. Friedrich and H. Nowack, "Improvement of bonding properties of polypropylene by low-pressure plasma treatment," *Surface abd Coating Technology,* Vols. 116-119, pp. 783-787, 1999.

[138] J. Lai, B. Sunderland, J. Xue, S. Yan, W. Zhao and M. Folkard, *Applied Surface Science,* vol. 252, no. 10, p. 3375–3379, 2006.

[139] F. Messines, N. Gherardi and F. Sommer, *Plasmas and Polymers,* vol. 5, no. 3, p. 151, 2000.

[140] S. Guimond, I. Radu, G. Czeremuszkin, D. J. Carsson and M. R. Wertheimer, *Plasmas and Polymers,* vol. 7, no. 1, p. 71–88, 2002.

[141] O.-J. Kwon, S. Tang, S.-W. Myung, N. Lu and H.-S. Choi, *Surface and coatings technology,* vol. 192, no. 1, pp. 1-10, 2005.

[142] Q. F. Wei, "Surface characterization of plasma-treated polypropylene fibers," *Materials Characterization,* vol. 52, no. 3, pp. 231-235, 2004.

[143] S. Köstler, A. V. Delgado and V. Ribitsch, *Journal of colloid and Interface science,* vol. 286, no. 1, p. 339–348, 2005.

[144] W. Brostow, V. Kovacevic, D. Vrsaljko and J. Whitworth, "Tribology of polymer and polymer-based composites.," *Journal of materials education,* vol. 32, no. 5-6, pp. 273-290, 2010.

[145] H. Unal, A. Mimaroglu, U. Kadioglu and H. Ekiz, "Sliding friction and wear behaviour of polytetrafluoroethylene and its composites under dry condition.," *Material and Design,* vol. 25, pp. 239-245, 2004.

[146] N. K. Myshkin, S. S. Pesetskii and A. Y. Grigoriev, "Polymer Tribology: Current State and Applications," vol. 37, no. 3, pp. 284-290, 2015.

[147] J. F. Archard, "Elastic deformation and the laws of friction," *Royal Society,* vol. 243, no. 1233, pp. 190-205, 24 December 1957.

[148] N. K. Myshkin, M. I. Petrokovets and A. V. Kovalev, "Tribology of polymers: Adhesion, friction, wear, and mass-transfer," *Tribology International,* vol. 38, no. 11-12, pp. 910-921, 2005-2006.

[149] K. Shooter and D. Tabor, "Frictional properties of plastics," *Proceedings of the Royal Society,* vol. B65, p. 661, 1952.

[150] R. C. Bowers, W. C. Clinton and W. A. Zisman, "Frictional behaviour of polyethylene,polytetrafluorethylene and halogenated derivatives," *Lubrication Engineering,* vol. 9, pp. 204-209, 1953.

[151] B. L. Rees, "Static friction of bulk polymer over a temperature range," *Research,* vol. 10, pp. 331-338, 1957.

[152] I. V. Kragelskii, Friction and Wear, Elmsford: Pergamon Press, 1982.

[153] T. Fort, "Adsorption and boundary friction of polymer surface," *J Phys Chem,* vol. 66, pp. 1136-1143, 1962.

[154] Y. Yamaguchi, Tribology of Plastic Materials, vol. 16, New York: Elsevier, 1990.

[155] R. F. King and D. Tabor, "The effect of temperature on the mechanical properties and the friction of plastics," *Pro Phys Soc,* vol. B66, pp. 728-37, 1953.

[156] W. Brostow, V. Kovacevic, D. Vrsaljko and J. Whitworth, "Tribology of polymer and polymer-based composites.," *Journal of Materials Education,* vol. 32, no. 5-6, pp. 273-290, 2010.

[157] M. Mofidi and B. Prakash, "Two-body abrasive wear and frictional characteristics of sealing elastomers under unidirectional lubricated sliding conditions. Tribology - Materials,," *Surfaces & Interfaces,* vol. 4, pp. 26-37., 2010.

[158] M. Salot, "Study on wear resistance of Al-Si alloy using a 3-body dry abrasive wear testing machine," 2016. [Online]. Available: https://www.researchgate.net/publication/332780432_STUDY_ON_WEAR_RESISTANCE_OF_Al-Si_ALLOY_USING_A_3-_BODY_DRY_ABRASIVE_WEAR_TESTING_MACHINE. [Accessed 7 11 2021].

[159] V. A. Bely, A. I. Sviridenok, M. I. Petrokovets and V. G. Savkin, Friction and wear in polymer-based materials., Oxford: Pergamon Press, 1982.

[160] B. Gorlach and W. Holweger, "Future polyimide coatings used in high loaded bearing," *Ind. Lubr. Tribol.,* vol. 57, p. 197–201, 5005.

[161] C. Kang and N. S. Eiss, "Fretting wear of polysiloxane-polyimide copolymer coatings as a function of varying humidity," *Wear,* vol. 158, p. 29–40 , 1992.

[162] A. Grill, "Review of the tribology of diamond-like carbon," *Wear,* vol. 163, p. 143–153., 1993.

[163] W. Kaczorowski, H. Świątek, K. Łuczak, M. Głuszek and M. Clapa, "Impact of Plasma Pre-Treatment on the Tribological Properties of DLC Coatings on PDMS Substrates," *Materials,* vol. 14, no. 433, pp. 1-13, 2021.

[164] W. Kaczorowski, D. Batory, W. Szymanski and P. Niedzielski, "Evaluation of the surface properties of PEEK substrate after two-step plasma modification: Etching and deposition of DLC coatings,," *Surface and Coatings Technology,* vol. 265, pp. 92-98, 2015.

[165] A. Erdemir and C. Donnet, "Prospects, Tribology of diamond-like carbon films: Recent progress and future," *Journal of Physics D: Applied Physics,* vol. 39, no. 18, pp. R311-R327, 2006.

[166] M. K. Menegazzo, R. Berghauser, W. Waldhauser and B. Mizaikoff, "Nitrogen-doped diamond-like carbon as optically transparent electrode for infrared attenuated total reflection spectroelectrochemistry," *Analyst,* vol. 136, pp. 1831-1839, 2011.

[167] B. J. Briscoe and S. K. Sinha, *J Eng Tribol,* vol. 216:401, pp. 216-401, 2002.

[168] W. Arch, "Civ. Mech. Eng.," pp. 7-185, 2007.

[169] N. A. M. Tahir, M. S. Azmi, M. F. Bin Abdollah and F. Redza, "Proceedings of mechanical engineering research Day," pp. 260-261, 2018.

[170] A. K. Sood, A. Equbal, V. Toppo, R. K. Ohdar and S. S. Mahapatra, "An investigation on sliding wear of FDM built parts," *CIRP Journal of Manufacturing Science and Technology,* vol. 5, pp. 48-54, 2012.

[171] B. He, W. Chen and Q. J. Wang, "Surface texture effect on friction of a micro-texture poly(dimethylsiloxane)(PDMS)," *Tribology Letter,* vol. 31, p. 187–197, 2008.

[172] X. Shi and T. Ni, "Effects of groove textures on fully lubricated sliding with cavitation," *Tribology International,* vol. 44, p. 2022–2028, 2011.

[173] A. Daekeon, J. H. Kweon, S. Kwon, J. Song and S. Lee, "Representation of surface roughness in fused deposition modelling," *Journal of material processing technology.,* vol. 209, pp. 15-16:5593-5600, 2009.

[174] H. Yasuda, C. E. Lamaze and L. D. Ikenberry, "Permeability of solutes through hydrated polymer membranes. Part 1 Diffusion of sodium chloride.," *Die Mukromolekulure Chemie,* vol. 118, p. 19–35, 1968.

[175] S. B. Harogoppad, T. M. Aminabhavi and R. H. Balundgi, "Sorption and transport of aqueous salt solution in polyurethane membrane at 25, 44, and 60 degree Celcius," *J. Appl. Polym. Sci,* vol. 42, p. 1297–1306, 1991.

[176] L. W. McKeen, Permeability properties of plastics and elastomers, Amsterdam: Elsevier, 2017.

[177] R. Cowling and G. S. Park, "Permeability, solubility and diffusion of gases in amorphous and crystalline 1,4-polybutadiene membranes.," *J. Membr. Sci.,* vol. 5, p. 199–207, 1979.

[178] B. Crater and T. G. J. Jones, "Permeation of a range of species through polymer layers under varying conditions of temperature and pressure: In Situ measurement methods," *Polymers,* vol. 11, p. 1056, 2019.

[179] I. Kikic, F. Vecchione, P. Alessi, A. Cortesi, F. Eva and N. Elvassore, "Polymer plasticization using supercritical carbon dioxide: Experiment and modelling," *Ind. Eng. Chem. Res.,* vol. 42, p. 3022–3029., 2003.

[180] R. Shogren, "Water vapor permeability of biodegradable polymers," *Journal of Environmental Polymer Degradation,* vol. 5, no. 2, 1997.

[181] M. H. Klopffer and B. Flaconnèche, "Transport properties of gases in polymers: Bibliographic review.," *Oil & Gas Science and Technology,* vol. 56, no. 3, pp. 223-244, 2001.

[182] T. V. Naylor, "Permeation properties, in comprehensive polymers science," *OilField engineering with polymers,* vol. 2, pp. 643-668, 1989.

[183] H. Ko, J. S. Lee and S. M. Kim, "2D Heterostructure for enhanced gas barrier performance via synerbetic effect," *Appl. Sci. Converg. Technol,* vol. 27, no. 6, pp. 144-148, 2018.

[184] D. Ding, H. Hibino and H. Ago, "Grain Boundaries and Gas Barrier Property of Graphene Revealed by Dark-Field Optical Microscopy," *J. Phys. Chem. C,* vol. 122, no. 1, p. 902–910, 2017.

[185] J. Fahlteich, M. Fahland, W. Schönberger and N. Schiller, "Permeation barrier properties of thin oxide films on flexible polymer substrates.," *Thin Solid Films,* vol. 517, no. 10, pp. 3075-3080, 2009.

[186] J. S. Park, H. Chae, H. K. Chung and S. Lee, "Thin film encapsulation for flexible AM-OLED: A review," *Semiconductor Science and Technology,* vol. 26, no. 3, p. 4001, 2011.

[187] J. S. Lewis and M. S. Weaver, "Thin-film permeation-barrier technology for flexible organic light-emitting devices," *in IEEE Journal of Selected Topics in Quantum Electronics,* vol. 10, no. 1, pp. 45-57, 2004.

[188] C. Charton, N. Schiller, M. Fahland, A. Holländer, A. Wedel and K. Noller, "Development of high barrier films on flexible polymer substrates.," *Thin Solid Films,* vol. 502, no. 1-2, pp. 99-103, 2006.

[189] T. Kim, J. Choi and S. Lee, "Water vapor barrier properties of Si–Zn–O/Al multilayer structures.," *Surface and Coatings Technology,* vol. 275, pp. 219-223, 2015.

[190] S. B. Jin, J. S. Lee, Y. S. Choi, Choi, I. S and J. G. Han, "Gas barrier properties of SiON films deposited by plasma enhanced chemical vapor deposition at low temperature as a function of the plasma process parameters.," *Surface and Coatings Technology,* vol. 228, no. 1, pp. S490-S494., 2013.

[191] J. H. Lee, C. H. Jeong, H. B. Kim, J. T. Lim, S. J. Kyung and G. Y. Yeom, "Characteristics of SiOxNy films deposited by inductively coupled plasma enhanced chemical vapor deposition using HMDS/NH3/O2/Ar for water vapor diffusion barrier," *Thin Solid Films,* vol. 515, no. 3, pp. 917-921, 2006.

[192] S. Iwamori, Y. Gotoh and K. Moorthi, "Characterization of silicon oxynitride gas barrier films," *Vacuum,* vol. 68, no. 2, pp. 113-117, 2002.

[193] A. G. Erlat, B. M. Henry, C. R. M. Grovenor, G. A. D. Briggs, R. J. Chater and Y. Tsukahara, "Mechanism of water vapor transport through PET/AlOxNy gas barrier films," *Journal Physical Chemistry B,* vol. 108, no. 3, pp. 883-890., 2004.

[194] W. Lohwasser, O. Frei, H. Serverus and A. Wisard, "Electron-Beam Oxide Coating on Plastic Film for Packaging, Development, Production and Application.," in *Proceedings of the 38th Annual Technical Conference of the Society of Vacuum Coaters,* 1995.

[195] S. Günther, S. Straach, N. Schiller, A. L. Quiceno, A. G. Contreras and R. Ludwig, in *Proceedings of the 52nd Annual Technical Conference of the Society of Vacuum Coaters*, Dresden, 2009.

[196] C. R. Sekhar, D. Mukherjeeb, S. Sarmaa, G. Bhattacharyac, A. Mathurd, S. S. Royc, McLaughlin and J. A, "Functional diamond like carbon (DLC) coatings on polymer for improved gas barrier performance," *Diamond & Related Materials,* vol. 80, pp. 59-63, 2017.

[197] H. Zhao, K.-C. Park and K.-Y. Law, "Effect of surface texturing on superoleophobicity, contact angle hysteresis, and "robustness"," *Langmuir : the ACS journal of surfaces and colloids,* vol. 28, pp. 14925-34, 2012.

[198] N. Man-Kwan, S. Ishan, F. E. Kornel and C. Jian, "Improving Surface Hydrophobicity by Microrolling-based Texturing," *Journal of Micro and Nano-Manufacturing,* vol. 4, no. 10, p. 1115, 2016.

[199] J.-B. Lee and M.-H. Cho, "The effect of surface micro texturing on friction and wear of polyoxymethylene," *Journal of the Korean Society of Tribologists and Lubrication Engineers,* vol. 25, 2009.

[200] F. Dangnan, C. Espejo, T. Liskiewicz, M. Gester and A. Neville, "Friction and wear of additive manufactured polymers in dry contact," *Journal of Manufacturing Processes,* vol. 59, pp. 238-247, 2020.

[201] Stratasys, "Polyjet 3D Printers," Stratasys, [Online]. Available: https://www.stratasys.com/3d-printers/objet1000-plus. [Accessed 1 March 2019].

[202] D. s. c. (DSC). [Online]. Available: http://www.analyses-surface.com/Differential-Scanning-Calorimetry. [Accessed 14 March 2017].

[203] A. Haz, M. Jablonsky, A. Orsagova and I. Surina, "Determination of Temperature Regionsin Thermal Degradation of Lignin," *International Conference Renewable Energy Sources,* pp. 21-23, 2013.

[204] C. Dreistadt, A.-S. Bonnet, P. Chevrier and P. Lipinski, "Experimental study of the polycarbonate behaviour during complex loadings and comparison with the Boyce, Parks and Argon model predictions," *Materials & Design* , vol. 30, no. 8, p. 3126–3140, 2009.

[205] N. M. Ames, V. Srivastava, S. A. Chester and L. Anand, "A thermo-mechanically coupled theory for large deformations of amorphous polymers. Part II: Applications," *International Journal of Plasticity,* vol. 25, no. 8, p. 1495–1539, 2009.

[206] M. R. A. a. O. A. Hasanuzzaman, "Characterization of Porous Glass and Ceramics by Mercury Intrusion Porosimetry.," *Reference Module in Materials Science and Materials Engineering,* pp. 1-9, 2017.

[207] H. Giesche, "Mercury porosimetry: A general (practical) cverview," *Particle&Particle system characterisation,* vol. 23, pp. 9-19, 2006.

[208] A. Riveiro, A. L. B. Maçon, J. del Val, R. Comesaña and J. Pou, "Laser surface texturing of polymers for biomedical applications.," *Front. Phys.,* vol. 6, no. 16, pp. 1-17, 2018.

[209] M. K. Kuzman, N. Ayrilmis, M. Sernek and M. Kariz, "Effect of selected printing settings on viscoelastic behaviour of 3D printed polymers with and without wood," *Materials Research Express,* vol. 6, pp. 1-7, 2019.

[210] V. Bursıkova, V. Navratil, L. Zajıckova´ and J. Janca, "Temperature dependence of mechanical properties of DLC/Si protective coatings prepared by PECVD," *Materials Science and Engineering,* vol. A324, pp. 251-254, 2002.

[211] R. Wiesendanger, "Atomic force microscopy," nanoscience , [Online]. Available: http://www.nanoscience.de/HTML/methods/afm.html. [Accessed 01 January 2020].

[212] N. Verma, "FTIR," [Online]. Available: https://www.iitk.ac.in/dordold/index.php?option=com_content&view=category&layout=blog&id=221&Itemid=. [Accessed 14 March 2017].

[213] W. C. Oliver and G. M. Pharr, "An improved technique for determining hardness and elastic modulus using load and displacement sensing indentation experiments," *J. Mater. Res.,* vol. 7, no. 4, p. 1564–1583, 1992.

[214] C. F.-C. Anthony, Nanoindentation., New York: Springer-Verlag, 2011.

[215] B. Ollivier and A. Matthews, "Adhesion of diamond-like carbon films on polymers: an assessment of the validity of the scratch test technique applied to flexible substrates.," *J. Adhesion Sci. Technol,* vol. 8, no. 6, pp. 651-662, 1994.

[216] P. Benjamin and C. Weaver, "Measurement of adhesion of thin films," *Proc. R. Soc. London,* vol. 254, no. 1277, p. 163, 1960.

[217] D. W. Butler, C. T. H. Stoddart and P. R. Stuart, *J. Phys. D, Appl. Phys. 3,* p. 887, 1970.

[218] N. M. Jennett and O.-J. S, "The scratch test: calibration, verification and the use of a certified reference material," National Physical Laboratory, 12 2002. [Online]. Available: https://www.npl.co.uk/special-pages/guides/mgpg54. [Accessed 01 11 2011].

[219] J. M. Wagner, X-ray Photoelectron Spectroscopy (XPS), New York: Nova Science Publishers, 2011.

[220] S. Bearings, "simplybearings.co.uk," [Online]. Available: https://simplybearings.co.uk/shop/files/52100.pdf. [Accessed 01 September 2020].

[221] B. Bhusha, Introduction to Tribology, New York: John Wiley, 2013.

[222] M. Arjmandia, M. Ramezania, A. Nand and T. Neitzerta, "Experimental study on friction and wear properties of interpenetrating polymer network alginate-polyacrylamide hydrogels for use in minimally-invasive joint implants," *Wear,* Vols. 406-407, pp. 198-204, 2018.

[223] Z. T. Whitepaper, "Friction and Wear of Polymers," Zeus Industrial Products, Inc, 2005. [Online]. Available: http://www.appstate.edu/~clementsjs/polymerproperties/$p$lastics_$f$riction$5f$w$ear.pdf. [Accessed 1 December 2019].

[224] G. Agarwal, A. Patnaik and R. K. Sharma, "Parametric Optimization and Three-Body Abrasive Wear Behavior of Sic Filled Chopped Glass Fiber Reinforced Epoxy Composites," *International Journal of Composite Materials,* vol. 3, no. 2, pp. 32-38 , 2013.

[225] PerkinElmer, "Characterisation of polymer using TGA," [Online]. Available: https://www.perkinelmer.com/labsolutions/resources/docs/APP_CharacterizationofPolymersUsingTGA.pdf. [Accessed 02 December 2018].

[226] C. L. Beyler and M. M. Hirschler, "Thermal decomposition of polymers," [Online]. Available: http://gbhint.tripod.com/papers_5_13_02/368_Beyler_Hirschler_SFPE_Handbook_3.pdf. [Accessed 19 March 2019].

[227] J. D. Peterson, S. Vyazovkin and C. A. Wight, "Kinetics of the thermal and thermo-oxidative degradation of polystyrene, polyethylene and poly(propylene)," *Macromol. Chem. Phys.*, vol. 202, p. 775–784, 2001.

[228] H. Staudinger and A. Steinhofer, *A. Ann. Chem.*, vol. 35, p. 517, 1935.

[229] H. Polli, L. A. M. Pontes, A. S. Araujo, J. M. F. Barros and V. J. Fernandes Jr., "Degradation behavior and kinetic study of ABS polymer," *J.Therm. Analy.Cal.*, vol. 95, p. 131–134, 2009.

[230] J. Charles and G. R. Ramkumaar, "FTIR and thermal studies on polyethylene terephthalate and acrylonitrile butadiene styrene.," *Asian Journal of Chemistry,* vol. 21, no. 6, pp. 4389-4398, 2009.

[231] P. Murray and J. White, *Trans. Br. Ceram. Soc.*, vol. 54, no. 151, 1955.

[232] B. E. Tiganis and L. S. Burn, "The effects Of heat aging On acrylonitrile–butadiene–styrene (ABS) blends," 1999. [Online]. Available: https://www.irbnet.de/daten/iconda/CIB1833.pdf.. [Accessed 19 March 2018].

[233] M. D. Wolkowicz and S. K. Gaggar, "Effect of Ageing on Impact strength of acrylonitrile-butadiene-styrene (ABS) terpolymer," *Polymer Engineering and Science.*, vol. 21, no. 9, pp. 571-575, 1981.

[234] C. Ziemian, M. Sharma and S. Ziemian, "Anisotropic mechanical properties of ABS parts fabricated by fuse deposition modelling," *in D.M. Gokcek (Ed.), Mechanical Engineering, In Tech,* 2012.

[235] I. Durgun and R. Ertan, "Experimental investigation of FDM process for improvement of mechanical properties and production cost„" *Rapid Prototypr,* vol. 20, no. 3, 2014.

[236] K. Lee, S. Wang, B. Fox, E. Ritman, M. Yaszemski and L. Lu, "Poly(propylene fumarate) bone tissue engineering scaffold fabrication using stereolithography: effects of resin formulations and laser parameters," *Biomacromolecules* , vol. 8, pp. 1077-1084, 2007.

[237] M. Stansbury and M. J. Idacavage, "3D printing with polymers: challenges among expanding options and opportunities," *Dent. Mater.*, vol. 32, pp. 54-64, 2016.

[238] J. R. C. Dizon, A. H. Espera Jr., Q. Chen and R. C. Advincula, "Mechanical characterization of 3D-printed polymers," *Additive manufacturing,* vol. 20, pp. 44-67, 2018.

[239] J. Fitoussi, F. Meraghni, Z. Jendli, G. Hug and D. Baptiste, "Experimental methodology for high strain-rates tensile behaviour analysis of polymer matrix composites," *Composites Science and Technology,* vol. 65, p. 2174–2188, 2005.

[240] G. M. Swallowe, Mechanical properties and testing of polymers an A-Z reference, Dordrecht: Springer Science+Business Media, 1991.

[241] S. Muhammad and P.-Y. Jar, "Determining stress–strain relationship for necking in polymers based on macro deformation behavior.," *Finite Elements in Analysis and Design,* Vols. s 70-71, pp. 36-43, 2013.

[242] N. Ayrilmis, M. Kariz, J. H. Kwon and M. K. Kuzman, "Effect of printing layer thickness on water absorption and mechanical properties of 3D-printed wood/PLA composite materials," *The International Journal of Advanced Manufacturing Technology,* vol. 102, no. 10, 2019.

[243] C. I. A. Cueto, "Anisotropy and humidity effect on tensile properties and electrical volume resistivity of fused deposition modeled acrylonitrile butadiene styrene composites," 15 July 2017. [Online]. Available: https://pdfs.semanticscholar.org/c922/53bdbbdec724ece67a3efaa2c5b417a7b639.pdf. [Accessed 02 March 2019].

[244] D. O. Hummel and F. Scholl, Infrared analysis of polymers, resins and additives: An atlas of polymer and plastic analysis, München: Weinheim/Carl Hanser Verlag, 1978.

[245] B. Stuart, "Infrared spectroscopy: Fundamentals and applications," [Online]. Available: http://www.kinetics.nsc.ru/chichinin/books/spectroscopy/Stuart04.pdf. [Accessed 20 March 2017].

[246] P. R. Griffiths and J. A. de Haseth, Fourier Transform Infrared Spectrometry, New York: Wiley, 1986.

[247] N. Vidakis, M. Petousis, N. Vaxevanidis and J. Kechagias, "Surface Roughness Investigation of Poly-Jet 3D printing," *Mathematics,* pp. 1-14, 2020.

[248] G. Chryssolouris, J. Kechagias, J. Kotselis, D. Mourtzis and S. Zannis, "Surface Roughness Modeling of the of the Helisys Laminated Object Manufacturing Process," in *Proceedings of the 8th European Conference on Rapid Prototyping and Manufacturing*, Nottingham, UK, 1999.

[249] T. Dikova, D. Dzhendov, D. Ivanov and K. Bliznakova, "Dimensional accuracy and surface roughness of polymeric dental bridges produced by different 3D printing processes," *Archives of Materials Science and Engineering,* vol. 2, pp. 65-75, 2018.

[250] M. Shimbo, M. Ochi and K. Arai, *J. Coat. Technol.,* vol. 45, p. 56, 1989.

[251] E. Riande, R. Diaz-Calleja, M. Prolongo, R. Masegosa and C. Salom, Polymer Viscoelasticity, Boca Raton: CRC Press, 2000, pp. 322-350.

[252] M. N. van den Donker, R. Schmitz, W. Appenzeller, B. Rech, W. M. M. Kessels and M. C. M. van de Sanden, "The role of plasma-induced substrate heating during high rate deposition of microcrystalline silicon solar cells," *Thin Solid Films,* vol. 511 – 512, pp. 562-566, 2006.

[253] D. F. Franceschini, "Plasma-deposited a-C(N):H Films.," *Brazilian Journal of Physics,* vol. 3, p. 30, 2000.

[254] P. Wang, X. Wang, T. Xu, W. Liu and J. Zhang, "Comparing internal stress in diamond-like carbon films with different structure," *Thin Solid Films,* vol. 515, p. 6899–6903, 2007.

[255] D. R. Mckenzie, D. Muller and B. A. Pailthorpe, *Phys. Rev. Lett.,* vol. 67, p. 773, 1991.

[256] M. Ban, T. Hasegawa, S. Fujii and J. Fujioka, *Diamond Relat. Mater.* , vol. 12, p. 47, 2003.

[257] D. Bootkul, B. Supsermpol, N. Saenphinit, C. Aramwit and S. Intarasiri, "Nitrogen doping for adhesion improvement of DLC film deposited on Si substrate by Filtered Cathodic Vacuum Arc (FCVA) technique," *Applied Surface Science,* vol. 310, p. 284–292, 2014.

[258] N. W. Khun and E. Liu, *Mater. Chem. Phys.,* vol. 126, p. 220, 2011.

[259] B. J. Jeon, S. Lee and J. K. Lee, "Adhesion characteristics of copper thin film deposited on PET substrate by electron cyclotron resonance–metal organic chemical vapor deposition," *Surface and Coating Technolgy,* vol. 202, no. 9, pp. 1839-1846, 2008.

[260] C. Lambare, P.-Y. Tessier, F. Poncin-Epaillard and D. Debarnot, "Plasma funtionalization and etching for enhancing metal adhesion onto polymeric substrates," *Royal Society of Chemistry,* vol. 5, pp. 62348-62357, 2015.

[261] P. A. Wiggins, R. Phillips and P. C. Nelson, "Exact theory of kinkable elastic polymers," *Phys Rev E Stat Nonlin Soft Matter Phys,* vol. 71, no. 2 Pt 1, 2005.

[262] A. Stylianou, D. Yova and K. Politopoulos, "Atomic force microscopy quantitative and qualitative nanoscale characterization of collagen thin films. emerging technologies in non-destructive testing," *V-Proceedings of the 5th Conference on Emerging Technologies in NDT,* vol. 10, no. 1201/b11837-75., pp. 415-420, 2012.

[263] G. E. Stan, D. A. Marcov, A. Popa and M. A. Chusan, "Polymer-like and diamond-like carbon coatings prepared by rf-pecvd for biomedical applications," *Digest Journal of Nanomaterials and Biostructures,* vol. 5, no. 3, p. 705 – 718, 2010.

[264] E. G. Gordeev, A. S. Galushko and V. P. Ananikov, "Improvement of quality of 3D printed objects by elimination of microscopic structural defects in fused deposition modelling," *PLOS ONE,* vol. 13, no. 6, 2018.

[265] J. Fastowicz, M. Grudzin, M. Tecław and K. Okarma, "Objective 3D printed surface quality assessment based on entropy of depth maps," *Entropy,* vol. 21, no. 97, 2019.

[266] M. Constantinou, M. Pervolaraki, P. Nikolaou, C. Prouskas, P. Patsalas, P. Kelires, J. Giapintzakis and G. Constantinides, "Microstructure and nanomechanical properties of pulsed excimer laser deposited DLC: Ag films: enhanced nanotribological response," *Surf. Coat. Technol,* vol. 309, pp. 320-330, 2017.

[267] W. A. Moller, "Appl. Phys.," vol. 56, p. 527, 1993.

[268] W. Moller, *Jpn. J. Appl. Phys,* vol. 34, p. 2163, 1995.

[269] W. Kessels, J. Gielen, M. van de Sanden, L. van Ijzendoom and D. Schram, "Surf. Coatings Technol.," vol. 98, p. 1584, 1998.

[270] A. von Keudel and W. Jacob, *J. Appl. Phys.,* vol. 79, p. 1092, 1996.

[271] A. von Keudell and W. Jacob, *J. Appl. Phys.,* vol. 81, p. 1531, 1997.

[272] F. D. A. Aarão Reis and D. F. Franceschini, "Statistical models for carbon-nitrogen film growth," *F. Phys.*, vol. 61, p. 3417, 2000.

[273] S. R. P. Silva, G. A. J. Amaratunga and J. R. Barnes, *Appl. Phys. Lett.*, vol. 71, p. 1477, 1997.

[274] R. Prioli, S. I. Zanette, A. O. Caride, D. F. Franceschini and F. L. Freire, *J. Vac. Sci. Technol. A*, vol. 14, p. 2351, 1996.

[275] A. C. Fischer-Cripps, Nanoindentation., New York: Springer-Verlag, 2011.

[276] D. F. Franceschini, F. L. J. Freire and S. R. P. Silva, *Appl. Phys. Lett.*, vol. 68, p. 2645, 1996.

[277] S. Bhattacharyya, C. Vallé, C. Cardinaud, O. Chauvet and G. Turban, *J. Appl. Phys.*, vol. 85, p. 2162, 1999.

[278] V. S. Veerasamy, J. Yuan, G. A. J. Amaratunga, W. I. Milne, K. W. R. Gilkes, M. Weiler and L. M. Brown, *Phys. Rev.*, vol. B48, p. 17954, 1993.

[279] J. Schwan, S. Ulrich, V. Batori, H. P. Ehrhardt and S. S. R, *J. Appl. Phys. 80, 440 (1996)*, vol. 80, p. 440, 1996.

[280] C. Liu, D. Hu, J. Xu, D. Yang and Q. Min, "In vitro electrochemical corrosion behavior of functionally graded diamond-like carbon coatings on biomedical Nitinol alloy," *Thin Solid Films*, vol. 496, no. 2, pp. 457-462, 2006.

[281] K.-R. Lee, K. Eun and J. S. Rhee, *Mat. Res. Soc. Symp. Proc.*, vol. 356, no. 233, 1995.

[282] D. F. Franceschini, C. A. Achete and F. L. Freire Jr., *Appl. Phys. Lett.*, vol. 3229, p. 60, 1992.

[283] M. Weiler, S. Sattel, T. Giessen, K. Jung, H. Ehrhardt and V. Veera, vol. 522, 1989.

[284] S. Metin, J. Kaufman, D. Saperstein, J. Scott, J. Heyman and E. Haller, *J. Mater. Res.* , vol. 9, no. 396, 1994.

[285] SchwanJ, D. W, J. K and E. H, *Diamond Relat. Mater*, vol. 3, no. 1034, 1994.

[286] J. Robertson, "Requirements of ultrathin carbon coatings for magnetic storage technology," *Tribology International*, vol. 36, p. 405–415, 2003.

[287] Q. F. Wang, Y. X. Wang, H. L. Wang, N. Fan and F. Y. Yan, "Experimental investigation on tribological behavior of several polymer materials under reciprocating sliding and fretting wear conditions," *Tribology International*, vol. 104, pp. 73-82, 2016.

[288] T. R. Ø. Larsen, "Tribological studies of polymer-matrix-composite," Frydenberg a/s, Copenhagen, 2007.

[289] K. Shooter and R. H. Thomas, "Frictional properties of some plastics," *Research*, vol. 2, pp. 533-539, 1952.

[290] M. Barquins, "Sliding Friction of Rubber and Schallamach Waves," *Materials Science and Engineering.*, vol. 73, pp. 45-63, 1985.

[291] S. Hashmi, "Sensor Materials, Technologies and Applications," in *Comprehensive Materials Processing*, Amsterdam, Elsevier, 2014.

[292] R. Y. Aguirre-Loredo, A. I. Rodriguez-Hernandez and G. Velazquez, "Modelling the effect of temperature on the water sorption isotherms of chitosan films," [Online]. Available: https://core.ac.uk/display/142989609.. [Accessed 03 March 2020].

[293] T. Koop, B. Luo, A. Tsiai and T. Peter, "Water activity as the determinant for homogeneous ice nucleation in aqueous solution," *Nature,* vol. 406, pp. 611-614, 2000.

[294] T. Koop, "The water activity of aqueous solution in equilibrium with ice," *Bulleton of the Chemical Society of Japn.,* vol. 75, pp. 2587-2588, 2002.

[295] O. Bley, J. Siepmann and R. Bodmeier, "Characterization of moisture-protective polymer coatings using differential scanning calorimetry and dynamic vapor sorption," *Journal of Pharmaceutical Sciences,* vol. 98, no. 2, pp. 651-664, 2009.

[296] A. Perrotta, G. Aresta, E. R. J. van Beekuma, J. Palmans, P. van de Weijer, M. R. van de Sandenc, W. E. Kessel and M. Creatore, "The impact of the nano-pore filling on the performance of organosilicon-based moisture barriers," *Thin Solid Films,* Vols. 595, Part B, pp. 251-257, 2015.

[297] G. Abbas, S. Roy, P. Papakonstantinou and J. McLaughlin, "Structural investigation and gas barrier performance of diamond-like carbon based filmon polymer susbstrates," *Carbon,* vol. 45, pp. 303-309, 2005.

[298] T. Šarac, J. Devaux, N. Quiévy, A. Gusarov and M. Konstantinović, "The correlation between elongation at break and thermal decomposition of aged EPDM cable polymer," *Radiation Physics and Chemistry,* vol. 132, pp. 8-12, 2017.

[299] A. Gu and G. Liang, "Thermal degradation behaviour and kinetic analysis of epoxy/montmorillonine Nanocomposite," *Polymer Degradation and Stability,* vol. 80, pp. 383-391, 2003.

[300] J. Shimada and K. Kabuki, " The mechanism of oxidative degradation of ABS resin. Part II. The mechanism of photooxidative degradation," vol. 12, no. 3, pp. 671-682, 1968.

[301] T. Letcher and M. Waytashek, "Material Property Testing of 3D-Printed Specimen in PLA on an Entry-Level 3D Printer," *Proceedings of the ASME 2014 International Mechanical Engineering Congress and Exposition,* vol. 2A, pp. 14-20, 2014.

[302] T. Letcher, B. Rankouhi and S. Javadpour, "Experimental Study of Mechanical Properties of Additively Manufactured ABS Plastic as a Function of Layer Parameters," *Proceedings of the ASME 2015 International Mechanical Engineering Congress and Exposition,* vol. 2A, pp. 13-19, 2015.

[303] A. K. Sood, A. Equbal, V. Toppo, R. K. Ohdar and S. S. Mahapatra, "An investigation on sliding wear of FDM built parts," *CIRP Journal of Manufacturing Science and Technology,* vol. 5, pp. 48-54, 2012.

[304] M. Weidner, O. Borrero-Lopez, M. Hoffman, A. Bendavid and P. J. Martin, "Effect of substrate roughness on the contact damage of thin brittle films," *Thin Solid Films,* vol. 518, no. 18, p. 5242–5248, 2010.

[305] N. Fujisawa, D. R. McKenzie, N. L. James, J. C. Woodard and M. V. Swain, "Combined influences of mechanical properties and surface roughness on the tribological properties of amorphous carbon coatings," *Wear,* vol. 260, no. 1-2, pp. 62-74, 2006.

[306] J. Jiang and R. D. Arnell, "The effect of substrate surface roughness on the wear of DLC coatings," *Wear,* vol. 239, pp. 1-9, 2000.

[307] F. P. Bowden and D. Tabor, The friction and lubrication of solids, Oxford: Clarendon Pres, 1950.

[308] H. Liu, S. I.-U. Ahmed and M. Scherge, "Microtribological properties of silicon and silicon coated with diamond like carbon, octadecyltrichlorosilane and stearic acid cadmium salt films: A comparative study," *Thin solid films,* vol. 381, no. 1, pp. 135-142, 2001.

[309] D. S. Kim, T. E. Fischer and B. Gallois, "The effects of oxygen and humidity on friction and wear of diamond-like carbon films," *Surf. Coat. Technol,* vol. 49, p. 537, 1991.

[310] B. Bhushan, Modern tribology handbook. vol. 2, Boca Raton: CRC Press, 2001, p. 871.

[311] E. S. Yoon, H. Kong and K. R. Lee, "Tribological behavior of sliding diamond-like carbon films under various environments," *Wear,* vol. 217, p. 262, 1998.

[312] O. Bley, J. Siepmann and R. Bodmeier, "Characterization of moisture- protective polymer coating using differential scanning calorimetry and dynamic vapor sorption," *Jorn. of Pharma. Sci.,* vol. 98, no. 2, 2009.

[313] L. B. Austin, "Evaluation and optimisation of diamond-like carbon for tribological applications," University of Leeds, 2014.

[314] W. Fruth, H. Meerkamm, T. Krumpiegl, C. Schaufler, G. Erkens and M. Ruttor, "Tribological behaviour of PVD-coated PA plastic material sliding against metal counterparts. Surface and Coatings Technology," *Surface and Coatings Technology,* vol. 120, pp. 470-475, 1999.

[315] A. Igarashi, H. Hayashi, T. Yamanobe and T. Komoto, "Structure and morphology of diamond-like carbon coated on nylon 66/poly (phenylene ether) alloy," *Journal of molecular structure,* vol. 788, no. 1, pp. 238-245, 2006.

Appendix I

1. Temperature Evolution during deposition (Conti. From Chapter 5)

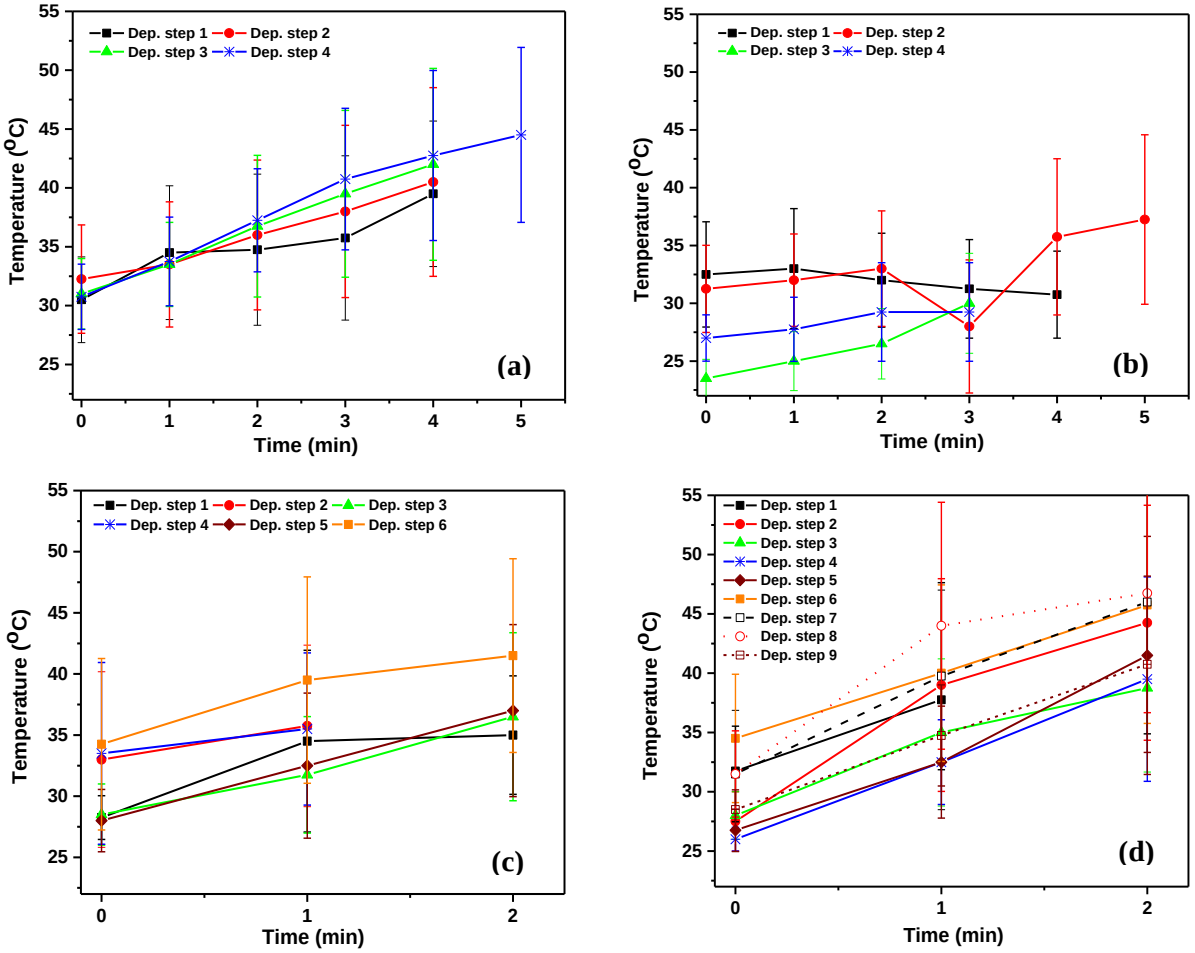

Appendix I- Temperature evolution for DLC/2(a),DLC/3(b),DLC/4(c),DLC/5(d)

Appendix II

Scratch Test (Cont. from Chapter 5)

(a)

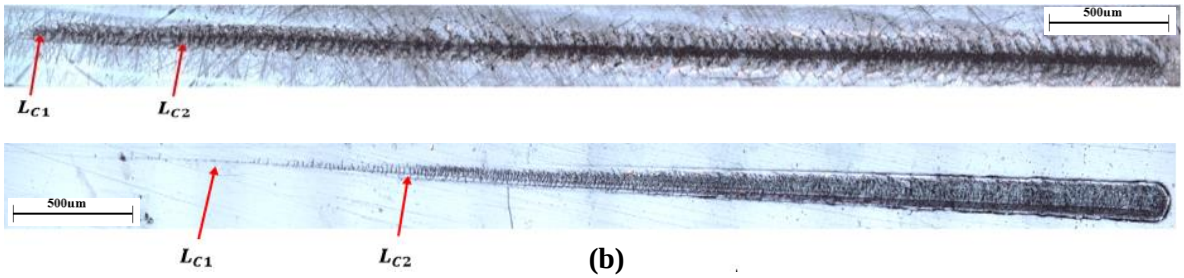

(b)

Figure 0-1- Typical failure mode of DLC/3 coatings on pristine 3D printed ABS (a) Unpolished (b) polished.

(c)

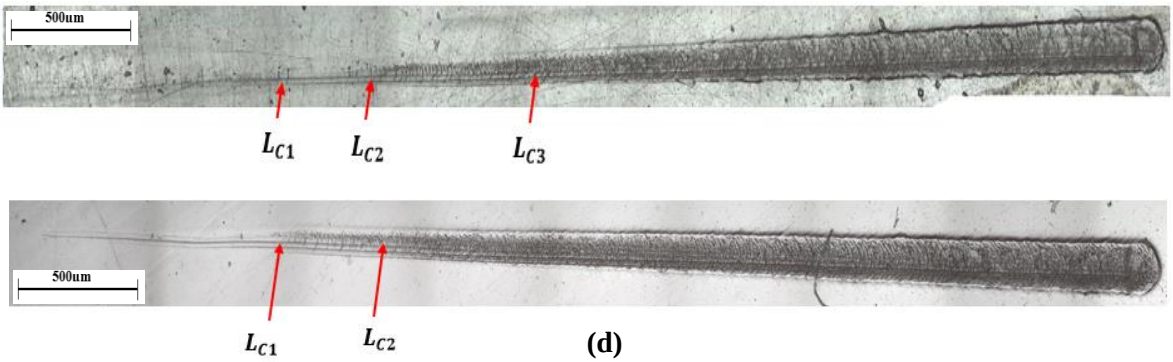

(d)

Figure 0-2- Typical failure mode of DLC/3 coatings on pristine 3D printed Verogray (c) Unpolished (d) polished.

(e)

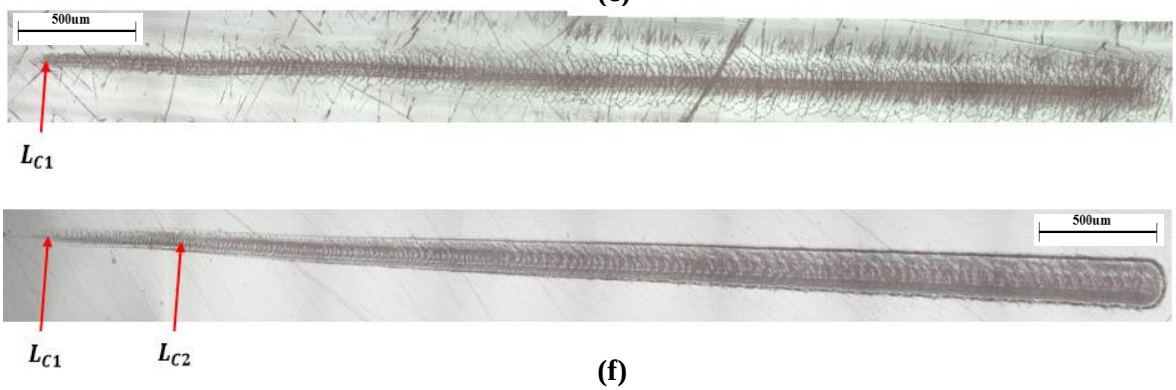

(f)

Figure 0-3- Typical failure mode of DLC/4 coatings on pristine 3D printed ABS (e) Unpolished (f) polished.

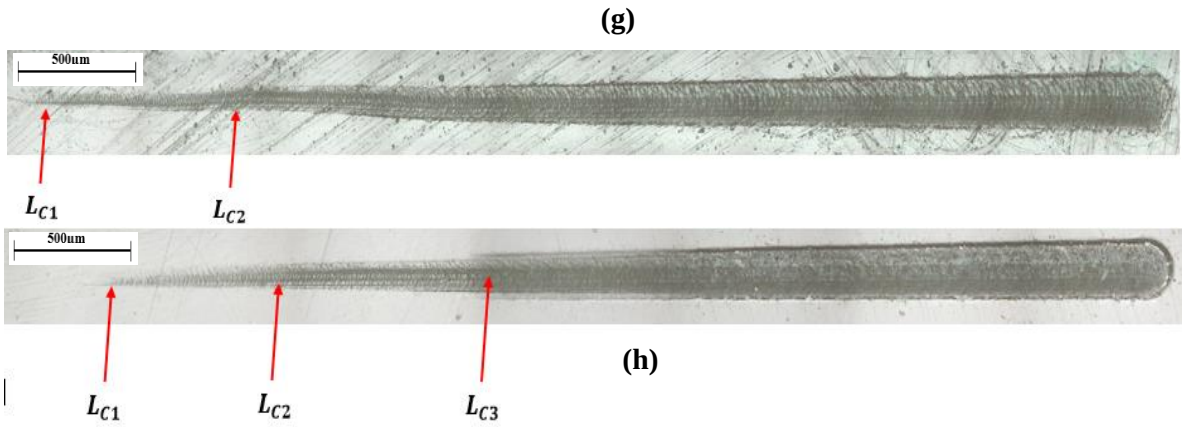

Figure 0-4- Typical failure mode of DLC/4 coatings on pristine Verogray (g) Unpolished (h) polished.

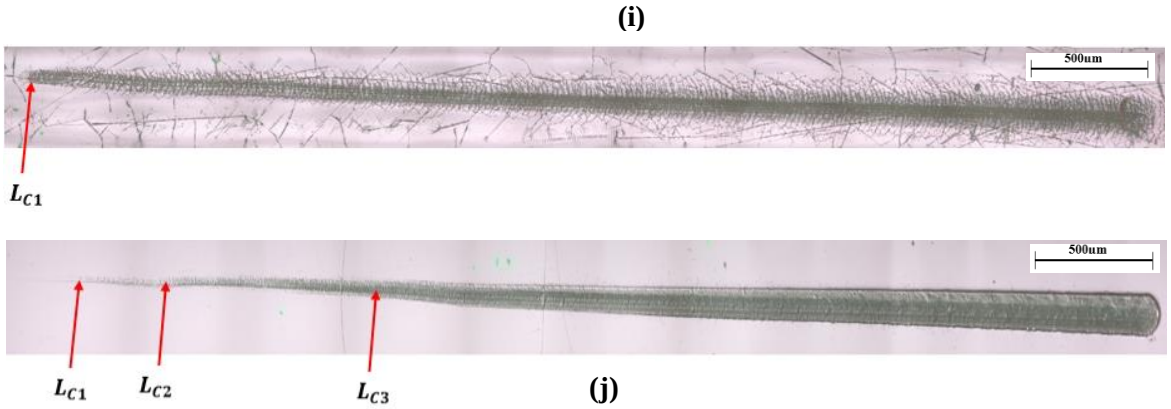

Figure 0-5- Typical failure mode of DLC/5 coatings on pristine 3D ABS (i) Unpolished (j) polished.

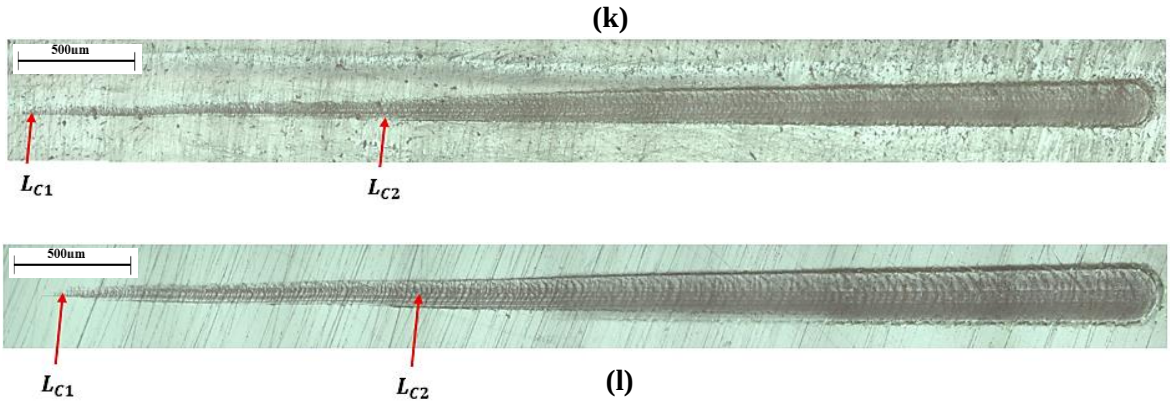

Figure 0-6- Typical failure mode of DLC/5 coatings on pristine Verogray (k) Unpolished (l) polished.

Appendix III

Coating failure after 3 points bending showing coating

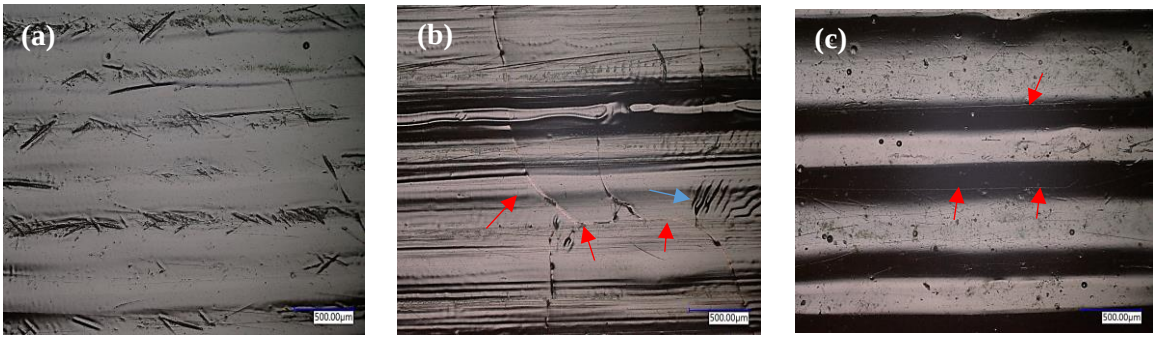

Figure 0-1- Cracking behaviour of DLC/3 coating on 3D ABS after bending showing coating deformation pattern on all three surfaces defined as (a) untextured coated surface (b) textured type A (c) textured type B.

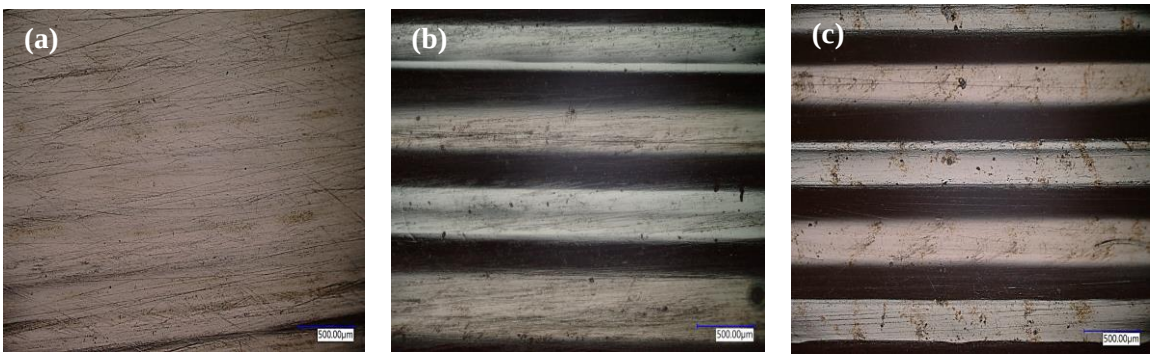

Figure 0-2- DLC/3 coating on Verogray after bending showing coating deformation pattern on all three surfaces defined as (a) untextured coated surface (b) textured type A (c) textured type B.

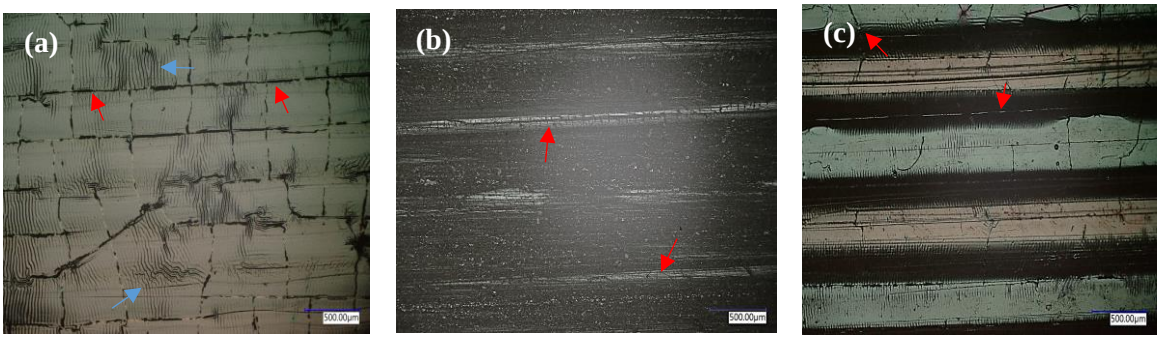

Figure 0-3- Cracking behaviour of DLC/4 coating on 3D ABS after bending showing coating deformation pattern on all three surfaces defined as (a) untextured coated surface (b) textured type A (c) textured type B.

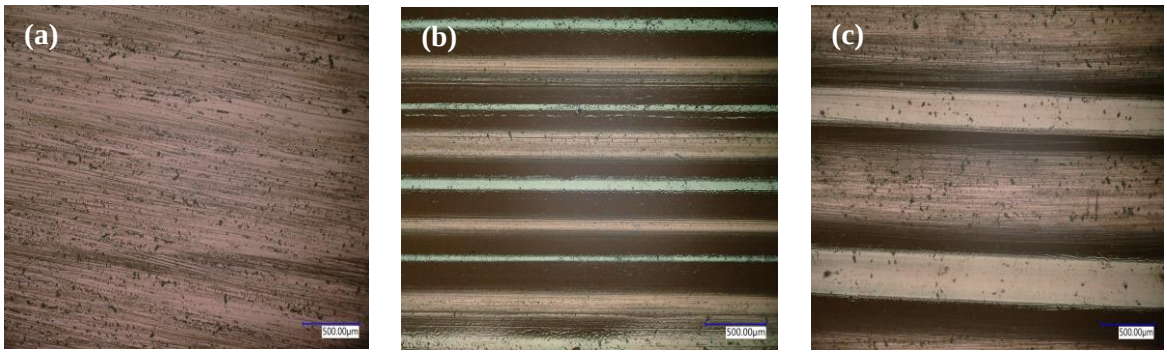

Figure 0-4- DLC/4 coating on Verogray after bending showing coating deformation pattern on all three surfaces defined as (a) untextured coated surface (b) textured type A (c) textured type B.

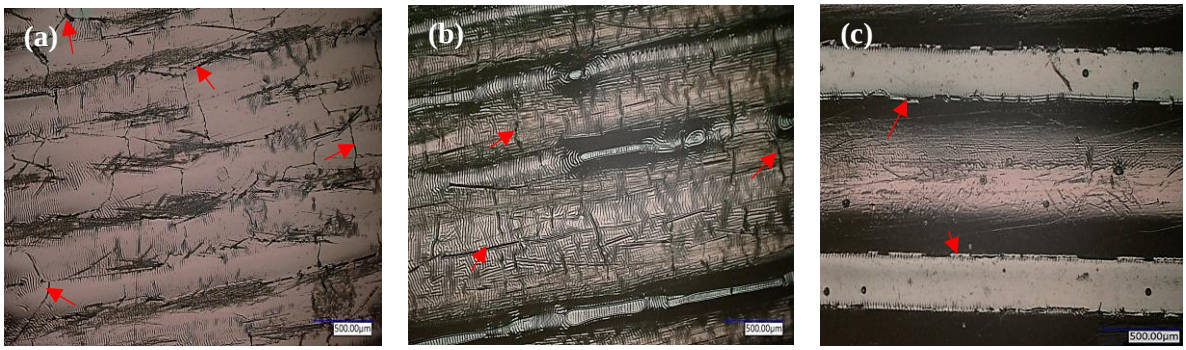

Figure 0-5- Cracking behaviour of DLC/5 coating on 3D ABS after bending showing coating deformation pattern on all three surfaces defined as (a) untextured coated surface (b) textured type A (c) textured type B.

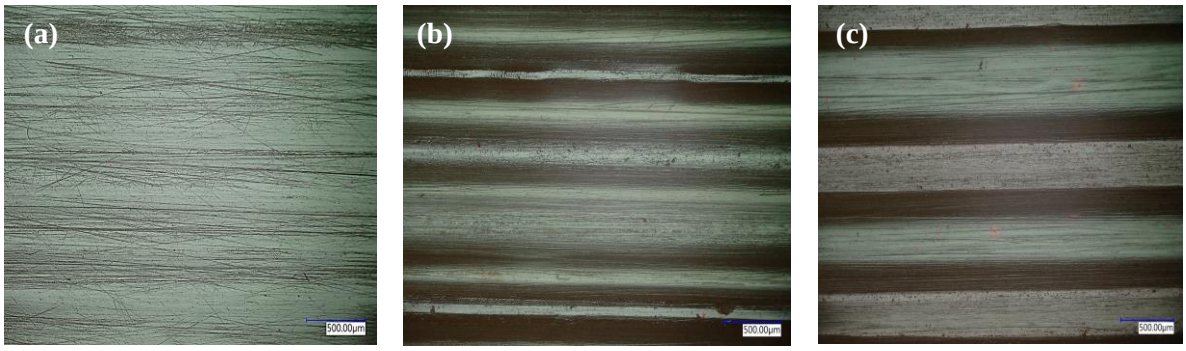

Figure 0-6- DLC/5 coating on Verogray after bending showing coating deformation pattern on all three surfaces defined as (a) untextured coated surface (b) textured type A (c) textured type B.

Appendix IV

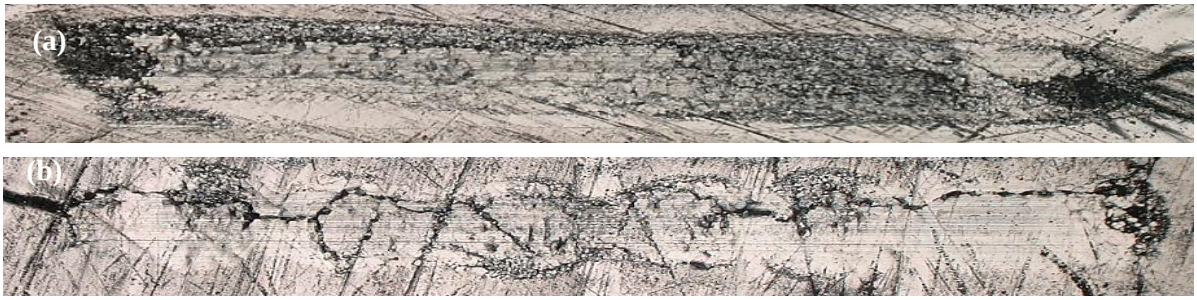

Figure 0-1- DLC/2 coated ABS substrate showing the deformation on (a) parallel (b) perpendicular orientation to the applied load of 1N.

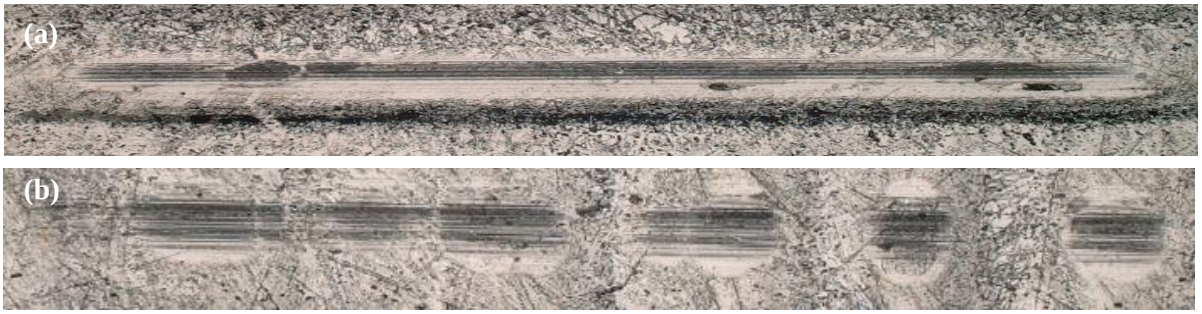

Figure 0-2- DLC/2 coated Verogray substrate showing the deformation on (a) parallel (b) perpendicular orientation to the applied load of 1N.

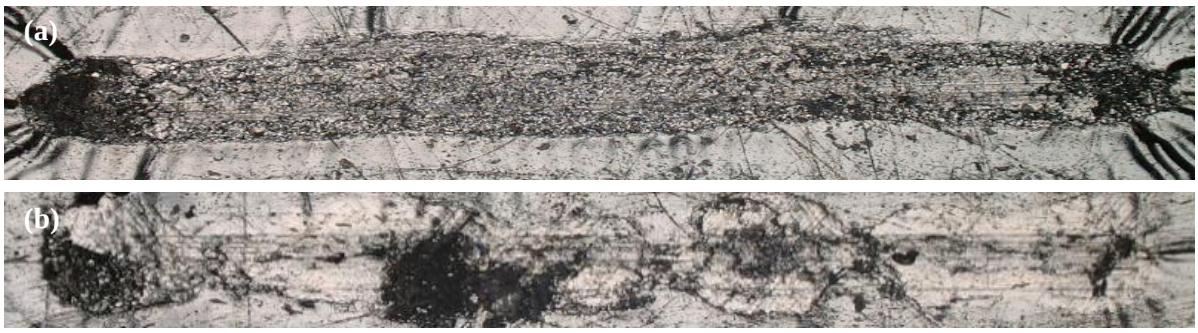

Figure 0-3- DLC/3 coated ABS substrate showing the deformation on (a) parallel (b) perpendicular orientation to the applied load of 1N.

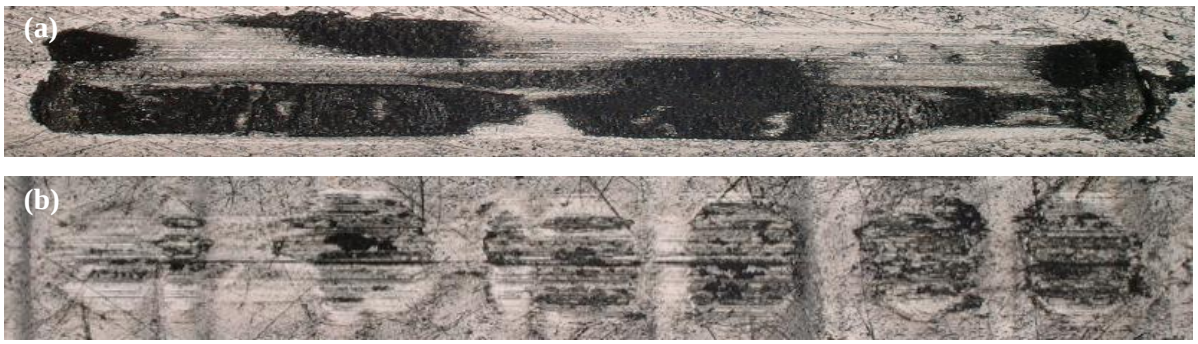

Figure 0-4- DLC/3 coated Verogray substrate showing the deformation on (a) parallel (b) perpendicular orientation to the applied load of 1N.

Appendix V

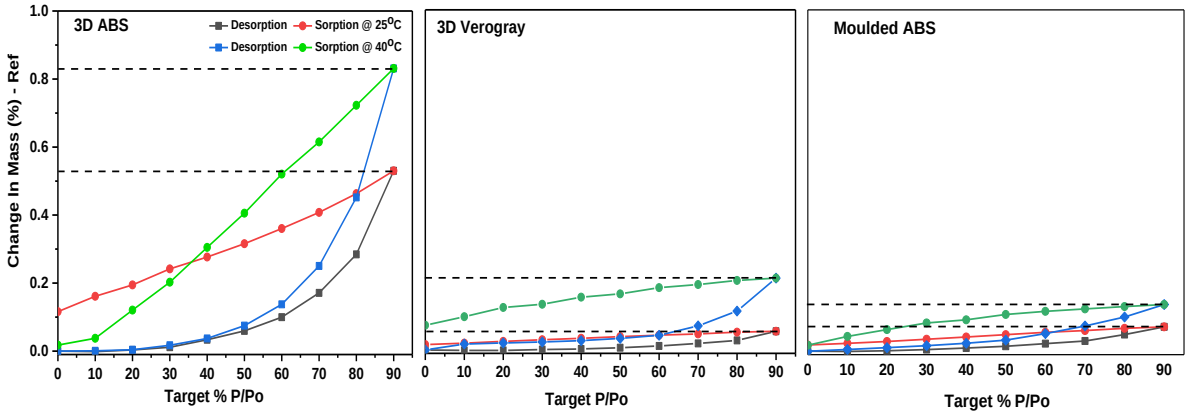

Figure 0-1- Typical isotherm plot for DLC/2 coated 3D ABS, Verogray and moulded ABS showing both sorption and desorption curves at 25 ℃ and 40 ℃.

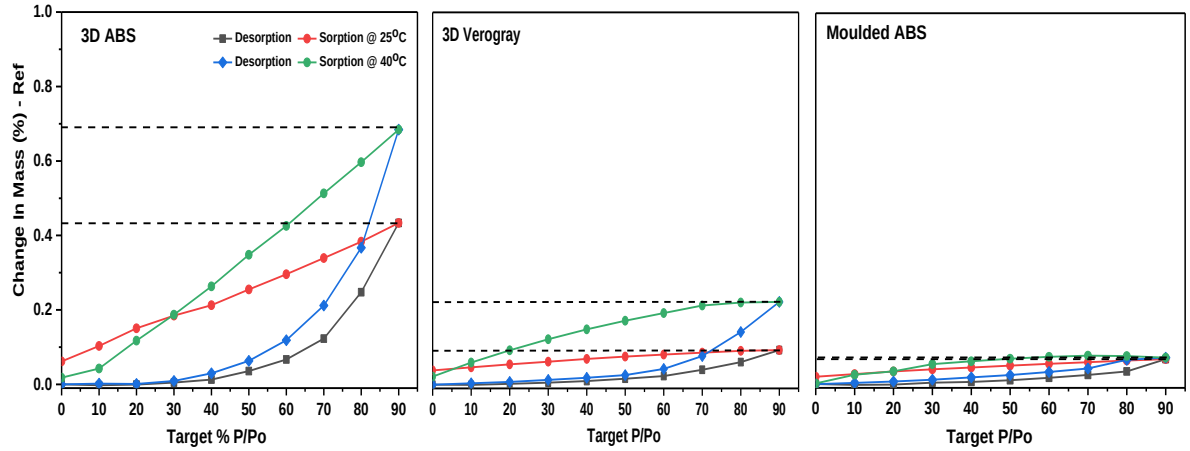

Figure 0-2- Typical isotherm plot for DLC/3 coated 3D ABS, Verogray and moulded ABS showing both sorption and desorption curves at 25 ℃ and 40 ℃.

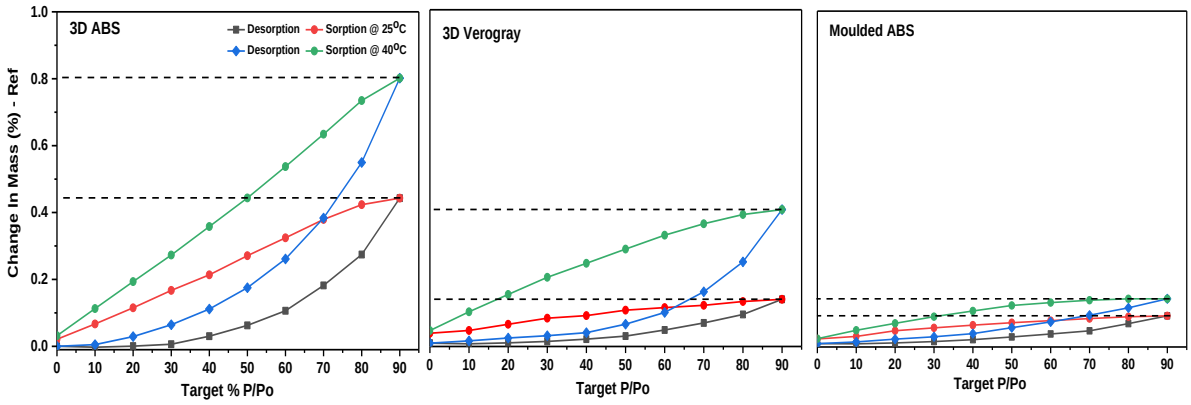

Figure 0-3- Typical isotherm plot for DLC/4 coated 3D ABS, Verogray and moulded ABS showing both sorption and desorption curves at 25 ℃ and 40 ℃

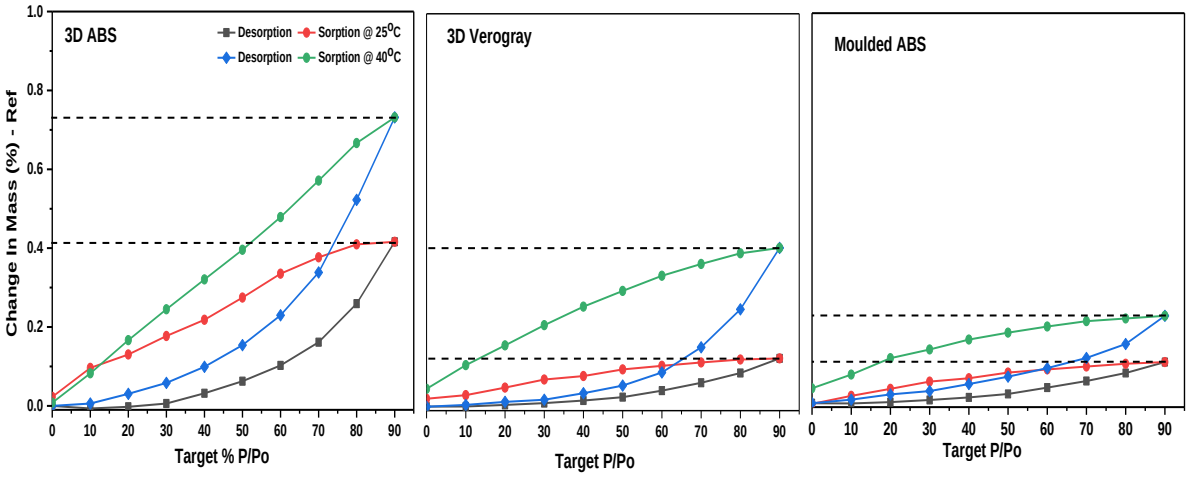

Figure 0-4- Typical isotherm plot for DLC/5 coated 3D ABS, Verogray and moulded ABS showing both sorption and desorption curves at 25 ℃ and 40 ℃

Appendix VI

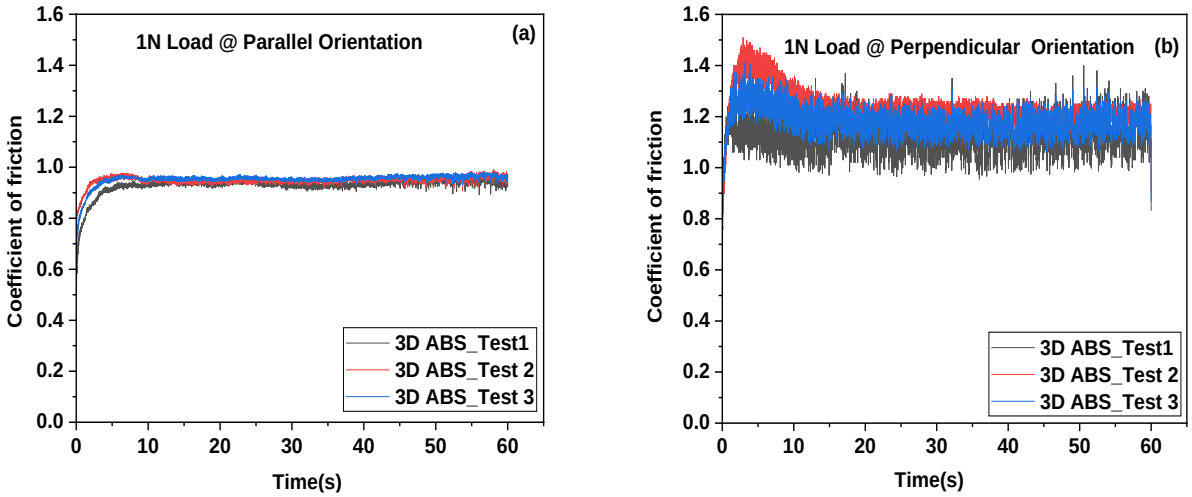

Figure 0-1- CoF plot showing experimental repeat for 1N load on 3D ABS (a) parallel orientation (b) perpendicular orientation.

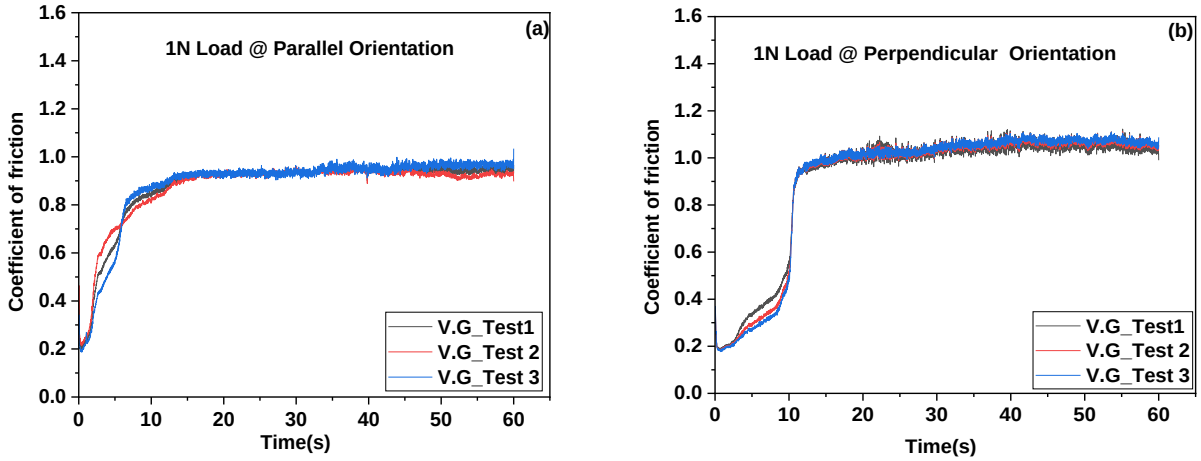

Figure 0-2- CoF plot showing experimental repeat for 1N load on Verogray (a) parallel orientation (b)perpendicular orientation.

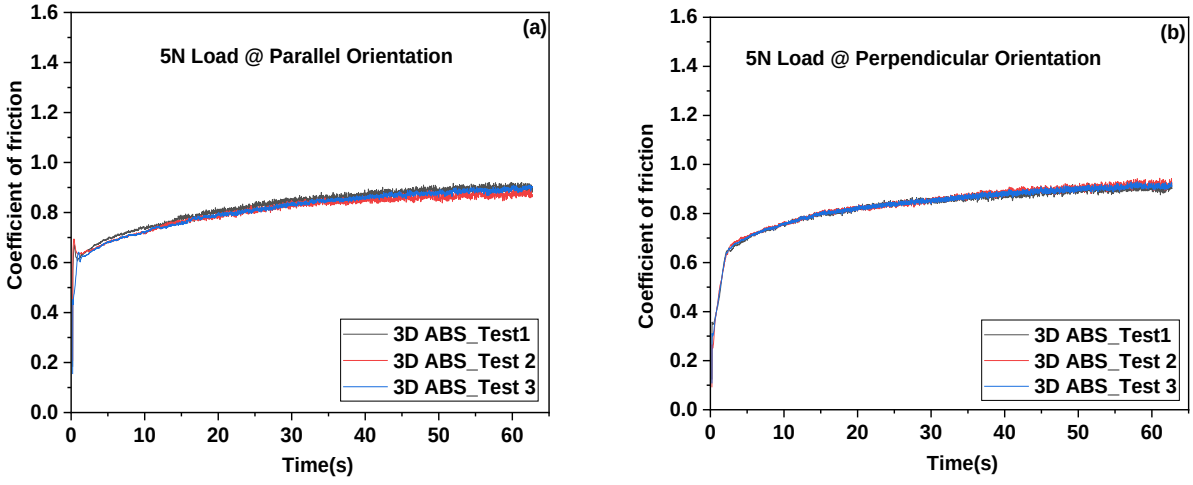

Figure 0-3- CoF plot showing experimental repeat for 5N load on 3D ABS (a) parallel orientation (b) perpendicular orientation.

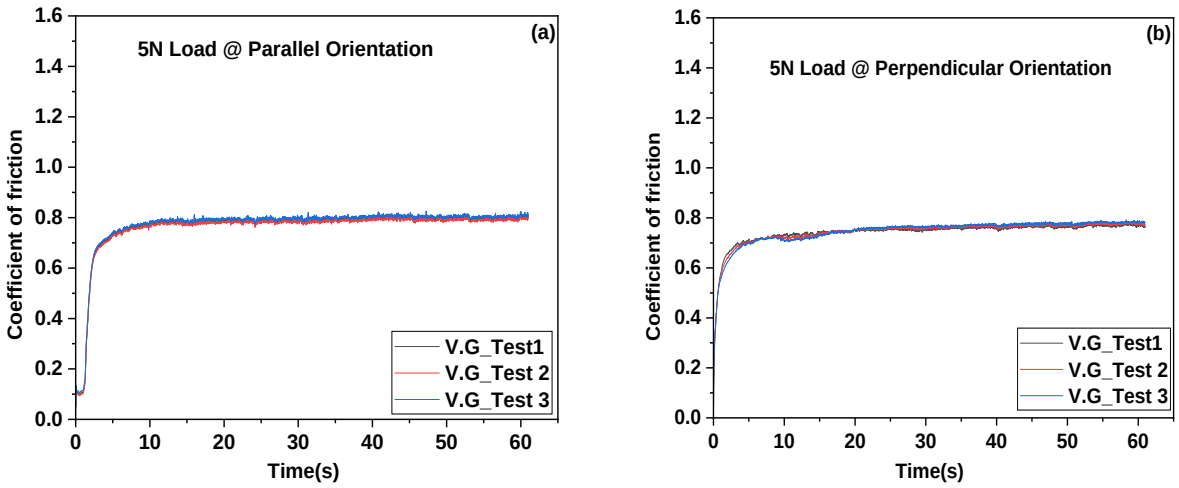

Figure 0-4- CoF plot showing experimental repeat for 5N load on Verogray (a) parallel orientation (b) perpendicular orientation.

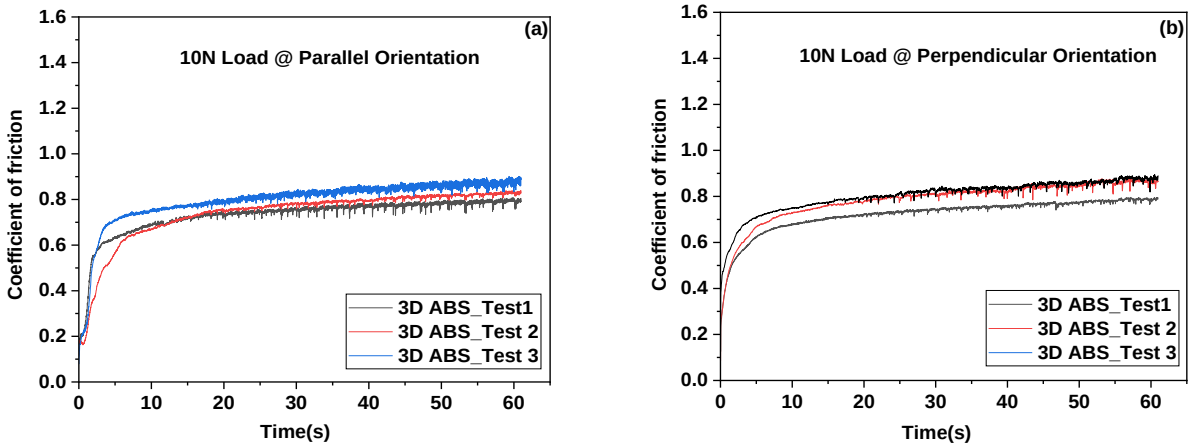

Figure 0-5- CoF plot showing experimental repeat for 10N load on 3D ABS (a) parallel orientation (b) perpendicular orientation.

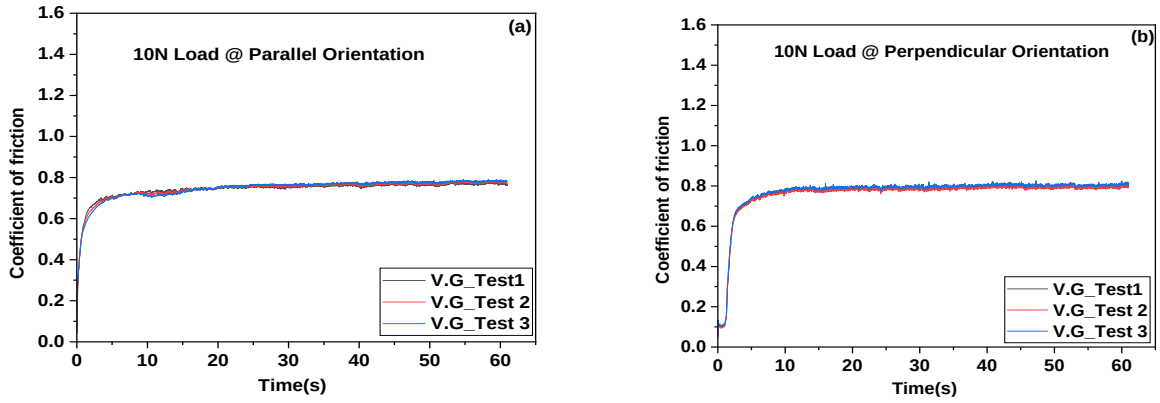

Figure 0-6- CoF plot showing experimental repeat for 10N load on Verogray (a) parallel orientation (b) perpendicular orientation.